DISS. ETH NO. 23382

OPTIMAL DESIGN OF TEMPERATURE SWING ADSORPTION PROCESSES FOR THE CAPTURE OF CO_2 FROM FLUE GASES

A thesis submitted to attain the degree of

DOCTOR OF SCIENCES OF ETH ZURICH

(Dr. sc. ETH Zurich)

presented by

LISA JOSS

MSc ETH PE, ETH Zurich

born on March 6th, 1988

citizen of Bern, Switzerland

accepted on the recommendation of

Prof. Dr. Marco Mazzotti (ETH Zurich), examiner

Prof. Dr. Giuseppe Storti (ETH Zurich), co-examiner

2016

ACKNOWLEDGEMENTS

First and foremost, I would like to express my gratitude to Marco Mazzotti, for accepting me as a master student, and later for giving me the opportunity of carrying out my Ph.D. studies in his group. I am grateful for his continuous support and for entrusting me with the occasional teaching of classes. There are many traits of Marco that I deeply admire. His enthusiasm for science, thoroughness and eye for detail make him a remarkable scientist, and his trust in his collaborators results in a highly cooperative atmosphere within the group. I feel lucky to have crossed roads with him, and hope that this collaboration will continue in the future.

I would also like to thank Giuseppe Storti, for accepting the task of co-examiner of this thesis, and for his interest in my work.

Special thanks go to my closest collaborators Max, Dorian and Matteo. I very much enjoyed working with them, and I am grateful that I always had someone with whom I could discuss ideas, or someone I could ask for an honest opinion. I also acknowledge all the students I have supervised or co-supervised for contributing directly to my work, and for giving me the opportunity to learn something more and hopefully become a better supervisor.

I would like to thank Mischa, Daniel and Markus, for coloring the daily life in G16 with music and an occasional laugh. The nice working climate extended beyond the barriers of G16 and of adsorption processes to the entire Separation Processes Laboratory. In this regard, I thank all former and present colleagues and friends, who have contributed to it by always being available to lend a hand. I would like to point out Fabio, Franziska, Hari, Martin, Johannes, Nathalie and Johanna.

A large part of the research reported in this work was conducted in the framework of a project co-funded by by the commission for technology and innovation and by Casale Group, Lugano. I would

like to thank Andrea Guarino, Cristina Ferrini and Ermanno Filippi for their continuous support, and for the insightful meetings.

Although this is not reflected in my thesis, I did spend a lot of time in the lab. I would like to thank Daniel Trottmann for his patience to fit yet another component to the small column setup and for his help and skills with the TSA setup.

Finally, a thought to my family, and special thanks to Thomas—for his support, for his friendship and for his love that reaches beyond seas and oceans.

For a successful technology, reality must take precedence over public relations, for Nature cannot be fooled.

Richard Feynman

ABSTRACT

The capture of CO_2 from flue gases is a relevant separation task in the set of carbon capture and storage technologies (CCS), which aim at reducing anthropogenic greenhouse gas emissions in order to mitigate climate change. Because of the very large flow rates of flue gas, and the rather high energy requirement of commercial liquid scrubbing technologies, a growing number of alternative technologies are being investigated. While liquid scrubbing processes are hampered by the volatility of the solvents used, adsorption processes rely on solid sorbents, which are non-volatile, exhibit a greater stability and lower desorption heat. Moreover, temperature swing adsorption (TSA) processes only require thermal energy, providing an additional benefit over pressure- or vacuum swing adsorption processes. TSA involves a multi-column and dynamic operation; the design of such processes is a challenging task due to the many degrees of freedom involved. The aim of this thesis is to advance the understanding of the design of TSA processes by developing and applying mathematical methods with different levels of complexity and accuracy.

In a first part of this work, a detailed model describing the operation of TSA processes is calibrated for a pertinent adsorbent-adsorbate system, namely zeolite 13X-CO_2/N_2. In particular, single column dynamic experiments are carried out for the estimation of transport parameters in a lab-scale setup. The performed experiments indicate that the adsorption dynamics of the investigated system are more sensitive to heat transfer than to mass transfer. After calibration, the model is able to predict the outcome of cyclic TSA experiments with sufficient accuracy.

An equilibrium-based shortcut model is developed with the aim of gaining a better understanding of the global behavior of TSA processes. A semi-analytical solution of the cyclic steady state is presented for a four step cycle. Important trends are revealed by performing a parametric analysis of the operating conditions on the relevant quan-

tities, that is, purity, recovery, specific thermal energy consumption and productivity. Optimal operating conditions are identified and a trade-off between productivity and specific energy consumption is presented and discussed.

Based on the insight gained from the shortcut model, more elaborate cycle configurations are designed and assessed for their use with zeolite 13X and for two applications: CO_2 capture and utilization and CO_2 capture and storage. The detailed model is used to investigate the different cycles by optimization of the operating conditions. The effect of plant-wide factors are accounted for in the optimization, namely the energy penalty assigned to flue gas drying, heat integration possibilities, and scheduling of the cycle steps for the continuous operation using multiple columns. The cycle configuration is observed to have a large impact on the process performance: among the investigated cycles, a novel six step cycle achieves for the first time stringent specifications required for CCS. Namely, 96% CO_2 purity and 90% recovery are achieved with a commercial adsorbent, a conventional shell and tube column and for heating temperatures below 150 °C. The performance of this optimized TSA process is similar to that of commercial amine scrubbing while keeping the inherent benefits of TSA.

Finally, a class of recently discovered materials is investigated for their use in TSA processes. Specifically, diamine-appended metal organic frameworks exhibit temperature dependent step-shaped CO_2 adsorption isotherms with negligible hysteresis. The shortcut and detailed models mentioned above are used to investigate the performance of five recently reported materials of this class for post-combustion CO_2 capture by TSA. Even though the isotherm shape of these materials seems promising, only two of the considered materials allow achieving CCS specifications. Recognizing that optimal performance can only result from a synergism between process design and material characteristics, step-shaped isotherms and process conditions were optimized simultaneously for highest productivity and lowest specific energy consumption. The resulting isotherms can be interpreted as a target for material design.

The results achieved in this thesis show that the separation of CO_2 from flue gases can indeed be carried out by TSA, and they present a methodology for the systematic design such processes.

SOMMARIO

La separazione della CO_2 dai fumi di combustione è un operazione che si situa nell'ambito della cattura e stoccaggio della CO_2 (CCS), il cui scopo è la riduzione di emissioni a effetto serra per attenuare i cambiamenti climatici. Al fine di sviluppare processi di cattura con ridotto impatto energetico, sono state proposte tecnologie alternative ai processi commerciali basati sull'assorbimento in fase liquida, con lo svantaggio inerente legato all'uso di solventi volatili. I processi di adsorbimento sono una delle alternative proposte. Questi processi necessitano di sorbenti solidi che, rispetto a quelli liquidi, presentano il vantaggio di non essere volatili, di essere maggiormente stabili, e di essere caratterizzati da un ridotto calore di desorbimento. Inoltre, i processi TSA (temperature swing adsorption), il cui funzionamento è basato sulla capacità differente di adsorbimento a diversa temperatura, necessitano principalmente di energia termica, fattore che costituisce un vantaggio ulteriore rispetto a una rigenerazione del sorbente basata su un cambiamento di pressione (processi PSA/VSA). I processi TSA coinvolgono più colonne a letto fisso operate in modo dinamico; la progettazione di questi processi è intrinsicamente laboriosa, dato l'elevato numero di gradi di libertà che comporta. Lo scopo di questa tesi è una comprensione approfondita della progettazione di processi TSA per la cattura di CO_2 dai fumi di combustione tramite modelli matematici di complessità e accuratezza variabile.

La prima parte del lavoro prevede l'uso di un modello dettagliato per la stima dei parametri di trasporto per il sistema binario CO_2/N_2 tramite esperimenti a singola colonna. I risultati indicano che il comportamento dinamico di questo sistema risulta significativamente influenzato dalla velocità di trasferimento di calore piuttosto che di materia. Il modello così calibrato è utilizzato per predire con adeguata accuratezza l'esito di esperimenti TSA ciclici a due colonne.

Una comprensione più approfondita del processo è ottenuta mediante l'uso di un modello semplificato, basato sull'assunzione di equilibrio locale tra fasi. Si presenta quindi una soluzione semi-analitica dell'o-

perazione di un ciclo a quattro stadi al suo stato stazionario ciclico. Le analisi parametriche effettuate permettono di mostrare come i parametri del processo influenzino le prestazioni in termini di purezza, recupero, consumo specifico termico e produttività. Sulla base delle condizioni operative ottimali e fattibili così identificate, è possibile individuare un compromesso tra produttività e consumo termico.

Sulla base dei risultati accolti e analizzati, sono concepite configurazioni di cicli più avanzate. Le prestazioni di questi cicli operati con un adsorbente zeolitico di tipo 13X sono valutate in condizioni operative ottimali nel caso di applicazioni di cattura e stoccaggio della CO_2, e di cattura e utilizzo in impianti chimici. L'ottimizzazione delle condizioni operative coinvolge anche aspetti dell'impianto esterni al TSA, ad esempio il consumo energetico legato all'essicamento dei fumi, il ricupero di calore via integrazione e la pianificazione degli stadi del ciclo per ottenere un processo continuo. In tale ambito, si osserva che la configurazione del ciclo ha un impatto significativo sulle prestazioni. Fra i cicli studiati, un nuovo ciclo a sei stadi permette per la prima volta di raggiungere le elevate specifiche richieste nell'ambito della CCS, ossia una purezza maggiore del 96% e un recupero maggiore del 90%, con un adsorbente commerciale e con una colonna a fascio tubiero. Questo particolare processo TSA raggiunge delle prestazioni paragonabili a quelle di unità commerciali basate sull'impiego di ammine, conservando tuttavia i vantaggi dei sorbenti solidi.

Infine, sono analizzate le potenzialità di una classe di materiali scoperta di recente per il suo utilizzo nei processi TSA. Si tratta di materiali metallorganici microporosi (MOFs) funzionalizzati con gruppi diamminici; le isoterme di adsorbimento della CO_2 di tali materiali presentano un peculiare andamento a "gradino". La valutazione delle prestazioni di cinque materiali diversi in un ciclo TSA a quattro stadi rivela come queste particolari isoterme consentano miglioramenti notevoli rispetto ad adsorbenti commerciali. L'analisi effettuata permette inoltre l'dentificazione di criteri di progetto per il raggiungimento di prestazioni ottimali e robuste sfuttando tali materiali.

I risultati ottenuti nell'ambito di questo lavoro sottolineano come i processi TSA siano una valida soluzione per la cattura della CO_2. Inoltre, le conclusioni a cui si è giunti rappresentano le basi per una progettazione sistematica dei processi analizzati.

CONTENTS

LIST OF FIGURES

LIST OF TABLES

1 INTRODUCTION

The intention of this chapter is to introduce the reader to the framework of this thesis, to basic concepts of adsorption processes and to present an overview of the state-of-the-art for the different topics covered in this thesis, i.e., modeling of cyclic adsorption processes, specifically temperature swing adsorption processes, as well as their design and optimization.

1.1 ADSORPTIVE SEPARATIONS IN THE CONTEXT OF CLIMATE CHANGE MITIGATION

Climate change mitigation is a topic currently more relevant than ever; the latest conference of the parties (COP) of the united nations convention on climate change (UNFCCC) held in Paris in December 2015 ended with 195 nations reaching an agreement to combat climate change.[1] A few elements in particular accredit this agreement as the start of a new era and triggered incommensurable enthusiasm.[2] These are (i) a collective consensus on the impact and risks of climate change, (ii) a collective consensus on the necessity of emission reduction, (iii) a clear and, for the first time, also long-term pathway for future emissions with the aim of containing global warming well-below 2 °C, (iv) the commitment of all countries to contribute, though regarding the specific needs of developing countries.

Global temperature rise is directly related to greenhouse gas emissions, among which CO_2 is the main contributor. Climate scenarios predict that a drastic transformation of the global energy supply is necessary in order to stay below the accepted target (2 °C to 1.5 °C warming as compared to pre-industrial era).[3] More particularly, three elements are decisive: energy efficiency measures, renewable energy

sources, and low-carbon energy supply technologies, such as CO_2 capture and storage (CCS).[4,5]

CO_2 capture and storage itself consists in a set of technologies aimed at capturing CO_2 transporting and utilizing and/or storing it in adequate geological formations. CO_2 can be captured at point sources such as flue gases of fossil-fueled industrial- or power-plants (post-combustion capture), in which case it enables a continued use of the existing plants while reducing their CO_2 emissions; it can also be captured from the atmosphere (direct air capture, or DACCS when combined with storage) to achieve a net reduction of atmospheric CO_2 (negative emissions). The common denominator to the aforementioned technologies is the separation of CO_2 from N_2 and/or from other components. One of the major differences lies in the composition of the feed, more particularly the corresponding CO_2 content, which varies significantly and heavily impacts the required energy to drive the separation.[6]

The most common approach for post-combustion CO_2 capture exploits liquid-phase absorption. However, absorption processes suffer from large energy penalties associated with the high heats of absorption and with the large heat capacity of the aqueous solvents. Moreover, it suffers from environmental issues tied to corrosion of process equipment, to the volatility of the solvent and to possible degradation products.[7,8] As an attempt to overcome these shortcomings, a considerable research effort has been invested in alternative separation processes.[9] Particularly, solid physical adsorbents possess several advantages compared to absorption approaches: they are not corrosive, non-volatile and are associated to a possibly lower energy penalty.[10]

This work focuses on post-combustion capture of CO_2, i.e., the separation of CO_2 from a flue gas at near-atmospheric pressure and with a CO_2 content of about 10% to 15% on a volume basis, and the rest primarily consisting of N_2. This composition is typical of flue gases originating from the combustion of coal, which represents a major contribution to the global CO_2 emissions amounting to 46% in 2013.[11] For such cases, temperature swing adsorption (TSA) is regarded as an interesting option: it requires practically only thermal energy, as opposed to the predominantly electrical energy penalty of pressure

or vacuum swing adsorption, and the regeneration could be driven by waste heat or low-grade heat sources. A niche of applications for a very similar separation task lies in the chemical industry. For instance, the CO_2 emitted in the flue gas of reformers or boilers in methanol and ammonia/urea plants could be recovered to enhance the yield of the methanol or urea synthesis.[12] Although the implementation of this CO_2 capture and utilization process would not directly contribute to climate change mitigation, it represents a very interesting case study, since it provides an economically viable framework to develop, implement and eventually test novel separation processes that must fulfill requirements similar to post-combustion CCS.

1.2 PRINCIPLES OF ADSORPTION PROCESSES

The essential requirement of adsorption separation processes is a selective adsorbent that preferentially adsorbs one component (or class of similar components) thereby creating a new phase, the adsorbed phase, whose composition differs significantly from the gas phase. Under equilibrium conditions, the adsorbed phase composition depends on the fugacity of the components in the gas phase, i.e., on temperature, pressure and composition, as well as on the chemical and physical properties of the solid. The interactions between the solid and adsorbed phase can be of different nature including electrostatic interactions (polarization, dipole and quadrupole), van der Waals interactions and chemical bonds. The pure component phase equilibrium is usually represented by the sorbent uptake vs. partial pressure at constant temperature. Such curves, denoted adsorption isotherms, are typically convex, as depicted in Figure 1.1 (note that according to IUPAC, a convex isotherm is characterized by a continuously decreasing slope, as opposed to a convex function). In the low-pressure regime, the isotherm is a nearly linear function of partial pressure, while at higher pressures, the saturation capacity is approached and the adsorption isotherm flattens. Adsorption is an exothermic process (with very few exceptions[13]), so that components can be desorbed upon an increase in temperature.

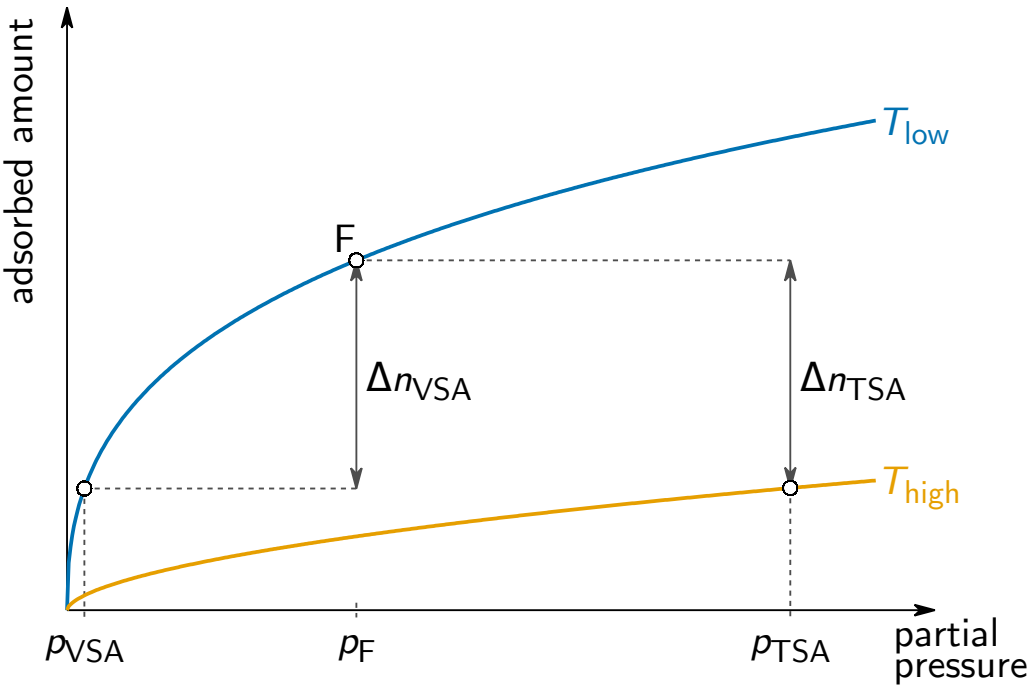

Figure 1.1. – Illustrative adsorption isotherms at two different temperatures. A given cyclic capacity can be achieved by desorbing under vacuum conditions (Δn_{VSA}), or by desorbing at a higher temperature (Δn_{TSA}).

In liquid equilibrium-based separation processes, e.g. absorption, the separation is carried out by counter-currently flowing the gas phase and the sorbent, thereby creating a cascade of spatially distributed equilibrium stages. Such a continuous operation cannot be easily implemented for adsorption-based processes due to the solid nature of the sorbent and the difficulties associated with their movement. Therefore, when exposed to a gas phase of a given composition, the adsorbent will gradually uptake adsorbate molecules and eventually become saturated. A separate regeneration step is required to remove or recover the adsorbed phase making such processes dynamic.

In order to simulate a continuous operation, adsorption processes are operated by cycling a fixed bed column through a given sequence of steps, called a cycle, consisting of at least one loading (adsorption) step and one regeneration (desorption) step. We consider as an example a binary system consisting of a non-adsorbing (light) target

component, and a non-desired component that adsorbs according to the isotherm shown in Figure 1.1. For the purification of the light component, the feed can be contacted with the sorbent at pressure and temperature conditions corresponding to point F in order to adsorb the undesired component and produce a pure light product. Upon an increase in temperature, the impurity will partially desorb, hence the adsorbed amount decreases as the partial pressure in the gas phase increases as compared to that of the feed. At the end of the regeneration the cycle can be started anew. A certain cyclic capacity (Δn_{TSA}) can be achieved by cycling the operating temperature (TSA), or else by cycling the operating pressure, i.e., by drawing vacuum to reduce the partial pressure (vacuum swing adsorption, VSA), or by first compressing the feed to a higher pressure and regenerating at or above atmospheric pressure (PSA, not shown in Figure 1.1).

In order for an adsorption-based process to be capable of treating a continuous feed and delivering a product continuously, several columns are typically operated in a cyclic manner simultaneously and appropriately shifted in time. The separation efficiency of the process and its performance (energy consumption and productivity) will not only depend on the operating conditions, e.g. step times, pressure levels, or temperature levels in the case of heating and cooling, but it will also depend on the cycle configuration, i.e., the number, sequence, direction and inter-connectivity of the cycle steps. It is clear that a multitude of possibilities exist, which makes the design of such processes challenging, but at the same time, it offers a higher flexibility than steady state processes.

Adsorptive separations are known since the 1930s when the first patents on pressure swing adsorption (PSA) were issued, and have gained momentum in the 1960s with the commercialization of synthetic zeolites and the publication of the Skarstrom cycle.[14] Since then, cyclic adsorption processes have been extensively studied and applied for gas separations, and purification processes can achieve purities as high as 99.999% whenever the product is the less retained (light) component.[15] This has created the basis for processes which are now commercially available and extensively applied at industrial scale. Examples are pressure swing adsorption (PSA) processes for H_2-purification,[15] or temperature swing adsorption (TSA) for prepu-

rification units in front of cryogenic air separators removing H_2O, CO_2, N_2O.[16,17] In 2005 the total worldwide H_2 production by PSA amounted to about 1×10^7 m^3/h, and the total worldwide air streams treated by TSA prepurification units amounted to about 5×10^7 m^3/h.[18]

1.3 RECOVERING THE HEAVY COMPONENT

In post-combustion CO_2 capture applications the feed stream is typically composed of CO_2 and N_2 together with some impurities (H_2O, O_2, SO_X, NO_X). The target CO_2 product will always adsorb more strongly on commercial adsorbents than N_2 because of its larger polarizability and its quadrupole moment.

Standard cycle configurations, which include a feed step carried out at high pressure or low temperature (stripping cycles) can theoretically achieve pure light component. When applied to the purification of the heavy component, the purity of the target heavy product is limited by the amount of non-selective gas phase contained in the column voids at the beginning of the desorption step, and is further decreased by the use of a purge gas. Cycle configurations aimed at producing the light product at high purity can therefore not by applied for CO_2 capture and the design of cycle configurations leading to high purity CO_2 still remains a challenge which is the topic of ongoing research. In the following, a review of the state-of-the-art in the design of cyclic adsorption processes aimed at recovering the heavy component is given. Note that while the large majority of the literature on this topic considers PSA/vacuum swing adsorption (VSA) processes, these concepts can be easily translated to TSA processes by substituting blowdown and pressurization steps with heating, and cooling steps, respectively.

A few works have dealt with a different class of cycles, so-called rectifying cycles, whose distinguishable characteristic is that a low pressure or high temperature feed step is carried out, during which the heavy component is produced at high purity. While theoretical considerations of these cycles have shown that pure heavy component can be achieved for linear isotherms,[19–21] a large portion of the heavy product must be recycled to the column at high pressure or

low temperature. Moreover, the conditions under which the heavy component is produced are such that, for favorable isotherms, a disperse composition front propagates through the column (simple wave transition), thus leading to a large portion of unused bed. From these considerations it can be concluded that this class of cycles is unattractive both from the point of view of the productivity and the energy consumption. The general trend in the design of adsorption processes aimed at recovering the heavy product at high purity is in fact directed towards the design of more complex stripping cycles (feed step at high pressure/low temperature).

Over the last decade, a series of works have investigated different cycle configurations for VSA/PSA separations aimed at recovering the heavy component. One of the two main strategies for cycle synthesis is based on heuristics, which arise from a solid understanding of the process and particularly of the adsorption dynamics, and where the operating conditions are optimized for a fixed cycle configuration.[22–26] Alternatively, a superstructure approach is used to rigorously optimize both the cycle configuration and the operating conditions simultaneously by solving the corresponding mixed integer non-linear problem.[27,28] Although there theoretically exist infinite different possible configurations, it is interesting to note that the best cycles obtained with both heuristic and superstructure approaches contain similar elements that appear to be decisive in obtaining high purity and recovery of the heavy product (separation specifications). These are (i) a blowdown step to an intermediate pressure carried out before the actual evacuation step from which the target product is collected, (ii) a heavy product reflux, where either a fraction of the pure product, or an enriched stream is recycled to the column after the adsorption step (iii) additional steps where streams possibly enriched in the light product are recycled back to the cycle with the aim of increasing the recovery of the heavy product. Cycles that result in high separation specifications are not necessarily the same as those achieving high productivity and low energy consumption (separation performance), and no real consensus has emerged on which cycle configurations are the most promising for achieving both high specifications and high performances. Agarwal et al.[27] showed how the superstructure converges to cycle configurations that include pressure equalization steps when optimizing the energy consumption subject to specifications on

the purity and recovery. On the other hand, the results of Casas et al.[24] clearly show that increasing the number of pressure equalization steps decreases the productivity of a pre-combustion capture PSA process. Haghpanah et al.[29] found that while a counter-current light product pressurization was crucial for obtaining larger performances, the addition of heavy reflux steps compromised both the productivity and the energy consumption, on the other hand, Reynolds et al.[22] found that for some of the investigated cycles, the addition of a heavy reflux could increase the productivity. These contradictory findings were, however, obtained in works that were carried out for the separation of different components and using different adsorbents. Realizing this, one concludes that there is no plug and play solution for the design of cyclic adsorption based processes: the cycle configuration and operating conditions, which make up for many degrees of freedom, must be tailor-designed for the specific material, and separation targets.

1.4 OPTIMIZATION OF CYCLIC ADSORPTION PROCESSES

Due to the possible formation of steep composition fronts, and the dynamic nature of the process, its performance in terms of product purity, component recovery, productivity and energy consumption can vary strongly upon a small change in the operating conditions. This is especially pertinent to step durations. The performance of a process must therefore be assessed for optimal operating conditions. Extensive parametric analysis yields robust solutions if the design space is scanned with an appropriate resolution. However, this approach requires a large number of simulations and hence computation time is very large.

Systematic optimization algorithms can direct the search towards optimal operating points, therefore reducing the number of necessary simulations. As far as adsorption cycles are concerned, three main approaches have been proposed. For example, Agarwal et al.[27] tackled the optimization problem with an equation oriented approach where the partial differential equations (PDEs) of the column model are ex-

pressed as constraints of the optimization problem, such as to impose cyclic steady state (CSS). As a consequence of the complete discretization of the PDE equations, the authors have to cope with a large scale nonlinear optimization problem with 30,000 to 50,000 variables and constraints. Jiang et al.[30] suggested an alternative approach, where the convergence to CSS is accelerated by incorporating the CSS condition as a constraint of the optimization problem in which both design variables and initial states are optimized. Therefore, the CSS condition must be guaranteed only at the optimal point with a considerable saving of computational time. Finally, black-box approaches[29,31,32] rely on efficient *ad hoc* solvers of the partial differential algebraic equations (PDAEs) of the column model and an external optimization algorithm to optimize the independent design and operation variables (typically between 3 and 10).

Black-box optimization is the most commonly used approach. Nevertheless, it is important to note that the related optimization problem turns out to be extremely challenging, in particular: (i) The numerical solvers employed to solve the PDEs of the model may make objective function and constraints noisy and non-smooth, (ii) every cycle simulation needs to reach the condition of CSS, which often requires considerable computation time (about 1 min to 10 min for every function evaluation), (iii) there exist nonlinear constraints, such as separation targets, and (iv) the nonlinear nature of the objectives and constraints introduces the possibility of multiple local minima, thus necessitating global optimization methods. As an additional challenge, the process performance is typically evaluated using conflicting objectives, i.e., energy requirement and productivity, which calls for the use of multi-objective optimization techniques.

To date there exists no commercially available optimization algorithm able to tackle all the difficulties associated to the black box optimization problem. The non-sorting genetic algorithm is most commonly used.[29,33] It can handle multiobjective problems, but the nonlinear constrained problem must be converted into a non-constrained problem, e.g. with a penalty approach, and proof of convergence does not exist.[34] On the other hand, efficient global optimization approaches which can handle non-linear constraints usually consider only a single objective.[35,36]

1.5 CARBON CAPTURE BY TEMPERATURE SWING ADSORPTION

While VSA/PSA processes have been receiving considerable attention as alternative post-combustion CO_2 capture technology in the last decade, and considerable work on cycle design and integration within coal-fired power plants was carried out,[37] development of TSA processes has been lagging behind, and the lessons learned from PSA processes have yet to be applied.

The reason for this seems to be two fold. First, conventional, industrially applied TSA processes aimed at purifying the light component are heated directly with a hot purge gas, which drastically dilutes the heavy product. For the purification of CO_2 indirect heating and cooling is indeed necessary, which calls for more complicated column geometries. As an additional challenge, TSA cycles are known to suffer from long heating/cooling times, hence long cycles of up to a few hours and low productivity.[21,38,39] On the other hand, TSA could prove advantageous because most of the energy requirement can be supplied by thermal energy, as opposed to the largely electrical power demand of PSA/VSA processes. Moreover, the regeneration could be driven by waste heat or low-grade heat sources. In fact, the heat demand is distributed over a range of temperatures typically found between 30 °C to 150 °C, as opposed to absorption based processes, for which most of the heat demand is at a constant temperature near the boiling point of the solvent, i.e., 100 °C for water, and is usually provided by steam.

The drive to develop more efficient TSA processes rests on three pillars: tailor-designed material synthesis, design of columns that enable heat transfer intensification, and the optimal design of cycle configuration and operating conditions. In the following, a brief overview of the most relevant and recent advances in these three research topics is provided.

MATERIALS ENGINEERING Metal organic frameworks (MOFs) are recognized to have the potential of making a significant impact on separation processes since this class of materials provides the enable the

synthesis of porous materials with controlled pore sizes, surface areas and chemical compositions. In order to tailor-design materials, insight into quantitative structure-property relationships are required to shed light on the relation between microscopic structural and chemical properties and macroscopic adsorption properties, such as adsorption capacity, Henry's coefficient or selectivity.[40,41] Potentially interesting metal organic framework (MOF) materials have emerged from the combination of high-throughput screening methods[42,43] with material engineering directed towards TSA processes. Examples of promising materials featuring mechanical and hydrothermal stability, large capacity for CO_2 and high CO_2/N_2 selectivity are MOF-74 (also known as CPO-27), UTSA-16 and UiO-66. Moreover, a remarkable class of diamine-appended MOFs were synthesized and studied[44–46] for which a reversible and cooperative insertion of CO_2 into the framework can happen. These materials exhibit a unique reversible step-shaped isotherm, and due to the chemical nature of their interaction with CO_2, the presence of water does not affect their affinity for CO_2.

HEAT TRANSFER INTENSIFICATION Intensification of heat transfer to overcome the hurdle of long cycle times and low productivity is either done by modifying the geometry of the column, more specifically decreasing the heat capacity of the column wall and increasing the surface area for heat exchange, or by formulating the adsorbent into structured packings with increased heat conduction properties. For example, Meunier and co-workers[47,48] designed a custom column consisting of concentric stainless steel tubes. The outer surface of the outer tube is insulated to prevent heat losses, while heating and cooling is performed by convection of a hot or cold fluid in the inner tube. The annular part of the construction is packed with spherical adsorbent particles, and the heat transfer is enhanced by the presence of 12 metallic fins welded on the inner tube, and traversing the packed bed. Structured sorbents, such as coated monoliths, foams or hollow fibers can also provide increased heat conduction properties of the fixed bed. For example, Rezaei et al.[49] investigated the use of hollow fibers loaded with adsorbent material, as a novel contactor type for rapid TSA. The used hollow fibers are hybrid materials: solid sorbent crystals are embedded into a porous polymeric hollow fiber matrix of ca 1 mm to 2 mm diameter. The inner lumen is coated with an

impermeable layer, such that a thermostatting fluid, e.g. hot and cold water, can be used to control the temperature. Their results indicate that the increased heat and mass transfer coefficients can be exploited for rapid cycling achieving cycle times as low as 3 min. While structured sorbents can provide increased heat transfer kinetics, the adsorbent loading in the bed, tends to be compromised due to the use of supports, and of thin adsorbent layers, hence decreasing the volumetric productivity.

CYCLE SYNTHESIS Studies dealing with indirectly heated TSA processes for the capture of CO_2 are rather recent, with the first ones appearing in the early 2000's.[50,51] Indirect heating has brought new possibilities in the design of TSA cycles, as compared to the traditional two step cycle consisting of an adsorption step, and a regeneration making use of a hot N_2 purge. Walton and LeVan[52] proposed a simple three step cycle aimed at producing high purity CO_2; the novel features were the absence of any purge gas for the regeneration, and the presence of a closed cooling step in order to avoid starting the adsorption step when the bed is still warm. Grande et al.[53] and Ntiamoah et al.[54] considered the use of a hot CO_2 product rinse step to avoid product dilution. Table 1.1 reports a summary of the most relevant research articles of CO_2 capture by TSA that consider the entire cycle at its CSS. The entries are ordered according to their date of publication, and it is striking that, although the cycle complexity has increased, the considered configurations are all much simpler than what is currently the state of the art in PSA/VSA cycle design. Moreover, a systematic analysis and optimization of the operating conditions is often lacking.

Research advances in materials engineering, heat transfer intensification and cycle synthesis all have the potential to individually contribute to enhancing process performance. The impact of such novel technology elements, should ultimately be assessed based on the process costs, or alternatively based on the metrics governing the process costs, i.e., for TSA specific energy consumption and productivity. Considering the entire process is indeed a necessity; it was nicely shown recently by Rajagopalan et al.[59] for a CO_2 capture process by VSA that the use of simple metrics, e.g. Henry coefficient, absolute

Table 1.1. – Summary of the most relevant literature on CO_2 capture by TSA. Only those studies that investigating the cyclic process at cyclic steady state (CSS) are considered. The performance of the set of operating conditions yielding the best results is shown for each reference and material. The number of studies operating conditions is indicated in brackets for experiments (exper.) and simulations (sim.)

Material	Column	Cycle[a]	y_{CO_2} (–)	T_{low} (K)	T_{high} (K)	Purity (–)	Recovery (–)	Productivity (kg/(m^3 h))	Energy (MJ/kg)	Comments	Ref.
13X	packed, fins	ads/purge	0.10	288	423	0.94	0.65	25	8.8	exper. (1)	[55]
5A	packed, fins	ads/purge	0.10	288	423	0.94	0.74	37	6.0	exper. (3): vary times	[55]
activated carbon	packed	ads/purge/cool	0.17	air[b]	373[c]	0.43	0.40	30	n.a.	exper. (1)	[56]
5A	packed, fins	ads/purge	0.10	293	433	0.95	0.80	n.a.	3.2[c]	sim. (55): vary purge, T_{high}	[48]
13X-APG	packed	ads/heat/purge/cool	0.15	298	443	0.92	0.78	69	n.a.	exper. (1) and sim. (3): vary purge rate	[25]
carbon composite	honeycomb monolith	ads/heat	0.13	298	403	0.95	0.19	n.a.	n.a.	exper. (1)	[57]
13X-APG	packed	ads/heat/purge/cool	0.15	298	423	0.79	0.77	61	4.7	sim. (5): vary T_{high}	[58]
supported amine	hollow fiber	ads/heat/purge/cool	0.13	308	393	0.90	0.81	n.a.	n.a.	sim. (1)	[49]
NaUSY	packed	ads/heat/rinse/purge	0.15	298	523	0.91	0.84	29	4.5[c]	sim. (6) and exper. (3)	[54]

[a] ads: adsorption, heat: indirect heating, purge: cold N_2 purge, cool: indirect cooling, rinse: hot CO_2 rinse
[b] heating via electrical coil wrapped around the column wall, cooling with air
[c] does not consider the contribution of the column wall

CO_2 capacity, selectivity or working capacity, typically used for adsorbent screening and ranking can be misleading. In fact, it usually does not correspond to the obtained ranking when considering the performance of the process at CSS and for optimal operating conditions. In order to reach the goal of developing truly more efficient processes, synergies between the materials, column design and cycle configuration must be analyzed, understood and exploited. This requires an in depth understanding of the process, more specifically how the operation is affected by model parameters, e.g. the adsorption equilibrium and heat transfer resistances. Moreover, a specific context must be considered, and the boundaries of the system must be broadened to include the integration of available mass and energy streams. Model-based process design provides the framework to carry out these activities in a systematic way. Models of different fidelity can be applied to different scopes. Although current computers provide the resources to solve rigorous models, which must be used for quantitative assessments, shortcut models remain very helpful tools because they provide an easy way of understanding the global behavior of complex systems, of understanding inherent limits imposed by thermodynamics, and of identifying qualitative trends.

1.6 STRUCTURE OF THE THESIS

Within this context, the goals of this thesis focus on providing a better understanding of TSA processes from the perspective of the cycle configuration, the operating conditions and how these are affected for different classes of materials.

Chapter 2 reviews mathematical models for the detailed simulation of adsorption processes and presents the model used in the subsequent chapters. Since most of the work is model based, the first objective of this thesis is a successful calibration and validation of an adsorption column model for the simulation of indirectly heated cyclic TSA processes, as reported in chapter 3.

In chapter 4, an equilibrium-based shortcut model of a simple four step TSA cycle is developed, validated against detailed simulations and used to study the effect of operating conditions on the key performance

indicators (KPIs) of the cycle, namely purity and recovery of the CO_2 product, productivity and energy consumption. It is shown how simplified models – or shortcut models – can be very useful tools for the preliminary design of separation processes, as they allow a thorougher comprehension of essential trends.

Chapter 5 deals with the design of TSA cycle configurations, presenting an extensive parametric analysis of the operating conditions on the key performance indicators for a post-combustion CO_2 capture application, namely CO_2 purity, CO_2 recovery, productivity and specific energy consumption. This analysis is performed by accounting for plant-wide factors such as the drying of the flue gas, the scheduling of the cycle, the minimum number of columns and possible heat integration strategies. The performance of the presented cycles is assessed for various target specifications corresponding to two rather different applications, namely CO_2 capture and utilization (CCU) and CCS and is compared to the state-of-the-art absorption technology.

The potential of a novel class of materials is investigated in chapter 6. The effect of step-shaped adsorption isotherms on the performance of a simple TSA cycle is assessed. A comprehensive analysis is used to devise the essential features of a well-performing step-shaped isotherm. These heuristics are finally tested against optimal adsorption isotherms resulting from rigorous optimization.

Finally, chapter 7 summarizes the findings of the thesis and provides an outlook on further research directions.

Note that this is a cumulative thesis and, as such, the contents of the various chapters coincide to a large extent with what has been published in a number of peer-reviewed journal papers[60–63] and in two patents[64,65] that are in the process of being filed. Each topic is presented in a complete form: the context is introduced and the necessary definitions are given in each corresponding chapter, separately.

2 MODELING ADSORPTION PROCESSES

PSA/TSA process models consist of material, energy and momentum balances complemented with the appropriate constitutive equations. The description of the pressure and time dependent composition, pressure, temperature and velocity profiles evolving in an adsorption column is obtained by solving the system of partial differential algebraic equations (PDAEs) with the appropriate boundary and initial conditions.

Initial and boundary conditions can be chosen to reflect a dynamic experiment, in which case the resulting outlet composition profiles and temperature profiles can be compared to experimental results. Or else, cyclic boundary conditions that reflect a sequence of cycle steps can be applied to predict the evolution of pressure, temperature and composition during a cyclic operation. Multi-column operation involving recycle steps is simulated by recording the outlet profiles and using them in the boundary conditions of the next cycle. Overall performance indicators are determined based on the outlet profiles once a cyclic steady state (CSS) is reached, i.e., once the state trajectory undergone during a cycle is identical to that of the previous cycle.

Different models with the above-mentioned features have been proposed in the literature; they primarily differ in one or more of the following points:

- The presence or absence of radial gradients.
- The form of the kinetic rate expression(s).
- The considered energy balances.

The reader is referred to a recent review[66] for more details on the available mathematical models of fixed-bed columns for CO_2 adsorption. For the sake of brevity, and without going into too many details, the

points above are discussed specifically in the light of modeling TSA processes, and then the model assumptions and equations considered in this thesis are presented.

RADIAL GRADIENTS It is most common to neglect radial gradients in velocity and concentration. Radial gradients in temperature, on the other hand might be more pronounced and affect the process significantly. Nevertheless, a few studies have investigated the validity of one-dimensional models for the simulation of non-isothermal, non-adiabatic adsorption columns subject to large heat effects by comparison to a two-dimensional model that accounts for radial gradients. Farooq and Ruthven[67] found that the application of a one-dimensional model provides reasonable accuracy for conditions that do not lead to a pure thermal wave, i.e, when the thermal front precedes the concentration wave. Kim et al.[68] did a similar study, but also considered thermal regeneration steps, and found a good agreement between one- and two- dimensional models, provided the energy balance for the column wall is included.

KINETIC EXPRESSION(S) One of the greatest differences among models lies in the level of detail granted to the description of mass transport. Several mechanisms affect the mass transport in porous adsorbent beds, e.g. transfer across the fluid film around an adsorbent particle, diffusive transport across the macropores, and diffusive transport through the micropores. Some researchers prefer accounting for all these resistances individually, leading to multi-dimensional models, where up to three spatial coordinated are discretized,[69–71] i.e., the longitudinal coordinate along the column, the radial coordinate within an adsorbent particle, and the radial coordinate within an adsorbent crystal. Although these models are more rigorous, they are computationally expensive. The simpler linear driving force model has been widely used, and was shown to suffice for equilibrium-controlled separations.[72–74]

ENERGY BALANCES Typically, two or three energy balances are considered when modeling TSA processes. The energy balance of the column wall is almost always accounted for separately. On the other

hand, the energy balances of the fluid phase and of the solid phase can be either accounted for separately,[54,58] or else, thermal equilibrium between solid and gas phases is assumed, and a single energy balance is required for the packed bed.[48,75] The impact of this widely used assumption has not been thoroughly studied, and while a more accurate description could be achieved by considering both energy balances of the gas and solid phases, this would imply an additional model parameter that is difficult to estimate,[76] and a larger system of PDEs.

2.1 MODEL ASSUMPTIONS AND EQUATIONS

The model considered in this thesis is essentially the same as described in Casas et al.[77] with a few minor modifications, previously described in Marx et al.[60] In order to provide a good compromise between accuracy and computational intensity, the following assumptions are made:

1. The gas phase is ideal; this is reasonable considering the low pressure conditions prevailing in TSA processes.
2. Radial gradients in concentration, temperature and velocity are negligible.
3. The momentum balance is accounted for with the Ergun equation, which describes the relation between pressure drop and velocity in porous media.
4. The kinetic and potential energies are neglected in the energy balance.
5. The fluid phase and solid phase are in thermal equilibrium.
6. The mass transfer resistance is described using a linear driving force (LDF) model, where the adsorbed phase concentration is assumed to be homogeneously distributed; this is a reasonable assumption for situations where the time constant of pore diffusion is smaller than that of solid diffusion.
7. The isosteric heats of adsorption, heat capacities, viscosity and heat conductivity are constant; they do not depend on temperature, composition, nor pressure.

Under the above-mentioned assumptions, the material and energy balances of the fixed-bed column can be expressed in differential form. The independent variables are the position z and time t, while the dependent variables to be integrated are the molar fraction of component i (y_i), the temperature (T), the pressure (p) and the adsorbed phase concentration (n_i).

2.1.1 Material balances:

The mass balance of component i is given by:

$$\epsilon_t \frac{\partial(y_i p/T)}{\partial t} + \frac{\partial(u y_i p/T)}{\partial z} + (1-\epsilon_t)\mathcal{R}\frac{\partial n_i}{\partial t} = \epsilon_b \frac{\partial}{\partial z}\left(D_L \frac{p}{T}\frac{\partial y_i}{\partial z}\right) \quad (2.1)$$

where u is the superficial velocity, D_L the dispersion coefficient, ϵ_t is the total porosity and ϵ_b is that of the bed.

The total mass balance is obtained by summing up all component balances:

$$\epsilon_t \frac{\partial(p/T)}{\partial t} + \frac{\partial(up/T)}{\partial z} + (1-\epsilon_t)\mathcal{R}\sum_{j=1}^{C}\frac{\partial n_j}{\partial t} = 0 \quad (2.2)$$

The rate of adsorption is proportional to the LDF:

$$\frac{\partial n_i}{\partial t} = k_i(n_i^{\mathrm{eq}} - n_i) \quad (2.3)$$

with k_i the mass transfer coefficient of component i, and $n_i^{\mathrm{eq}} = n_i^{\mathrm{eq}}(\boldsymbol{y}, T, p)$ is the equilibrium adsorbed phase concentration at the prevailing conditions.

2.1.2 Energy balances

Since fluid, solid and adsorbed phases are assumed to be in thermal equilibrium, a single energy balance is required:

$$(\epsilon_t \overline{C}_g + (1-\epsilon_t)(C_s + \overline{C}_{\text{ads}}))\frac{\partial T}{\partial t} - \epsilon_t \frac{\partial p}{\partial t} - (1-\epsilon_t)\sum_{j=1}^{C}(-\Delta H_j)\frac{\partial n_j}{\partial t} + \\ + uC_g \frac{\partial T}{\partial z} + \frac{2h_b}{R_{\text{in}}}(T - T_w) = \frac{\partial}{\partial z}\left(K_T \frac{\partial T}{\partial z}\right) \tag{2.4}$$

where h_b is the heat transfer coefficient between column wall and adsorbent bed. An average value for the heat of adsorption ΔH_j is considered (depending on the isotherm and operating conditions), as well as average heat capacities of the gas and adsorbed phases:

$$\overline{C}_g = \sum_{i=1}^{C} c_i C_{g,i}^{\text{mol}} \qquad \overline{C}_{\text{ads}} = \sum_{i=1}^{C} n_i C_{g,i}^{\text{mol}} \tag{2.5}$$

The temperature of the column wall is described by the corresponding energy balance:

$$\frac{\partial T_w}{\partial t} = \frac{2}{C_w(R_{\text{out}}^2 - R_{\text{in}}^2)}\left(h_b R_{\text{in}}(T - T_w) - h_w R_{\text{out}}(T_w - T_{\text{fluid}})\right) + \\ + \frac{1}{C_w}\frac{\partial}{\partial z}\left(K_w \frac{\partial T_w}{\partial z}\right) \tag{2.6}$$

The column wall exchanges heat both with the adsorbent bed, and with the thermostatting fluid whose temperature T_{fluid} will either be larger or smaller depending on the nature of the step type, e.g. heating or cooling steps.

2.1.3 Momentum balance

The Ergun equation is used to replace the momentum balance in porous media.

$$\frac{\partial P}{\partial z} = -\frac{150\mu(1-\epsilon_b)^2}{\epsilon_b^3 d_p^2}u - \frac{1.75(1-\epsilon_b)\rho}{\epsilon_b^3 d_p}|u|\,u \tag{2.7}$$

Where d_p is the diameter of the particles and μ the viscosity of the gas. This equation gives a direct relation between the pressure drop and the velocity, therefore, the velocity is not treated as a state variable which is integrated in time, but it is determined solely based on the pressure drop in the column.

2.1.4 Adsorption isotherm

The adsorbed phase concentration in equilibrium with the gas phase, $\boldsymbol{n}^{\mathrm{eq}}(\boldsymbol{y}, T, p)$ is described by a non-linear equation, that must be continuous in order to avoid numerical issues. In chapters 3 to 5, the Sips equation was used to describe the phase equilibrium of CO_2 and N_2 onto zeolite 13X, and in chapter 6 a dedicated weighted dual site Langmuir isotherm was devised and used to describe the equilibrium of CO_2 onto diamine-appended metal organic frameworks.

2.2 SOLUTION PROCEDURE

Equations (2.1)–(2.2),(2.4) and (2.6) are discretized in space into N cells to yield a system of $(2C + 3)N$ ordinary differential equations (ODEs). Discretization of the spatial coordinate is done according to the finite volume technique, as illustrated in Figure 2.1. A more detailed description of how this method is implemented can be found elsewhere.[78,79] The state variables at the first and last half-cell define the boundary conditions, and the VanLeer flux limiter[80] is used to calculate the fluxes at the cell boundaries within the column. The spatial discretization of the Ergun equation (2.7) results in an algebraic equation which is used to determine the velocity from the local pressure drop for every position and time.

The equations are implemented in an in-house developed Fortran simulator, where the ODEs are integrated in time using an available solver (IVPAG, IMSL Visual Numerics or LSODE, LAPACK).

2.2.1 Boundary conditions

Four different types of boundary conditions are used to describe adsorption or purge steps (I), semi-open heating steps (II), semi-open cooling steps (III) and closed steps (IV). These are briefly explained in the following, by referring to Figure 2.1 and always assuming that the flow direction goes from left to right, i.e., from grid point z_1 to grid point z_N.

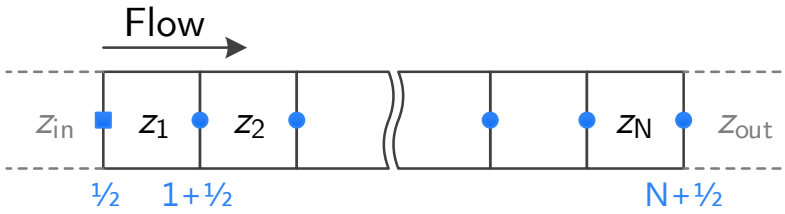

Figure 2.1. – Scheme of the spatial discretization in finite volumes.

BOUNDARY CONDITIONS I These boundary conditions must be such as to reflect the presence of an inlet stream conveyed through the column and an outlet stream exiting from the other column end. The Dankwerts condition cannot be directly applied to a finite volume discretization scheme as it is usually done for finite differences. The formulation of the Dankwerts condition for the inlet is:

$$D\frac{\partial \boldsymbol{y}}{\partial z}\bigg|_{1/2} = v_{in}\left(\boldsymbol{y}_{in} - \boldsymbol{y}_{1/2}\right) \tag{2.8}$$

Determination of the spatial derivative at the column inlet would require an estimate of $\boldsymbol{y}_{1/2}$, which is not known *a priori*. This can be solved by using several ghost cells upstream of the column inlet[80] (the required number depends on the flux limiter), or by using the half-cell approximation, as done by Haghpanah et al.[29] The most common approach, which is also used in this work, is to assume that $\boldsymbol{y}_{1/2} = \boldsymbol{y}_{in}$,[79] in which case the diffusive flux at $z_{1/2}$ must be equal to zero in order to satisfy the conservation law in the first cell. Note that with a finite volume discretization scheme, all these approaches conserve mass across the interface.

The state variables at the first half cell ($z_{1/2}$) are therefore given by the values at the inlet (z_{in}). The pressure and velocity at the inlet must

satisfy the Ergun equation over the first cell, and satisfy the molar flow rate of the inlet stream ($\dot{N}_{\text{stream}}$). These two conditions can be combined in a third-order polynomial equation with unknown u_{in} resulting from the combination of the mass balance:

$$\dot{N}_{\text{stream}} = \frac{p_{\text{in}}}{\mathcal{R}T_{\text{in}}} u_{\text{in}} \tag{2.9}$$

and of the Ergun equation:

$$\frac{p(1) - p_{\text{in}}}{\Delta z} = -\frac{150\mu(1-\epsilon_b)^2}{\epsilon_b^3 d_p^2} u_{\text{in}} - \frac{1.75(1-\epsilon_b)\rho}{\epsilon_b^3 d_p} \left|u_{\text{in}}\right| u_{\text{in}} \tag{2.10}$$

While the inlet pressure depends on the state of the column, the outlet pressure is fixed to a set value, e.g. atmospheric pressure, and the outlet velocity is obtained by solving the Ergun equation over the last cell. For the temperature and composition, the boundary condition at the outlet of the column is fixed by setting the spatial derivatives equal to zero. This is implemented by equaling the respective fluxes at the last half cell to those of the last cell: $T_{\text{out}} \equiv T_N$, $\boldsymbol{y}_{\text{out}} \equiv \boldsymbol{y}_N$.

BOUNDARY CONDITIONS II In order to simulate an open heating step, where one extremity of the column is open, the boundary conditions are such that at the closed end of the column the composition, pressure and temperature of the first half cell are equal to those of the first cell ($z_{\text{in}} \equiv z_1$). This condition ensures a zero flow crossing the column boundary at its closed end. The boundary conditions at the column outlet are the same as for the adsorption and purge steps (boundary conditions I).

BOUNDARY CONDITIONS III Open cooling steps can be of practical interest in order to cool the column under constant pressure, without using any excess feed. Only the necessary material is fed to the column from one open end; the boundary conditions are such that the temperature, composition and pressure at the inlet are given by those of a given inlet stream, and the velocity is calculated with the Ergun equation. This way, the molar flow rate fed to the column is not imposed, but is dynamically adjusted such that the pressure of the column remains constant. The boundary conditions at the column

outlet are such that all spatial derivatives are equal to zero. This is implemented by equaling the pressure, composition and temperature of the outlet to those of the last cell ($z_{\text{out}} \equiv z_N$).

BOUNDARY CONDITIONS IV If a closed column is to be simulated, the boundary conditions are set by fixing all spatial derivatives at the extremities equal to zero. This ensures that no material enters nor leaves the column.

2.2.2 Convergence to cyclic steady state

Cyclic adsorption processes are simulated by integrating the governing equations in time for one column undergoing each step of a given cycle configuration sequentially until reaching a cyclic steady state (CSS). The operation and performance of the cycle at CSS are those of interest. Since it is not foreseeable how many cycles are needed to reach the CSS, and it is of interest to simulate only the strictly minimum number of cycles, it is important that a mathematical model of cyclic adsorption processes provides a means to estimate whether or not the simulation has converged. This is done by monitoring four quantities:

1. The maximum value over the different cycle steps of the sum over all grid points and components of the squared errors on the dimensionless temperatures the end of the step for two consecutive cycles (labeled 'old' and 'new'):[24]

$$\Psi_1 = \max_k \left(\sum_{j=1}^{N} \sum_{i=1}^{C} \left(y_{i,j,k}^{\text{new}} - y_{i,j,k}^{\text{old}} \right)^2 \right) \quad k = 1, \ldots, n_{\text{steps}} \tag{2.11}$$

2. The maximum value over the different cycle steps of the sum over all grid points of the squared errors on the dimensionless temperatures the end of the step for two consecutive cycles (labeled 'old' and 'new'):[24]

$$\Psi_2 = \max_k \left(\sum_{j=1}^{N} \left(\frac{T_{j,k}^{\text{new}} - T_{j,k}^{\text{old}}}{T_{\text{ref}}} \right)^2 \right) \quad k = 1, \ldots, n_{\text{steps}} \tag{2.12}$$

3. The sum over all components and product streams (P_m with $m = 1, \ldots, n_{\text{prod}}$) of the overall product compositions between two consecutive cycles (labeled 'old' and 'new'):[81]

$$\Psi_3 = \sum_{m=1}^{n_{\text{prod}}} \sum_{i=1}^{C} \left| \frac{\overline{y}_{i,m}^{\text{new}} - \overline{y}_{i,m}^{\text{old}}}{\overline{y}_{i,m}^{\text{new}}} \right| \tag{2.13}$$

   In order to avoid dividing by zero, the maximum value between machine precision and the mole fraction are considered in the denominator.

4. The sum of the relative error on the overall mass balance over all components calculated based on the total amount entering (n_i^{in}) and leaving (n_i^{out}) the column during an entire cycle:[81]

$$\Psi_4 = \sum_{i=1}^{C} \left| \frac{n_i^{\text{out}} - n_i^{\text{in}}}{n_i^{\text{in}}} \right| \tag{2.14}$$

These quantities are used in the expression of three criteria; when satisfied simultaneously, cyclic steady state is assumed to be reached. Both the first two quantities (Ψ_1 and Ψ_2) must be below a given threshold of 1×10^{-5}, as suggested by Casas et al.[24], and the sum of the last two quantities ($\Psi_3 + \Psi_4$) must be lower than a threshold of 1×10^{-2}, as suggested by Minceva et al.[81]

3 CALIBRATION AND EXPERIMENTAL VALIDATION OF A TEMPERATURE SWING ADSORPTION MODEL

3.1 INTRODUCTION

Adsorption processes benefit from a high degree of flexibility in their design. In particular, the configuration of a cycle comprises many degrees of freedom, such as the number, type and sequence of the steps (adsorption, heating, purge, etc), their inter-connectivity and the direction of flow. On top of this, the operating conditions are defined not only by the high/low pressure and temperature levels, but also by the step duration.

Model-based process design is a powerful tool to tackle such complex design problem, as it allows to screen cycle configurations and operating conditions in an efficient and systematic manner. Its usefulness, however, is strongly influenced by the mathematical model used to predict the outcome of the process. The model must be able to describe the physical phenomena quantitatively, without being computationally too intensive, since this would make systematic screening and/or process optimization too time consuming.

This therefore requires a sound and not too complex model describing the relevant physicochemical phenomena, and an appropriate

The material in this chapter summarizes for the sake of completeness results reported in Marx, D.; Joss, L.; Hefti, M.; Mazzotti, M. Temperature Swing Adsorption for post-combustion CO_2 capture: Single- and multicolumn experiments and simulations. *Ind. Eng. Chem. Res.* **2016**, *54*, 1401–1412.

calibration of the model parameters, which in the case of adsorption processes, are specific of the considered adsorbent/adsorbate system. While some of these system-specific parameters are available in the literature (e.g. heat capacities or diffusivity of gases), the thermodynamic and kinetic properties of the adsorption system must be characterized in the relevant temperature, pressure, composition range.

Among the available commercial materials, zeolite 13X is one of the most promising adsorbents for post-combustion CO_2 capture. The pure and binary adsorption isotherms of CO_2 and N_2 on commercial 13X pellets were previously measured gravimetrically and described with appropriate temperature dependent adsorption isotherms.[83] In this chapter, the heat and mass transport parameters are estimated by means of single column dynamic experiments. The fully calibrated model is then validated by comparison of cyclic TSA experiments against predictive simulations.

3.2 EXPERIMENTAL

3.2.1 Materials

All experiments presented in this chapter were performed with zeolite 13X formulated in spherical particles with a diameter between 1.6 mm and 2.0 mm (ZN10-02, ZeoCHEM, Switzerland). A premixed 12:88 mol/mol CO_2/N_2 gas mixture was used as feed gas (Pangas, Switzerland), with a $\pm 2\,\%$ relative tolerance on the CO_2 content. Regeneration was carried out with helium, also obtained from Pangas, and with a purity of 99.999%.

The columns of the lab-scale setup were manually packed with the adsorbent particles, and before the first experiments, the zeolite was regenerated by heating the columns to 250 °C over night under a low flow of helium. Between each experiment, regeneration was carried out by heating the columns to 250 °C during 2 hours under a low flow of helium.

3.2.2 Experimental setup

The existing two-column PSA setup presented in Schell et al.[84] was extended with an active heating and cooling system in order to upgrade it to a PSA/TSA setup; a scheme of the setup is shown in Figure 3.1. The 1.2 m long tube in tube columns are made of stainless steal; the inner tube has a diameter of 25 mm and a wall thickness of 2.5 mm, and the outer tube has an inner diameter of 44 mm and a wall thickness of 2.15 mm. The columns are equipped with five thermocouples distributed along the longitudinal axis (10 cm, 35 cm, 60 cm, 85 cm and 110 cm from the bottom). The thermocouples are mounted in specifically designed shafts that traverse the outer jacket, so that the tip of the thermocouples can be inserted within the packed bed at any desired radial position. All the gas pipes, including mass flow controllers (MFCs), back pressure regulators (BPRs) and valves remained unchanged as compared to the original PSA setup.[84] A cooling and a heating circuit were added; they connect the column jackets to two thermostats (Huber, Kältemaschinenbau GmbH, Germany). In order to achieve fast temperature cycles, one thermostat is kept at the low temperature level, while the other is kept at the high temperature level. The heating and cooling circuits are designed such that by switching of the automatic valves (GSR Ventiltechnik GmbH&Co, Germany) both columns can be connected to both thermostats. The temperature of the thermofluid (Therminol 62, Eastman) is measured with thermocouples located at the inlet and outlet of the column jackets. The thermostats were chosen with the goal of achieving a 120 °C temperature change of the packed bed within ca. 10 min. The dimensions of the column and the physical properties of the adsorbent material are reported in Table 3.1.

The gas phase composition at the column outlet is measured with a mass spectrometer (MS) (Pfeiffer Vacuum, Switzerland), which can monitor either the light (N_2) or heavy (CO_2) product stream. The MS was calibrated by using two mixtures with different molar ratios of CO_2 to N_2, accounting for the fact that both components generate a signal at a mass-to-charge ratio of 28. The flow rate of the light product is measured with a rotameter (Vögtlin Instruments, Switzerland) in conjunction with a web-cam and an image analysis script.

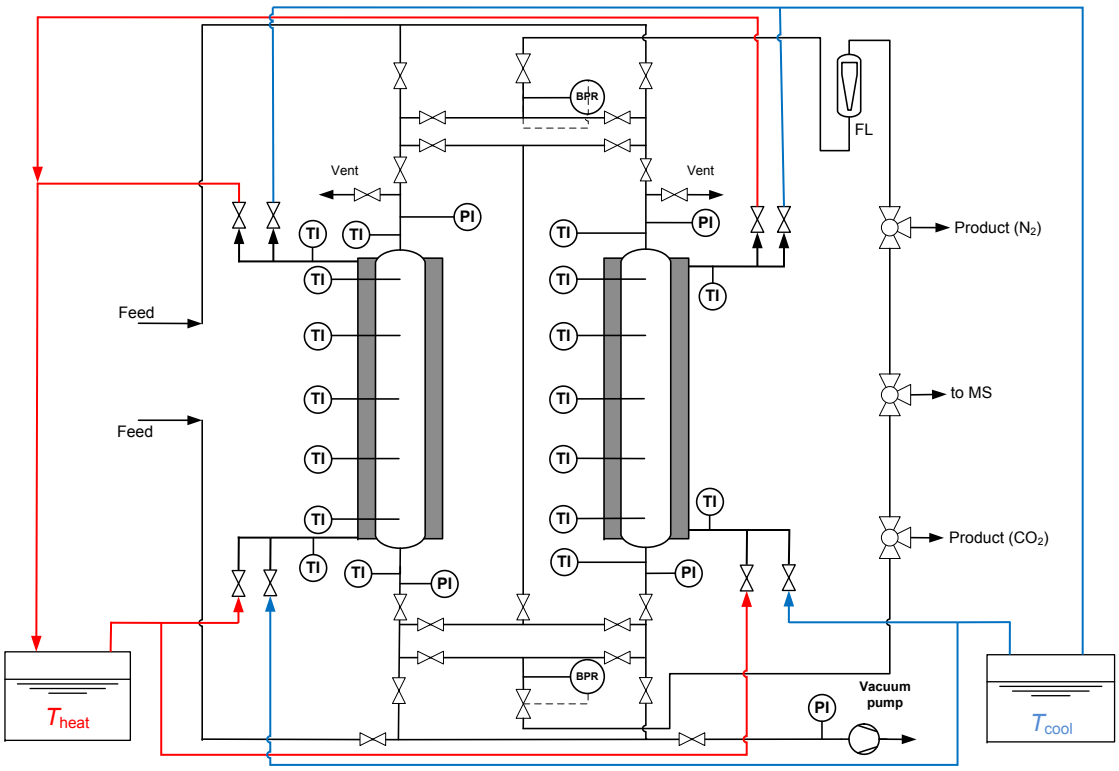

Figure 3.1. – Flow sheet of the 2-column setup used for the TSA experiments. The five thermocouples in each of the columns are placed along the center axis, at 10 cm, 35 cm, 60 cm, 85 cm and 110 cm from the inlet of the column.

3.2.3 Single column experiments

HEATING AND COOLING EXPERIMENTS Two sets of heating and cooling experiments were performed to characterize the heat transfer between the thermofluid and the inner column wall; one set was performed under helium atmosphere, and the other in the presence of CO_2 and N_2. The column was prepared by equilibrating the adsorbent bed with the respective gas phase (100% He, or 12:88 CO_2/N_2) at 25 °C and 1 bar. Each set of experiments was carried out by heating the column to 100 °C, and then cooling it down to 25 °C. For the heating experiments the column jacket was connected to the hot thermostat; the state of the column at the end of the heating was the initial state of the column for the cooling experiment. For the cooling experiments, the column jacket was connected to the cold thermostat. The column

Table 3.1. – Setup dimensions and physical properties of the adsorbent material.

column length	L	[m]	1.2
internal radius	R_i	[m]	12.5×10^{-3}
external radius	R_o	[m]	15×10^{-3}
heat capacity wall[a]	C_w	[J/(K m^3)]	4×10^6
13X material density	ρ_M	[kg/m^3]	2359
particle density	ρ_p	[kg/m^3]	1085
bed density	ρ_b	[kg/m^3]	652
particle diameter	d_p	[m]	1.6–2.0 $\times 10^{-3}$
heat capacity sorbent [a]	C_s	[J/(K kg)]	920

[a] at a temperature of 25 °C.

was kept at atmospheric pressure by flowing the feed past the open valve at the lower end of the column.

BREAKTHROUGH EXPERIMENTS Eight breakthrough experiments were performed to characterize the mass and heat transfer within the packed bed. The same feed composition 12:88 CO_2/N_2 on a molar basis was used for all breakthrough experiments. The experiments were conducted at two feed flow rates (200 cm^3/s and 300 cm^3/s at standard conditions) and four temperatures (25 °C, 45 °C, 65 °C and 100 °C); all at atmospheric pressure.

The experimental procedure was similar as that outlined in Marx et al.[85], with the exception of the method of regeneration. The regenerated column was first brought to the desired initial temperature. The CO_2/N_2 gas mixture was passed through the bypass with the desired flow rate to flush the piping with any residual helium, before feeding it through the column. The temperature and pressure of the column, and the outlet composition were recorded throughout the experiment.

3.2.4 Cyclic TSA experiments

Three cyclic TSA experiments were performed using both columns, which underwent the same three-step process cycle, out of phase by a half-cycle. The desorption temperature, i.e., the set point of the

Table 3.2. – Operating conditions of the three cyclic TSA experiments.

	Run 1	Run 2	Run 3
T_{heat} [°C]	100	125	150
T_{heat} [°C]	25	25	25
$y_{CO_2,feed}$ [–]	0.12	0.12	0.12
$\dot{V}_{feed}$ [cm^3/s]	300	300	300
t_{ads} [s]	480	240	360
t_{heat} [s]	1380	960	1080
t_{cool} [s]	900	720	720

hot thermostat was varied; three different temperature levels were considered: 100 °C, 125 °C and 150 °C. The cycle consisted of: (i) an adsorption step, in which feed was conveyed through the column from bottom to top at a flow rate of 300 cm^3/s (at standard conditions) producing the N_2-rich product, while the column jacket was connected to the cold thermostat; (ii) a heating step during which the column was left open at the lower end producing the CO_2 rich product, and the jacket was connected to the hot thermostat; (iii) a cooling step, during which the column jacket was connected to the cold thermostat, and atmospheric pressure was ensured by flowing the feed mixture past the open valve at the lower end of the column. Each of the thermostats was connected to one of the columns at all times, such that the timing of the cycle steps was constrained in that $t_{heat} = t_{ads} + t_{cool}$. The operating conditions of the three experiments are reported in Table 3.2. Each experiment was performed for at least five cycles, achievement of CSS was confirmed by comparison of the measurements taken from two consecutive cycles. The outputs which were directly measured are the temperature profiles within the columns, the exit composition and flow rate profiles. From the exit composition and flow rate measurements, the overall composition of the light product, and the corresponding amount of N_2 recovered was determined. This allows to close the overall mass balance and estimate the CO_2 purity, recovery and sorbent mass specific productivity.

3.3 MODELING AND PARAMETER ESTIMATION

The column dynamics, i.e., the variation of temperature, pressure and composition in time and space, are described by the model equations reported in chapter 2. For the sake of completeness, the most relevant assumptions are stated anew:

- radial gradients of velocity, composition and temperature are neglected;
- the gas phase and the solid phase are in thermal equilibrium;
- the mass transfer rate of adsorption is described by the LDF;
- mass transfer rates, heats of adsorption, heat capacities, heat conductivity and viscosity are constant.

Radial profiles are bound to develop, especially during the heating and cooling steps. While a more accurate description could be obtained with a two-dimensional model, researches have shown that a well calibrated one-dimensional model is able to describe temperature and composition profiles with sufficient accuracy.[67,68,86]

The adsorption equilibrium $n_i^{\mathrm{eq}}(p, T, \boldsymbol{y})$ is described with the ideal adsorbed solution theory (IAST) applied to the Sips equation. The relevant parameters are taken from Hefti et al.[83], who measured pure and binary adsorption equilibria of CO_2 and N_2 on the same zeolite 13X material as used in this work, and in the relevant range of pressures and temperatures, namely 0.2 bar to 10 bar and 25 °C to 140 °C, respectively. The isotherm equations and parameters used are reported in appendix B.1.

For the simulation of the breakthrough experiments, the temperature of the thermofluid is assumed to be constant in space and in time, and equal to the average measured inlet and outlet temperature profiles. During heating/cooling steps as well as TSA cycles, on the other hand, the temperature of the thermofluid varies drastically. For the simulation of these cases, the thermofluid temperature is linearly interpolated in space and time according to the measured inlet and outlet temperature profiles.

3.3.1 Parameter estimation

Heat and mass transfer parameters are estimated by comparing the experimental results of the single column experiments (heating, cooling and breakthrough) to the simulations, particularly, by minimizing the maximum likelihood estimator objective function, Φ:

$$\begin{aligned}\Phi =& w_y \sum_{k=1}^{N_{\text{comp}}} \ln\left(\frac{1}{N_{\text{obs},y}} \sum_{j=1}^{N_{\text{obs},y}} \left(\frac{y_{j,k} - \hat{y}_{j,k}(\boldsymbol{p})}{y_{j,k} + \gamma}\right)^2\right) + \\ & w_T \sum_{k=1}^{N_{\text{temp}}} \ln\left(\frac{1}{N_{\text{obs},T}} \sum_{j=1}^{N_{\text{obs},T}} \left(\frac{T_{j,k} - \hat{T}_{j,k}(\boldsymbol{p})}{T_{j,k}}\right)^2\right)\end{aligned} \tag{3.1}$$

where $y_{j,k}$ and $T_{j,k}$ are the measured output (mole fraction or temperature) k at time j, $\hat{y}_{j,k}$ and $\hat{T}_{j,k}$ are the corresponding simulated values, $N_{\text{obs},y}$ and $N_{\text{obs},T}$ are the number of observed data points for the composition and temperature, respectively, $\gamma = 1$ is a constant introduced to avoid dividing by zero when a mole fraction is zero, $N_{\text{comp}} = 2$ and $N_{\text{temp}} = 5$ are the number of measured composition and temperatures profiles, and w_y and w_T are the weighting factors. As their purpose is to relate the importance of the two measured mole fractions to the five temperatures, an unnecessary degree of freedom was eliminated by constraining the weighting factors to: $N_{\text{comp}} w_y + N_{\text{temp}} w_T = 1$.

For the heating and cooling experiments, which were used to estimate the heat transfer coefficient between thermofluid and column wall (h_w), and the heat transfer coefficient between the column wall and the adsorbent bed under static conditions (h_b^0), only the five adsorbent temperature profiles were used for comparison ($w_y = 0$, and $w_T = 0.2$). For the breakthrough experiments, which were used to estimate the heat transfer coefficient between the column wall and the bed for convective conditions (h_b) and the mass transfer coefficients (k_{CO_2} and k_{N_2}), the considered outputs were the five temperature profiles and the outlet CO_2 and N_2 composition profiles. In this case, the weighting factors were $w_y = 0.25$ and $w_T = 0.1$. Since the output profiles are very sensitive to the feed velocity, which is measured with an accuracy of $\pm 2\,\%$, for the fitting of the breakthrough experiments,

the feed velocity was fitted contemporaneously with the heat and mass transfer coefficients as described in Marx et al.[85].

3.3.2 Heat transfer

An accurate description of heat transfer within the packed bed is crucial for a correct description of temperature swing adsorption processes. Despite the long history in research on heat transfer, there is no truly well established consensus to how the heat transfer in packed beds must be described.[87] In fact, heat transfer in packed beds involves various mechanisms, including conduction within the different phases and materials (gas, solid sorbent, column wall) and across interfaces (gas/solid, gas/wall, solid/wall), and convection in the gas phase within the bed porosity. Heat transfer rates therefore depend not only on the adsorbent material, but also on geometrical factors (pellet size and shape, size of the packed bed) and on the operating conditions (pressure, temperature, composition, velocity).

The estimated heat transfer coefficient between the column wall and the packed bed h_b is compared to two correlations, whose validity range covers the low Reynolds numbers typical of ambient pressure conditions. DeWasch and Froment[88,89] found a linear relationship between the Nusselt and Reynolds numbers, and Specchia et al.[90] worked with a two-dimensional model, considering separately the effective heat transfer within the packed bed, and the heat transfer at the column wall, with each a static and a convective component. The expressions used can be found in appendix B alongside a more detailed discussion.

There exist well-established correlations for the heat transfer within concentric tubes[91] under laminar and turbulent flow conditions, for the transition region between the two regimes, as well as for the entry region. Many of the physical quantities that are needed to evaluate these expressions are already known or are available from the manufacturer of the thermofluid; however some are more difficult to obtain, such as the thermofluid flow rate, which depends on the pressure drop through the pipes and jacket in addition to the pump power and efficiency. While this makes it difficult to use the available correlations to calculate quantitative values for h_w, the expressions therein make

it clear that the Nusselt number, and accordingly the heat transfer coefficient, increase significantly near the entrance. Considering these entrance effects in the simulation leads to an improved description of the heating and cooling experiments – therefore, all simulations of heating, cooling, and TSA cycle simulations in this chapter account for them as described in appendix B. A fixed functional dependence of the heat transfer coefficient on position was assumed, and during the fitting, only the heat transfer coefficient at the column end, $h_{w,L}$, was estimated.

3.4 RESULTS OF THE SINGLE COLUMN EXPERIMENTS

In this section, the transient experiments performed to determine the transport parameters are presented, followed by a discussion on the estimated transport parameters. This characterization is then used to predict the outcome of the performed TSA experiments.

3.4.1 Experimental results

Results of an illustrative breakthrough experiment performed at 25 °C and with a feed flow rate of 300 cm^3/s are shown in Figure 3.2 alongside the simulated profiles. Only a limited amount of nitrogen is observed to adsorb, as it breaks through the column almost immediately; some does adsorb, however, as evidenced by the moderate temperature increase throughout the bed. The CO_2, on the other hand, adsorbs significantly more, and breaks through much later. A very notable feature of these results is that the adsorbing CO_2 creates a front of very high temperature as it advances through the column, with temperatures in excess of 90 °C. The results of all breakthrough experiments performed are shown in appendix B.

The temperature profiles of the heating and cooling experiments using the same CO_2/N_2 feed as the breakthrough experiment are shown in Figure 3.3. Along with the temperatures measured in the bed (symbols) and the corresponding simulation results (lines), the

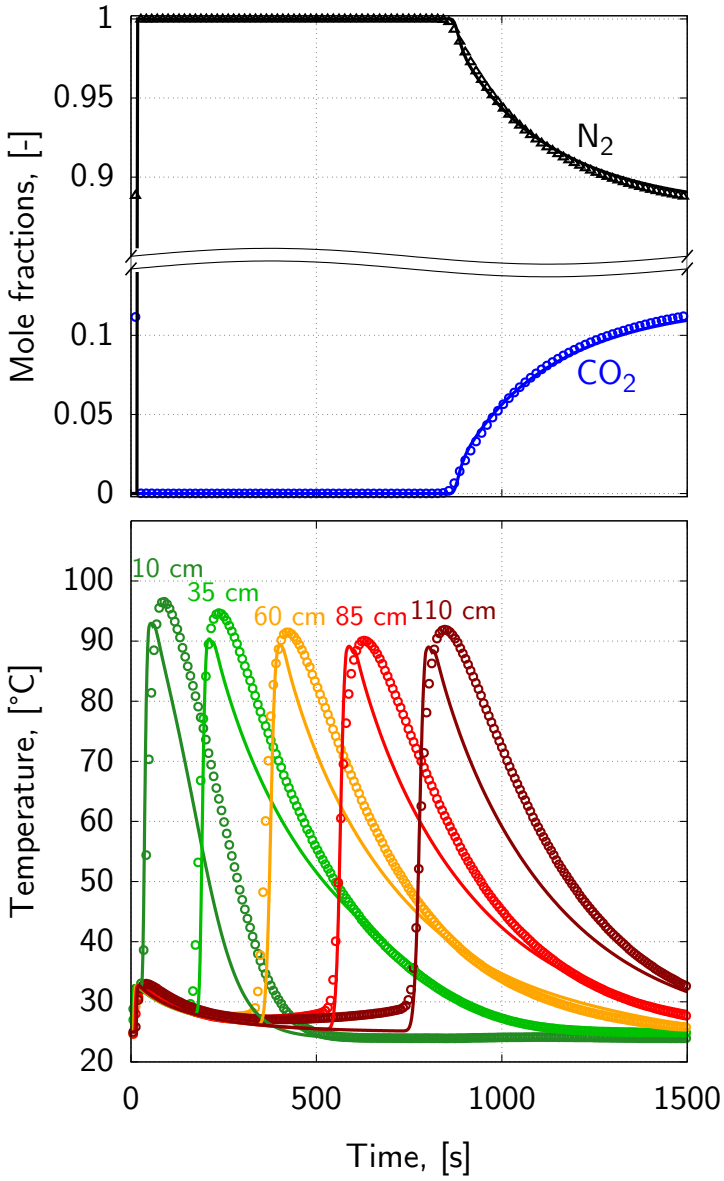

Figure 3.2. – Concentration profiles at the column outlet (top) and temperature profiles (bottom) for the breakthrough experiment performed at 25 °C and with a feed flow rate of 300 cm^3/s. Experimental data is shown with symbols, while the simulated profiles ($k_{CO_2} = 0.1\,s^{-1}$, $k_{N_2} = 0.5\,s^{-1}$, $h_b = 35.3\,W/(m^2K)$) are shown with lines.

measured temperature of the heat exchange fluid at the jacket inlet and outlet is shown using dots (dark and light gray, respectively). These data were not simulated, but rather were treated as an input into the model, as discussed in section 3.3. The following points are worth noting concerning the experimental results:

- The thermofluid temperature initially oscillates a bit, and in both cases overshoots past the set point temperature. This is in part due to back-mixing of the fluid from the heating jacket to the thermostat, e.g. the cold fluid going into the hot thermostat.
- The temperature of the thermofluid entering the column and exiting the column are fairly similar. This is due to the relatively short residence time of the fluid in the column jacket. If the difference were large, the linear interpolation used to calculate the fluid temperature along the length of the column might not be accurate enough, and the energy balance for the thermofluid might have to be included in the model.
- A temperature gradient develops along the length of the bed. As indicated in Figure 3.3 by the gray arrow, the temperature measured in the lower part of the bed changes considerably faster than in the upper portion of the column.

3.4.2 Parameter estimation

The single column experiments were used to estimate heat and mass transfer coefficients as described in section 3.3. All of the transport parameters that were established via the transient experiments reported above are summarized in Table 3.3. These are the values that are used for all following simulations of TSA processes.

MASS TRANSFER While the agreement between the simulations and the breakthrough experiments is good, the parameter identifiability of the mass transfer coefficients was poor. In fact, the shape of the CO_2 breakthrough fronts were mainly limited by heat transfer, and showed only very little sensitivity to mass transfer coefficients $k_{CO_2} \geq 0.05\,s^{-1}$. The large amount of heat released as CO_2 adsorbs hinders adsorption, to the point where the uptake rate is limited by the rate at which the

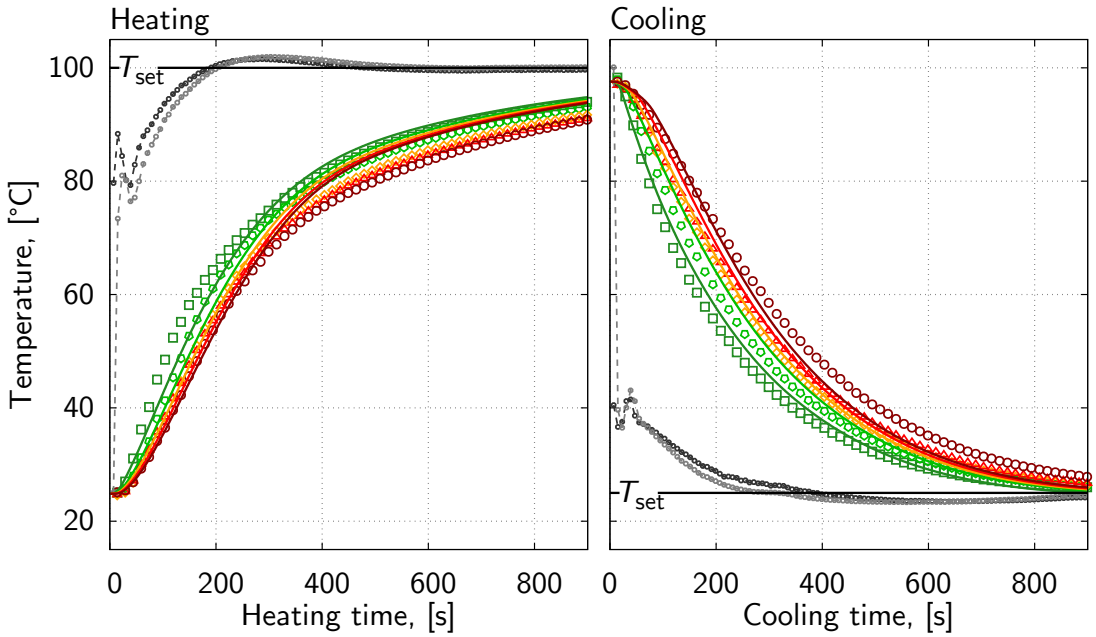

Figure 3.3. – Temperature profiles for the heating (left) and cooling (right) experiment. Experimental data is shown with symbols for the five axial positions. The measured inlet and outlet temperature of the thermofluid are shown with gray dots. The simulated profiles ($h_b = 22\,\mathrm{W/(m^2K)}$, $h_{w,L} = 220\,\mathrm{W/(m^2K)}$) are shown with lines.

bed cools, rather than by the adsorption kinetics, i.e., pore diffusion and/or solid diffusion of CO_2 in the adsorbent particle. Uptake rates of CO_2 on 13X that were limited by heat transfer have been observed by both Giesy et al.[92] who use a frequency response apparatus to study adsorption kinetics at 23 °C and up to 1 bar, and by Hu et al.[93], who use a zero-length column system to study adsorption kinetics of gas mixtures containing between 0.1% and 10% CO_2, and found that for the higher concentrations, heat transfer indeed determined the uptake rate of CO_2. The height of the temperature front exhibited a somewhat stronger dependency to the mass transfer, and it was found that a value of $k_{CO_2} = 0.1\,\mathrm{s^{-1}}$ worked quite well to describe the breakthrough experiments – this value was used for all simulations. The mass transfer of N_2 was sufficiently fast that the measured concentration profiles did not allow for an accurate estimation of the mass transfer coefficient since the profiles were described similarly well with any value $k_{N_2} \geq 0.5\,\mathrm{s^{-1}}$.

Table 3.3. – Transport parameters used for the simulation of the TSA experiments.

Transport parameter		value	
mass transfer coefficient CO_2	k_{CO_2}	0.1	s^{-1}
mass transfer coefficient N_2	k_{N_2}	0.5	s^{-1}
heat transfer coefficients			
internal (flow)	h_b	33	$W/(m^2\,K)$
internal (static)	h_b^0	22	$W/(m^2\,K)$
external (column end)	$h_{w,L}$	220	$W/(m^2\,K)$

HEAT TRANSFER Heat transfer coefficients between column wall and bed (h_b) could be determined for every breakthrough experiment and for the heating/cooling experiments. A dependency on both the temperature and flow rate was observed, such that the heat transfer coefficients estimated for the experiments carried out at the larger flow rates and lower temperature (higher density) were higher. This observation is inline with available literature correlations, which predict an increased heat transfer coefficient with Reynolds number, as illustrated in Figure 3.4. The estimated heat transfer coefficient are shown on the same figure plotted against the Reynolds number calculated according to the pressure, temperature and velocity of the feed.

The temperature gradient that develops along the column axis during heating and cooling (Figure 3.3) is seen in both the heating and the cooling step, and was stronger than expected. A careful analysis of the temperature profiles during heating and cooling under helium atmosphere (appendix B) revealed that the heat transfer between fluid and wall is enhanced at the entrance of the jacket. This effect could only by be described when accounting for hydrodynamically and thermally developing flow in the entry region of the heating jacket with a dependency of the heat transfer on position.

3.5 TSA CYCLIC EXPERIMENTS

Finally, the mass and heat transfer coefficients determined above were used to predict the behavior of cyclic TSA experiments. In the

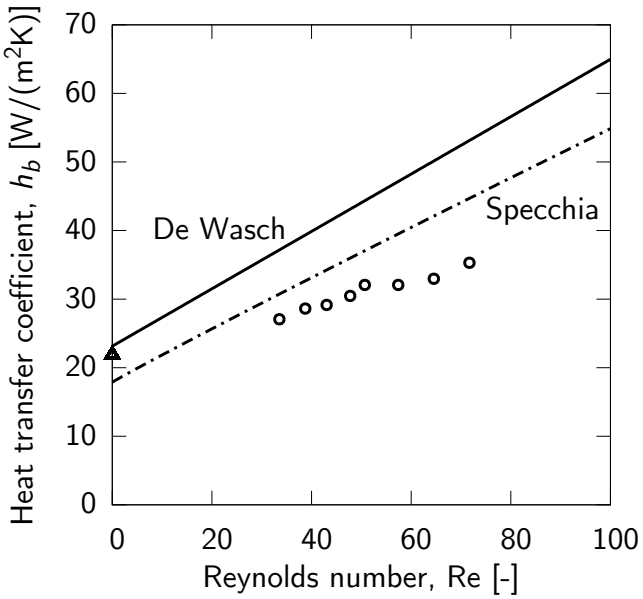

Figure 3.4. – Heat transfer coefficients fitted to each of the experiments performed (symbols), together with a selection of correlations found in literature (lines). Breakthrough experiments (circles), heating/cooling experiments (triangle).

following, the results of the TSA experiment with a desorption temperature $T_{\text{heat}} = 150\,^{\circ}\text{C}$ are reported and discussed in detail. The measured temperature, composition and flow rate profiles as well as the calculated quantities, i.e., the product purities, component recoveries, and productivity are considered and compared with simulation results.

3.5.1 Prediction of column behavior during cyclic TSA experiments

The temperature profiles measured inside one column during the TSA experiment are shown in Figure 3.5 along with the simulation results. During the adsorption step the heat released by the adsorption of the advancing CO_2 front is clearly visible in both experiment and simulation, and the timing of the experimental temperature front is matched rather well by the simulations. The height of the temperature is not described as well, which might be a consequence of assuming negligible radial gradients. The simulated temperature is a cross-sectional average, while the temperature at the center of the bed might

be somewhat higher. During the heating step, the axial gradient seen in the heating and cooling experiments is not quite as evident, as the column does not start out in a homogeneous state, but rather has an initial axial profile. Nevertheless, the simulations describe the temperature increase well, and by the end of the heating step simulations and measured data are all within a narrow band. During the cooling step that follows, the axial gradient is much more visible in both experiment and simulation.

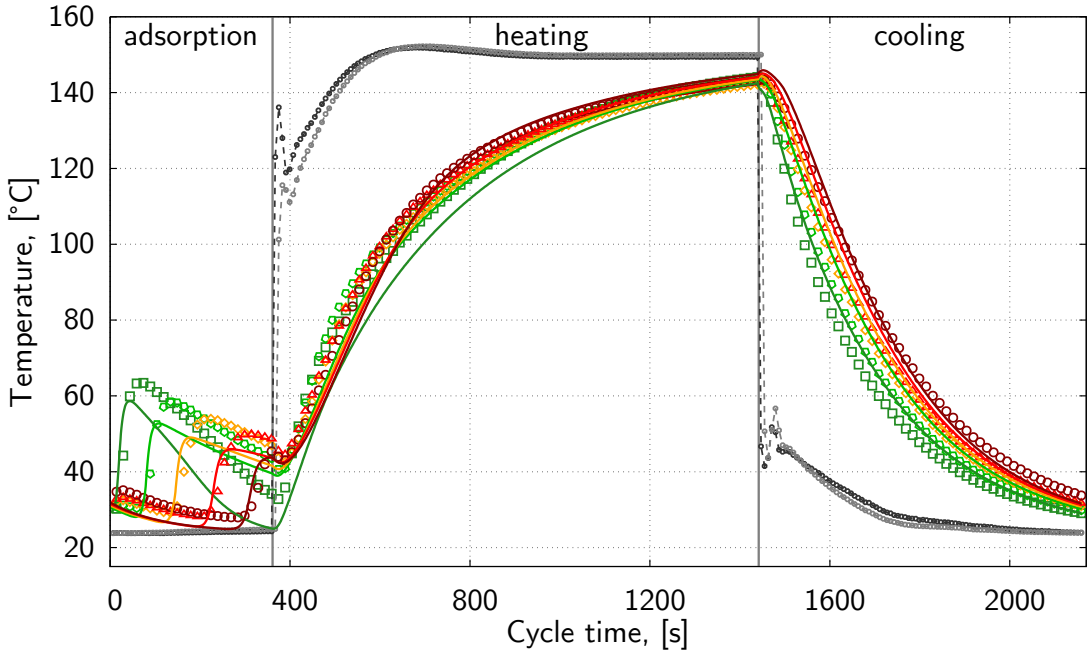

Figure 3.5. – Temperature profiles inside the column during the TSA experiment with a desorption temperature of 150 °C. Symbols are measurements at the five axial positions; the dots are the measured thermofluid temperature at the inlet (dark) and outlet (light) of the jacket. Lines represent simulations. The vertical gray lines indicate the switch times between steps.

Figure 3.6 shows the composition and flow rate of the light product (N_2) over the duration of the adsorption step and heating steps. Data from both columns are shown, to illustrate that the two columns operate in the same way, and to verify the reproducibility of the experiment. Differences at the beginning of the adsorption step are experimental artifacts that can be attributed to the effect of the piping of the setup. In fact, the high flow rate present during the adsorption step induces a considerable pressure drop across the downstream piping. During the

first few seconds of this step until the pressure in the column builds up, the measured flow rate is lower than the prediction and the measured outlet composition is that initially contained in the downstream piping. In addition, the simulations systematically indicate a slightly lower flow rate than measured. While the difference is not large, it is consistent throughout the entire duration of the adsorption step; it should be noted, however, that it is within the uncertainty of the flow meter.

The composition of the CO_2 product exiting the column during the heating step can be seen in Figure 3.6 *bottom*. The outlet flow rate of the heating step was so low that it could not be measured and the composition shown here did not enter the purity and recovery calculations. However, as the course of the composition is very sensitive to both the isotherm and the rate of heating, which in turn depends on the heat transfer into the column, it constitutes a good test of the model and of the parameters used. Initially, this product is mostly nitrogen, as it is determined by the (non-selective) gas phase present in the column at the end of the adsorption step. As the column heats, and the CO_2 desorbs, it displaces the N_2 in the gas phase, until the gas phase consists of pure CO_2. The simulations match this development remarkably well.

3.5.2 Process performance of TSA experiments

The composition and flow rate measured during the adsorption step can be used to close the mass balance and calculate the amount of CO_2 and N_2 contained in each of the two product streams. From these values, the product compositions, the respective component recoveries and the productivity expressed in mass of CO_2 captured per hour and per ton of zeolite can be determined. Table 3.4 summarizes the calculated performances for the TSA experiments performed, together with the corresponding simulation results. The values reported are the mean of the values of both columns during the final cycle performed, while the uncertainties reported are propagated from the uncertainties considered in the measured quantities.

The comparison between predicted and experimental quantities raises a few points, which are worth making:

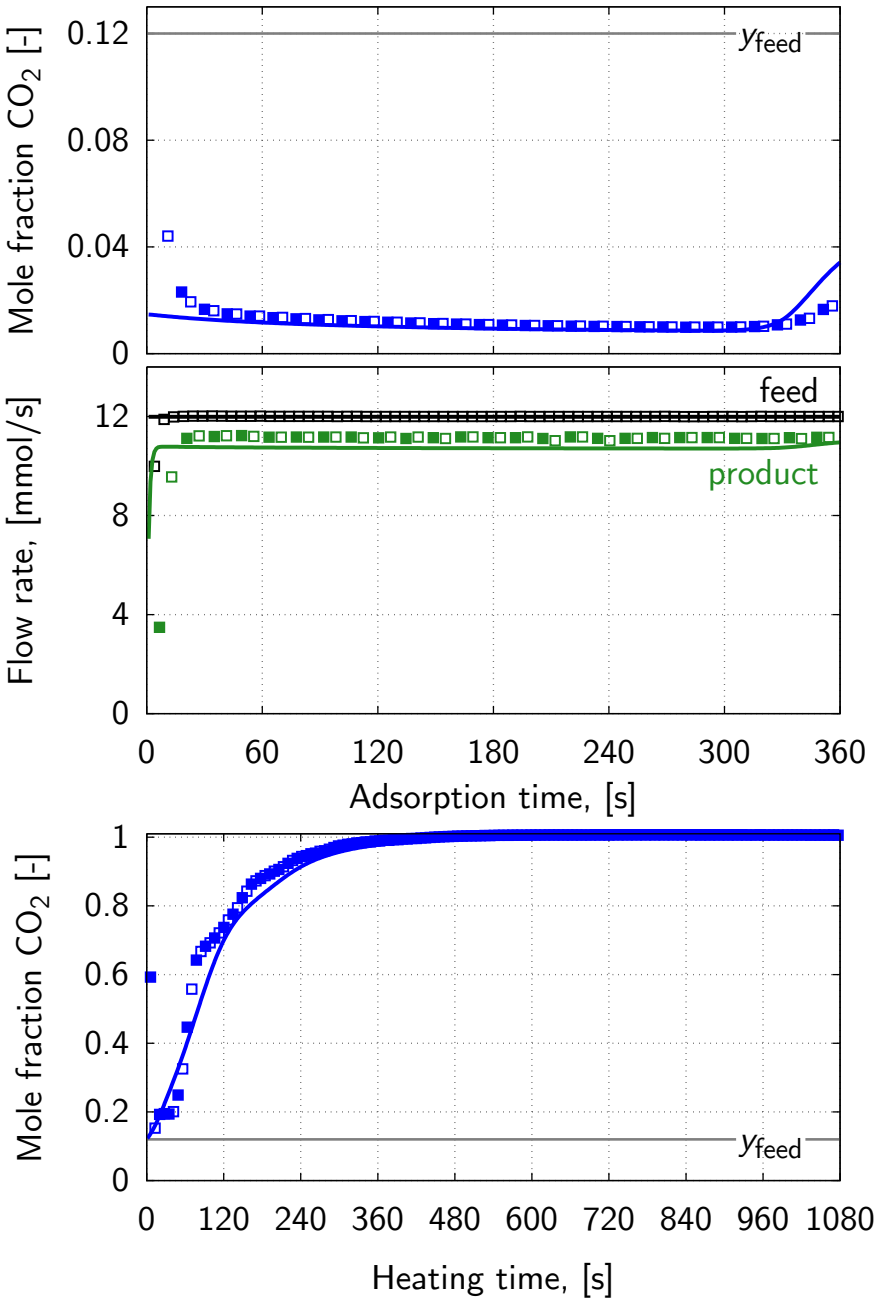

Figure 3.6. – Comparison of simulation (lines) and experimental (symbols) results for the light product (top) and the heavy product (bottom). *top:* shows the mole fraction of CO_2 in the N_2 product throughout the adsorption step, as well as the feed composition. *middle:* shows the flow rate of the light product together with the feed flow rate. *bottom:* shows the mole fraction of CO_2 in the heavy product. To show that the two columns operate consistently, data from both columns are shown (empty and filled symbols).

Table 3.4. – Comparison of experimental and simulated process performance figures for the three operating conditions. All experiments used the same feed composition and flow rate.

		Run 1	Run 2	Run 3
N_2 purity [%]	sim.	92.0	97.4	98.9
	exp.	92.1 ± 0.6	97.4 ± 0.6	98.6 ± 0.6
N_2 recovery [%]	sim.	99.6	99.1	99.4
	exp.	100 ± 4.2	103 ± 4.4	103 ± 4.3
CO_2 purity [%]	sim.	90.2	90.1	93.9
	exp.	106 ± 101	137 ± 71	127 ± 55
CO_2 recovery [%]	sim.	36.5	80.5	91.9
	exp.	36.9 ± 4.5	79.6 ± 5.4	89.7 ± 5.6
productivity [$kg_{CO_2}/(t\,h)$]	sim.	37.8	60.4	91.7
	exp.	38.0 ± 4.3	58.6 ± 3.1	88.4 ± 4.2

- Generally, a good agreement is observed between predictive simulations and measured values, with all the values for the predicted performance indicators lying within the experimental uncertainties.
- The experimentally determined N_2 recovery and CO_2 purity exceed 100% in some cases. Although this indicates an error on the overall mass balance probably caused by the uncertainty of the flow rate measurement of the feed and light product, the error is within the experimental uncertainty.
- The confidence intervals of the measured values range from very narrow in the case of the N_2 purity to very large in the case of CO_2 purity. In order to determine the performance indicators reported in Table 3.4, four quantities must be either directly measured, or inferred from measurements, i.e., the amount of each component ending in the light and heavy product, respectively. While the amount of both N_2 and CO_2 in the light product is directly obtained from the composition and flow rate measurements, the respective amounts ending in the heavy product must be determined by subtracting the light product from the feed.

The indirect computation of the CO_2 purity and recovery in particular lead to a large uncertainty on these values.

- The four quantities corresponding to the purity and recovery of both products are not independent: whenever two of these values are known, the other can be computed. We therefore consider the very good agreement between experiments and predictive simulations for the recovery and purity of the N_2 product to be a pertinent result, even though it is the purity and recovery of the CO_2 that are relevant for the assessment of a post-combustion CO_2 capture process.

3.6 CONCLUSIONS

In this chapter, the the transport parameters involved in the fixed bed adsorption of CO_2 and N_2 on zeolite 13X were estimated by comparison of the mathematical model presented in chapter 2 to single column experiments.

It could be shown that the column model used for adsorption processes could be used for the description of TSA cycles by determining the parameters relevant for the adsorption equilibrium and kinetics separately in targeted experiments. Indirect heating and indirect cooling experiments were used to estimate the heat transfer between the thermostatting fluid and the column wall, while breakthrough experiments were used to determine mass transfer coefficients and heat transfer coefficients between the column wall and the adsorbent bed. The adsorption kinetics of N_2 were found to be quite fast, making an accurate determination of a mass transfer coefficient impossible; and those of CO_2 were found to be strongly impacted by heat transfer. The heat transfer within the adsorption column exhibited a dependence on the flow conditions that is consistent with what is found in literature,[88,90,94] while the heat transfer in the heating jacket around the column exhibited a clear influence of entrance effects that needed to be accounted for.

After incorporation of the determined parameters, the model was capable of simulating the behavior of two adsorption columns during

three cyclic TSA processes, predicting not only the temperature and composition fronts, but also the separation performance of the operating conditions tested. The entrance effects on the side of the heating jacket had a significant impact on temperature development during the heating and cooling steps; however their effect on the process performance was very minor, so in general during process design these effects should be neglected, as they pertain only to the setup used in this work. Although it was found that the laboratory setup in its current form and with its current experimental uncertainties cannot accurately confirm the CO_2 purity, the other performance figures were predicted accurately by the model. This shows that the model can be used to design more complicated cycle configurations, optimize the operating conditions, and assess scale, energy requirements, and feasibility of TSA processes for CO_2 capture.

4 TEMPERATURE SWING ADSORPTION FOR THE RECOVERY OF THE HEAVY COMPONENT: AN EQUILIBRIUM-BASED SHORTCUT MODEL

4.1 INTRODUCTION

Cyclic adsorption processes for gas separations aiming at the purification of the less retained components have been extensively studied, and purities as high as 99.999% can be achieved. This extensive research activity has formed the basis for processes which are now commercially available, such as pressure swing adsorption (PSA) for H_2-purification,[15] or temperature swing adsorption (TSA) for gas drying.[16,17] In recent years, TSA has been considered as an interesting option for CO_2 capture from flue gases[47,95–98] (both from industrial plants and power plants) particularly in the light of the potential utilization of low-grade heat for regenerating the fixed beds.[99] However, the development of a TSA process for post-combustion CO_2 capture poses several challenges: (i) the feed flow exceeds by far the amount treated in commercial TSA/PSA processes – the flue gas flow rate of a state-of-the-art ultra super critical (USC) coal plant is around

The results presented in this chapter have been reported in: Joss, L.; Gazzani, M.; Hefti, M.; Marx, D.; Mazzotti, M. Temperature Swing Adsorption for the Recovery of the Heavy Component: An Equilibrium-Based Shortcut Model. *Ind. Eng. Chem. Res.* **2015**, *54*, 3027–3038.

700 kg/s[100] which corresponds to about 160 kg/s of CO_2, (ii) CO_2 purity and recovery should be around 96% and 90%,[100] respectively, (iii) the adsorption/desorption steps are governed by heat transfer, which is inherently more complex than pressure swing, and (iv) the energy requirement should be lower than the conventional amine-scrubbing processes (3–4 MJ/kg_{CO_2}[101]).

In addition, the design and optimization of cycles aimed at enriching the heavy (more retained) component are not established yet. CO_2 usually adsorbs more strongly than N_2 on typical adsorbents,[6] thus the purity of the CO_2 product will be thermodynamically limited in traditional cycles, which are characterized by the production of the light product at high pressure/low temperature during the feed step. Although there exist rectifying cycles, which theoretically can yield 100% pure heavy product,[21] these have a very low productivity. In fact the heavy component is produced during the feed step, i.e., at low pressure/high temperature; under these conditions and for favorable isotherms a disperse composition front is obtained (simple wave transition), which implies a large portion of unused bed. This, together with the low density feed, part of which is possibly recycled as a purge at the high density state, makes this class of cycles unattractive both from the point of view of productivity and the energy consumption.

Model-based process design is the standard procedure for studying cyclic adsorption separations and for the design and development of cycles.[29,102–105] Commonly used mathematical models consist of energy and mass balances of the fixed bed along with a constitutive equation for the pressure field; the resulting partial differential equations (PDEs) are numerically solved for every cycle step sequentially until a cyclic steady state (CSS) is reached. This makes solving detailed models computationally intensive and time consuming. Simplified models can be very useful for the preliminary design of separation processes, and for a better understanding of the inherent limits imposed by thermodynamics. Moreover, shortcut methods usually are rapid and robust, hence quite useful especially for cyclic processes.[106] The complexity of the detailed model is usually reflected in the complexity of the corresponding simplified model, or in its accuracy: the existing shortcut methods for PSA processes are often limited to linear isotherms such as the equilibrium theory framework developed by

Chan et al.,[107] or they consider Langmuir isotherms and are substantially more complex.[108] More recently, a simplified model of P/VSA processes which considers frozen fronts during the non-isobaric steps was developed by Maring et al.[109] with the aim of assessing the specific power consumption for sorbent screening.

Although TSA cycles are conceptually very similar to PSA cycles, the reduction to a linear problem is impossible because the temperature dependence of the adsorption equilibrium is always non-linear. This issue was solved in the early 70s by the equilibrium theory framework for adiabatic adsorbers,[110,111] which can be used for TSA processes with direct contact heating/cooling. However, a non-adiabatic column is necessary in order to avoid dilution when the heavy component is the high purity product.[51] Therefore the existing shortcut methods for PSA are not appropriate for thermal regeneration. There exist a few studies, which consider a simplified TSA cycle for the estimation of the specific thermal energy requirement[98] or of the total "parasitic energy".[42] Although these figures of merit are more appropriate than figures based solely on the adsorption isotherms such as selectivity or cyclic capacity, one must keep in mind that for a separation process to be viable, the plant must yield reasonable productivity. To our knowledge a limited number of such studies have taken into account the entire cycle and also considered the productivity.[48,58]

In this work we present a simplified semi-analytical TSA model for a four step cycle which takes into account the heat transfer rate, but neglects mass transfer resistances. Such framework is not limited to any particular functional form of the adsorption isotherm, provided it is favorable (concave downward). As compared to detailed model simulations, the simplified model computes the cyclic steady state directly; it allows for a better understanding of TSA processes for the production of the heavy component, and provides insight into the inherent performance trade-offs.

4.2 MATHEMATICAL MODEL AND METHODOLOGY

The solution to cyclic adsorption processes is typically obtained by numerically solving the system of partial differential algebraic

equations (PDAEs) (consisting of mass and energy balances) for a single column undergoing every step sequentially with the appropriate boundary conditions, which reflect the sequence of steps in every cycle. Cycles are simulated iteratively until converging to a cyclic steady state (CSS), where the internal column profiles do not change from one cycle to the next. In other words, at the CSS the state of the column at the beginning of the cycle equals that at the end of the cycle. The detailed model presented by Casas et al.[24] will be used as a benchmark to test the shortcut model presented in the following. For the sake of simplicity we consider the feed as a binary mixture of a more adsorbing species (CO_2), and a less adsorbing species (N_2) throughout this work.

4.2.1 TSA shortcut model

For certain cycles, properly developed simplifications make it possible to compute a direct semi-analytic solution of the CSS. This exercise is performed in the following section for the four step cycle illustrated in Figure 4.1. Although the presented model is restricted to this specific cycle, the methodology could in principle be extended to other cycles, depending on their complexity. The cycle considered in this work has been chosen so as to capture the main features of a TSA cycle aimed at extracting high purity CO_2 from a dry flue gas, while minimizing complexity. Accordingly, the number of cycle steps is limited to four. Initially we consider a column saturated at feed conditions, which is heated with one open end. Thereby the pressure is kept constant at atmospheric level and the desorbed material, i.e., the target CO_2 product, is recovered. Next, the column is closed and cooled to its initial temperature,thus leading to a pressure decrease. The column is then repressurized to atmospheric pressure using the feed. Finally, the regenerated column is loaded during the adsorption step thereby producing a N_2 stream at high purity. This last step is over once the CO_2 front reaches the end of the column. CSS is ensured because the final state of the bed equals the initial one, namely a column saturated at feed conditions.

The following assumptions are made:

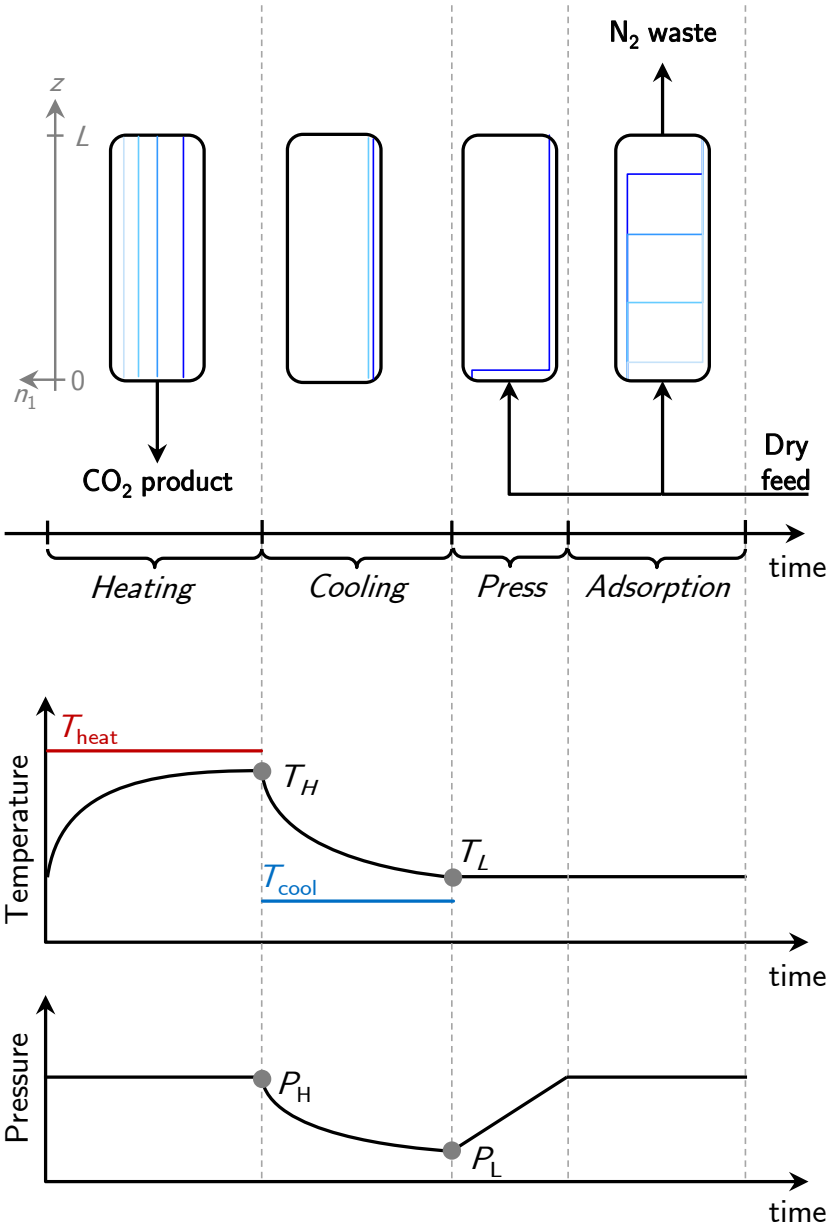

Figure 4.1. – Schematic diagram of the investigated four step TSA cycle. Indirect heating is performed with an open end, whereas cooling is carried out with a closed column, leading to a decrease in pressure. The temperature, pressure and CO_2 adsorbed phase concentration profiles (for increasing times, from lighter to darker blue) are indicative and reflect the behavior reported in Sections 2.1.1 to 2.1.4. The adsorbed phase concentrations profiles are homogeneous during the heating and cooling steps, whereas a front develops and propagates through the column in the pressurization and adsorption steps.

1. negligible mass transfer resistances , i.e, equilibrium between fluid and adsorbed phase is reached instantaneously;
2. the fluid phase is treated as a perfect gas;
3. negligible influence of the heat capacity of the column wall on the bed dynamics;
4. the temperature of the heat exchange fluid is homogeneous along the column;
5. negligible radial gradients, thermal dispersion and axial mixing;
6. negligible heat capacity of the sorbate, i.e., gas and adsorbed phases, as compared to that of the adsorbent material;
7. negligible pressure drop;
8. constant heat transfer coefficient is, i.e., independent of composition, temperature and pressure of the fluid phase.

These assumptions are of a general character, i.e., they do not reduce the applicability of the model to a specific cycle. The equilibrium assumption is clearly the strongest one and it is never exactly fulfilled in a physical system. Nevertheless, equilibrium models have proven to be very useful in several adsorption processes for preliminary design purposes. Another important assumption is that of neglecting the effect of the column wall on the heat transfer to and from the bed. This hypothesis allows omitting the energy balance of the heat transfer fluid and of the wall thus substantially reducing the complexity of the model. Although this is a reasonable approximation for a simplified model, the energy balances of the column wall and of the thermofluid should be considered when designing a real system as it might be important for the total heat duty estimation and the cycle time. Finally, the assumption of negligible heat capacity of the sorbate is reasonable at low to moderate pressure conditions, where the sensible heat of the gas and adsorbed phases is much smaller as compared to that of the adsorbent material. Note that this assumption implies that the energy associated to the inlet and outlet streams is negligible.

The governing equations are given by the mass and energy balances of the bed:

$$\epsilon \left(\frac{\partial (yP/T)}{\partial t} + P \frac{\partial (vy/T)}{\partial z} \right) + \rho_b R \frac{\partial n_1}{\partial t} = 0 \tag{4.1}$$

$$\epsilon \left(\frac{\partial P/T}{\partial t} + P \frac{\partial v/T}{\partial z} \right) + \rho_b R \sum_{i=1}^{2} \frac{\partial n_1}{\partial t} = 0 \tag{4.2}$$

$$C_{p,b} \frac{\partial T}{\partial t} - \rho_b \sum_{i=1}^{2} (-\Delta H_i) \frac{\partial n_1}{\partial t} = US(T_{\mathrm{HX}} - T) \tag{4.3}$$

where y is the CO_2 mole fraction, $n_i = n_i(T, P, y)$ is the adsorbed phase concentration of component i (component 1 refers to the more retained component CO_2, and 2 to the less retained one, namely N_2), $C_{p,b}$ is the heat capacity of the adsorbent, ΔH_i the isosteric heat of adsorption, and $US(T_{\mathrm{HX}} - T)$ is the heat exchanged with the heat transfer medium at temperature T_{HX}.

Eqs. (4.1) to (4.3) must be solved with the appropriate initial and boundary conditions. In the following, the analytic or semi-analytic solutions are derived for the individual steps of the cycle of interest here.

4.2.1.1 *Heating step*

At the beginning of the heating step, the column is assumed to be in a homogeneous state corresponding to saturation with the feed. As the column is heated, material desorbs and induces a flow, which leaves the column from its open end (see Figure 4.1).

For an initially homogeneous state of the column, i.e. no axial gradients in composition, temperature or pressure, and negligible pressure drop, it can be shown that there is no axial composition gradient as the temperature increases (further details are given in appendix C.1). Hence, this step can be modeled as a semi-batch process at constant pressure, with an outgoing flow velocity v_{out}. The material and energy balances are given by:

$$\frac{\epsilon P}{R} \frac{\mathrm{d}(y/T)}{\mathrm{d}t} + \rho_b \frac{\mathrm{d}n_1}{\mathrm{d}t} + \frac{v_{\mathrm{out}} y}{L} \frac{P}{RT} = 0 \tag{4.4}$$

$$\frac{\epsilon P}{R} \frac{\mathrm{d}(1/T)}{\mathrm{d}t} + \rho_b \sum_{i=1}^{2} \frac{\mathrm{d}n_i}{\mathrm{d}t} + \frac{v_{\mathrm{out}}}{L} \frac{P}{RT} = 0 \tag{4.5}$$

$$C_{p,b} \frac{\mathrm{d}T}{\mathrm{d}t} - \rho_b \sum_{i=1}^{2} (-\Delta H_i) \frac{\mathrm{d}n_i}{\mathrm{d}t} = US(T_{\mathrm{heat}} - T) \tag{4.6}$$

with unknowns y, T and v_{out}. By eliminating v_{out} from Eqs. (4.4) and (4.5), the system can be recast as the following two ordinary differential equations (ODEs):

$$\left(\frac{\epsilon P}{RT} + \rho_b \left[(1-y)\frac{\partial n_1}{\partial y} - y\frac{\partial n_2}{\partial y}\right]\right)\frac{\mathrm{d}y}{\mathrm{d}t} + \\ + \rho_b \left((1-y)\frac{\partial n_1}{\partial T} - y\frac{\partial n_2}{\partial T}\right)\frac{\mathrm{d}T}{\mathrm{d}t} = 0; \tag{4.7}$$

$$\left(C_{p,b} - \rho_b \sum_{i=1}^{2}(-\Delta H_i)\frac{\partial n_i}{\partial T}\right)\frac{\mathrm{d}T}{\mathrm{d}t} + \\ - \rho_b \sum_{i=1}^{2}(-\Delta H_i)\frac{\partial n_i}{\partial y}\frac{\mathrm{d}y}{\mathrm{d}t} = US(T_{\text{heat}} - T); \tag{4.8}$$

to be solved for the following initial condition and final constraint:

$$t = 0: \qquad T = T_L; \quad y = y_F$$
$$t = t_{\text{heat}}: \quad T = T_H; \quad y = y_{\text{heat}}^{end}$$

The outgoing flow velocity v_{out} varies with time, and it is calculated at every integration step in order to verify the mass balance.

4.2.1.2 *Cooling step*

The cooling step has no in/out flows (see Figure 6.2), and for an initially homogeneous bed, no gradients will develop. Hence, it can be modeled as a batch with varying pressure and temperature:

$$\frac{\epsilon}{R}\frac{\mathrm{d}(yP/T)}{\mathrm{d}t} + \rho_b \frac{\mathrm{d}n_1}{\mathrm{d}t} = 0 \tag{4.9}$$

$$\frac{\epsilon}{R}\frac{\mathrm{d}(P/T)}{\mathrm{d}t} + \rho_b \sum_{i=1}^{2}\frac{\mathrm{d}n_i}{\mathrm{d}t} = 0 \tag{4.10}$$

$$C_{p,b}\frac{\mathrm{d}T}{\mathrm{d}t} - \rho_b \sum_{i=1}^{2}(-\Delta H_i)\frac{\mathrm{d}n_i}{\mathrm{d}t} = US(T_{\text{cool}} - T) \tag{4.11}$$

with unknowns y, T and P. These equations can be recast as a system of three ODEs:

$$\left(\rho_b \frac{\partial n_1}{\partial P} + \frac{\epsilon y}{RT}\right)\frac{\mathrm{d}P}{\mathrm{d}t} + \left(\rho_b \frac{\partial n_1}{\partial T} - \frac{\epsilon y P}{RT^2}\right)\frac{\mathrm{d}T}{\mathrm{d}t} + \left(\rho_b \frac{\partial n_1}{\partial y} + \frac{\epsilon P}{RT}\right)\frac{\mathrm{d}y}{\mathrm{d}t} = 0; \tag{4.12}$$

$$\left(\rho_b \sum_{i=1}^{2} \frac{\partial n_i}{\partial P} + \frac{\epsilon}{RT}\right)\frac{\mathrm{d}P}{\mathrm{d}t} + \left(\rho_b \sum_{i=1}^{2} \frac{\partial n_i}{\partial T} - \frac{\epsilon P}{RT^2}\right)\frac{\mathrm{d}T}{\mathrm{d}t} = 0; \tag{4.13}$$

$$-\rho_b \sum_{i=1}^{2}(-\Delta H_i)\frac{\partial n_i}{\partial P}\frac{\mathrm{d}P}{\mathrm{d}t} + \left(C_{p,b} - \rho_b \sum_{i=1}^{2}(-\Delta H_i)\frac{\partial n_i}{\partial T}\right)\frac{\mathrm{d}T}{\mathrm{d}t} - \rho_b \sum_{i=1}^{2}(-\Delta H_i)\frac{\partial n_i}{\partial y}\frac{\mathrm{d}y}{\mathrm{d}t} = US(T_{\mathrm{cool}} - T); \tag{4.14}$$

to be solved for the following initial condition and final constraint:

$$\begin{aligned} t = 0: &\quad T = T_H; \quad y = y_{\mathrm{heat}}^{end}; \quad P = P_H \\ t = t_{\mathrm{cool}}: &\quad T = T_L; \quad y = y_{\mathrm{cool}}^{end}; \quad P = P_L \end{aligned}$$

4.2.1.3 *Pressurization step*

The composition fronts developing during this step will affect the ensuing adsorption step. Equilibrium theory for pressure-varying steps is very complex; the equations have been derived for linear isotherms, but when nonlinear isotherms are involved the additional complexity makes the equations very cumbersome and their solution is of similar complexity as that of detailed models.[112]

It can be shown that for moderate values of the high pressure level, little molar fraction of the heavy component in the feed and highly selective adsorbents, the mass of CO_2 fed to the column in order to achieve the desired pressure increase is very small as compared to the total mass present. Detailed simulations performed under conditions of fast mass transfer, low axial dispersion and low pressure drop reveal that assuming a flat composition profile at the end of the pressurization step is a reasonable approximation (discussed in appendix C.1).

At constant temperature, and for a given initial state ($P_L, y^{\text{end}}_{\text{cool}}$) and end pressure ($P_H$), the composition at the end of the pressurization step can be determined through a mass balance, which yields an implicit equation in $y^{\text{end}}_{\text{press}}$:

$$\frac{\rho_b}{\epsilon} RT \left((n^{\text{end}}_{1,\text{press}} - n^{\text{end}}_{1,\text{cool}}) - y_F \sum_{i=1}^{2} (n^{\text{end}}_{i,\text{press}} - n^{\text{end}}_{i,\text{cool}}) \right) + (y^{\text{end}}_{\text{press}} P_H - y^{\text{end}}_{\text{cool}} P_L) - y_F (P_H - P_L) = 0 \tag{4.15}$$

The pressurization time is given again by a material balance as the ratio of the amount of material needed to pressurize and the flow rate:

$$\begin{aligned} t_{\text{press}} &= \frac{N_{\text{press}}}{A\, v_F} \frac{RT_L}{\epsilon\, P_H} \\ &= \frac{L}{v_F} \left[\frac{R\, T_L}{P_H} \frac{\rho_b}{\epsilon} \sum_{i=1}^{2} (n^{\text{end}}_{i,\text{press}} - n^{\text{end}}_{i,\text{cool}}) + \left(1 - \frac{P_L}{P_H} \right) \right] \end{aligned} \tag{4.16}$$

where v_F is the interstitial feed velocity and A is the column cross-section.

4.2.1.4 *Adsorption step*

The partial pressure of CO_2 in the feed is larger as compared to the state of the column at the beginning of the adsorption step. It can be shown that a shock-wave separating two constant states will travel through the column, provided that the initial state is indeed constant.[113] The adsorption time t_{ads} will be given by the time needed for the shock to travel from the column inlet to the column outlet:

$$t_{\text{ads}} = \tilde{\sigma} L \tag{4.17}$$

where $\tilde{\sigma}$ is the reciprocal of the shock velocity. Its value is determined by solving the total and component mass balances in integral form under the assumption that a shock transition separates two constant states;[114] one obtains:

$$t_{\text{ads}} = \frac{L}{v_F} + \frac{\frac{\rho_b}{\epsilon} \frac{RT}{P} \left([n_1] - y^{end}_{\text{press}} ([n_1] + [n_2]) \right)}{v_F\, [y]} L \tag{4.18}$$

where v_F is the interstitial feed velocity and the terms between the square brackets represent a jump across the shock, i.e., the difference of the quantity enclosed in the square brackets evaluated at the two states separated by the shock, namely:

$$[y] = y_F - y^{\text{end}}_{\text{press}} \qquad [n_i] = n^{\text{end}}_{i,\text{ads}} - n^{\text{end}}_{\text{press}} \tag{4.19}$$

4.2.2 Solution procedure

The model equations and unknowns are listed in Table 4.1. The cycle is described by 8 equations which contain 10 unknowns, thus two unknowns must be specified in order to solve the equations. A reasonable choice is that of fixing the high and low temperature levels (T_{H} and T_{L}), since they are easy to control and they directly affect the thermodynamic states of the column, which define the effective cyclic capacity.

For known high and low temperature levels, Eqs. (4.7), (4.8) and (4.12) to (4.14) form a subsystem in 5 unknowns ($y^{\text{end}}_{\text{heat}}$, $y^{\text{end}}_{\text{cool}}$,$t_{\text{heat}}$, t_{cool}, P_L), which can be solved separately. Thereby the two sets of ODEs are recast in such a way that temperature is the independent variable; time and molar fraction profiles (and of pressure for the cooling case) are then obtained by integration. The remaining three unknowns, namely $y^{\text{end}}_{\text{press}}$, t_{press} and t_{ads} are determined from Eqs. (4.15), (4.16) and (4.18), respectively.

It is worth noting that the cyclic steady state (CSS) condition is enforced by setting the initial state of the column for the heating step equal to the feed state, which in fact corresponds to the end of the adsorption step.

4.2.3 Model results and performance indicators

Process optimization entails minimizing costs, namely both the capital and the operating costs. As a first approximation, the capital costs are governed by the total volume of the plant (in other words by the corresponding mass of adsorbent) that determines the total number of columns. For a specified production rate, the volume of

Table 4.1. – List of equations and unknowns of the model. The remaining variables summarized in Table 4.2 are treated as model parameters.

Equations	**8**	
Heat.	Eq. (4.7)	$\left(\frac{\epsilon P}{RT}+\rho_b\left[(1-y)\frac{\partial n_1}{\partial y}-y\frac{\partial n_2}{\partial y}\right]\right)\frac{\mathrm{d}y}{\mathrm{d}t}+\rho_b\left((1-y)\frac{\partial n_1}{\partial T}-y\frac{\partial n_2}{\partial T}\right)\frac{\mathrm{d}T}{\mathrm{d}t=0}$
	Eq. (4.8)	$\left(C_{p,b}-\rho_b\sum_{i=1}^{2}(-\Delta H_i)\frac{\partial n_i}{\partial T}\right)\frac{\mathrm{d}T}{\mathrm{d}t}-\rho_b\sum_{i=1}^{2}(-\Delta H_i)\frac{\partial n_i}{\partial y}\frac{\mathrm{d}y}{\mathrm{d}t}=US(T_{\mathrm{heat}}-T)$
Cool.	Eq. (4.12)	$\left(\rho_b\sum_{i=1}^{2}\frac{\partial n_i}{\partial P}+\frac{\epsilon}{RT}\right)\frac{\mathrm{d}P}{\mathrm{d}t}+\left(\rho_b\sum_{i=1}^{2}\frac{\partial n_i}{\partial T}-\frac{\epsilon}{RT^2}\right)\frac{\mathrm{d}T}{\mathrm{d}t}=0$
	Eq. (4.13)	$-\sum_{i=1}^{2}(-\Delta H_i)\frac{\partial n_i}{\partial P}\frac{\mathrm{d}P}{\mathrm{d}t}+\left(C_{p,b}-\rho_b\sum_{i=1}^{2}(-\Delta H_i)\frac{\partial n_i}{\partial T}\right)\frac{\mathrm{d}T}{\mathrm{d}t}-\rho_b\sum_{i=1}^{2}(-\Delta H_i)\frac{\partial n_i}{\partial y}\frac{\mathrm{d}y}{\mathrm{d}t}=US(T_{\mathrm{heat}}-T)$
	Eq. (4.14)	$\left(\rho_b\frac{\partial n_1}{\partial P}+\frac{\epsilon y}{RT}\right)\frac{\mathrm{d}P}{\mathrm{d}t}+\left(\rho_b\frac{\partial n_1}{\partial T}-\frac{\epsilon yP}{RT^2}\right)\frac{\mathrm{d}T}{\mathrm{d}t}+\left(\rho_b\frac{\partial n_1}{\partial y}+\frac{\epsilon P}{RT}\right)\frac{\mathrm{d}y}{\mathrm{d}t}=0$
Press.	Eq. (4.15)	$\frac{\rho_b}{\epsilon}RT\left((n^{\mathrm{end}}_{1,\mathrm{press}}-n^{\mathrm{end}}_{1,\mathrm{cool}})-y_F\sum_{i=1}^{2}(n^{\mathrm{end}}_{i,\mathrm{press}}-n^{\mathrm{end}}_{i,\mathrm{cool}})\right)+(y^{\mathrm{end}}_{\mathrm{press}}P_H-y^{\mathrm{end}}_{\mathrm{cool}}P_L)-y_F(P_H-P_L)=0$
	Eq. (4.16)	$t_{\mathrm{press}}=\frac{L}{v_F}\left[\frac{RT_L}{P_H}\frac{\rho_b}{\epsilon}\sum_{i=1}^{2}(n^{\mathrm{end}}_{i,\mathrm{press}}-n^{\mathrm{end}}_{i,\mathrm{cool}})+(1-P_L/P_H)\right]$
Ads.	Eq. (4.18)	$t_{\mathrm{ads}}=\frac{L}{v_F}+\frac{\rho_b}{\epsilon}\frac{RT}{P}\left([n_1]-y^{\mathrm{end}}_{\mathrm{press}}([n_1]+[n_2])\right)\frac{L}{v_F[y]}$
Unknowns	**10**	
Heat.+Cool.		$y^{\mathrm{end}}_{\mathrm{heat}}$, $y^{\mathrm{end}}_{\mathrm{cool}}$,$t_{\mathrm{heat}}$, t_{cool}, T_{H}, T_{L}, P_L
Ads.+Press.		$y^{\mathrm{end}}_{\mathrm{press}}$, t_{ads}, t_{press}, (P_L)

adsorbent is proportional to the inverse of the productivity, which is defined as the amount of target product produced, i.e, CO_2 captured, per unit time and unit mass of adsorbent:

$$\mathrm{Pr} = \frac{N_{\mathrm{CO_2,heat}} / t_{\mathrm{cycle}}}{\rho_b \, V_{\mathrm{col}}} \tag{4.20}$$

where $N_{\mathrm{CO_2,heat}}$ is the amount of CO_2 produced during one cycle, t_{cycle} is the total cycle time and V_{col} is the bed volume.

A major contribution to the operating costs is generally the energy consumption, which is particularly relevant in the context of CO_2 capture applications. For a generic TSA it is given in terms of the electrical and the thermal energy consumption. In this work, consistently with the model equations, the pressure drop is assumed to be negligible; therefore, no power consumption associated with the use of a flue gas blower is considered. Moreover, all the investigated cases consider constant superficial gas velocity (at the inlet) and column length, which would lead to the same pressure drop in a real system. Accordingly, only the thermal energy consumption of the TSA (Q_{TSA}) is considered, which can be computed from the sensible heat duty of the system and the isosteric heat of adsorption. Note that in order to obtain a fair evaluation of the heating duty, it is important to account also for the thermal inertia of the column wall. The wall temperature will experience temperatures between that of the bed and that of the heat exchange fluid; the value will depend on the relative magnitude of the heat transfer resistances fluid/wall vs. wall/sorbent (cfr. appendix C.4). In the best case, the wall will cycle between T_H and T_L similarly to the sorbent material, and the additional energy requirement will depend on the geometry of the wall. For a given $V_{\mathrm{wall}} \, C_{p,w}$ the minimum heat duty is given by:

$$\begin{aligned} Q_{\mathrm{TSA}} = V_{\mathrm{col}} \left(C_{p,b}(T_H - T_L) - \rho_b \sum_{i=1}^{2} \Delta n_i (-\Delta H_i) \right) \\ + V_{\mathrm{wall}} \, C_{p,w}(T_H - T_L) \end{aligned} \tag{4.21}$$

where Δn_i is the difference in loadings over the heating step, ΔH_i is the isosteric heat of adsorption, and $C_{p,w}$ the heat capacity of the wall.

The specific thermal energy requirement e_{th} is given per unit mass of CO_2 produced as:

$$e_{\text{th}} = \frac{Q_{\text{TSA}}}{N_{\text{CO}_2,\text{heat}}\, M_{w,\text{CO}_2}} \tag{4.22}$$

Thermal regeneration is of interest mainly due to the possibility of recovering the sensible heat of the flue gas. However, for high CO_2 recovery the sensible heat contained in the flue gas is not sufficient for the regeneration (e.g. for 12% mol CO_2 in the feed and 50% CO_2 recovery, an efficient heat integration in which the flue gas temperature is decreased by 120 °C corresponds to 1.4 $\text{MJ/kg}_{\text{CO}_2}$: hardly half of the needed 3–4 $\text{MJ/kg}_{\text{CO}_2}$ thermal energy for a TSA separation[48,98]).

The performance indicators used for the assessment of the process performance are the productivity Pr and the specific energy consumption e_{th}. A valid comparison can only be made for process conditions which yield similar specifications. For the considered application, the specifications are given in terms of CO_2 purity and CO_2 recovery, defined by the following equations, respectively:

$$\Phi = \frac{N_{\text{CO}_2,\text{heat}}}{N_{\text{CO}_2,\text{heat}} + N_{\text{N}_2,\text{heat}}} \tag{4.23}$$

$$r = \frac{N_{\text{CO}_2,\text{heat}}}{N_{\text{CO}_2,\text{in}}} \tag{4.24}$$

where $N_{i,\text{heat}}$ and $N_{i,\text{in}}$ are the amount of moles of species i leaving the column during the heating step, and being fed to the column over the entire cycle, respectively.

4.3 SIMULATION RESULTS AND PARAMETRIC ANALYSIS

By solving the model equations presented above for a given set of high and low temperature levels, the duration of each step as well as the temperature, pressure and composition profiles along the column during the entire cycle can be calculated. All the simulations have

been performed for a binary 0.12/0.88 (v/v) CO_2/N_2 feed mixture, using zeolite 13X as adsorbent; all column and gas-phase parameters are listed in Table 4.2. The pure component adsorption isotherms were previously measured with static experiments and described with the Sips isotherm according to Eqs. (3) to (6) of Hefti et al.[83] (summarized in appendix B.1), and combined into a competitive isotherm with the extended binary Sips equation:

$$n_i^{\mathrm{eq}} = n_{\mathrm{ref}}^{\infty} \frac{(b_i p_i)^{c_i}}{1 + \sum_{i=1}^{2} (b_i p_i)^{c_i}} \tag{4.25}$$

where p_i is the partial pressure of component i, $n_{i,\mathrm{ref}}$ and b_i are its saturation capacity and adsorption equilibrium constant, respectively. The third parameter c_i accounts for the surface inhomogeneity.

Table 4.2. – Parameter values used for the simulations.

Parameter	Value	Comment
y_F	0.12	flue-gas composition
P_H	1.0 bar	atmospheric pressure
T_{heat}	$\{420, 440, 460\}$ K	–
T_{cool}	300 K	ambient temperature
ϵ	0.70	13X pellets (2 mm)
d_i	3.00 cm	shell and tube geometry
d_o	3.18 cm	*id.*
S	$133.5\,\mathrm{m^2/m^3}$	*id.*
U	$16.8\,\mathrm{J/(m^2\,s\,K)}$	*id.*
$C_{p,b}$	$0.65\,\mathrm{MJ/(m^3\,K)}$	adsorbent bed
$C_{p,w}$	$4.0\,\mathrm{MJ/(m^3\,K)}$	stainless steel wall
ρ_b	$708\,\mathrm{kg/m^3}$	adsorbent bed
L	1.2 m	–
v_F	0.5 m/s	below fluidization
adsorption equilibrium		Hefti et al.[83]
ΔH_1 (CO_2)	−37 000 J/mol	Clausius-Clapeyron[83]
ΔH_2 (N_2)	−18 510 J/mol	Clausius-Clapeyron[83]

Figure 4.2 shows a stack graph of the step durations as function of the high (T_H) and low temperature (T_L) values achieved within the cycle. For the sake of clarity, only a few values of T_L are shown. Note

that the sum of the individual step durations represents the total cycle time. An increase in total cycle time is observed for the extreme values of the high and low temperature levels, with an asymptotic behavior as $T_H \rightarrow T_{\text{heat}}$ and $T_L \rightarrow T_{\text{cool}}$ (the latter is not visible because of the choice of showing only discrete values of T_L). When moving along the diagonal, i.e., increasing both T_H and T_L, the duration of the heating step increases at the expense of the duration of the cooling step (the relative contribution of each step is more clearly visible in Figure C.3, where the duration of each step divided by the total cycle time is shown in a similar manner). While the contribution of the adsorption step is of similar magnitude as that of the heating and cooling steps, the pressurization step represents less than one percent of the total cycle time, which is in agreement with the assumption that the required amount of mass fed to pressurize the column is small. Generally, heating times are longer than cooling times. This is explained by the relative importance of the adsorption heat during heating and cooling: while the adsorbate amount corresponding to the total effective cyclic capacity is desorbed during heating, only a part of it is adsorbed during the cooling step.

4.3.1 Comparison with detailed simulations: outlet profiles

The T-, P- and y-profiles calculated using the shortcut model were compared to those calculated with the detailed model at the CSS for a variety of operating conditions (see Figsures C.5 to C.12 of the appendix). A region of operating conditions can be identified, in which the CO_2 desorbed during the heating step does not completely displace the nitrogen, and hence the composition within the column is not pure CO_2 at the end of the heating step. Under these conditions, the obtained CO_2 purity is low and the agreement between the shortcut model and the detailed model is poor. In the cases of interest, where pure CO_2 prevails within the column at the end of the heating step and high CO_2 purity is achieved, a rather good agreement is observed. A representative example thereof is shown in Figure 4.3 (cfr. Fig. C.5 of the appendix), for high and low temperature levels of $T_H = 430\,\text{K}$ and $T_L = 310\,\text{K}$, respectively. Whereas for the shortcut model the profiles within the column are constant in position with the exception

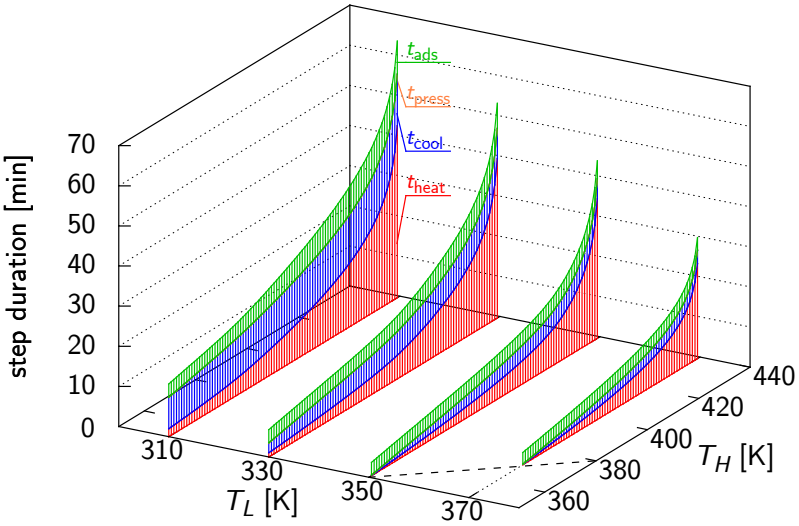

Figure 4.2. – Total cycle duration and duration of the individual steps as function of the effective high and low temperature levels. Simulations have been carried out with $T_{\text{cool}} = 300\,\text{K}$, $T_{\text{heat}} = 440\,\text{K}$, $P_H = 1\,\text{bar}$ and $y_F = 0.12$

of the adsorption step, this is not necessarily the case for the profiles calculated with the detailed model. This is partly due to the non-zero pressure drop, and partly due to the non-isothermal adsorption step, which yields a temperature profile at the beginning of the heating step. Note that the profiles shown in Figure 4.3 are those at the column outlet, which is located according to the flow direction at $z = 0$ for the heating and cooling steps, and at $z = L$ for the pressurization and adsorption steps (see Figure 4.1). A large difference is observed in the adsorption step, where the early CO_2 breakthrough calculated with the detailed model is due to the dispersed front and to the temperature rise. The non-isothermal nature of the adsorption step also induces a temperature profile within the column at the beginning of the heating step which is observed to range between ca. 310 K and 330 K. A further consequence thereof is a lower CO_2 loading in the column at the end of the adsorption step in the detailed model as compared to the shortcut model.

Despite these differences, the main characteristics of the temperature, pressure and composition profiles are captured by the shortcut model, and we believe that this is accurate enough to describe important trends correctly. This is particularly true for the range of operating conditions where the optimum is found. In fact a rather good agreement is observed for high values of T_H and low values of T_L (refer to the symbols shown in Figure 4.4(B)), which also lead to optimal process performance, as discussed in the following sections. Moreover, the assumptions of adsorption equilibrium and of an isothermal adsorption step make the predictions by the shortcut model representative of an upper performance bound, which is approached with a very efficient column and fast heat removal during the adsorption step. Based on these considerations, the shortcut model is used in the following sections to investigate the purity, recovery, specific energy consumption and productivity of the four step TSA cycle aimed at extracting the heavy component at high purity.

4.3.2 Purity and recovery

The purity obtained using this four step cycle will only depend on the states of the column at the beginning and the end of the heating

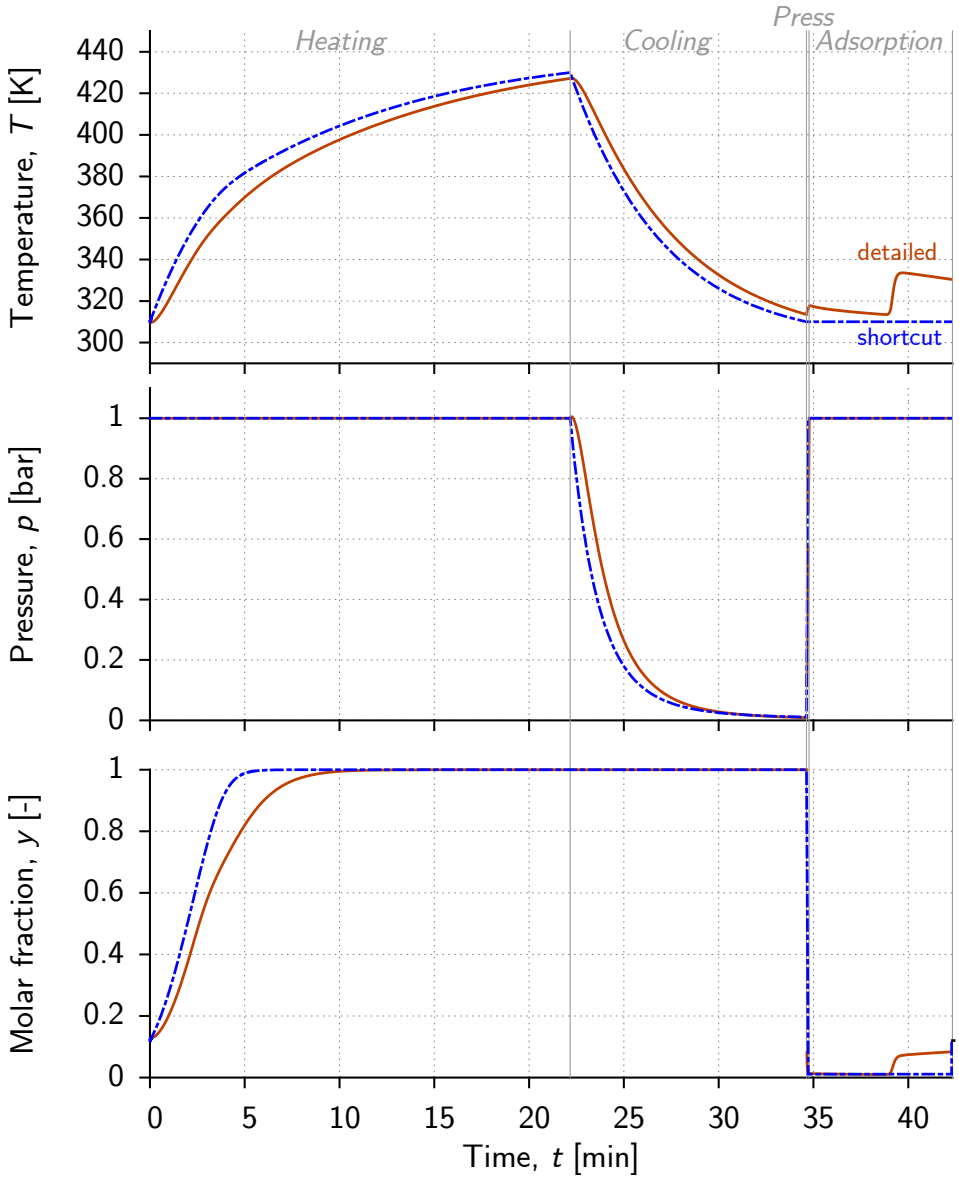

Figure 4.3. – Temperature, pressure and composition outlet profiles as predicted by the shortcut model (dashed lines) and by the detailed model[24] (solid lines) for an exemplary set of operating conditions: $T_H = 430\,\mathrm{K}$ and $T_L = 310\,\mathrm{K}$ (Figure C.5 of the appendix). The outlet is located according to the flow direction at $z = 0$ for the heating and cooling steps, and at $z = L$ for the pressurization and adsorption steps

step. For a given feed composition, these states are governed by the attained high and low temperature levels, regardless of the heating rate. The contour map of purity, Φ, against T_H and T_L is shown in Figure 4.4(A). The region of possible operating conditions is restricted by $T_H > T_L$, $T_L > T_{\text{cool}}$ and $T_H < T_{\text{heat}}$; its limits for an exemplary case with $T_{\text{cool}} = 300\,\text{K}$ and $T_{\text{heat}} = 440\,\text{K}$ are indicated by the dashed lines.

As expected, the purity always increases with the desorption temperature T_H, because the target component is desorbed to a larger extent. However, a decrease in the adsorption temperature T_L does not only increase the adsorbed phase concentration of CO_2 at the beginning of the production (heating) step, thus providing a larger amount of the target component which can be desorbed at a given desorption temperature, but it also increases the hold-up of the less retained component because of the larger density of the (non-selective) gas phase at the beginning of the heating step. These opposing trends lead to the presence of a hump in the surface: for every fixed desorption temperature, there exists an adsorption temperature that corresponds to a global maximum of the purity.

On the other hand, the recovery, shown in Figure 4.4(B), has a monotonic behavior: it increases with the temperature difference $\Delta T = T_H - T_L$. In fact, the larger this difference, the lower the pressure at the end of the cooling step, hence the lower the fraction of CO_2 in the gas phase at the beginning of the adsorption step. It is worth noting that since the recovery is governed by the state of the column at the end of the cooling step, it is independent of the heat transport coefficient and depends solely on the T_L and T_H temperature levels, likewise for purity.

A high recovery approaching $r = 1$ can be reached at moderate desorption temperatures ($T_H > 450\,\text{K}$), whereas the attainable purity is more strongly limited. This behavior is typical for stripping-like adsorption cycles, where the feed step is conducted at low temperature or high pressure and the adsorbent bed extracts the heavy component from the gas phase. These cycles are known to perform well at producing the light component at very high purity and moderate recovery.[112] For a binary system, this implies very high recovery of the heavy component and moderate purity. It is worth mentioning that

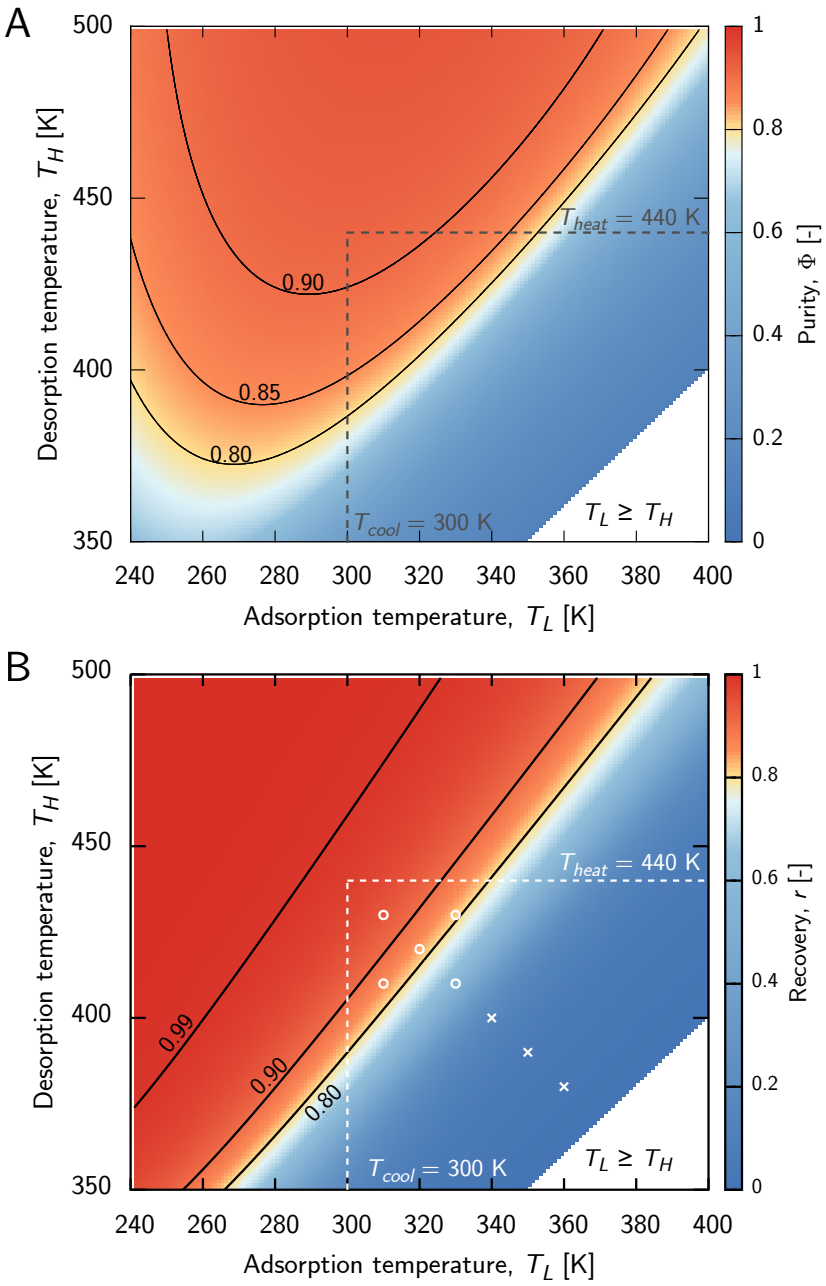

Figure 4.4. – Purity (A) and recovery (B) maps in the T_L, T_H plane as calculated according to Eqs. (4.23) and (4.24), respectively. The dashed lines indicate the region of feasible temperature levels for typical values of $T_{\text{heat}} = 440\,\text{K}$ and $T_{\text{cool}} = 300\,\text{K}$. The symbols shown in (B) indicate the operating conditions considered for the comparison to the detailed model (see Figures C.5 to C.12 of the appendix). White circles indicate a rather good agreement between shortcut model and detailed simulation, whereas in the case of white crosses the agreement is rather poor

with this shortcut model no trade-off is observed between CO_2 purity and recovery because of the step-like composition front during the adsorption step. This front will spread when considering a finite mass transfer rate; complete column loading (which leads to the highest purity) can only be reached if the front breaks through the column and some CO_2 is lost during the adsorption step. Therefore, the purity and recovery predicted by the shortcut model constitute the theoretical maxima that can be achieved in such a system.

4.3.3 Specific energy requirement and productivity

The specific thermal energy requirement e_{th} is shown in Figure 4.5(A). The region $T_L < 290\,\text{K}$ is not colored because the estimation of the specific energy consumption based only on the heating duty is no more a valid approximation if the bed is to be cooled below ambient temperature. The contour lines of e_{th} computed with Eqs. (4.21) and (4.22) are shown nonetheless in order to illustrate the general trends.

In the lower right quadrant, the specific energy consumption decreases with increasing ΔT. In fact, larger ΔT values result in a larger effective capacity. The provided heat is more efficiently used, and a larger fraction is consumed for the actual desorption of CO_2. However, an increase in ΔT does not only lead to an increase in effective cyclic capacity, but also to an increase in the energy required to heat the adsorbent bed. These opposing trends result in the presence of a minimum, which is observed at $T_L = 260\,\text{K}$ and $T_H = 455\,\text{K}$ for this sorbent material if one extrapolates the calculation of the specific energy consumption for heating to temperatures $T_L < 290\,\text{K}$.

Reasonable temperature ranges for TSA applications will typically be such as to not enclose the global minimum of e_{th} as shown by the dashed lines in Figure 4.5, which limit the feasible region to $T_H < 440\,\text{K}$ and $T_L > 300\,\text{K}$. Hence, in the investigated range of desorption temperatures, the regeneration is more efficient at larger ΔT, where a smaller fraction of heat is lost due to thermal inertia (a more detailed discussion on the subject is found in appendix C.5).

The other performance indicator of interest is the productivity, which is high when the total cycle time is short and the amount

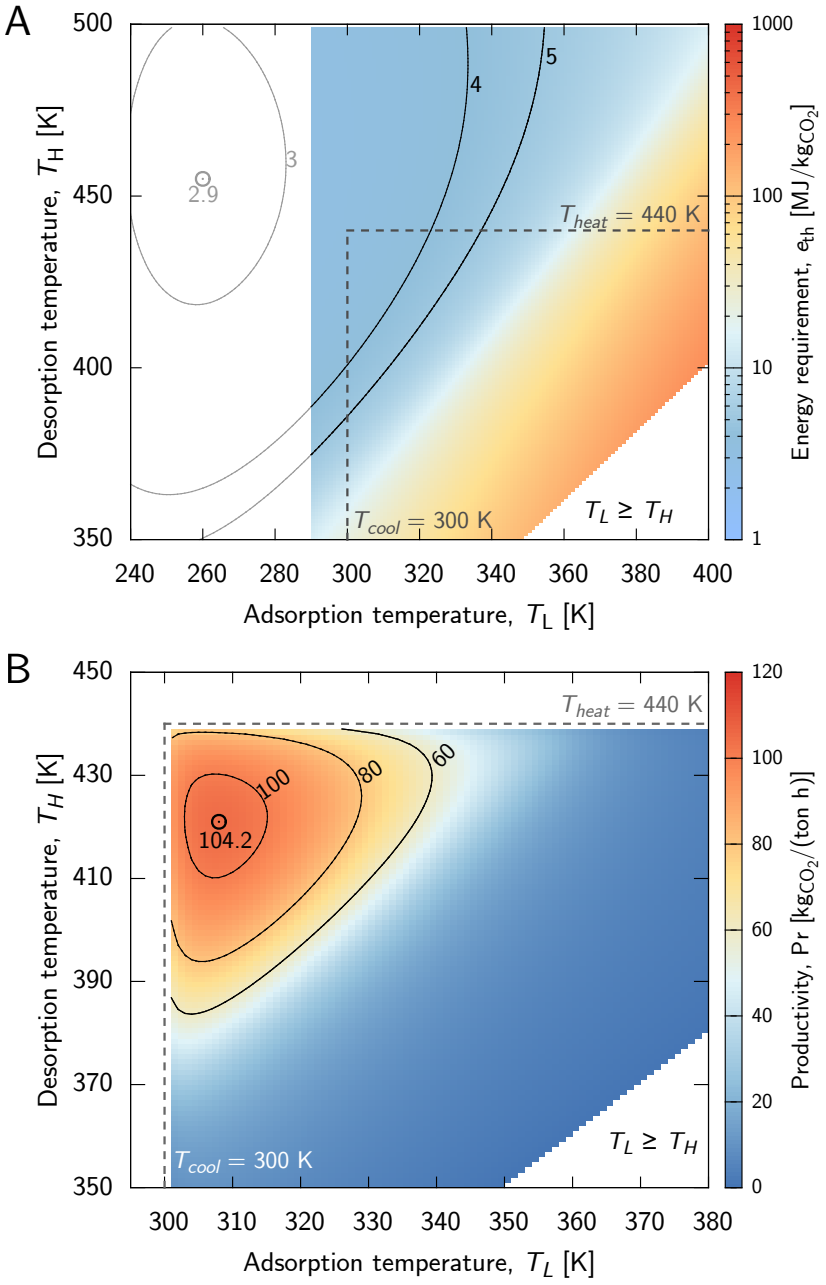

Figure 4.5. – Energy requirement (A) and productivity (B) maps in the T_L, T_H plane. The dashed lines indicate the region of feasible temperature levels for typical values of $T_{\text{heat}} = 440\,\text{K}$ and $T_{\text{cool}} = 300\,\text{K}$. The specific energy requirement calculated considering solely heating and desorption duty is extrapolated to temperatures $T_L < 290\,\text{K}$ (white region). The minimum energy consumption and maximum productivity is indicated by the empty circle, respectively.

of CO_2 produced per cycle is large. Since larger ΔT values result in larger cyclic capacity, but require longer cycle times, there exists a maximal productivity regardless of the considered temperature range. This is shown in Figure 4.5(B), which illustrates the contour plot of the productivity in the (T_L, T_H) plane.

It is worth noting that, as predicted by this shortcut model the purity, recovery and the specific energy requirement depend only on the states of the column reached during the cycle and hence on the heating/cooling temperature levels. The productivity, on the other hand, depends also on the times required to reach these states, and thus it also depends on heat transfer and column dimensions. Therefore, the contour plot shown in Figure 4.5(B) is specific for the values of T_{cool}, T_{heat}, U, L and v_F chosen in this example.

The optimal process conditions are those that maximize the productivity and minimize the specific energy requirement. Since the corresponding optima are independent and in general different, a trade-off is most likely to exist. In the case illustrated above, where the maximal productivity is located at lower desorption temperatures (T_H) and higher adsorption temperatures (T_L) as compared to the minimal specific energy requirement, the optimal operating points will be located in the upper left corner of the (T_L, T_H) plane for given heating and cooling temperatures (see Figure 4.5(B)), which corresponds to the maximal achievable purities under those conditions. As anticipated in Section 4.3.1, the region of optimal operating conditions coincides with the operating region where a greater accuracy is observed when comparing outlet profiles predicted by shortcut and detailed model at the cyclic steady state (cf. Figure 4.4(B)).

4.4 THEORETICAL PERFORMANCE LIMITS

As expected from the analysis above there is not a single optimal operating point with respect to productivity and energy consumption, but there is a set of optimal points. This set, called a Pareto front, separates the region of feasible operating conditions from that of unfeasible operating conditions, and it is such that when moving

along the front one performance indicator approaches its optimum while the other drifts away from its optimum.

Figure 4.6(A) shows the Pareto front for different values of the heating temperature (420 K, 440 K and 460 K), as well as the Pareto fronts at $T_{\text{heat}} = 440\,\text{K}$ for different values of the heat transfer coefficient ($\pm 10\,\%$ of $U = 16.8\,\text{J}/(\text{m}^2\,\text{s}\,\text{K})$). Note that all the operating points belonging to the Pareto fronts achieve a purity $\Phi \geq 0.85$.

An increase in the overall heat transfer coefficient (U) only impacts the productivity by decreasing the heating and cooling times. In fact, the specific energy required depends on the states reached during the cycle, and not on the heat transfer rate. On the other hand, an increase in the temperature of the heat exchange medium will also impact the specific energy consumption, since larger ΔT values, hence greater desorption efficiency can be achieved. Moreover, the increase in productivity is further enhanced because of the larger cyclic capacity, which allows that the column be loaded to a larger extent during the adsorption step. On the other hand, the higher the heating temperature, the higher the quality of the energy (exergy) needed by the TSA process, which can result in an overall larger primary energy requirement for CO_2 capture. Therefore, it is good design practice to limit the desorption temperature to a level below 200 °C.

The purity associated with the operating conditions belonging to the Pareto fronts is shown in Figure 4.6(B). Since the Pareto-optimal operating conditions are located in the upper left corner of the (T_L, T_H) plane, they will not be affected by the relaxation of the specification on the purity. The effect of a more stringent specification on the purity, for instance $\Phi \geq 0.9$, can be deduced from Figure 4.6(B). The Pareto obtained with the highest heating temperature $T_{\text{heat}} = 460\,\text{K}$ would not be affected, since all the optimal operating points yield a purity which is larger than the specification. For a slightly lower heating temperature ($T_{\text{heat}} = 440\,\text{K}$), the operating points yielding a purity lower than the specification would not be considered, thereby truncating the Pareto and decreasing the maximal achievable productivity. Finally, at the lowest heating temperature no set of operating conditions reaches a purity of $\Phi \geq 0.9$.

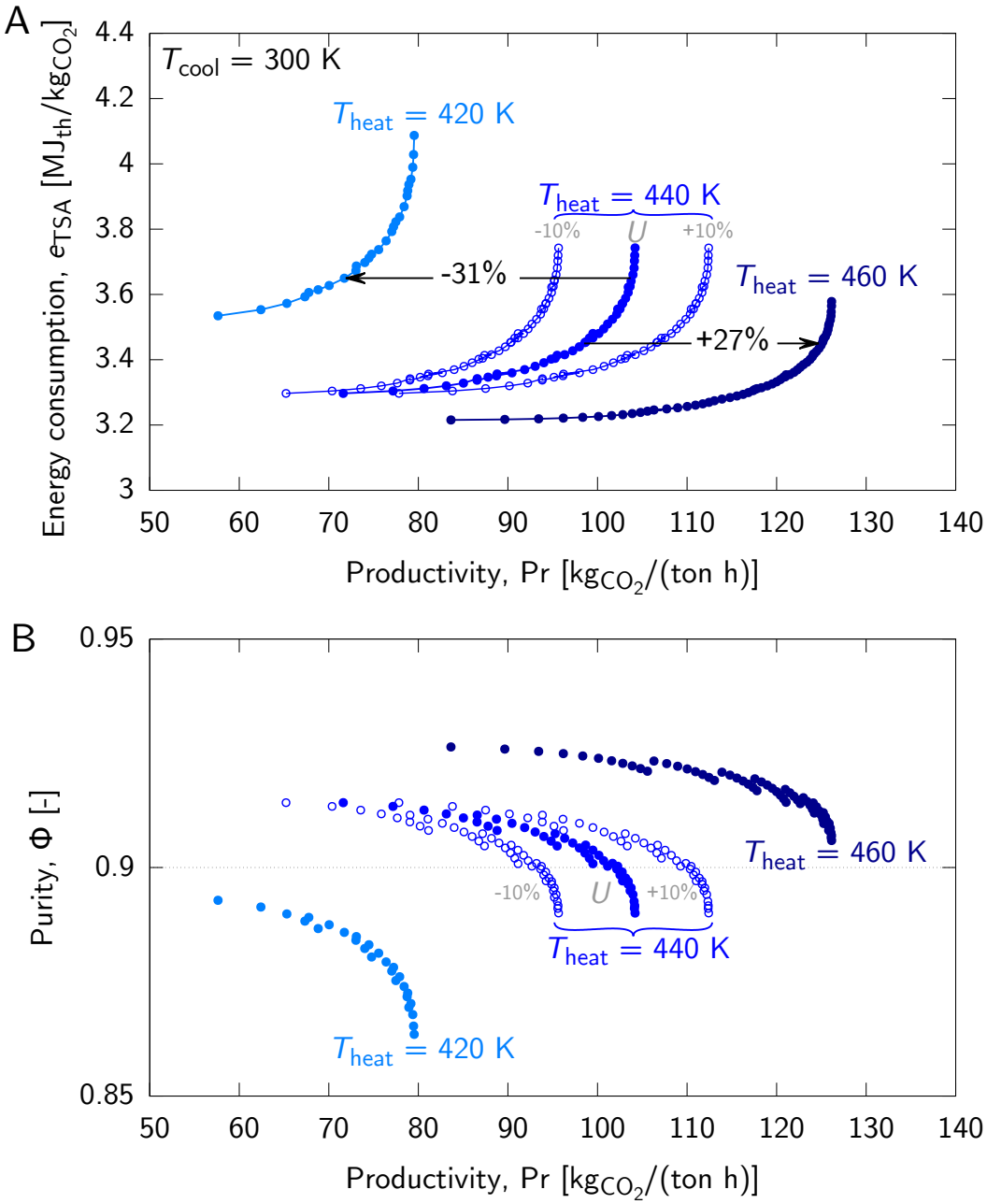

Figure 4.6. – (A) Pareto fronts of the specific energy requirement vs. productivity for different heating temperatures and $U = 16.8\,\mathrm{J/(m^2\,s)}$ (filled symbols), and for $T_{heat} = 440\,\mathrm{K}$ and different heat transfer coefficients: $\pm 10\,\%$ of $U = 16.8\,\mathrm{J/(m^2\,s)}$ (empty symbols). (B) Purity of the CO_2 product along the corresponding Pareto curves

4.4.1 Comparison with detailed simulations

The detailed model has more degrees of freedom than the shortcut model; this makes a meaningful comparison difficult. In the shortcut model, a shock wave composition front, i.e., a discontinuity in the composition profile separating the initial state from the feed state, travels along the column during the adsorption, and the time for this front to reach the end of the column provides the only reasonable choice for the duration of this step. On the contrary, in a detailed model accounting for finite mass transfer rates, the composition front during the adsorption step is more or less sharp, thus leading to a range of possible times for the adsorption step, and of corresponding loadings at the end of the step. A possible basis for comparison is to consider the extreme case of long adsorption times, hence loadings that approach the ones predicted by the shortcut model, and low recovery.

Figure 4.7 compares the energy-productivity Pareto sets obtained from the simplified model with those predicted by detailed simulations. These were determined using the model described in Casas et al.[24] using the same parameters as for the optimization performed with the shortcut model shown in Figure 4.6 (with the exception of the cases with varying heat transfer coefficient). An extensive parametric analysis was carried out, in which the operating conditions (step times) were varied, and the best performance was extracted.

In Figure 4.7(A) the energy-productivity Pareto set obtained from the shortcut model with $T_{\text{heat}} = 440\,\text{K}$ is compared to that calculated via detailed simulations (only one temperature is considered for the sake of clarity). Both sets of operating conditions achieve a CO_2 purity $\Phi \geq 0.85$, and a CO_2 recovery $r \geq 0.3$.

A good qualitative agreement is observed between shortcut model and detailed model, especially in the achieved purity, shown in Figure 4.7(B) for the three values of heating temperature. The overestimated performance predicted by the shortcut model in terms of both productivity and specific energy requirement is due to several effects. Firstly and most importantly, heat effects and mass transfer resistance, which are accounted for in the detailed model, lead to an incomplete loading of the bed at the end of the adsorption step. The

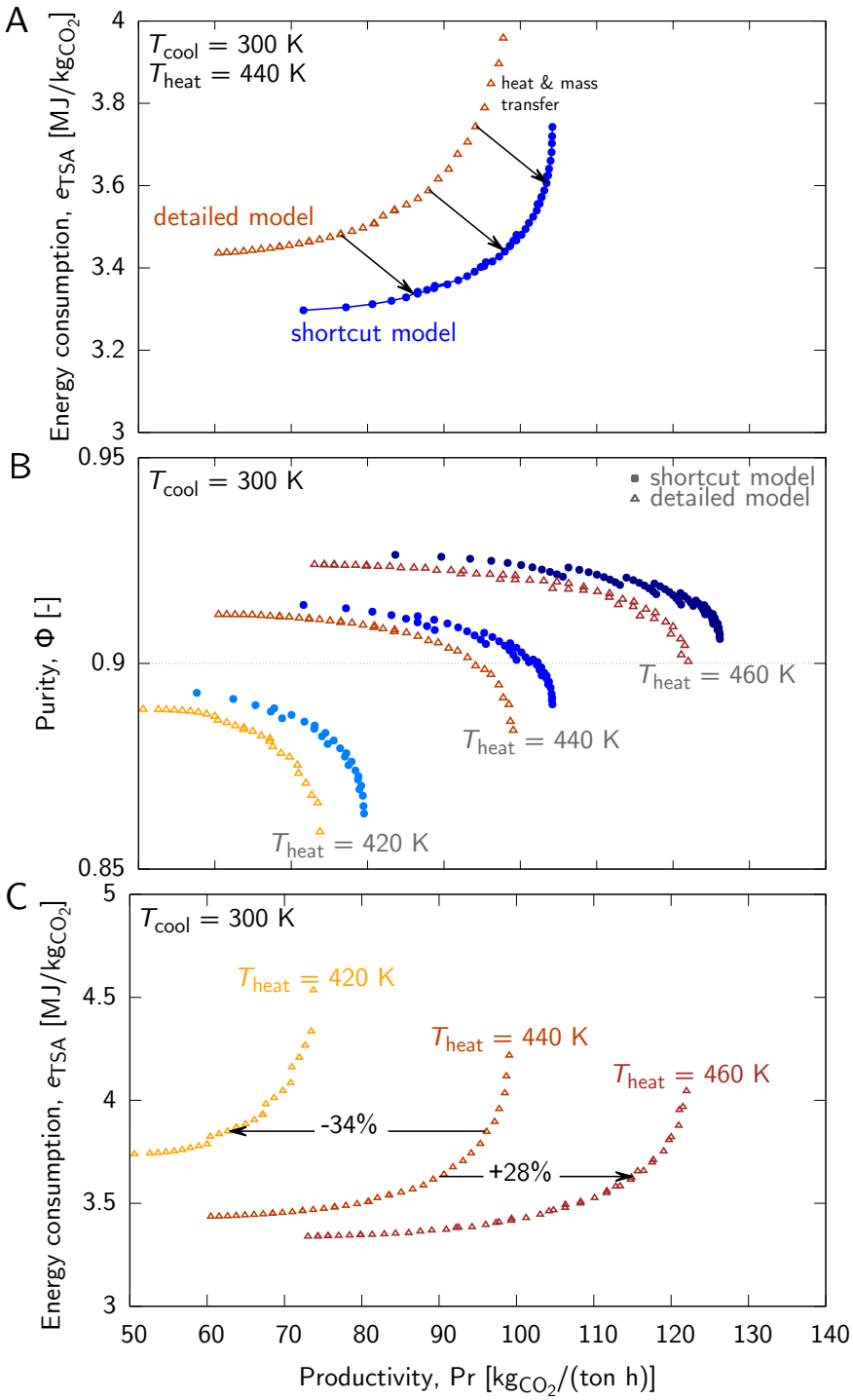

Figure 4.7. – (A) Comparison between the pareto predicted by the shortcut model and the best-performance set as obtained from detailed simulations in the specific energy productivity plane (only the case $T_{heat} = 440\,K$ is shown for the sake of clarity). (B) Purity along the pareto fronts for the shortcut model and detailed model. (C) Pareto fronts of the specific energy requirement vs. productivity for different temperatures as predicted by the detailed model. All simulations satisfy the specifications given as CO_2 purity $\Phi \geq 0.85$, and CO_2 recovery $r \geq 0.3$.

shortcut model does not account for these effects and therefore over-predicts the amount of CO_2 desorbed during heating. This explains the slightly higher purity, higher productivity and the lower specific energy consumption predicted by the shortcut model. As a matter of fact, the purity and desorption efficiency were shown to increase with the amount of desorbed CO_2 in Sections 4.3.2 and 4.3.3, and the higher productivity is in part also due to the shorter adsorption times ensuing from the discontinuous front. Secondly, the thermal inertia of the column wall is underestimated in the shortcut model, since the column wall temperature is assumed to be equal to that of the bed. A more conservative approximation would be to consider the wall at the same temperature as the heat exchange fluid. Since the Pareto optimal points correspond to temperatures for which the differences $(T_{\text{heat}} - T_H)$ and $(T_{\text{cool}} - T_L)$ are small, accounting for the wall will only slightly influence the specific energy consumption under those operating conditions (see appendix C.4).

Although the prediction of the shortcut model is not always quantitative and accurate, trends are well predicted. Figure 4.7(C) shows the Pareto curves obtained from detailed simulations for three temperatures of the heating fluid. A comparison to Figure 4.6(A) reveals that the shortcut model captures the observed trends very well. In addition to the accurate qualitative agreement, the shortcut model also predicts semi-quantitatively the change in productivity upon an increase or decrease in the heating temperature, e.g. an increase in heating temperature from 440 K to 460 K would yield an increase in productivity at constant specific energy consumption by 27% and 28% for the shortcut and detailed model, respectively (indicated by the arrows in the corresponding figures; refer to appendix C.6 for a more extensive analysis). Additionally, the conditions that achieve a given purity are also in excellent agreement between the two models, as seen from Figure 4.7(B), where a CO_2 purity of 90% cannot be achieved when using the lowest heating temperature of 420 K, as indicated by both models.

We believe that some important general features of TSA processes have been elucidated in the previous sections by analyzing the four step cycle; we think that they are of general validity, and applicable for the interpretation of other results in the literature. For example,

in the works of Clausse et al.[48] and Liu et al.[58], detailed simulations where used to investigate the effect of the heating temperature on performance indicators of a two step TSA cycle (cooled adsorption and heated purge step), and a five step cycle in which a light product purge is present, respectively. Despite the shortcut model cannot be directly applied to analyze their cycles, which are different from the one considered here, the trends observed in both studies coincide with those discussed in this work. These are: an increase in CO_2 purity, recovery and productivity with the temperature of the heating thermofluid, and the presence of a minimum specific energy consumption. The good agreement between the works of Clausse et al.[48] and Liu et al.[58] and ours supports the opinion that the simple four step cycle that we have studied represents generic characteristics of TSA cycles aimed at enriching the heavy component. Thus, our analysis based on the shortcut model highlights trends of general character, which are applicable beyond the specific four step cycle to other more complex cycles, e.g where a reflux is introduced to increase the purity.[22]

4.5 CONCLUSION

In this work, we present a shortcut model of a four step TSA cycle aimed at enriching the heavy component, and we show its utility for process design and optimization by considering a CO_2 capture application from flue gas. As compared to a conventional detailed model, the shortcut model shows a rather good accuracy in the description of T-, P- and y-profiles, particularly in the region of operating conditions where high CO_2 purity, high productivity and low specific energy consumption are achieved. The main discrepancy between the two models stems from the description of the adsorption step; in fact, in the case of the shortcut model during this step the temperature rise is neglected, the breakthrough time is overestimated and the width of the front is not accounted for.

Nonetheless, the development of the shortcut model allows for a thorough comprehension of the TSA process for the recovery of the target component. The assumption of adsorption equilibrium and the ensuing semi-analytical solution of the CSS give insight into the

propagation of the composition fronts within the column; such an understanding is a key requirement for the design of well-conditioned cycles. Furthermore, the availability of a model that computes the CSS directly enables very fast computation (0.1 s/cycle ca. 600 times faster as compared to detailed simulations) and it has been exploited to perform a thorough parametric analysis. The effect of the governing operating variables, T_H and T_L, on the relevant performance indicators has been rationalized. This has allowed to elucidate the presence of a trade-off between productivity and specific energy consumption, and to localize the range of optimal operating conditions.

The use of the shortcut model to assess the effect of the temperature of the thermofluid and of the heat transfer resistance demonstrated its utility for the qualitative investigation of trends and the interpretation of detailed simulations. Although it is not suited to produce absolute quantitative data, relative quantitative information can be extracted, e.g. for the system investigated in this work the shortcut model correctly predicts the achievable increase in productivity upon an increase in the heating temperature from 440 K to 460 K of 27% vs. 28%, as determined by the detailed model. Such relative quantitative information is very useful for preliminary assessment of potential process intensification possibilities.

Thanks to the fast computation, this tool can be of practical interest in the design of TSA processes with regards to the screening of existing adsorbents, and with regards to determining good initial guesses of the operating conditions when performing a multi-objective optimization with a detailed model. Finally, such a shortcut model could be helpful in guiding the development of novel sorbent materials for CO_2 capture by TSA following an approach that accounts directly for the key considerations related to the applicability of the materials in the process. In fact, there remains a gap to bridge between the emerging works aiming at determining quantitative structure property relationships[41,42,95] of adsorbents and the actual process performance.

NOTATION

A	column cross section, (m^2)

$C_{p,b}$	heat capacity of the bed, (J/(m^3_{bed} K))
$C_{p,w}$	lumped heat capacity of the wall, (J/(m^3_{wall} K))
e_{th}	specific thermal energy consumption, (MJ/kg_{CO_2})
d_i	inner column diameter, (m)
d_o	outer column diameter, (m)
ΔH	isosteric heat of adsorption, (J/mol)
L	column length, (m)
M_w	molar mass, (kg/mol)
n	adsorbed phase concentration, (mol/kg)
N	moles fed or produced per cycle, (mol)
Δn_1	Effective cyclic capacity $n^{end}_{1,ads} - n^{end}_{1,heat}$, (mol/kg)
P	pressure, (Pa)
P_L	low pressure (end of pressurization), (Pa)
P_H	high pressure (ambiant), (Pa)
Pr	productivity, (kg_{CO_2}/(ton h))
Q_{TSA}	heating duty of the TSA cycle, (J)
r	CO_2 recovery, (–)
R	ideal gas constant, (J/mol)
S	specific heat eschange surface area, (m^2/m^3_{bed})
T	temperature, (K)
T_{HX}	temperature of the heat exchange fluid, (K)
T_{heat}	temperature of the thermofluid during heating, (K)
T_{cool}	temperature of the thermofluid during cooling, (K)
T_H	high (desorption) temperature, (K)
T_L	low (adsorption) temperature, (K)
ΔT	Temperature difference $T_H - T_L$, (K)
t	time, (s)
U	global heat transfer resistance, (J/(m^2 K))
v	velocity, (m/s)
V_{col}	column volume $\pi d_i^2/4$, (m^3)
V_{wall}	wall volume $\pi(d_o^2 - d_i^2)/4$, (m^3)
y	molar fraction of the heavy component (CO_2), (–)
z	axial coordinate, (m)

Greek letters

ϵ	total porosity, (m^3_{void}/m^3_{bed})
Φ	CO_2 purity, (–)
ν	phase ratio, (m^3_{ads}/m^3_{void})

ρ_b	bed density, (kg/m^3)
$\tilde{\sigma}$	slope of shock characteristic in the physical plane, (–)

Sub- and super-scripts

i	component 1 for CO_2, 2 for N_2
ads	adsorption step
cool	cooling step
heat	heating step
press	pressurization step
end	end of the step
F	feed condition

5 RATIONAL DESIGN OF TEMPERATURE SWING ADSORPTION CYCLES FOR POST-COMBUSTION CO_2 CAPTURE

5.1 INTRODUCTION

The design and engineering of novel materials for CO_2 capture applications has grown rapidly in the last few years; particularly impressive advances have been made in the engineering of materials with tailored properties such as sorption capacity, heat of ab/adsorption, permeability, selectivity, etc.[44,115,116] This represents important progress for the development of $2^{nd}/3^{rd}$ generation post-combustion capture processes based on absorption, membrane and adsorption technologies, since these rely on CO_2-selective materials as liquid sorbents, membranes or solid sorbents, respectively. Within the latter category, i.e., adsorption based technologies, temperature swing adsorption (TSA) is attractive due to the non-volatility of solid sorbents, the potentially low energy consumption[117] due to the moderate heat of adsorption (between 25 kJ/mol and 50 kJ/mol[118,119]) and the moderate regeneration temperature, which might offer attractive heat integration opportunities using low-grade heat sources.[120]

The results presented in this chapter are reported in: Joss, L.; Gazzani, M.; Mazzotti, M. Rational Design of Temperature Swing Adsorption Cycles for Post-Combustion CO_2 Capture. *Chem. Eng. Sci.* **2016**, *under review*. This content also represents the basis for two patents[64,65]

Although some claim that the material design is the (only) key point for achieving breakthrough performances of adsorption processes,[10,99] it is well known that the cycle design can heavily impact the performance of cyclic adsorption processes. In the case of post-combustion carbon dioxide capture the feed stream typically contains CO_2, N_2 and some impurities; CO_2 will always adsorb more strongly then N_2 because of its larger polarizability and larger quadrupole moment.[99] Therefore, traditional cycles designed for recovering the light component (less adsorbing) at high purity, as the Skartrom cycle,[14] cannot be applied.

Many studies, which deal with thermally regenerated adsorption processes, consider a TSA cycle consisting of an adsorption step at low temperature and a light product (N_2) purge step at high temperature,[38,48,121] sometimes complemented with extra heating and/or cooling steps.[49,58,95] Although several works have dealt with the design of vacuum/pressure swing adsorption (V/PSA) cycles for the recovery of the heavy component,[22–24] to the best of the authors' knowledge there has been only a very limited effort in the design of TSA cycles to date,[54] and the lessons learned from PSA processes must yet be applied to TSA processes.

There are two main strategies for the cycle synthesis of adsorption processes. It can be carried out based on *heuristics*, which arise from a solid understanding of the process and particularly of the adsorption dynamics, and where the operating conditions are optimized for a fixed cycle configuration.[24,29,32] Alternatively, using a *superstructure* approach the cycle steps and direction – the cycle configuration – are treated as decision variables leading to a mixed integer non-linear problem (MINLP) in which cycle configuration and operating conditions are optimized simultaneously.[28,122] This latter approach has the advantages of not requiring a thorough analysis of the adsorption process in order to implement it, and of possibly yielding non-trivial and non intuitive solutions, which would not be obtained by following a more heuristic approach. On the other hand, the first approach, based on heuristics, offers the advantage of readily ruling out non-sensible solutions. By combining it with a parametric analysis it gives the possibility of rationalizing the findings and helps in directing future cycle designs.

In this work, the focus is explicitly set on the design of TSA cycles for the recovery of the heavy component, i.e., for the case of CO_2 capture from flue gas of industrial- or power-plants. Thereby the questions we address are: (i) To which extent can an increase in performance be achieved with a limited increase in complexity of the cycle configuration? (ii) How do different recycle steps affect the relevant performance indicators (CO_2 purity, recovery, energy requirement and productivity)? With this aim, TSA cycles are developed and their performance is assessed by carrying out an extensive parametric analysis of the operating conditions, i.e., step time duration. The results are analyzed with regards to the achievable purity and recovery of the CO_2 product, and the productivity and energy requirement associated to different specifications on the minimum purity and minimum recovery.

This paper is structured as follows: in the next section we outline the mathematical model and methodology used for the analysis. In section 5.3 relevant features of adsorption dynamics are reviewed and accounted for in the rational design of different TSA cycles aimed at recovering the heavy component. The results are presented in section 5.4 with a thorough discussion of the effect of the operating conditions on the key performance indicators. Finally, the findings are applied to different test case applications including a CO_2 capture and storage (CCS) scenario and a CO_2 capture and utilization (CCU) scenario.

5.2 MATHEMATICAL MODEL AND METHODOLOGY

The separation considered in this work is the recovery of CO_2 from a flue gas, which is modeled as a binary CO_2/N_2 stream containing 4 mol% water, and with a CO_2:N_2 molar ratio of 12:88. A commercial zeolite 13X adsorbent is used, for which the CO_2 and N_2 temperature dependent adsorption isotherms have been measured by Hefti et al.[83]. Indirect heating and cooling is performed with an external fluid at 420 K and 300 K, respectively.

Similarly to many other physisorbents, 13X cannot cope with the presence of water. In fact, even at very low relative humidity, water molecules interact so strongly with the solid that they hinder any

CO_2 adsorption.[123] Water must therefore be managed with the use of a layered bed, or it must be removed upstream of the adsorption process. A drying unit upstream of the TSA is considered as shown in the simplified scheme in Figure 5.1.

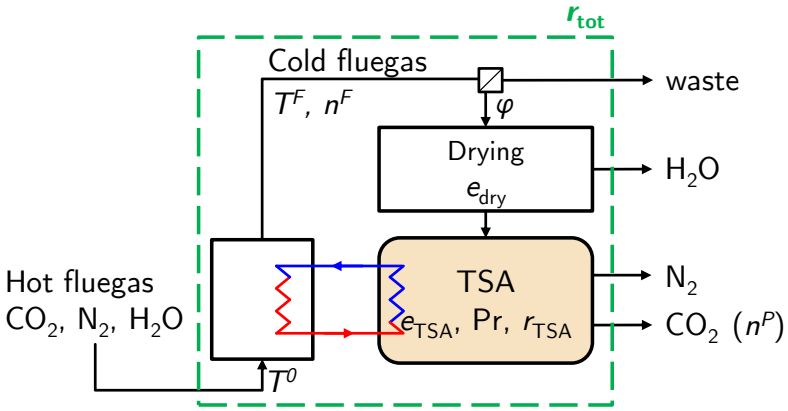

Figure 5.1. – Scheme of the considered TSA unit with an upstream drying step.

The operation of the TSA is modeled by solving the mass, energy and momentum balances for the column through the whole cycle until a cyclic steady state (CSS) is reached. The one-dimensional adsorption column model used in this work is described in more detail in earlier works,[24,77] and was validated experimentally for 2-column PSA cycles[60,84] and for a 3 step TSA cycle.[82] The model equations are those reported in chapter 2 and the underlying assumptions are enumerated anew:

- radial gradients of concentration, velocity and temperature are neglected;
- the gas phase and the solid phase are in thermal equilibrium;
- the gas phase is described by the ideal gas law, which is reasonable considering the low pressures;
- axial dispersion and conductivity are neglected, as discussed in a previous work;[24]
- the mass transfer resistance upon adsorption is assumed to be limited by solid-diffusion, and a linear driving force (LDF) model is used to describe the adsorption kinetics;
- the isosteric heat of adsorption, the molar heat capacities, the viscosity and the mass transfer coefficients are constant;

- thermal gradients for the thermostatting fluid are neglected.

The cyclic steady state (CSS) is determined using the successive substitution method, i.e., the entire TSA cycle is simulated as a unique column undergoing each step of the cycle sequentially for as many cycles as required to reach CSS. As additional criterion to those used by Casas et al.[24] (no change in the internal composition and temperature profiles from one cycle to the other), the sum of the errors on the overall product composition between two consecutive cycles and on the total mass balance must be smaller than 1%, as suggested by Minceva et al.[81] All the model parameters are reported in Table 5.1.

5.2.1 Key performance indicators

The optimization of a process involves minimizing its costs, namely both the capital and operating costs, which are controlled primarily by the productivity and the specific energy consumption, respectively. The process must thereby fulfill certain separation specifications, which are a minimum recovery of CO_2 in the product and a minimum CO_2 purity.

CO_2 PURITY The purity (Φ) is calculated as the average composition of the CO_2 product:

$$\Phi = \frac{n^P_{CO_2}}{n^P_{CO_2} + n^P_{N_2}} \tag{5.1}$$

where $n^P_{CO_2}$ is the amount of CO_2 produced from one column during one cycle and collected in the target product, and $n^P_{N_2}$ is the amount of N_2 collected in the same target product.

CO_2 RECOVERY The recovery (r_{TSA}) is the fraction of CO_2 recovered in the target product:

$$r_{TSA} = \frac{n^P_{CO_2}}{n^F_{CO_2}\varphi} \tag{5.2}$$

where $n^F_{CO_2}$ is the amount of CO_2 fed to the process during one cycle and φ is the fraction of flue gas processed in the TSA (see the scheme

Table 5.1. – Model parameters

Parameter	Value
Column geometry	
length	1.2 m
internal radius	15×10^{-3} m
external radius	16×10^{-3} m
heat capacity wall	4×10^{6} J/(K m^3)
heat transfer fluid/wall[a]	100 W/(K m^2)
heat transfer wall/bed[a]	20 W/(K m^2)
heating temperature	420 K
cooling temperature	300 K
Adsorbent material	
13X material density	2359 kg/(m^3)
particle density	1085 kg/(m^3)
bed density	708 kg/(m^3)
particle diameter	2.0×10^{-3} m
heat capacity sorbent	920 J/(K kg)
Feed	
temperature	303 K
pressure	1.3 bar
flow rate	3.5×10^{-4} m^3/s
CO_2 content	0.12 mol/mol
Adsorption equilibrium	
isotherm	Binary Sips[b]
isosteric adsorption enthalpy CO_2[b]	−37.0 kJ/mol
isosteric adsorption enthalpy N_2[b]	−18.5 kJ/mol
mass transfer CO_2[c]	0.15 s^{-1}
mass transfer N_2[c]	1.00 s^{-1}

[a] These dimensions correspond to those of a shell and tube type heat exchanger, where the adsorbent is packed within the tubes

[b] Temperature dependent isotherm parameters and isosteric enthalpies of adsorption from Hefti et al.[83]

[c] The values of the transport parameters were chosen so as to be inline with the literature[25,60,124]

in Figure 5.1). Note that whenever only a fraction $\varphi < 1$ of the flue gas is processed in the TSA, the CO_2 recovery of the TSA, r_{TSA}, and the fraction of the flue gas treated must be chosen so as to ensure the specified overall recovery, r_{tot}.

$$r_{tot} = \frac{n^P_{CO_2}}{n^F_{CO_2}} = \varphi\, r_{TSA} \tag{5.3}$$

ENERGY CONSUMPTION The specific thermal energy consumption of the TSA unit is determined by integrating the heat flow into the column ($\dot{Q}_{in}$):

$$e_{TSA} = \frac{1}{n^P_{CO_2}} \int_0^{t_{cycle}} \max(0, \dot{Q}_{in})\, \mathrm{d}t \tag{5.4}$$

Whenever the drying of the flue gas is necessary, the associated energy penalty must be accounted for in the overall specific energy consumption. A thermal-based gas drying unit, such as a silica guard, is typically regenerated at 150 °C and produces a gas stream which dew point is lower than −60 °C.[125] The required thermal energy, given per unit water removed, is $e_w = 8\,\mathrm{MJ/kg_{H_2O}}$. The specific energy penalty of the drying step per amount of produced CO_2 will depend on the fraction of the feed processed (φ), and is defined as:

$$e_{dry} = \frac{e_w\, \varphi n^F_{H_2O}}{n^P_{CO_2}} \tag{5.5}$$

where the amount of water removed per cycle is $\varphi n^F_{H_2O}$. The total specific energy consumption will be given as the sum of both contributions:

$$e_{tot} = e_{TSA} + e_{dry} \tag{5.6}$$

Whenever heat is recovered from the flue gas, as illustrated in Figure 5.1, the amount of heat recovered is given by the specific heat of the flue gas itself ($\overline{C}^F_p$) and the temperature difference across the heat exchanger, where T^0 and T^F are the temperatures of the hot and

cold flue gas, respectively. The heat recovered per unit produced CO_2 is:

$$e_{\text{rec}} = \frac{n^F \, \overline{C}_p^F \, (T^0 - T^F)}{n^P_{\text{CO}_2}} \tag{5.7}$$

PRODUCTIVITY The productivity is given by the amount of produced CO_2 per unit time and adsorbent mass:

$$\text{Pr} = \frac{n^P_{\text{CO}_2}}{m_{\text{ads}} \, t_{\text{cycle}}} \tag{5.8}$$

where m_{ads} is the adsorbent mass contained in one column, and t_{cycle} is the cycle time given as the sum of the individual step times. Cyclic adsorption processes usually involve a series of adsorption columns executing the same sequence of steps properly shifted in time. The scheduling of a given number of columns that enables a continuous feed and continuous production will typically require a certain idle time. The effective productivity of the process should therefore be calculated by considering the overall cycle time including all idle times (t_{idle}), which are calculated according to the equations reported in section 5.3.3.

$$\text{Pr}_{\text{eff}} = \frac{n^P_{\text{CO}_2}}{m_{\text{ads}} \, (t_{\text{cycle}} + t_{\text{idle}})} \tag{5.9}$$

Whenever comparing different adsorbents or technologies, it might be more sensible to consider the volume specific productivity, which is obtained by scaling the mass specific effective productivity by the density of the column.

5.2.2 Parametric analysis

There exist many degrees of freedom in designing cyclic adsorption processes; these may be subdivided into different categories: (i) the adsorbent related variables (void fractions, density, adsorption isotherms, heat capacity, etc); (ii) variables related to the column geometry and size (heat exchange area, heat transfer coefficients, column length, etc); (iii) the operating parameters (cycle configuration, step

durations). The aim of this work is to design different cycles, and it is important to keep in mind that when comparing different cycle configurations, it is essential to assess their performance at the optimal operating conditions. Since this work also aims at elucidating the effect of the operating conditions on the key performance indicators (KPIs), a systematic optimization was not carried out, instead an extensive parametric analysis was performed by exploring the entire search space of the cycle step durations within predefined bounds. The upper bounds were chosen so as each step duration does not exceed 3000 s. A total of 49,100 simulations was carried out over the four investigated cycles.

5.3 DESIGN OF TSA CYCLES

5.3.1 Guidelines based on equilibrium theory

The adsorption dynamics can be described by a system of quasi-linear partial differential equations (PDEs) which for non-linear isotherms result in non-linear waves, i.e., traveling composition fronts. Based on a solid understanding of the involved dynamics, cycles can be rationally designed with the goal of recovering the heavy component at high purity. Equilibrium theory is a powerful tool to gain insight into adsorption-based processes and it was successfully used in the development of a shortcut model for a simple TSA cycle.[61] For a binary system, where the pure component isotherms are of type I (most common for CO_2 and N_2), some of the key features worth keeping in mind are summarized below.

- When the feed state is at a larger partial pressure of CO_2 as compared to the initial state of the column, then a sharp composition front of the shock-wave type will travel through the column separating the initial state from the feed state.
- If the opposite situation occurs, i.e., the partial pressure of the feed state is lower than that of the initial state of the column, a dispersed composition front separating these two states will form and propagate through the column.

- For a constant initial state of the column, no composition front will form when indirectly heating or cooling the column, if there is no feed stream entering the column.

While these features are qualitative and strictly valid under certain assumptions (adsorption equilibrium, negligible pressure drop, etc) they can be helpful in understanding the rationale behind the design of the cycles presented and analyzed below.

5.3.2 TSA cycles

CYCLE A Cycle A consists of the simple 3-step cycle proposed by Walton and LeVan[52], which does not make use of a purge gas. Let us assume as initial condition an equilibrated bed at low temperature, with a concentration of CO_2 in the gas phase lower than the feed concentration. This simple cycle consists in three steps as shown in Figure 5.2: (i) an adsorption step in which the mixture is fed to the low temperature bed and the light product (N_2) is produced; (ii) a semi-open heating step which brings the bed to the high temperature level and thereby the heavy product (CO_2) stream is recovered; (iii) a closed cooling step down to the low temperature level. Note that since the cooling reduces the pressure to sub-atmospheric, the initial phase of the adsorption step effectively pressurizes the column back to the operating pressure.

CYCLE B A limitation of cycle A is the low level of achievable CO_2 purity, which can be increased by implementing a heavy-product recycle. The five step cycle in Figure 5.2 consists of the same sequence of cycle A, with additional purge and recycle steps, conducted after the heating step and after the adsorption step, respectively. The former step, carried out after the heating step, is a nitrogen purge, which cleans the bed further. During this step a rather disperse composition front forms, which results in a product of intermediate CO_2 concentration (larger than the feed). Recycling this product into the column after the adsorption step increases the CO_2 content within the column before the heating thus leading to increased CO_2 purity (heavy-product recycle). Cycle B is a novel TSA cycle with some

analogy to PSA cycles proposed in the literature, e.g. by Reynolds et al.[22].

CYCLE C The purity of the heavy product is largely affected by the high N_2 content in the gas phase before the heating step. An alternative way to increase the CO_2 purity is to perform a preliminary heating step to an intermediate temperature level, and to recycle the product into the feed stream, before heating to the high temperature level for the actual CO_2 desorption, as shown in Figure 5.2. Cycle C is a novel TSA cycle bearing some analogy to the electric swing adsorption cycle proposed by Grande et al.[126].

CYCLE D The preliminary heating step of cycle C can be combined with the purge and recycle steps of cycle B, as seen in Figure 5.2. In fact, the addition of purge and recycle steps is expected to increase the effective cyclic capacity of the column, hence to be beneficial in terms of the energy consumption and productivity, provided that the increase in complexity is affordable. With cycle D, which is also a novel TSA cycle, the attainable purity and recovery of the CO_2 product are expected to be the highest.

5.3.3 Scheduling equations

The number of columns and total cycle time are calculated according to the method of Mehrotra et al.[127]. Let us first define the time D as the shift in time between two columns ($DN = t_{\text{tot}}$); continuous feed is enforced by the following equality constraint:

$$t_{\text{ads}} = J_f\, D \qquad J_f \in \mathbb{Z} \tag{5.10}$$

and the constraint on the synchronization of heating and cooling steps is enforced by:

$$J_1\, D \geq t_{\text{heat},1} + t_{\text{heat},2} + t_{\text{purge}} \qquad J_1 \in \mathbb{Z} \tag{5.11}$$

$$J_2\, D \geq t_{\text{ads}} + t_{\text{cool}} + t_{\text{rec}} \qquad J_2 \in \mathbb{Z} \tag{5.12}$$

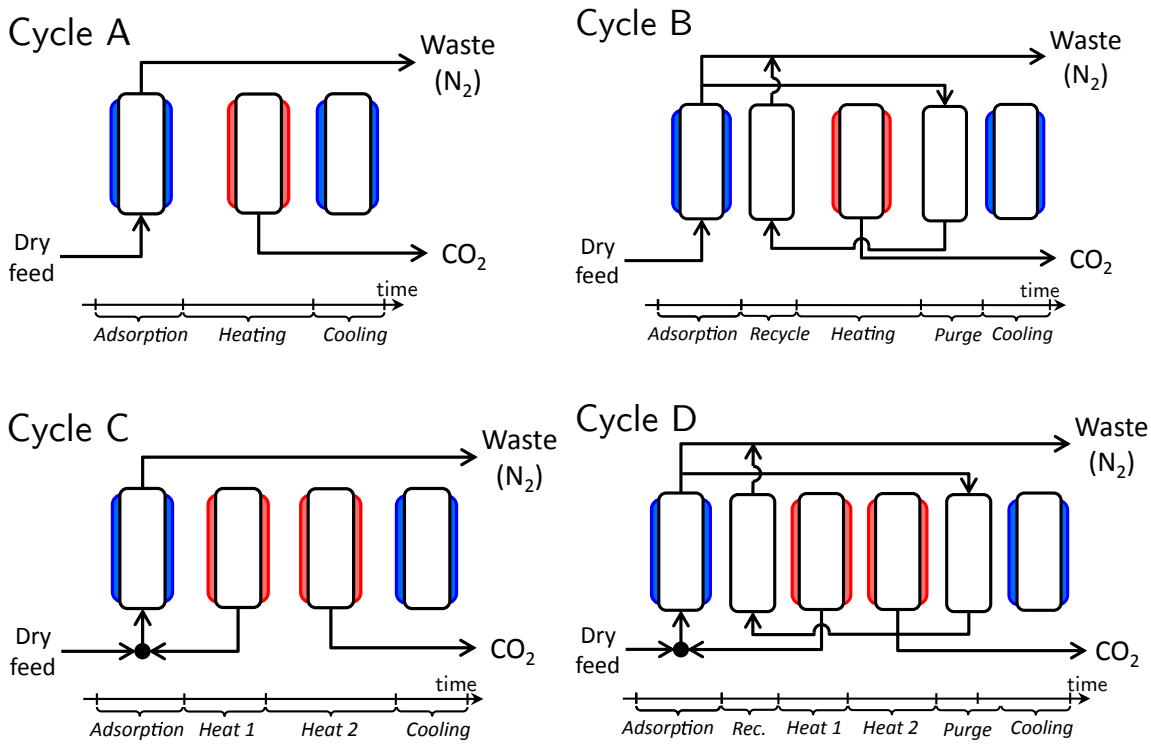

Figure 5.2. – Schematic cycle diagrams; the red and blue colors indicate external heating and cooling, respectively. Cycles B and D present recycle and purge steps in order to increase the effective cyclic capacity during the cycle. In cycles C and D, the heating is carried out in two separate steps, where the outlet stream of the first heating step is recycled back to the column, and the target product is the outlet stream of the second heating step.

Equations 5.10 to 5.12 can be combined to solve for J_1 and J_2:

$$J_1 \geq J_f \left(\frac{t_{\text{heat},1} + t_{\text{heat},2} + t_{\text{purge}}}{t_{\text{ads}}} \right) \qquad J_1 \in \mathbb{Z} \tag{5.13}$$

$$J_2 \geq J_f \left(1 + \frac{t_{\text{cool}} + t_{\text{rec}}}{t_{\text{ads}}} \right) \qquad J_2 \in \mathbb{Z} \tag{5.14}$$

The number of columns required for the separation is and the total cycle time are given by:

$$N = J_1 + J_2 \qquad t_{\text{tot}} = \left(\frac{J_1 + J_2}{J_f} \right) t_{\text{ads}} \tag{5.15}$$

Note that the number of required columns is minimum for a schedule where one column only undergoes the adsorption step at a time, i.e.,

when $J_f = 1$. These equations are valid for all cycles A, B, C and D; they can be directly applied by setting the times t_{rec}, t_{purge} or $t_{heat,1}$ equal zero whenever necessary.

5.4 SIMULATION RESULTS AND PARAMETRIC ANALYSIS

5.4.1 Effect of process steps

The results of a cyclic simulation can be presented and illustrated in at least two different ways. For specific cases, temperature and composition profiles at the column outlet at CSS can be plotted, as shown in Figures 5.3 and 5.4 for exemplary operating conditions applied to cycles D and A, respectively. The applied step times and the resulting performances are reported in Table D.1. Note that in Figure 5.3 a scaled time axis is used, so as though the duration of the same step in the different runs might be different, the same interval along the horizontal coordinate is used for all the cases. In the case of an extensive parametric analysis, as presented in this work, a more effective analysis of the results is based on the overall performance metrics presented in section 5.2.1, as shown in Figures 5.5 and 5.6. Each set of simulation results (represented by symbols, namely yellow, green, blue and black for cycles A, B, C and D, respectively, and obtained for each cycle by varying the cycle times) is plotted twice: once in terms of CO_2 recovery vs. CO_2 purity (separation specifications, calculated according to equations 5.1 and 5.2) and once in terms of energy requirement vs. productivity (separation performance, calculated according to equations 5.4 and 5.8) for each cycle. The solid line and markers indicate the boundary of the feasible region. The direction of change of the operating conditions is indicated by the arrows drawn in Figure 5.5 and 5.6. Trade-offs are observed between purity and recovery of the desired product, as well as between specific energy consumption (which is related to the operating expenditures OPEX) and productivity (associated to capital expenditures CAPEX).

The effect of the individual step types is discussed in the following for all cycles, since it is similar for all of them.

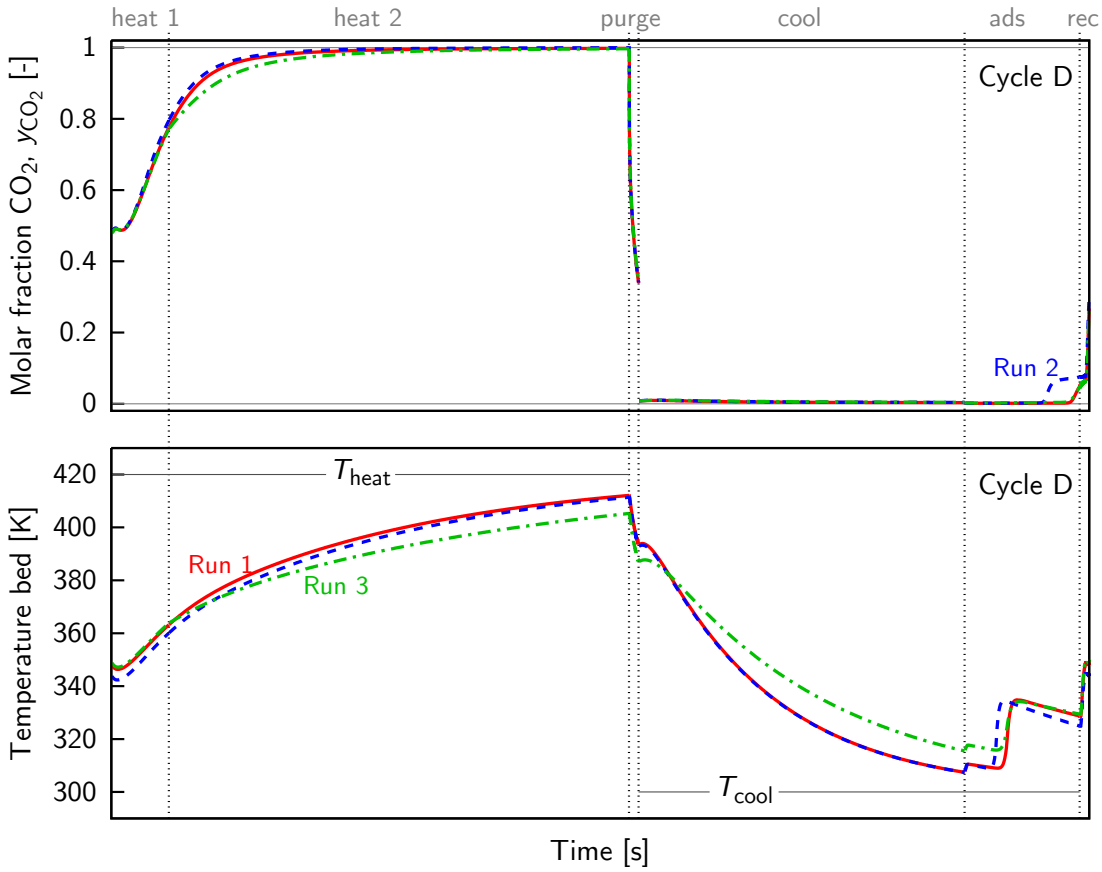

Figure 5.3. – Outlet composition and temperature profiles of cycle D with the operating conditions Run 1 (solid), Run 2 (dashed) and Run 3 (dash-dotted): see Table D.1 for the corresponding operating conditions. A scaled time axis is used, so as though the duration of the same step in the different runs might be different, the same interval along the horizontal coordinate is used for all the cases.

5.4.1.1 *Adsorption step*

As the time of the adsorption step increases, the transition front through which CO_2 is adsorbed approaches the end of the column. The purity will increase because the column is increasingly loaded with CO_2 until the front eventually breaks through, at which point the

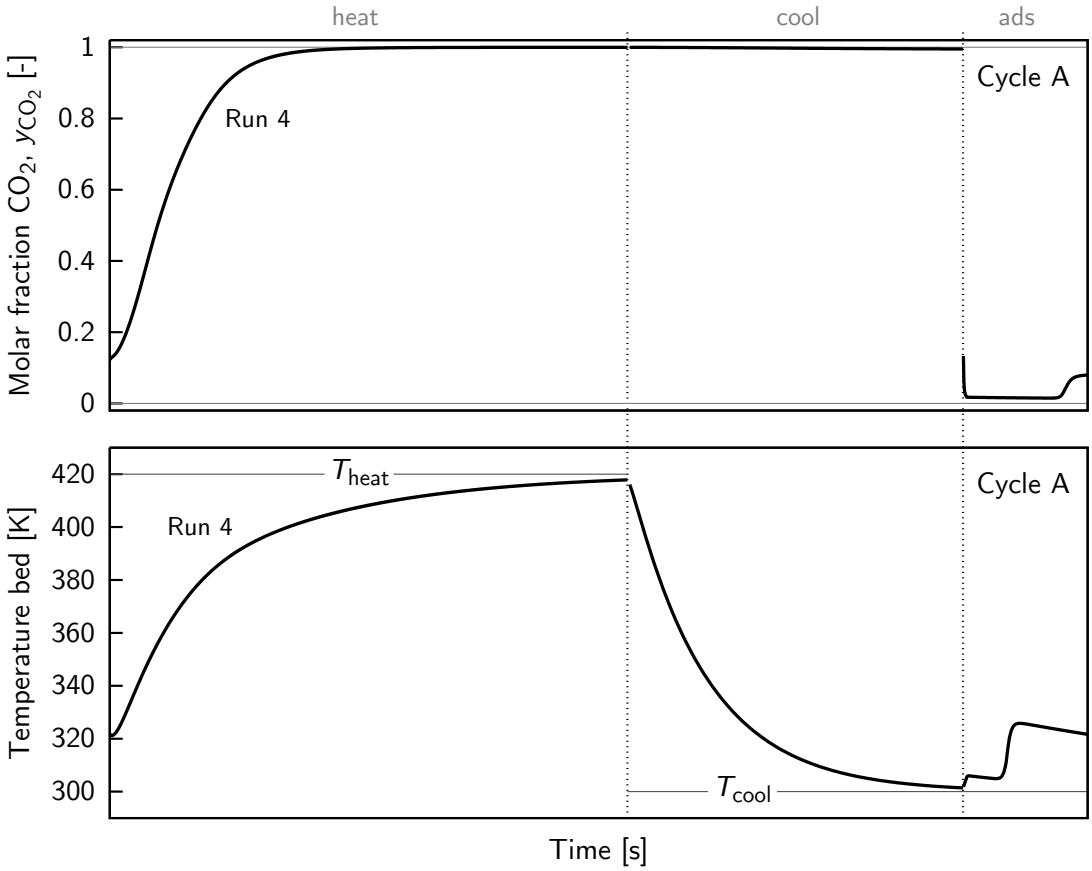

Figure 5.4. – Outlet composition and temperature profiles of cycle A with the operating conditions of Run 4.

recovery decreases rapidly. The increase in CO_2 loading within the column at the end of the adsorption step will also result in a lower specific energy consumption because the provided heat is more efficiently used (a larger fraction is consumed for the actual desorption of CO_2). This effect can be seen when comparing the outlet composition profile of Runs 1 and 2 in Figure 5.3, where the CO_2 front clearly breaks through the column to a greater extent in the case of Run 2, whose adsorption step is longer.

5.4.1.2 *Heating and cooling steps*

An increase of the heating and cooling times results in a greater amplitude in the temperature differences experienced by the bed and

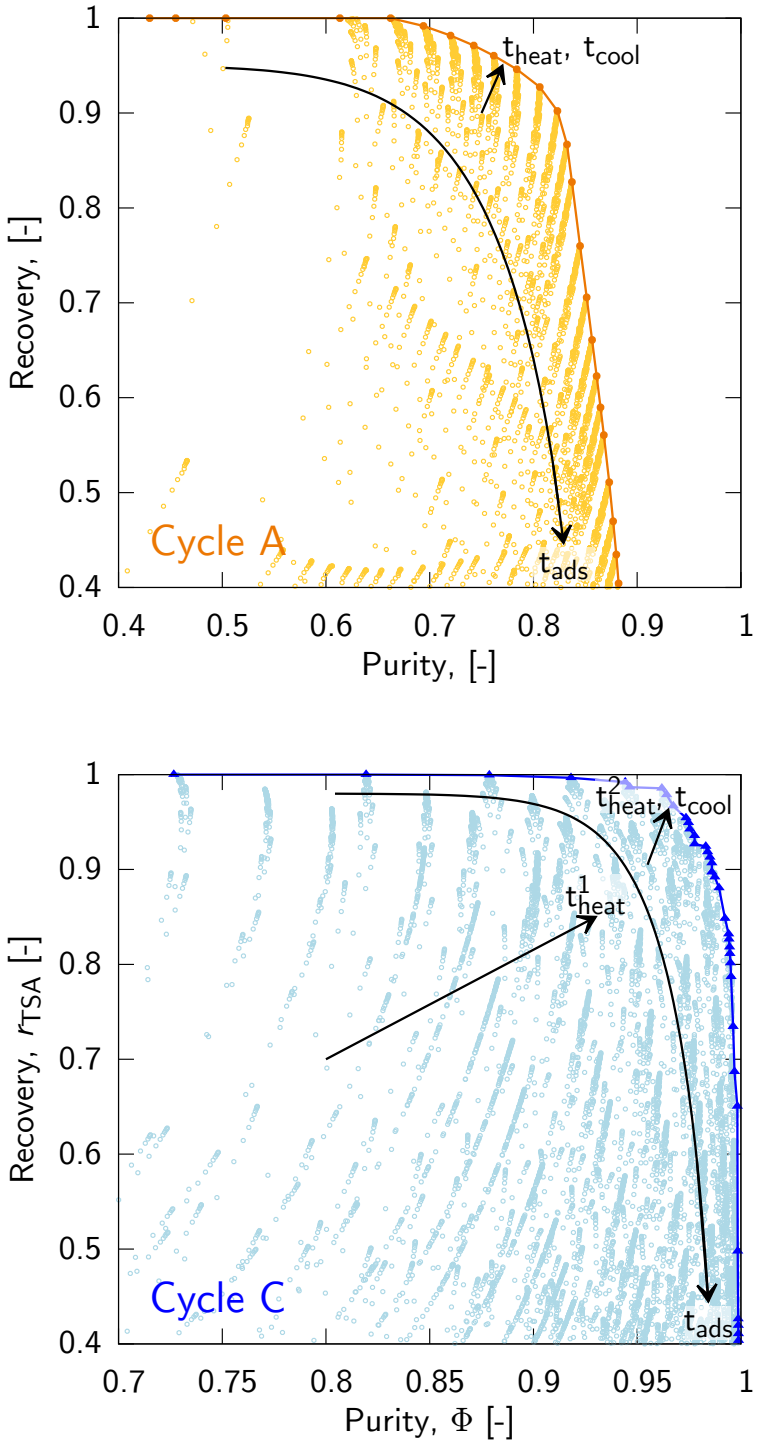

Figure 5.5. – Effect of the operating conditions on the CO_2 purity and recovery for the four investigated cycles.

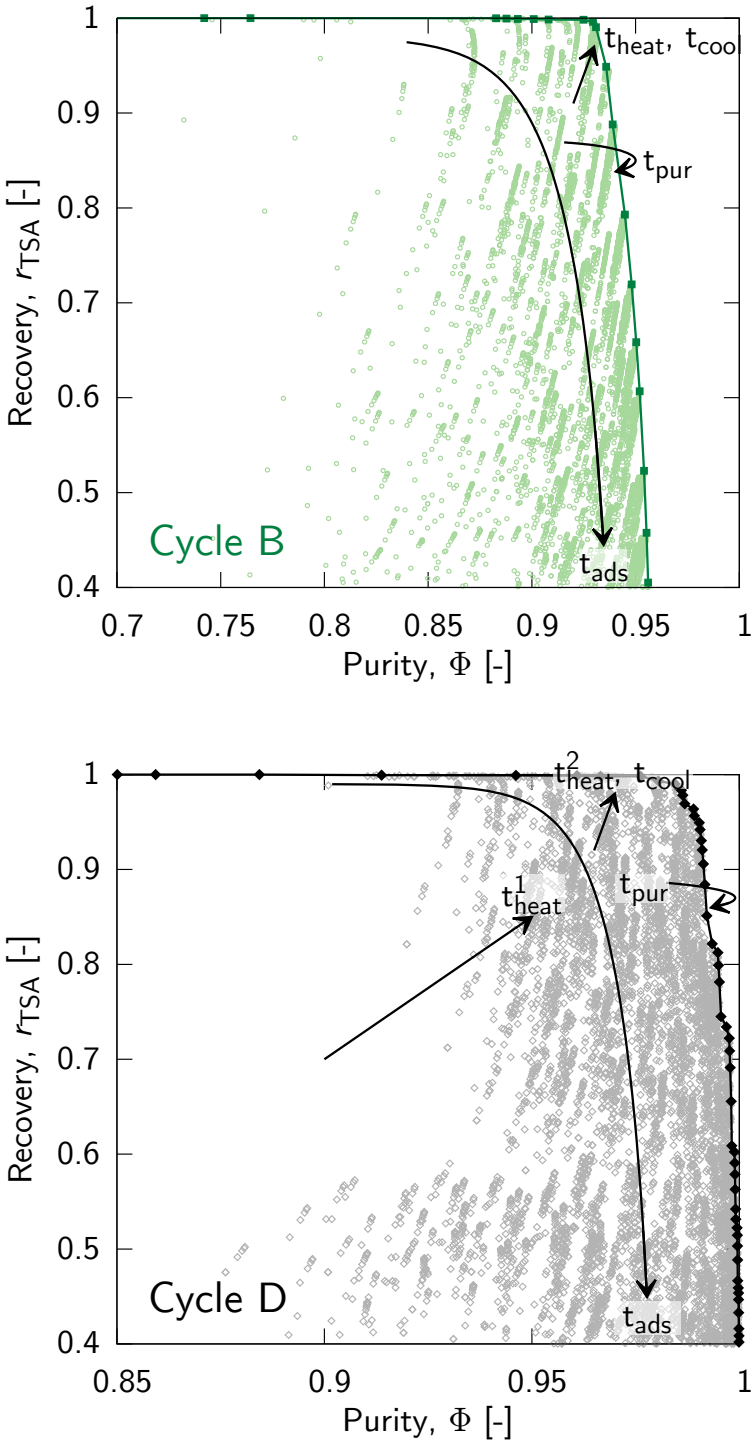

Figure 5.5. – Effect of the operating conditions on the CO_2 purity and recovery for the four investigated cycles.

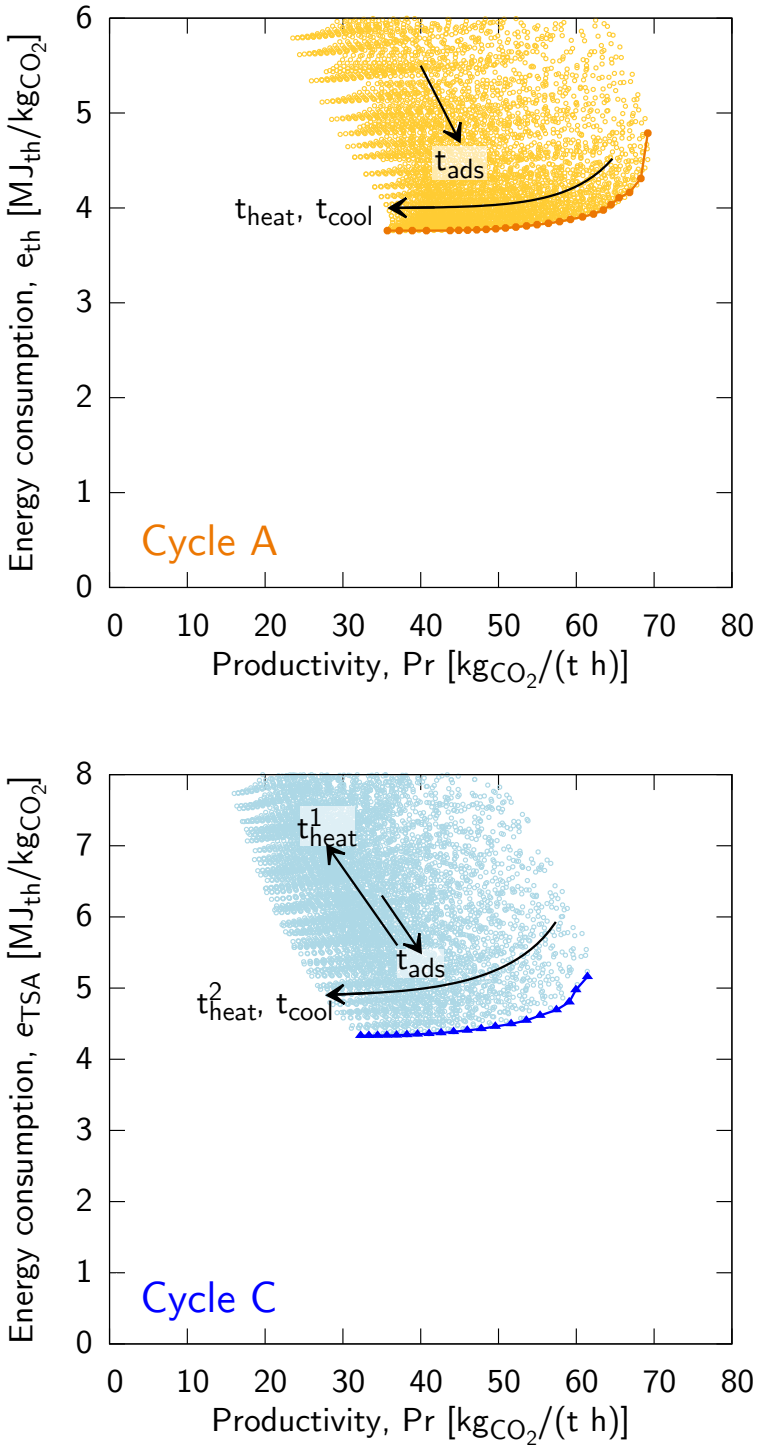

Figure 5.6. – Effect of the operating conditions on the specific energy consumption and productivity for the four investigated cycles.

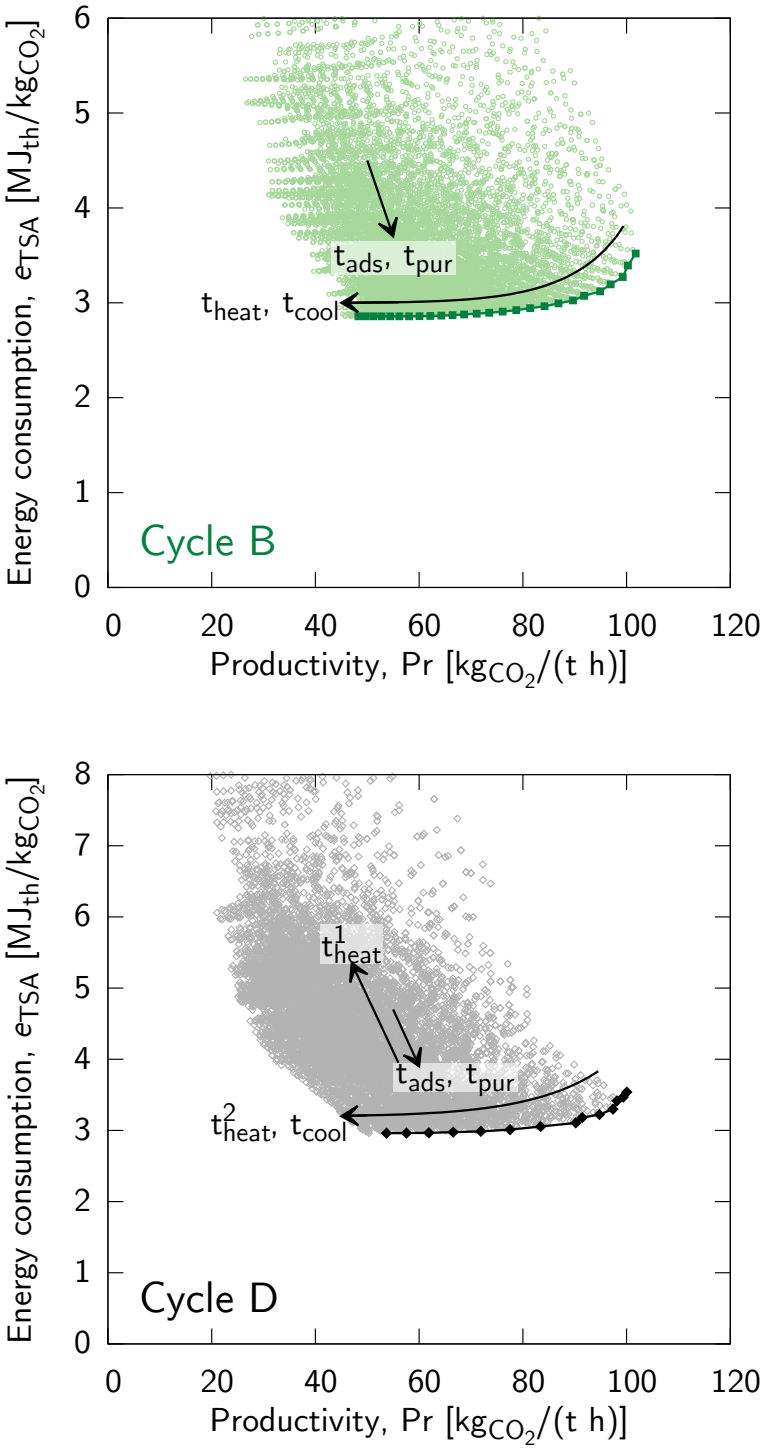

Figure 5.6. – Effect of the operating conditions on the specific energy consumption and productivity for the four investigated cycles.

Table 5.2. – Operating conditions and performances of Runs 1 to 4 shown in Figures 5.3 and 5.4.

		Run 1	Run 2	Run 3	Run 4
cycle	[–]	D	D	D	A
$t_{heat,1}$	[s]	150	150	150	–
$t_{heat,2}$	[s]	1200	1200	800	2100
t_{pur}	[s]	25	25	25	–
t_{cool}	[s]	850	850	600	1450
t_{ads}	[s]	300	400	250	300
t_{pur}	[s]	25	25	25	–
Φ	[–]	0.97	0.97	0.96	0.83
r_{TSA}	[–]	0.90	0.77	0.88	0.80
e_{TSA}	$[MJ/kg_{CO_2}]$	4.39	4.07	5.00	5.73
Pr	$[kg_{CO_2}/(t\,h)]$	60.5	66.4	67.5	35.7

thereby in a larger cyclic capacity and a higher CO_2 purity for all four cycles. This is illustrated by the temperature profiles of Runs 1 and 3 shown in Figure 5.3, where the temperature of the column is lower at the end of the heating step and higher at the end of the cooling step for Run 3 as compared to Run 1. The heating rate is limited by indirect heat transfer to the fixed bed, which is a slow process. The duration of the heating and cooling steps is the major contribution to the cycle time (see Figures 5.3 and 5.4), and an increase in heating/cooling times will substantially lower the productivity (see Figure 5.6). At the same time though, the specific energy consumption decreases owing to the larger effective cyclic capacity. Note that this applies to heating steps for which the outlet stream is collected in the target product, as opposed to heating steps for which the outlet stream is recycled (cf. section 5.4.1.4).

5.4.1.3 *Purge and recycle*

Comparison of Figures 5.3 and 5.4 illustrates the effect of the purge and recycle steps: by purging the column with the nitrogen product before the cooling and adsorption steps, the remaining CO_2 is desorbed from the top of the column and less CO_2 is lost during the

ensuing adsorption step, hence larger recovery is achieved. Moreover, an increased purity is achieved by enriching the gas and adsorbed phases in CO_2 before the heating step. In fact, the outlet molar fraction of CO_2 during the heating steps of cycle D (Figure 5.3) is larger than that of cycle A (Figure 5.4). While all simulations shown in Figure 5.3 were carried out for the same duration of purge and recycle steps, the effect of a change in duration can be seen in Figures 5.5 and 5.6 for cycles B and D. Generally, longer purge times are beneficial to the recovery, since more CO_2 is desorbed prior to the adsorption step. On the other hand, an increase in purity is only achieved provided that the average CO_2 content of the recycled stream is larger than in the feed. This is the case for short purge times; when the purge step is too long, the nitrogen used to purge leaves the column and dilutes the recycle, hence the existence of an optimal purge/recycle time.

The effect of this combined step on the process performance is driven by similar effects: for short purge times, an increase in duration yields a larger effective cyclic capacity, hence lower energy consumption and higher productivity; but for too long a purge time, the recycled product gets diluted thereby lowering the effective cyclic capacity. Moreover, the heat effects arising during the purge and recycle steps are beneficial to both energy consumption and productivity. In fact, the desorption of CO_2 happening during the purge step cools down the bed, thus requiring a shorter cooling step, while the heat released during the recycle step due to CO_2 adsorption contributes to heating the bed before the actual heating step. This is indeed observed in the temperature profiles shown in Figure 5.3.

5.4.1.4 *Preliminary heating*

The preliminary heating step of cycles C and D has a large effect on the purity and recovery of the CO_2 product, as seen in Figure 5.5. In fact, most of the nitrogen contained in the bed after the adsorption step will be present in the product of the initial heating phase; this is confirmed by the profiles shown in Figures 5.3 and 5.4. By recycling this fraction back to the adsorption step, i.e., not collecting it in the target product, the purity can approach 100%. However, an increased duration of the preliminary heating requires longer cycle time and

larger energy consumption without the benefit of producing more CO_2 (Figure 5.6).

5.4.2 Influence of external factors

To allow for a fair assessment of the different cycles, it is worth accounting for a few factors that are external to the TSA itself. A critical aspect of cyclic processes to consider is a scheduling of the cycle steps that allows for a continuous process. Another important aspect already mentioned in section 5.2 is that the flue gas typically contains water, which must be removed for most sorbents, and certainly when using zeolite 13X. Beside these two external factors, also heat integration possibilities enabled by the multi-column operation ensuing from the scheduling are briefly discussed. While the purity and recovery of the different TSA cycles reported in Figure 5.2 are independent of the drying and of the scheduling, the drying will affect the overall energy consumption, whereas a proper cycle scheduling introduces idle times and reduces the effective productivity of the cycle.

5.4.2.1 *Scheduling*

For most applications a continuous operation is desired, which is ensured by operating several columns in parallel in a synchronous manner, with the operating cycles of the different columns properly shifted in time. Cycle scheduling consists in determining the number of columns and the idle times required to run a continuous operation; this has obviously an effect on the effective productivity of the cycle. The schedule will depend on the imposed constraints, e.g. a continuous feed, or continuous production, or synchronization of purge/recycle steps, etc. For TSA cycles, a further constraint to be considered is that of having a column starting the cooling phase at the same time when another column starts the heating phase, thus allowing the reuse of the hot thermofluid present in the former column to heat up the latter column (so called temperature equalization).

For CO_2 capture from flue gases, the scheduling shall ensure a continuous feed at all times, while at the same time guaranteeing: (i) synchronization of purge/recycle steps, whenever present, and

(ii) synchronous start of the heating and cooling steps. Due to the configuration of cycles B and D, the former criterion will automatically be satisfied if the latter is.

As an example, the above defined scheduling constraints are applied to the specific operating point of cycle D previously discussed with reference to Run 1 (see Table 5.2) according to the equations reported in section 5.3.3. In order to ensure a continuous production and synchronous purge/recycle steps, an idle time of 150 s, splitted in two intervals of 130 s and 20 s, and 9 columns are required, which are operated shifted in time by 300 s, as shown in Figure 5.7.

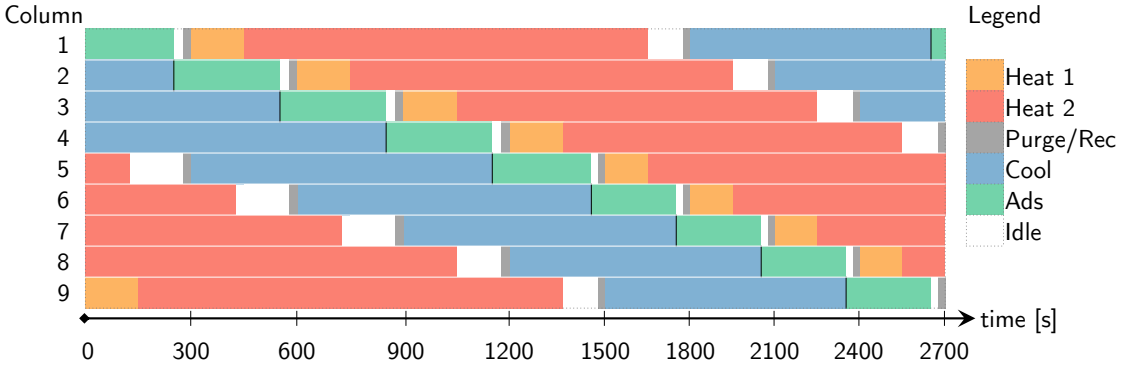

Figure 5.7. – Schedule for the operation of cycle D with the operating conditions corresponding to those of Run 1 (see Table 5.2).

5.4.2.2 *Heat integration*

TSA processes offer interesting heat integration opportunities. First, the heat demand is distributed over the range spanned by the high and low temperature levels. This distributed heat duty is in contrast to liquid absorption-based processes, where most of the heat duty must be provided at the reboiler at a temperature close to the boiling point of the solvent, i.e., 100 °C for water. Using steam for the regeneration of the solid sorbent is therefore not a must; low-grade heat streams can be exploited. Then, the multi-column dynamic operation of such processes is such that several heat sources (cooling steps) and heat sinks (heating steps) are present at the same time. Two heat integration possibilities are described below, and an attempt to quantify their potential is made based on the exemplary operating conditions of cycle D discussed above.

In the exemplary scheduling shown in Figure 5.7, every 300 s a column switches from heating mode to cooling mode at the same time when another column switches from cooling mode to heating mode. Temperature equalization can be carried out by recycling the thermofluid of the former column to the latter, e.g. from column 6 to column 1 in Figure 5.7 at $t = 0$. The potential heat integration that can be achieved by temperature equalization can be estimated by considering the temperature vs. heat duty curves of a column being heated and of one being cooled. In Figure 5.8 the column wall temperature is plotted vs. the total heat uptake for the preliminary heating step (heat 1) and for the first 150 s of the cooling step at the specific operating conditions illustrated in Figure 5.7. The energy demand of the column being heated can be covered by internal heat recovery as long as its temperature is lower than the temperature of the column being cooled. For this example we consider a pinch point of 30 K, which would enable the use of a heat transfer loop. In this case, the energy recovered is 0.67 MJ/kg_{CO_2}, which corresponds to about 12% of the total energy demand of the cycle, including drying, i.e., a significant fraction of the energy penalty.

Moreover, it is worth noting from Figure 5.7 that at each time several columns are being heated simultaneously; since the start of each heating step is shifted in time, these columns feature different temperature levels, namely at time $t = 0$, $T_{col,5} > T_{col,4} > T_{col,3} > T_{col,2} > T_{col,1}$. An efficient recovery of the heat contained in the used thermofluid used can be achieved by simulating a counter-current operation: the thermofluid is contacted first with the warmest column (column 5), then to the second warmest, and so on.

This strategy can also be applied to recover the specific heat of the flue gas itself, whenever possible. For an efficient heat exchange corresponding to a temperature difference of $T^0 - T^F = 100$ K across the heat exchanger (refer to Figure 5.1), equation 5.7 is used to estimate that 0.70 MJ/kg_{CO_2} can be recovered from a TSA process that provides an overall CO_2 recovery of 90%.

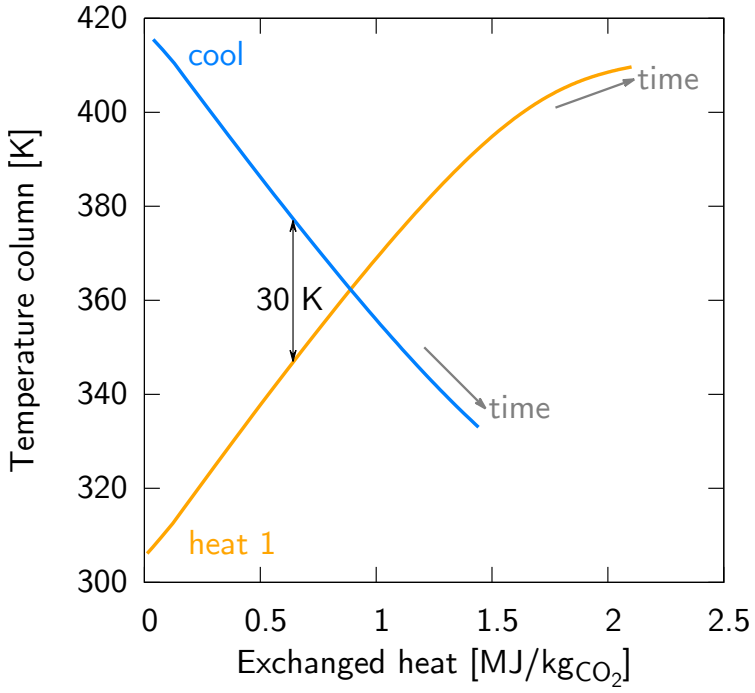

Figure 5.8. – Temperature vs. heat curves of the preliminary heating step (heat 1) and of the beginning of the cooling step. 0.67 MJ/kg$_{CO_2}$ can be recovered for a minimum temperature difference of 30 K.

5.4.2.3 *Drying step*

The energy penalty associated to an additional thermally driven drying step is estimated according to equation 5.5. For the specific cyclic operation illustrated in Figure 5.7, drying of the flue gas requires to 1.26 MJ/kg$_{CO_2}$.

A breakdown of the energy consumption of this cycle including heat integration is reported in Table 5.3. It is worth noting that more than 20% of the total energy demand is required for the drying of the flue gas. While these figures specifically highlight the importance of considering and the drying step, they also suggest that the design of TSA processes for CO_2 capture should be based on a systems approach, which strives to consider the entire value chain of process design, i.e., from materials characterization to integrated process optimization.

Table 5.3. – Breakdown of the energy consumption of the TSA process shown in Figure 5.12.

Contribution	value [MJ/kg$_{CO_2}$]	
TSA process	4.39	
flue gas drying	1.26	
total w/oheat integration		5.65
temperature equalization	−0.67	
recovery from flue gas	−0.70	
total w/heat integration		4.28

5.5 DISCUSSION

Any separation process must fulfill certain separation specifications while incurring in minimal expenses. In order to make a fair comparison among different processes, or among different operating modes of the same process, the relevant context must be defined and several factors should be kept in mind: (i) for CO_2 recovery applications, the separation targets need to be specified in terms of minimum purity and minimum recovery of the CO_2 product; (ii) in a first approximation, the costs of such a process are proportional to the energy consumption and to the equipment volume (inversely proportional to the productivity); (iii) the overall performance of a CO_2 recovery process based on TSA is affected also by the drying of the flue gas and the scheduling of the cycle; (iv) optimal operating conditions should be considered, i.e., those operating conditions of each process that optimize both the overall energy consumption and the effective productivity.

While different heat integration possibilities were presented in section 5.4.2.2, in the following, heat integration calculations are not considered in the determination of the optimal operating conditions. The reason for this is that the estimation of the potential internal recovery requires not only knowledge of the overall process metrics (e.g. recovery, purity, energy consumption), but it depends on the temperature and heat profiles during the cycle. The deliberate choice was made to omit saving this data for all the simulation runs in or-

der to save computation time, while carrying out a rather extensive parametric analysis. On the other hand, while a rough estimation of the potential heat recovery from the flue gas itself does not require such information and can be directly computed from equation 5.7, this calculation would affect all cycles and operating conditions in the same way, i.e., by reducing the overall energy consumption of a fixed amount.

In the following, the cycles are compared for their use in two applications with different specifications. First, a comparison based on the achievable separation specifications is carried out. Then, the separation performance is assessed by considering only those operating points that fulfill the specified minimal purity and minimal recovery. The performance is then evaluated in terms of energy consumption and productivity by selecting the set of operating conditions resulting in minimal overall energy consumption and maximal productivity.

In literature, it is common to find works where the performance of TSA processes is assessed based on productivity and energy consumption considering neither the idle times associated to scheduling nor the energy penalty due to the drying unit.[31,48,54,56,58] In the following section, the performance will be assessed by considering the effect of drying and of scheduling first separately, and then together, in order to appreciate their importance.

5.5.1 Separation specifications

Figure 5.9 shows the comparison of the purity and recovery of the CO_2 product achievable when running cycles A, B, C and D. Note that only the sets of maximal purity and recovery for each cycle taken from Figure 5.5 are shown for the sake of clarity. The highest purity/recovery are reached by cycle D and C, followed by cycle B, and finally cycle A.

Two case studies with different target specifications are considered in the following:

CASE 1 Recovery ≥ 0.3 and purity ≥ 0.90. This is representative of a CO_2 capture and utilization (CCU) scenario, where relatively

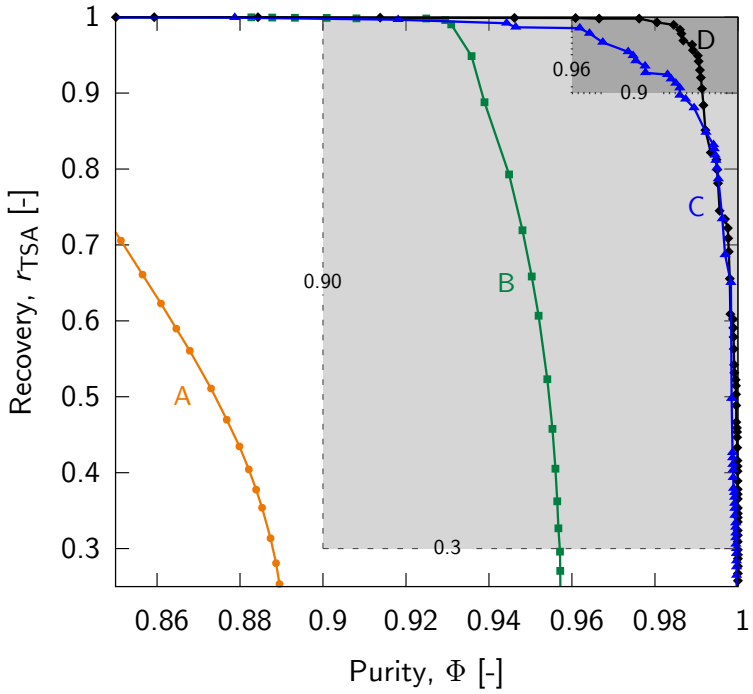

Figure 5.9. – Comparison of cycles A, B, C and D in terms of achievable CO_2 purity and recovery.

high purity is required, while recovery is limited, possibly because of the downstream process requirements. A possible application is for example the enhancement of production capacity of urea and methanol plants by recovering a portion of the CO_2 contained in the flue gases, as suggested by Filippi and Zardi.[12]

CASE 2 Recovery ≥ 0.9 and purity ≥ 0.96. This is representative of a CO_2 capture and storage (CCS) scenario. When captured CO_2 is to be stored in the subsurface, the capture process must satisfy rather stringent specifications on both purity and recovery of the CO_2 product, which should be at least 96% and 90%,[100] respectively.

The corresponding regions in the recovery vs. purity plane in Figure 5.9 are represented by rectangles. This figure highlights that the cycle design greatly affects the achievable separation specifications; by tailoring the cycle to the application requirements, the attainable separation performance moves significantly towards the upper-right corner in the recovery–purity plane. More specifically, cycles C and D are the only ones able to meet stringent specifications, as those required for

CCS (case 2). The very high purity is achieved with the preliminary heating step, whose specific purpose is that of removing nitrogen from the gas phase before the actual heating step that produces the target CO_2 product.

5.5.2 Separation performance

The Pareto sets in the productivity vs. energy consumption plane corresponding to the two case studies presented above are shown in Figures 5.10 and 5.11. Three curves are shown for each cycle which achieves the separation specifications: the set of operating points yielding maximum productivity (Pr) and minimum energy consumption when drying and scheduling are not considered (e_{TSA} vs. Pr seen in Figure 5.10), the Pareto set of points accounting for drying but not for scheduling (e_{tot} vs. Pr seen in Figures 5.10 and 5.11), and the Pareto set of the operating points, when accounting for both drying and scheduling (e_{tot} vs. Pr_{eff} seen in Figure 5.11).

The data presented in these figures consider a large number of operating conditions and contain a large amount of information. Some general considerations on the effect of the flue gas drying, the scheduling and the number of columns are worth making before proceeding to a comparative assessment of the different cycles among themselves, and with respect to the state-of-the-art CO_2 capture technology.

DRYING The effect of the flue gas drying is visible in Figure 5.10, when comparing the Pareto sets for which the energy penalty for drying was neglected (labeled "w/o drying") to the Pareto sets that account for it (labeled "w/ drying"). The energy penalty associated to the drying step ranges between $2\,\text{MJ}/\text{kg}_{\text{CO}_2}$ to $3\,\text{MJ}/\text{kg}_{\text{CO}_2}$ depending on the cycle, target specifications and operating conditions.

It is interesting to notice, that the optimal operating conditions for the CCU case when accounting for the flue gas drying are such that only a fraction $\varphi < 1$ of the total flue gas is dried and processed in the TSA unit (refer to Figure 5.1 for an illustration of the split fraction φ). In such a case, the energy consumption of the drying unit is decreased by treating only a fraction of the flue gas. On the other hand, a larger

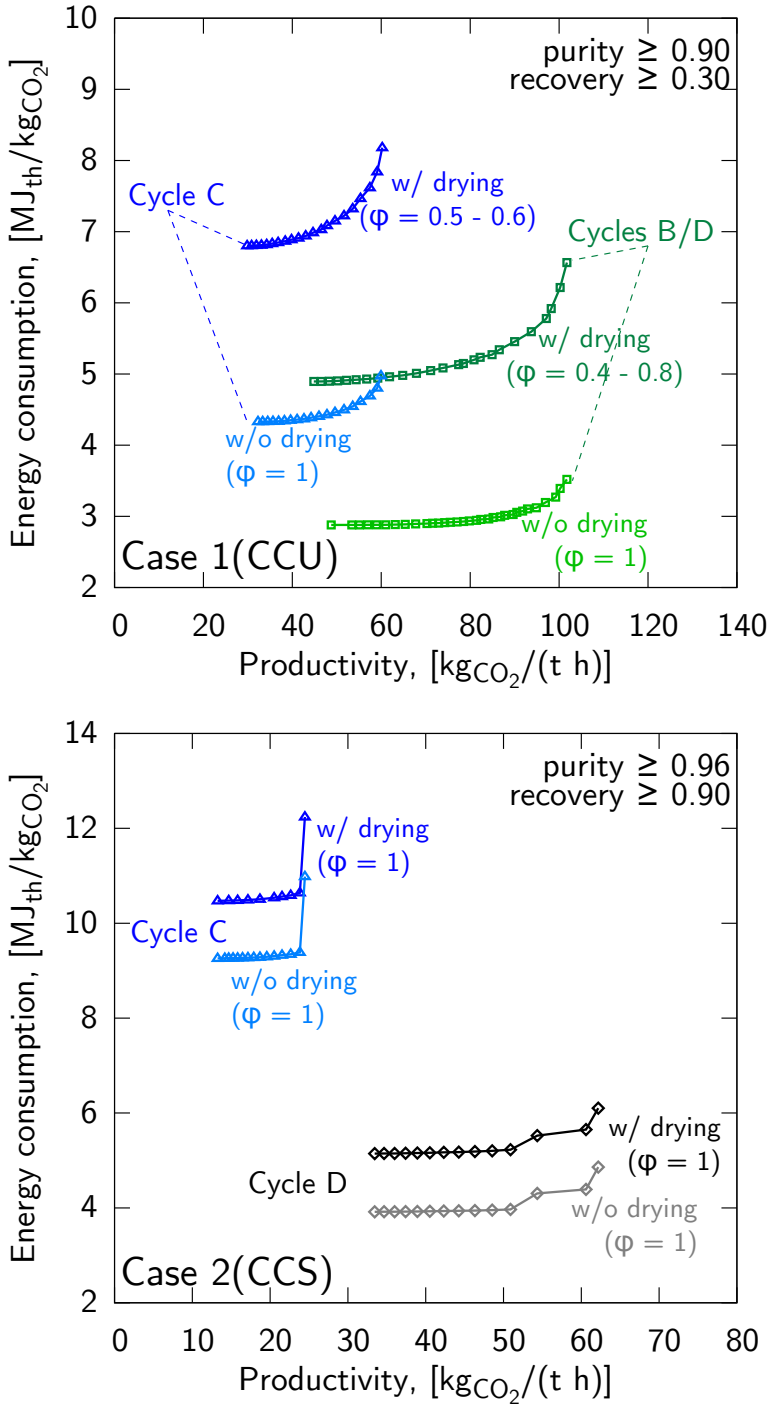

Figure 5.10. – Effect of drying on the process performance of cycles B, C and D for different sets of target specifications. The Pareto sets which do not consider drying are shown with the light empty symbols ("w/o drying"), the Pareto sets that consider drying are shown with the dark empty symbols ("w/ drying"). The effect of scheduling is not accounted for in any curve.

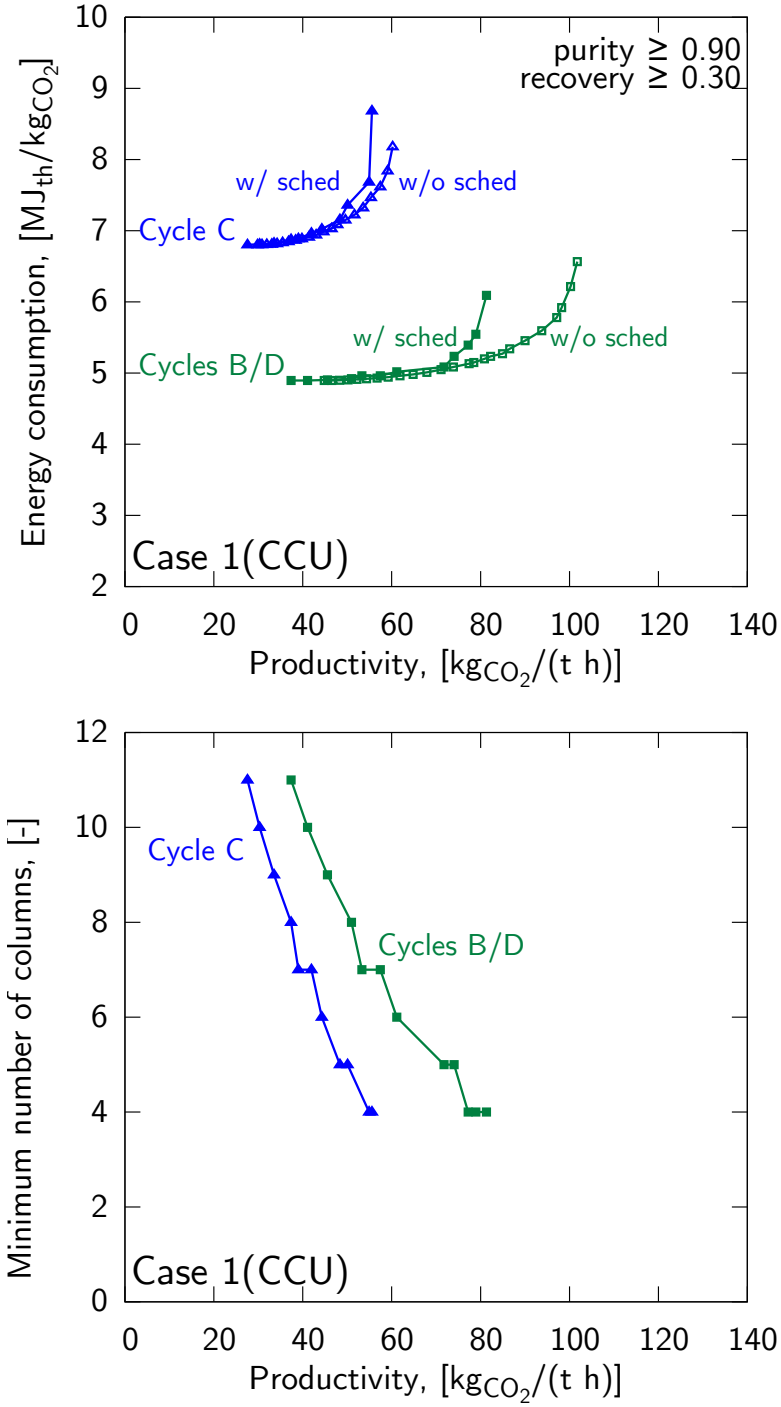

Figure 5.11. – Comparison of cycles B, C and D in terms of process performance for different sets of target specifications (top). The Pareto sets which do not consider scheduling are shown with the dark empty symbols ("w/o sched") and the Pareto sets that consider scheduling are shown with the dark filled symbols ("w/ sched"). Number of columns for the Pareto sets that consider scheduling (bottom). All the curves consider the effect of drying.

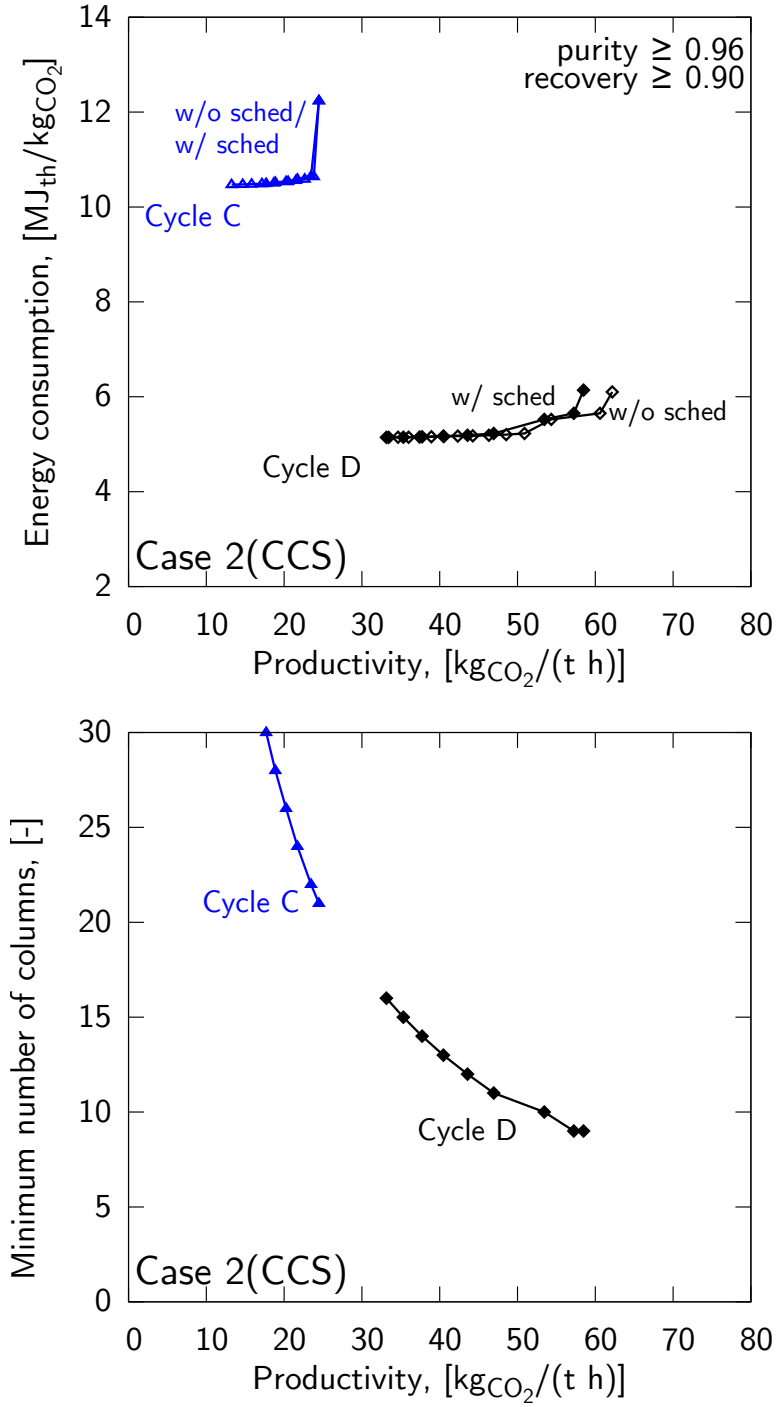

Figure 5.11. – Comparison of cycles B, C and D in terms of process performance for different sets of target specifications (top). The Pareto sets which do not consider scheduling are shown with the dark empty symbols ("w/o sched") and the Pareto sets that consider scheduling are shown with the dark filled symbols ("w/ sched"). Number of columns for the Pareto sets that consider scheduling (bottom). All the curves consider the effect of drying.

fraction of the fed CO_2 must be recovered in the TSA unit in order to match the overall recovery, thus increasing the energy penalty of the TSA with respect to the case where the whole flue gas is treated. Because of these two opposing trends, an optimal waste to feed ratio will most likely exist, and will depend on the energetic requirement for H_2O removal and on the target overall recovery. When a more stringent overall recovery is specified, such as in the CCS case, it becomes worthwhile processing all the feed ($\varphi = 1$). In this case, the effect of the drying step is equal for every point along the Pareto set.

SCHEDULING AND NUMBER OF COLUMNS The scheduling constraints considered are those presented in section 5.3.3, together with that of a maximum number of 30 columns. The effect of the cycle scheduling on the effective productivity is illustrated in Figure 5.11, when comparing the Pareto sets that consider drying but not scheduling (labeled "w/o sched") with the Pareto sets that account for both these effects (labeled "w/ sched"). The reduction in productivity significantly varies for different separation specifications, for the different cycles and for different operating conditions.

It is difficult to analyze the effect of the scheduling without considering the number of columns required for each specific schedule. The bottom plots in Figure 5.11 show the number of columns associated to the Pareto sets with scheduling. Interestingly, the operating points that achieve higher productivity require fewer columns. In the case of the slow heat transfer characteristic of indirect heating/cooling of a packed bed under near-static conditions, the heating and cooling times will typically be considerably longer than the adsorption time. In order to allow for the process to treat the feed continuously, the number of columns must be at least equal to the total cycle time divided by the adsorption time. Therefore, shorter heating/cooling times will lead to fewer columns, and according to Figure 5.6, these conditions also lead to higher productivity. This observation supports the use of the productivity as a metric representative of the capital expenditures associated to the investigated cycles.

Let us first consider the CCU case, which is characterized by less stringent separation targets. The cycles of interest in this case are C and B (the absence of additional sets of curves for cycle D is explained

in the next section). In this case, the scheduling yields similar results for both cycles: The required number of columns is moderate and varies from 4 to 11; the impact on the productivity is significant with reductions ranging between −10 % and −20 %.

The CCS case on the other hand requires higher purity and recovery of the CO_2 product. The adsorption times tend to be shorter as compared to the CCU case in order to achieve a high recovery; this explains the larger number of required columns. It is interesting to note that while cycle C requires more than 20 columns to reach the specified separation targets, the resulting scheduling is such that idle times are hardly required, and the Pareto sets with and without scheduling coincide. The situation is different for cycle D, for which 9 to 16 columns are needed. There, the scheduling impacts the productivity to a larger extent (up to −6 %) as compared to cycle C (up to −1.5 %) for the CCS specifications.

Summarizing, operating conditions yielding larger productivity typically require less columns in order to ensure a continuous operation. On the other hand, an increased number of columns can allow for a schedule with less idle times, hence a smaller relative impact on the effective productivity.

5.5.3 Comparative assessment of cycle performances

Comparison of the different cycles for the two applications of interest must be undertaken based on the Pareto sets considering drying and scheduling that are shown in Figure 5.11. The following points are worth noting:

- Generally, out of the four cycles, cycles B and D exhibit the best performances. Cycle A does not reach high separation specifications; its performance cannot therefore be compared with that of the other cycles.
- The performance of cycles B and D is always better than that of cycle C thanks to the presence of a purge/recycle step, which is highly beneficial in terms of productivity and specific energy consumption. This is particularly striking in the CCS case, where cycle D, as compared to cycle C, attains a productivity that is

twice as large, has an energy penalty that is only half, and requires only half of the columns.

- Whenever the specifications can be reached by cycle B, the Pareto set of cycle D reduces to that of cycle B. In fact, the optimal operating conditions are such that the duration of the preliminary heating step reduces to zero, because it requires energy and time but does not contribute to increasing the amount of CO_2 recovered during the cycle. The additional energy for the pre-heating step heavily penalizes the specific energy consumption, whereas the longer cycle times penalize the productivity of the cycle and increase the number of columns required to continuously process the feed.

These trends can be generalized for TSA systems similar to those investigated in this work, where the key features are (i) favorable isotherms, (ii) adsorption isotherm and feed conditions for which an increase in the adsorbed amount can be achieved through an increase in CO_2 partial pressure, (iii) longer characteristic time for heat transfer as compared to the characteristic time of concentration waves propagating through the column.

Cycle D shows very promising results for the operation as a post-combustion capture process for subsequent CO_2 storage. To the best of our knowledge, this is the first time that a TSA process is reported to reach the target specifications for TSA, while using a commercial sorbent with regeneration temperatures up to 420 K and without making use of compression or vacuum.

Figure 5.12 shows the Pareto set of cycle D considering drying and scheduling as compared to the state-of-the-art technology, namely amine scrubbing. The performance of the amine scrubbing technology is given as a representative range of monoethylamine (MEA)[101,128] and of the Cansolv process operated at Boundary Dam, Canada.[129,130] In order to make a fair comparison, the productivity and the energy consumption of the scrubbing process are calculated based on the total absorber and stripper volume and on the thermal energy for the sorbent regeneration, respectively. Accordingly, the productivity of the TSA process was scaled using the density of the adsorbent bed and by a factor 0.5 in order to account for the total volume of a shell and tube type adsorber. Moreover, heat integration calculations as described in

section 5.4.2.2 (temperature equalization and recovery from the flue gas) were performed on all the operating conditions of the Pareto set in order to estimate the energy savings made possible by proper heat recovery.

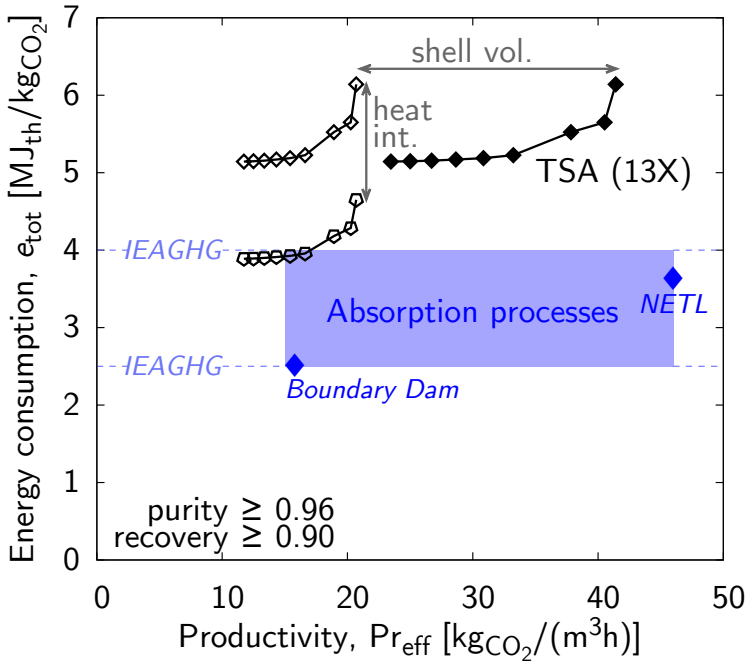

Figure 5.12. – Comparison between a TSA process with 13X and absorption-based processes (according to reporty by IEAGHG[101] and NETL,[128] and data reported from the process operated at Boundary Dam[129,130]). The energy consumption is limited to the thermal energy demand, and the productivity is given per volume, i.e, absorber and stripper volume for the absorption processes, and volume of the shell and tube for the TSA case.

As observed in Figure 5.12, similar performances can be achieved with a commercial 13X zeolite adsorbent in a TSA process as in the state-of-the-art process. While this specific TSA process does not outperform absorption-based processes, it is worth noting that only a minimal heat integration, a commercial material and a standard shell and tube geometry have been considered in this study; we believe that there is still potential for further improvements.

5.5.4 Summary and conclusions

In this chapter we have presented a methodology for the design and evaluation of temperature swing adsorption (TSA) processes for post-combustion CO_2 capture. The comprehensive parametric analysis that we have performed has unveiled the effect of the different steps (heating, cooling, purge, recycle), and of their scheduling into a continuous process, onto the process performance. Moreover, the effect of external elements on the overall performance has been assessed: The energy penalty of the drying unit should always be accounted for, as it might change for varying operating conditions and it makes up for a significant fraction of the overall specific energy consumption (up to 20%); on the other hand, heat integration between heating and cooling steps can reduce the overall energy penalty by a significant fraction (about 12%). Because of the large number of operating conditions considered, the results obtained can serve as a basis to guide the cycle design tailored to given separation specifications.

A specific cycle was selected for a separation task in the context of CO_2 capture and storage system, and its operating conditions were optimized, while accounting for both drying of the flue gas and for a schedule that ensures a continuous feed and a synchronization of recycle steps. As compared to the state-of-the-art CO_2 capture process, namely amine scrubbing, the designed and optimized TSA process achieves similar productivity and specific energy consumption, which by and large govern capital and operating expenditures.

The obtained results are very encouraging for TSA processes for CO_2 capture applications, as this technology does not yet have the same maturity level as that of amine scrubbing. In fact, the complexity of TSA processes offers many degrees of freedom beyond the configuration, scheduling and operation of a cycle, e.g. the adsorbent material, the packing structure or the design of the column with integrated heat exchanger modules. Novel technology elements such as alternative materials on which CO_2 adsorption is not affected by water,[44] hence would not require any drying step, or the use of structured packings with high thermal conductivity, such as foams[131] or hollow-fiber sorbents[49] could provide opportunities for improvement. Although the impact of such novel elements should ultimately be assessed based

on the process costs, the presented methodology provides the tools to evaluate and quantify the possible improvement in terms of achievable separation specifications, productivity and energy consumption.

6 ON THE POTENTIAL OF PHASE-CHANGE ADSORBENTS FOR CO_2 CAPTURE BY TEMPERATURE SWING ADSORPTION

6.1 INTRODUCTION

In an effort to reduce emissions of CO_2 to the atmosphere, researchers have proposed a variety of processes[132–134] relying on different mechanisms to capture CO_2 from large point sources. Large amounts of the total CO_2-emissions stem from power generation (e.g. coal- or gas-fired power plants) or from industry (e.g. cement plants). For post-combustion CO_2-capture, amine based liquid absorption processes are commercial; however, the amine solvents face considerable issues regarding their corrosive nature, stability and potential slip due to volatility.[135] Recently, adsorption processes using solid materials have received significant attention[134] due to the stability and non-volatility of the sorbent, and have demonstrated the possibility of producing a CO_2 stream at high purity with high recovery in pre-[136] and post-combustion[55,82] scenarios considering pre-dried feed streams.

The results presented in this chapter have been reported in: Joss, L.; Hefti, M.; Bjelobrk, Z.; Mazzotti, M. Investigating the potential of phase-change materials for CO_2 capture. *Faraday Disc.* **2016**, DOI: 10.1039/C6FD00040A. This paper was published with a shared first authorship between myself and Max Hefti; this chapter appears in a similar form as presented here also in his dissertation.

Remarkable advances have been made regarding the synthesis of solid materials with tailor-designed properties,[134] e.g. heat of adsorption, selectivity, adsorption capacity, etc. A class of materials that could possibly improve the separation performance compared to more traditional materials, such as activated carbons and zeolites, consists of metal organic frameworks (MOFs). It is expected that these materials can be particularly well tailored towards optimal properties for CO_2-capture, due to the tunability of their pore size and surface functionality.[95] Indeed, numerous MOFs[137] with remarkable properties relevant for CO_2 capture have been synthesized and characterized, e.g. Mg-MOF-74[138] with a very high uptake capacity, i.e. about 8 mmol/g at 0.2 bar CO_2 partial pressure and 296 K, CuBTC[139] and UTSA-16[140] with high CO_2/N_2 selectivity (as predicted by ideal adsorbed solution theory) at 296 K, flexible (breathable) MOF MIL-53[141] with stepwise CO_2 isotherms in certain temperature ranges that could allow for a large working capacity upon a small temperature swing. A major drawback of many MOFs is their relatively low thermal stability[142] and their susceptibility to moisture.[99]

In a recent contribution, McDonald et al.[44] presented six diamine-appended MOFs, i.e., mmen-M_2(dobpdc) where M is the metal center, i.e. Mg, Mn, Fe, Co, Ni or Zn, which appear to overcome some of the issues encountered with MOFs and exhibit some advantages, thus seeming particularly well suited for CO_2 capture.[44] With the exception of mmen-Ni_2(dopdc), these materials exhibit step-shaped CO_2 adsorption isotherms, due to a unique cooperative insertion of CO_2 into the framework at and above a characteristic temperature dependent step pressure. Compared to breathable MOFs, hysteresis upon CO_2 desorption seems to be small.[44,142] Moreover, these materials have high working capacity and high CO_2/N_2 selectivity, and appear to be stable under moist conditions.[45]

Thus far, the potential for CO_2 capture of these materials relies on qualitative predictions, without clear figures on process performance (e.g. purity, recovery, energy consumption, productivity) for a specific cyclic adsorption process. Hence, it is the purpose of this work to quantitatively assess the performance of these novel materials by using model-based process design, and to elucidate the effect of this non-standard isotherm shape on the process performance. While a number

of process options are thinkable, we focus on treating the exhaust gas of a coal-fired power plant by temperature swing adsorption (TSA).

In this chapter, a novel adsorption isotherm model is first developed to describe the adsorption equilibrium of these materials. Second, an equilibrium-based shortcut model[61] is employed to gain a deeper insight into the effect of a step-shaped adsorption isotherm onto the optimal operation and performance of a TSA cycle. The feasibility of these materials in a post-combustion CO_2 capture process by TSA is then assessed by means of detailed simulations. Based on this analysis, the most promising candidates are examined in more detail for a quantitative assessment of the separation performance against the state-of-the-art adsorbent material, i.e. zeolite 13X, and against state-of–the-art amine scrubbing processes.

6.2 MODELING

6.2.1 Adsorption equilibrium isotherm

Figure 6.1 shows the CO_2 adsorption isotherms measured by McDonald et al.[44] on five diamine-appended MOF materials that exhibit a step: the mmen-M_2(dobpdc) (mmen = N,N'-dimethylethylenediamine; dobpdc^{4-} = 4,4'-dioxido-3,3'-biphenyldicarboxylate) frameworks are abbreviated MOF-M, where M stands for the relevant coordination metal. A temperature dependent step-like increase in the adsorbed phase concentration is present for all materials, and the width of the step varies with temperature and among materials. A model for the mathematical description of these adsorption isotherms was presented in the original paper;[44] however, the presence of a discontinuity makes it unsuitable for its use in process simulations. We therefore propose a different, continuous isotherm equation for the description of the CO_2 adsorption equilibrium on the MOFs.

The rationale behind the proposed weighted dual site Langmuir (w-DSL) isotherm arises from the observation that these materials present adsorption sites of different , i.e., chemisorption on terminal amines of the pristine framework, insertion into the framework and

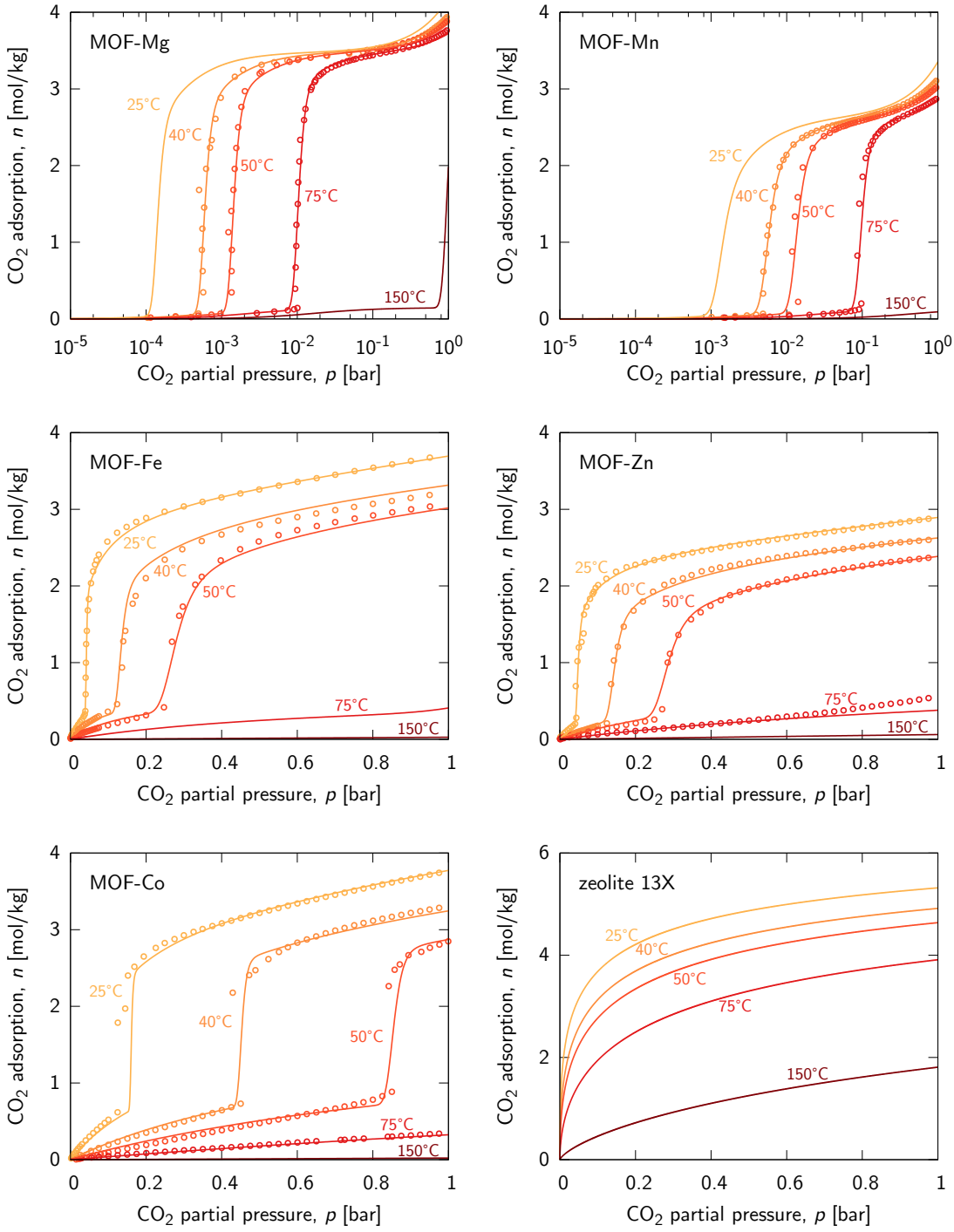

Figure 6.1. – Adsorption isotherms for five different diamine appended MOF materials (labeled as MOF-M, where M is the corresponding metal center). Experimental CO_2 adsorbed amount from McDonald et al.[44] (symbols) and fitted adsorption isotherms (lines). The isotherms for zeolite 13X are shown as well. Five isotherms are shown for each material, each at the same temperatures: 25 °C, 40 °C, 50 °C, 75 °C and 150 °C, going from the lighter to the darker color.

physisorption onto the CO_2-inserted framework.[143] CO_2 adsorption is modeled with two contributions describing the uptake before and after the characteristic step. The solid-solid transition, i.e., from the pristine framework to that with inserted CO_2, is accounted for by a weighting function, as typically done for breathing MOFs:[144]

$$n(p,T) = n_L(p,T)(1 - w(p,T)) + n_U(p,T)w(p,T) \tag{6.1}$$

where n_L represents the Langmuir isotherm prevailing below the step partial pressure, p_{step}, and n_U accounts for adsorption beyond the step pressure via a dual site Langmuir-linear isotherm:

$$n_L = n_L^{\infty} \frac{b_L p}{1 + b_L p} \qquad b_L = b_L^{\infty} \exp\left(\frac{E_L}{RT}\right) \tag{6.2}$$

$$n_U = n_U^{\infty} \frac{b_U p}{1 + b_U p} + b_H p \qquad b_U = b_U^{\infty} \exp\left(\frac{E_U}{RT}\right) \tag{6.3}$$

$$b_H = b_H^{\infty} \exp\left(\frac{E_H}{RT}\right) \tag{6.4}$$

The smooth step-like weighting function $w(p,T)$ is supposed to vary between 0 and 1 in a monotonic way. In this work, the cumulative log–logistic function has been observed to provide a good fit for all five materials of interest:

$$w(p,T) = \left(\frac{\exp\left(\frac{\ln(p) - \ln(p_{\text{step}}(T))}{\sigma(T)}\right)}{1 + \exp\left(\frac{\ln(p) - \ln(p_{\text{step}}(T))}{\sigma(T)}\right)} \right)^{\gamma} \tag{6.5}$$

where $p_{\text{step}}(T)$ and γ determine the position of the step and $\sigma(T)$ its width.

The parameter $\sigma(T)$ depends on temperature according to:

$$\sigma(T) = \chi_1 \exp\left(\chi_2 \left(\frac{1}{T_0} - \frac{1}{T}\right)\right), \tag{6.6}$$

The temperature dependent description of the step pressure, $p_{\text{step}}(T)$, is taken from McDonald et al.[44], according to the following equation, and with the parameters reported in Table 6.1:

$$p_{\text{step}}(T) = p_{\text{step},0} \exp\left(\frac{-H_{\text{step}}}{R}\left(\frac{1}{T_0} - \frac{1}{T}\right)\right) \tag{6.7}$$

Table 6.1. – Parameters for the description of the temperature dependency of the step pressure for the five materials for which a step was observed (from McDonald et al.[44]).

	$p_{\text{step},0}$ [mbar]	H_{step} [kJ/mol]
MOF-Mg	0.5	−74.1
MOF-Mn	4.3	−75.9
MOF-Fe	120.8	−56.9
MOF-Co	450.0	−53.5
MOF-Zn	127.0	−57.3

where $p_{\text{step},0}$ is the step partial pressure at a reference temperature $T_0 = 313.5\,\text{K}$, and H_{step} is the enthalpy of the phase transition.

The step separates two distinct adsorbed phase concentrations, whose value varies for the different MOF-M materials (Figure 6.1). The difference between the values of n_U^∞ and n_L^∞ is used as an estimate of the nominal cyclic capacity of the corresponding MOF-M adsorbent.

$$\Delta n^\infty = n_U^\infty - n_L^\infty \tag{6.8}$$

The isosteric heat of adsorption, ΔH_{ads}, is calculated according to the Van't Hoff relation[76] using equations (6.1) to (6.6):

$$\frac{\Delta H_{\text{ads}}(n,T)}{RT^2} = -\left(\frac{\partial \ln p}{\partial T}\right)_{n(p,T)} \tag{6.9}$$

The heat of adsorption is mainly affected by the parameters governing the temperature dependence of the isotherm, i.e., E_L, E_U, E_H and H_{step}.

6.2.1.1 *Parameter estimation*

The parameters of the w-DSL isotherm were estimated by fitting the single component adsorption isotherm measurements provided by McDonald et al.[44]; the chosen objective function is the non-linear

chi-square test function, which was minimized using the non-linear optimization algorithm of the `fminsearchbnd` Matlab routine:

$$\Psi = \sum_{k=1}^{N_T} \sum_{j=1}^{N_{\text{obs},k}} \left(\frac{\left(n_{j,k} - \hat{n}_{j,k}(\boldsymbol{q}) \right)^2}{n_{j,k}} \right) \tag{6.10}$$

where $n_{j,k}$ is the measured adsorbed amount of CO_2 at pressure p_j and temperature T_k, $\boldsymbol{q}$ is the parameter vector and $\hat{n}_{j,k}(\boldsymbol{q})$ is the adsorbed amount calculated according to equations 6.1 to 6.6. The isotherm parameters were fitted sequentially, i.e., the Langmuir parameters of the adsorption before the step ($n_L^\infty, b_L^\infty, E_L$) were estimated first considering the data before the step, and then fixed for the estimation of the remaining isotherm parameters, for which all data were considered. The associated 90% confidence intervals were quantified according to the method described by Smith[145].

6.2.2 Modeling TSA processes

In this work the potential of the MOF-M materials as adsorbents for a TSA process within the context of post-combustion CO_2 capture aimed at CO_2 storage (CCS) is assessed.

The cyclic, hence dynamic nature of TSA processes make their design a non-trivial task, as it involves many degrees of freedom, including the sequence, direction and inter-connectivity of cycle steps (cycle configuration), the geometry of the columns, and the operating conditions, i.e., the heating and cooling temperatures, the superficial velocity and the duration of the individual step times. In this work, we consider a simple four step cycle, which contains the most important features of a TSA cycle aimed at recovering the heavy component, while minimizing complexity.

The configuration is illustrated in Figure 6.2 and the individual steps of the cycle are briefly explained in the following. We consider a partially regenerated bed at low temperature as the initial state. During the adsorption step, the mixture is fed to the column; thereby the adsorbent uptakes CO_2 from the gas phase, so as the product of this step is enriched in N_2. Next, the bed is heated indirectly by means

of a thermostatting fluid at a high temperature T_{heat}; CO_2 is desorbed as the temperature increases, and a CO_2-rich stream leaves the column. A closed cooling step follows, during which both the temperature and the pressure of the column decrease. Finally, a pressurization step brings the column back to its initial state.

The TSA unit is preceded by a drying step that is assumed to remove water vapor completely; hence the feed to the TSA is a dry gas. For the drying unit, we consider a silica guard,[125] which is commonly regenerated at 150 °C and requires $8\,\text{MJ}/\text{kg}_{\text{H}_2\text{O}}$.

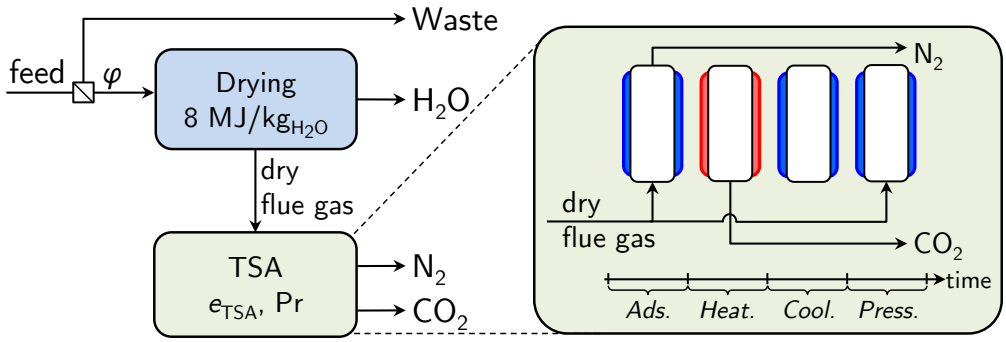

Figure 6.2. – Considered four step cycle configuration. A thermally driven drying unit prior to the TSA unit is accounted for. Depending on the specified recovery, it can be worthwhile to treat only a fraction $\varphi < 1$ of the feed.

For a fixed flow rate and for given column dimensions, the operating conditions for this TSA cycle are the heating and cooling temperatures, which are typically given by the temperature of the available heat sources and sinks, and the duration of the individual steps. The operation of the TSA cycle is modeled by solving the mass and energy balances at CSS, i.e., when each cycle is identical to the previous one. Models of varying complexity can be used to simulate such a process. In this work we consider both a shortcut model that provides lower accuracy with the advantage of a low computational effort, and a detailed model that is computationally more intensive but provides higher accuracy.

6.2.2.1 *Detailed modeling*

A one-dimensional detailed model, which was presented in earlier works[24] and validated for a TSA cycle by comparison to experiments,[82] is used to quantitatively assess the performance of the MOF materials. For the sake of completeness, the most relevant model assumptions are stated anew:

- radial gradients of concentration, velocity and temperature are neglected,
- the solid and fluid phases are in thermal equilibrium,
- the isosteric heat of adsorption, the molar heat capacities, the viscosity and the heat and mass transfer coefficients are constant,
- longitudinal gradients of the heat exchange fluid are neglected.

The partial differential algebraic equations describing mass and energy balances are solved for one column sequentially until a CSS is reached, with the appropriate boundary conditions reflecting the sequence of steps and the choice of operating conditions.

6.2.2.2 *Shortcut TSA model*

A semi-analytical solution of the operation of the considered four step cycle at CSS can be obtained with the equilibrium-based model presented by Joss et al.[61], that considers the following additional assumptions:

- thermodynamic equilibrium between the solid and fluid phases,
- negligible dispersive effects,
- negligible heat capacity of the sorbate, i.e., gas and adsorbed phases, as compared to that of the adsorbent material,
- negligible pressure drop,
- isothermal adsorption step.

In the original shortcut model,[61] the equations were developed specifically for convex isotherms. While the structure of the solution for the pressurization, heating and cooling steps is not affected by the shape of the isotherm, that of the adsorption step depends on

the derivatives of the isotherm. The adsorption isotherm presented in section 6.2.1 exhibits two inflection points, so as the equilibrium theory solution of the adsorption step is not only given by the most common simple wave and shock transitions, but it can also be given by "multipart transitions".[83,146] The following five scenarios are possible depending on the temperature of the adsorption step, on the initial and on the feed concentrations: (i) a shock transition (S), (ii) a wave transition (W), (iii) a shock-wave transition (SW), (iv) a wave-shock transition (WS) and (v) a shock-wave-shock transition (SWS). Note that SW- and WS-transitions are classically called semi-shocks.

While a shock profile corresponds to a step transition between the initial and the feed state, the other types of profile will be more or less disperse depending on the specific isotherm shape, and on the initial and feed concentrations. Figure 6.3 shows illustrative outlet concentration profiles for initial and feed conditions resulting in a shock transition, and in a shock-wave-shock transition; the initial, and feed states are indicated with the letters "i" and "f", respectively. Whenever the isotherm derivative at the initial state is larger than that at the feed state and the chord connecting both states does not intersect the isotherm, a shock transition that separates the initial state from the feed state evolves. Otherwise, a more disperse breakthrough profile evolves during the adsorption step, which will lead to a larger amount of CO_2 in the nitrogen product, hence lowering the recovery. An illustrative example of initial and feed conditions leading to a shock-wave-shock profile are shown in the lower part of Figure 6.3, where "a" and "b" are intermediate states.

The shortcut model has four design variables: the cooling and heating temperatures (T_{heat} and T_{cool}), and the adsorption and desorption temperatures (T_{ads} and T_{cool}). The latter can be directly linked to the durations of the times of the heating and cooling steps. The duration of the adsorption step is fixed so as the feed composition reaches exaclty the end of the column at the end of the adsorption step, and the pressurization time is determined by the flow rate and the amount of feed required to pressurize the column.

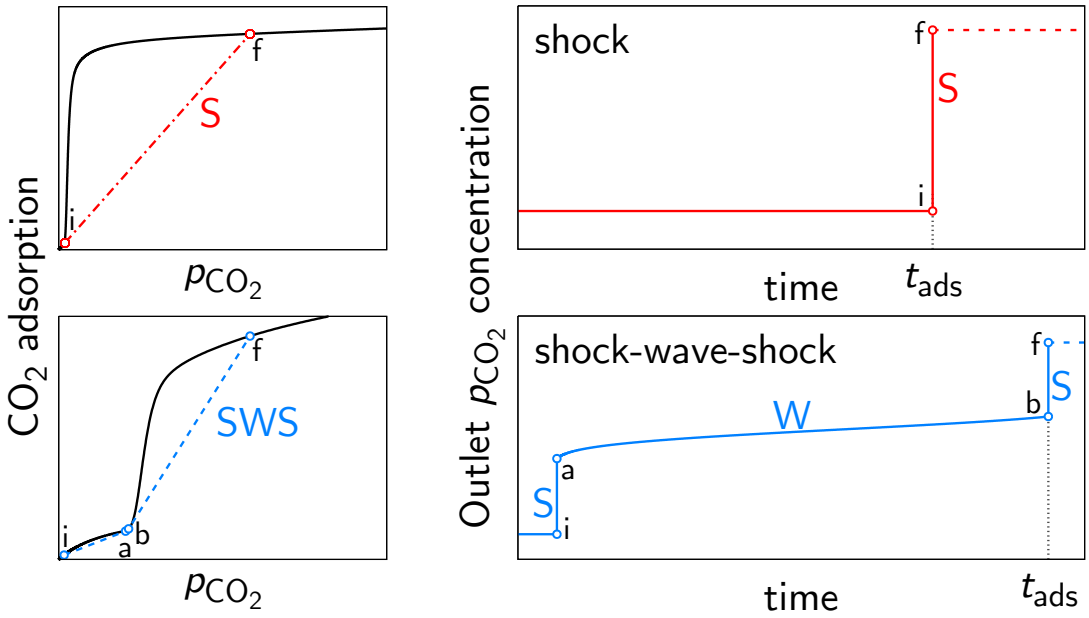

Figure 6.3. – Illustrative breakthrough profiles for initial and feed concentrations resulting in the formation of a shock transition (top) and in the formation of a shock-wave-shock transition (bottom). The duration of the adsorption step is indicated by t_{ads}, i.e., the time required for the column to be fully saturated.

6.2.2.3 *Model parameters*

For both detailed and shortcut models, accurate system parameters, or an educated guess thereof whenever they are unknown, are crucial in order to obtain trustworthy simulation results. All relevant parameters are reported in Tables 6.2 and 6.3, and selected parameters are discussed in more detail in the following.

ADSORPTION EQUILIBRIA Mason et al.[45] investigated the multicomponent adsorption on MOF-Mg of a mixture at 1 bar, 40 °C and with a comparable composition as the one considered in this work, i.e., 19:78:3 $CO_2/N_2/H_2O$ v/v. They found that the affinity of the material towards CO_2 was not reduced by neither N_2 nor H_2O, that N_2 adsorption was negligible and that a significant amount of H_2O was adsorbed. Because of this, the presence of water vapor in the feed stream must be accounted for: water vapor could be fed directly to the TSA unit, or, it could be removed upstream of the TSA unit. While the first option does seem attractive because of the absence of competitive behavior between CO_2 and H_2O adsorption, a more thorough characterization would be required. Hence, a drying step is considered, as shown in Figure 6.2. Therefore, and because N_2 adsorption was shown to be negligible, CO_2 is considered as the only adsorbing component in this work; the phase equilibrium is described by the isotherm model introduced in section 6.2.1. The impact of drying the flue gas before the TSA unit on the energy consumption will be thoroughly accounted for.

HEAT OF ADSORPTION The heat of adsorption is an important quantity, and, as described by the van't Hoff equation it is both loading and temperature dependent. Nonetheless, it is common to use an average, representative value within the range of pressure and temperature covered in the process simulations.[147] Here, we average the heat of adsorption over both loading and temperature according to:

$$\Delta\overline{H}_{\text{ads}} = \frac{1}{N_T}\sum_{i}^{N_T}\left(\frac{1}{n_f(T_i)}\int_0^{n_f(T_i)}\Delta H_{\text{ads}}(n,T_i)\mathrm{d}n\right) \tag{6.11}$$

The temperature range is chosen so as the entire range of values that can be reached during the TSA process is considered, i.e., from T_{cool} to T_{heat} using $N_T = 10$ intervals in between. The averaging in coverage is estimated at each temperature over a range from zero loading to the highest possible loading encountered in the process, $n_f(T) = n(p = 1\,\text{bar}, T)$, i.e. when the gas phase consists solely of CO_2.

PORE AND VOID VOLUMES While the micropore volume is the quantity of interest when interpreting adsorption data,[148] it is the non-selective pore volume, i.e., the specific pore volume accessed by the entire gas phase, that should be used in process calculations to estimate the total void fraction. In the absence of helium pycnometry measurements, the particle void fraction was estimated from micropore volume and crystal density.[44] This corresponds to the assumption that the non-selective gas phase accesses the entire micropore volume, and that the particles are perfectly pelletized leaving no macropores between crystals. The bed void volume was estimated to be 35% as in the dense packing of spherical particles.

PARAMETERS FOR ZEOLITE 13X The studied MOF-M adsorbents are compared to zeolite 13X with regard to their isotherm properties and process performance of the same TSA cycle. The adsorption equilibrium of CO_2 on zeolite 13X has been reported in a previous work[83] and was successfully described by the Sips isotherm model. For the sake of completeness, the CO_2 adsorption isotherms on zeolite 13X at five different temperatures are shown in Figure 6.1 and the Sips equation along with the parameters and the corresponding heat of adsorption are reported in appendix D. All parameters that are required for the simulation of the TSA process are reported in Tables 6.2 and 6.3. It is important to note that in order to draw a fair comparison with the MOF materials considered in this work, the process simulations for zeolite 13X were done considering CO_2 as the only adsorbing compound.

HEAT TRANSFER COEFFICIENTS Not having better information about heat transfer rates in the original paper,[44] we have used a conservative

Table 6.2. – Model parameters: setup dimensions, feed and properties of the feed.

Parameter	Value
Column geometry	
length	1.2 m
internal radius[a]	15×10^{-3} m
external radius[a]	16×10^{-3} m
heat capacity wall	4×10^{6} J/(m^3 K)
heat transfer fluid/wall[b]	100 W/(m^2 K)
heat transfer wall/bed stagnant[b]	20 W/(m^2 K)
heat transfer wall/bed convective[b]	20 W/(m^2 K)
heating temperature (T_{heat})	420 K
cooling temperature (T_{cool})	300 K
Feed	
temperature	303 K
pressure	1.3 bar
flow rate	3.5×10^{-4} m^3/s
CO_2 content	0.12 v/v

[a] These dimensions correspond to those of a shell and tube type heat exchanger, where the adsorbent is packed within the tubes

[b] For the shortcut model, both resistances were lumped into a global heat transfer coefficient $U = 16.8$ W/(m^2 K)

value for the heat transfer coefficients, namely 20 W/(m2 K), for the TSA process simulations presented below. This value is representative of a fixed bed packed with zeolite particles.[82] It is worth noting, that in the shortcut model the assumption of isothermal conditions during the adsorption step would correspond to an infinitely fast heat transfer during that step.

6.2.2.4 *Performance indicators and optimization*

For it to be economically viable, a separation process should reach the desired separation target, specified in this work as a minimum CO_2

Table 6.3. – Material related parameters.

Fixed bed	MOF-M	zeolite 13X
material density	$3200\,\mathrm{kg/m^3}$	$2359\,\mathrm{kg/m^3}$
particle density	$860\,\mathrm{kg/m^3}$	$1085\,\mathrm{kg/m^3}$
bed density (ρ_b)	$575\,\mathrm{kg/m^3}$	$708\,\mathrm{kg/m^3}$
particle diameter	$2.0 \times 10^{-3}\,\mathrm{m}$	$2.0 \times 10^{-3}\,\mathrm{m}$
heat capacity sorbent[a]	$1500\,\mathrm{J/(K\,kg)}$	$920\,\mathrm{J/(K\,kg)}$
CO_2 mass transfer[b]	$0.15\,\mathrm{s^{-1}}$	$0.15\,\mathrm{s^{-1}}$

[a] For MOF-M: Value measured for MOF-Mg is considered for all materials except MOF-Mn, for which $1600\,\mathrm{J/(K\,kg)}$ was measured.[44]

[b] For MOF-M: In line with mass transfer coefficients of other physisorbents.[77,82,124]

purity and a minimum CO_2 recovery, while entailing minimal costs. In the case of a TSA process, the capital and operational expenditures are governed by and large by the productivity and the specific energy consumption, respectively. These four indicators, i.e., the purity of the CO_2 product (Φ), the CO_2 recovery (r), the productivity (Pr) and the specific thermal energy consumption ($e_{\mathrm{tot}} = e_{\mathrm{TSA}} + e_{\mathrm{dry}}$), will therefore be used to assess the process performance:

$$\Phi = \frac{N^P_{\mathrm{CO_2}}}{N^P_{\mathrm{CO_2}} + N^P_{\mathrm{N_2}}} \tag{6.12}$$

$$r = \frac{N^P_{\mathrm{CO_2}}}{N^F_{\mathrm{CO_2}}} \tag{6.13}$$

$$\mathrm{Pr} = \frac{N^P_{\mathrm{CO_2}}}{V_{\mathrm{bed}}\, t_{\mathrm{cycle}}} \tag{6.14}$$

$$e_{\mathrm{TSA}} = \frac{1}{N^P_{\mathrm{CO_2}}} \int_0^{t_{\mathrm{cycle}}} \max(0, \dot{Q}_{\mathrm{in}})\, \mathrm{d}t \tag{6.15}$$

$$e_{\mathrm{dry}} = \frac{e_{\mathrm{w}}\, \varphi\, N^F_{\mathrm{H_2O}}}{N^P_{\mathrm{CO_2}}} \tag{6.16}$$

where $N^P_{CO_2}$ is the amount of CO_2 produced from one column during one cycle and collected in the target product, $N^P_{N_2}$ is the amount of N_2 collected in the same target product, and $N^F_{CO_2}$ is the amount of CO_2 fed to the process during one cycle. The volume specific productivity is considered, where V_{bed} is the volume of one column, and t_{cycle} is the cycle time given by the sum of the individual step times. The specific thermal energy consumption of the TSA unit is determined by integrating the heat flow into one column ($\dot{Q}_{in}$) during one cycle. The energy penalty for the drying of the flue gas should also be accounted for in the total energy consumption. In some cases, it might be worthwhile to dry and process only a fraction $\varphi < 1$ of the feed, in which case the amount fed to the TSA process is $\varphi N^F_{CO_2}$.

Frequently, there is not a single optimal operating point, but a set of such points in which the improvement in one indicator can only take place if the other worsens. For example, the minimal energy consumption and the maximal productivity in general do not coincide in the same operating point. Instead, there exists a so called Pareto frontier ranging from the minimum energy consumption to the maximum productivity. Pareto frontiers are obtained by solving the multi-objective optimization problem:

$$\begin{aligned} \underset{\boldsymbol{x}}{\text{minimize}} \quad & (-\text{Pr}, e_{tot}) \\ \text{subject to} \quad & r \geq r_{spec} \\ & \Phi \geq \Phi_{spec} \end{aligned} \tag{6.17}$$

where $\boldsymbol{x} = \{t_{ads}, t_{heat}, t_{cool}\}$ is the decision variables vector, i.e. the duration of the steps of the TSA process. The constraints to be fulfilled by every admissible point on the Pareto frontier in terms of recovery and purity are given by r_{spec} and Φ_{spec}, respectively. The objectives and constraint violation are computed at each iteration by solving the model equations.

A modified version of the global optimization algorithm MCS (multi-level coordinate search),[149] which can handle multiple objectives as well as non-linear constraints[63] was employed to solve problem (6.17). Because of the fast and direct computation of the CSS in case of the shortcut model, the Pareto frontiers are obtained by parametric analysis.

6.3 RESULTS

6.3.1 Adsorption equilibria

6.3.1.1 *Parameter estimation*

The CO_2 adsorption equilibrium data on five MOF-M materials from McDonald et al.[44] are shown in Figure 6.1 together with the fitted w-DSL isotherms. Calculated adsorption isotherms are shown for each material at five temperatures : 25 °C, 40 °C, 50 °C, 75 °C and 150 °C; the lowest and highest temperature are representative of typical cooling and heating temperatures of a TSA cycle, respectively. The w-DSL isotherm describes the measured data well; the accuracy is of similar quality as for the previously proposed discontinuous isotherm.[44,150]

The estimated parameters are listed in Table 6.4 for all MOF-M materials together with the corresponding 90 % confidence intervals, the average heats of adsorption and the nominal cyclic capacity. The description of the adsorption isotherms for MOF-Mg, MOF-Co and MOF-Zn was observed to be insensitive to the parameter χ_2, hence a temperature independent shape width factor of the weighting function was used: $\chi_2 = 0$ and $\sigma = \chi_1$. The 90 % confidence intervals are rather large; this is mainly due to some data points that are likely associated with significant error, particularly in the region near p_{step}, where the isotherms are very steep. It is worth pointing out, however, that the parameters are identifiable and provide a good description of the experimental data for all five materials, as clearly shown in Figure 6.1.

6.3.1.2 *Analysis of the adsorption properties*

To obtain a better understanding of the role of the step in the CO_2 adsorption within the context of a TSA process, it is helpful to represent the CO_2 adsorption as *isobars* rather than isotherms. Isobars for CO_2 partial pressures representative of three different CO_2-containing gas mixtures, i.e. air, 4×10^{-4} bar, flue gas from burning natural gas (NG), 0.05 bar, and coal, 0.12 bar, are shown in Figure 6.4 for MOF-Mn (top), MOF-Fe (middle) and for zeolite 13X (bottom). Note that the TSA process (see Figure 6.2) relies purely on thermal regeneration

Table 6.4. – Estimated CO_2 adsorption isotherm parameters for the five MOF materials, together with the 90% confidence intervals and average heat of adsorption. Note that even though the isotherm model describes well the data for the six materials, some confidence intervals that are rather large. This is mainly due to some data points that are associated with significant error (e.g. CO_2 isotherm on MOF-Mg at 40 °C, on MOF-Mn at 50 °C, etc.) leading to large confidence intervals. Note that $\alpha = 4$ was observed to provide a good fit for all the materials of interest.

		MOF-Mg	MOF-Mn	MOF-Fe	MOF-Co	MOF-Zn
n_L^∞	[mol/kg]	0.146(68)	0.138(26)	0.62(11)	1.93(25)	0.97(25)
b_L^∞	[bar^{-1}]	0.009(91)	$6(13) \times 10^{-6}$	$1.0(15) \times 10^{-8}$	$1.62(68) \times 10^{-8}$	$2.3(17) \times 10^{-6}$
E_L	[kJ/mol]	31(26)	44.8(55)	54.1(41)	47.3(12)	36.3(14)
n_U^∞	[mol/kg]	3.478(64)	2.629(64)	3.08(13)	3.26(26)	2.466(90)
b_U^∞	[bar^{-1}]	$9(46) \times 10^{-7}$	$1.4(99) \times 10^{-5}$	$4.0(73) \times 10^{-9}$	$1.4(55) \times 10^{-7}$	$1.3(21) \times 10^{-9}$
E_U	[kJ/mol]	59(13)	45(19)	56.8(47)	45.8(97)	59.6(45)
b_H^∞	[mol/(kg bar)]	$5(27) \times 10^{-4}$	$6(25) \times 10^{-4}$	$2.1(67) \times 10^{-4}$	$3(18) \times 10^{-5}$	$8.4(19) \times 10^{-4}$
E_H	[kJ/mol]	18(13)	18(11)	20.1(79)	25(15)	15.8(56)
χ_1	[–]	0.124(50)	0.183(69)	0.076(16)	0.0174(24)	0.090(42)
χ_2	[K^{-1}]	0	$-9(15) \times 10^2$	$3.31(56) \times 10^3$	0	0
γ	[–]	4	4	4	4	4
$\Delta\overline{H}_{ads}$	[kJ/mol]	67.2	58.1	54.6	47.6	42.1
Δn^∞	[mol/kg]	3.33	2.50	2.46	1.33	1.50

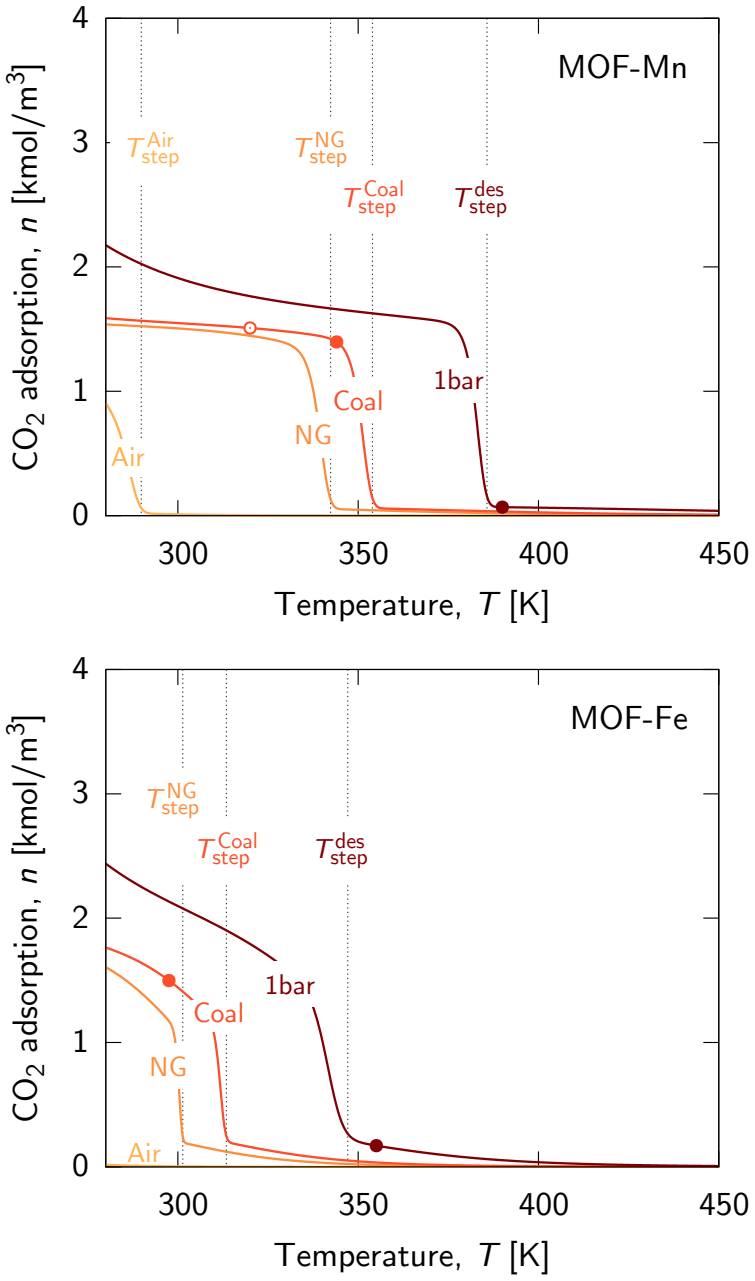

Figure 6.4. – Isobars of MOF-Mn (top), MOF-Fe (middle) and zeolite 13X (bottom) for different feed partial pressures of CO_2, corresponding to capture of CO_2 from different sources, i.e. air (4×10^{-4} bar), flue gas of a natural gas fired power plant (0.05 bar, labeled NG), flue gas of a coal fired power plant (0.12 bar). The isobar at 1 bar CO_2 partial pressure representative of regeneration conditions is also shown. For MOF-Mn and MOF-Fe, the temperatures at which the step pressure corresponds to the CO_2 partial pressure of the corresponding isobars are indicated as dotted lines as well. Note that the CO_2 adsorption is given in units of [kmol/m^3].

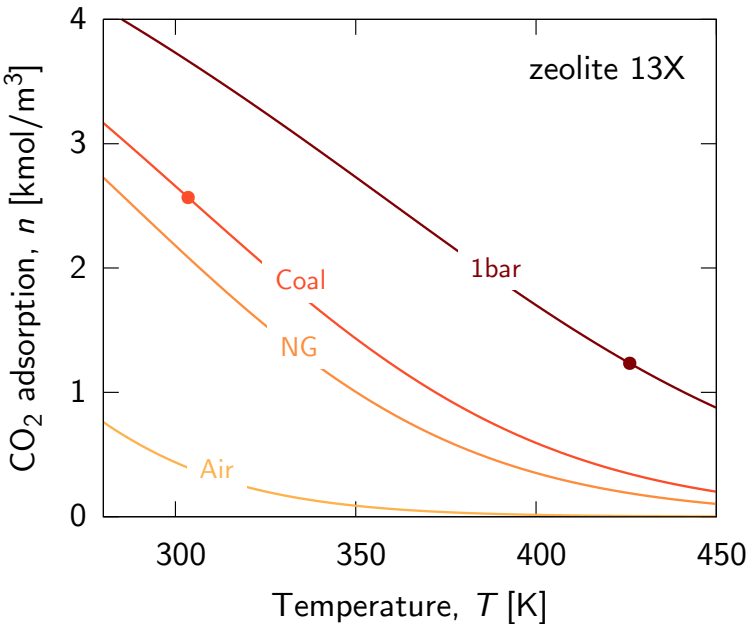

Figure 6.4. – Isobars of MOF-Mn (top), MOF-Fe (middle) and zeolite 13X (bottom) for different feed partial pressures of CO_2, corresponding to capture of CO_2 from different sources, i.e. air (4×10^{-4} bar), flue gas of a natural gas fired power plant (0.05 bar, labeled NG), flue gas of a coal fired power plant (0.12 bar). The isobar at 1 bar CO_2 partial pressure representative of regeneration conditions is also shown. For MOF-Mn and MOF-Fe, the temperatures at which the step pressure corresponds to the CO_2 partial pressure of the corresponding isobars are indicated as dotted lines as well. Note that the CO_2 adsorption is given in units of [kmol/m^3].

at atmospheric pressure, hence, to produce a product stream with high CO_2 purity, the CO_2 partial pressure at the end of the heating step needs to be 1 bar. The isobars representing these regeneration conditions are shown in Figure 6.4 as well. Finally, for MOF-Mn and MOF-Fe the temperature at which the step pressure corresponds to the CO_2 partial pressure of the corresponding isobar is indicated as a dotted line:

$$T^{\mathrm{F}}_{\mathrm{step}}: \quad p_{\mathrm{step}}\left(T^{\mathrm{F}}_{\mathrm{step}}\right) = p^{\mathrm{F}} \tag{6.18}$$

where the superscript "F" indicates either the CO_2 source gas, i.e. air, flue gas from burning natural gas and coal, or the desorption conditions.

Comparing the shape of the isobars for the MOF-M adsorbents and for zeolite 13X, a striking difference is observed due to the step in the CO_2 adsorption. For zeolite 13X, the decrease of the CO_2 adsorption with temperature proceeds rather uniformly without large variations in the slope of the isobars. On the other hand, the isobars of MOF-M reflect the properties of the step, i.e., there are two distinct levels, at high and low CO_2 adsorbed phase concentration, separated by the step occurring at a temperature close to $T^{\mathrm{F}}_{\mathrm{step}}$.

To exploit the step in the CO_2 adsorption of the MOF-M materials efficiently, two conditions with regard to the operating temperatures have to be fulfilled. First, the adsorption temperature must be *at least* a few degrees lower than $T^{\mathrm{F}}_{\mathrm{step}}$, i.e. where the capacity is high, as, for example, indicated with the filled circles on the "Coal"-isobars (note that in this case $T^{F}_{\mathrm{step}} = T^{\mathrm{Coal}}_{\mathrm{step}}$). It is important to note that in a TSA process, the heat transfer rate is finite and thus the heat released upon adsorption of CO_2 will lead to a temporary increase in the temperature of the column. If the adsorption temperature is in vicinity of the step temperature T^{F}_{step}, even a slight rise in temperature may cause a large reduction in the adsorption capacity. Hence, a "safety-margin" is required: the adsorption temperature should be chosen sufficiently low so as to maintain a high CO_2 capacity even when temperature increases, as for example indicated by the open circle on the "Coal"-isobar of MOF-Mn. The second condition to be fulfilled concerns regeneration during the heating step of the TSA cycle. The regeneration temperature must be higher than $T^{\mathrm{des}}_{\mathrm{step}}$ so as the adsorption capacity is low, i.e. beyond the step in the isotherm,

as, for example, indicated by the filled circle on the isobar at 1 bar of MOF-Mn and MOF-Fe. Operation of a TSA process meeting these two requirements will lead to an efficient use of the step in the CO_2 adsorption. On the other hand, reaching a similar cyclic capacity using zeolite 13X requires a much larger temperature swing, as indicated with the filled circles on the zeolite 13X isobars in Figure 6.4 (bottom).

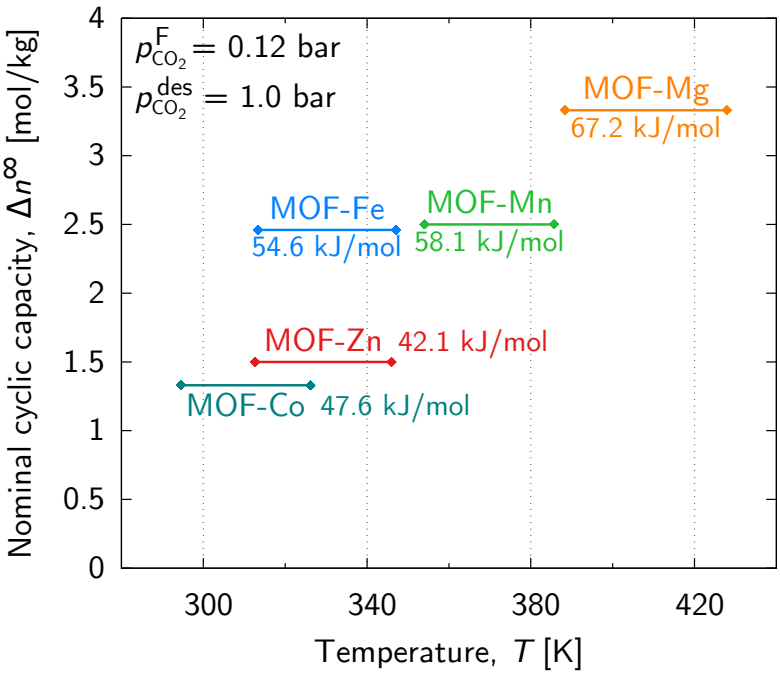

Figure 6.5. – Temperature range (T^{F}_{step} to T^{des}_{step}) and nominal cyclic capacity computed with eq. (6.8) for the investigated MOF-M adsorbents. The corresponding average isosteric heat of adsorption are also indicated for each material. An effective use of the material can be achieved if a TSA process is operated with a temperature swing that encompasses the indicated range. The width of this range is governed by the temperature dependency of the step, and is about 40 K for MOF-Mg, about 35 K for MOF-Fe and MOF-Zn and about 30 K for MOF-Mn and MOF-Co.

Figure 6.5 provides a graphical representation of the nominal cyclic capacity, Δn^{∞} versus temperature for conditions representative of the flue gas of a coal fired power plant. The temperature interval defined by the step temperatures at adsorption and desorption conditions, i.e. T^{des}_{step} and T^{F}_{step}, respectively, is shown as horizontal bars, and scales

with the minimum required temperature swing leading to an efficient use of the step.

A rather wide range of nominal cyclic capacities is observed for the MOF-M materials. MOF-Mg has the highest nominal cyclic capacity of 3.3 mol/kg, followed by MOF-Mn and MOF-Fe with a capacity of approximately 2.5 mol/kg and finally MOF-Zn (1.5 mol/kg) and MOF-Co (1.33 mol/kg) with the lowest capacities. Note that in general, a large cyclic capacity is expected to improve the process performance, i.e. to yield high purity and productivity at decreased specific energy consumption.

Differences in the minimally required temperature swing are less visible in Figure 6.5 but nonetheless significant; this is from about 30 K for MOF-Mn and MOF-Co to about 40 K for MOF-Mg. This temperature interval is primarily governed by the temperature dependence of the step, i.e. the parameters $p_{\text{step},0}$ and H_{step}. At fixed $p_{\text{step},0}$, a large H_{step} leads to a small difference of T^{F}_{step} and $T^{\text{des}}_{\text{step}}$. A moderate temperature swing can lead to short heating and cooling times, hence a large productivity. On the other hand, the isosteric heat of adsorption increases with H_{step}, therefore leading to increased energy consumption.

It is clear that these five materials represent a class of compounds, whose properties span rather broad ranges of values. It is therefore thinkable that by tuning the metal center, the organic linker or the appended diamine one may be able explore other desirable combinations of properties; this possibility is explored in section 6.4.1.

6.3.2 Simulation results and parametric analysis

In this section, the shortcut model is used to investigate relevant features of the operation and performance of the four step TSA cycle for two illustrative materials, MOF-Mn and MOF-Fe. The case of a flue gas from a coal fired power plant is considered, i.e. a CO_2/N_2 stream (12:88 v/v on a dry basis) containing 4 % water vapor, on a volume basis, which is fed at ambient pressure and 303 K. We consider the operation of the TSA process where cooling and heating are performed with available sources at 300 K and 420 K, respectively,

and the remaining operating conditions, i.e. the step times, are varied. The results of the parametric analysis performed with the shortcut model are reported as contour maps for each performance indicator in the plane (T_{ads}, T_{des}).

6.3.2.1 *CO_2 purity and recovery*

Figure 6.6 shows the purity and recovery contour maps in the (T_{ads}, T_{des}) plane for MOF-Fe and MOF-Mn. Results of a type I material, zeolite 13X, are also shown for the sake of comparison. As discussed in Joss et al.[61], for zeolite 13X the achieved purity increases with increasing T_{des} and decreasing T_{ads}. On the other hand, for the materials with a step-shaped isotherm, a steep change in purity is observed around a well-defined rectangular region. It is interesting to note that the high purity rectangular region ($\Phi \geq 0.95$) coincides to a large extent with the region delimited by $T_{ads} < T_{step}^{F}$ and $T_{des} > T_{step}^{des}$ for both MOF-M materials.

The recovery for zeolite 13X exhibits a similar behavior as its purity; it increases monotonically towards the upper left corner of the (T_{ads},T_{des}) plane. Such behavior is expected because the adsorption front is always of the shock type, as illustrated in Figure 6.3 (upper). In the case of MOF-Fe two regions that yield rather high recovery separated by an intermediate valley are observed in Figure 6.6. In the region right of T_{step}^{F}, the trend is similar to zeolite 13X, because the adsorption front is under these conditions of the shock type. Note that in contrast to zeolite 13X, the purity obtained in this region with MOF-Fe is low. In the region highlighted with dots left of T_{step}^{F}, the adsorption front is of the shock-wave-shock type, as illustrated in Figure 6.3 (lower), and the recovery drops drastically before increasing again towards lower adsorption temperature. Finally, the third adsorbent, MOF-Mn, achieves high recovery (> 0.90) within a rather large portion of the rectangular region delimited by T_{step}^{F} and $T_{step}^{des}$where the adsorption front is of the shock type. To a large extent, this high recovery region coincides with high purity. On the right of this region recovery drops quickly for reasons similar to the case of MOF-Fe.

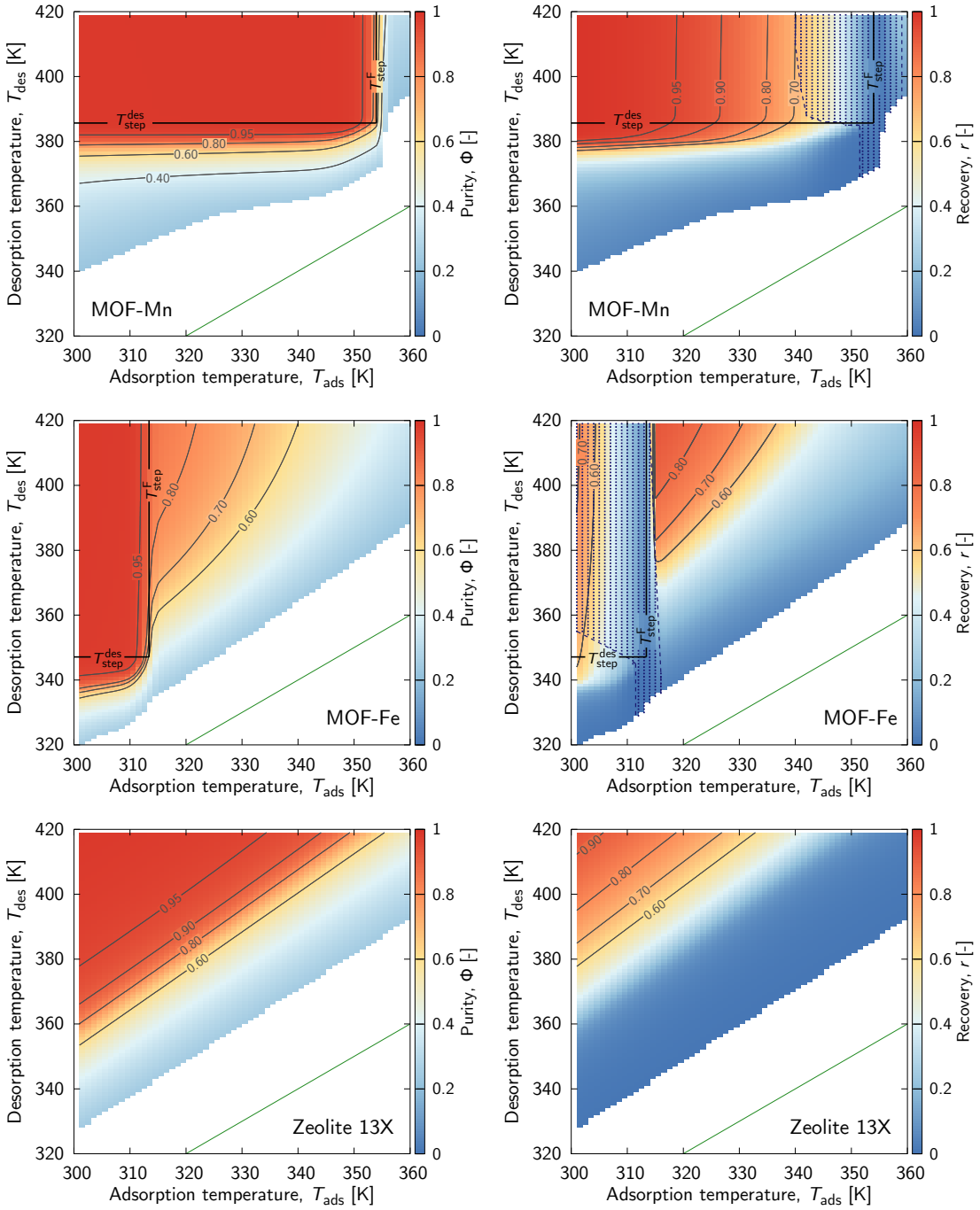

Figure 6.6. – Purity and recovery contour maps for MOF-Mn, MOF-Fe and zeolite 13X. The diagonal, indicated by the green line, delimits the unfeasible region (below) from the feasible region. The gap between the diagonal and the colored region stems from numerical issues in the calculations; however the performance for those operating points is so poor (purity, recovery and productivity are very low and the energy consumption is very high) that these points are anyhow not of interest.

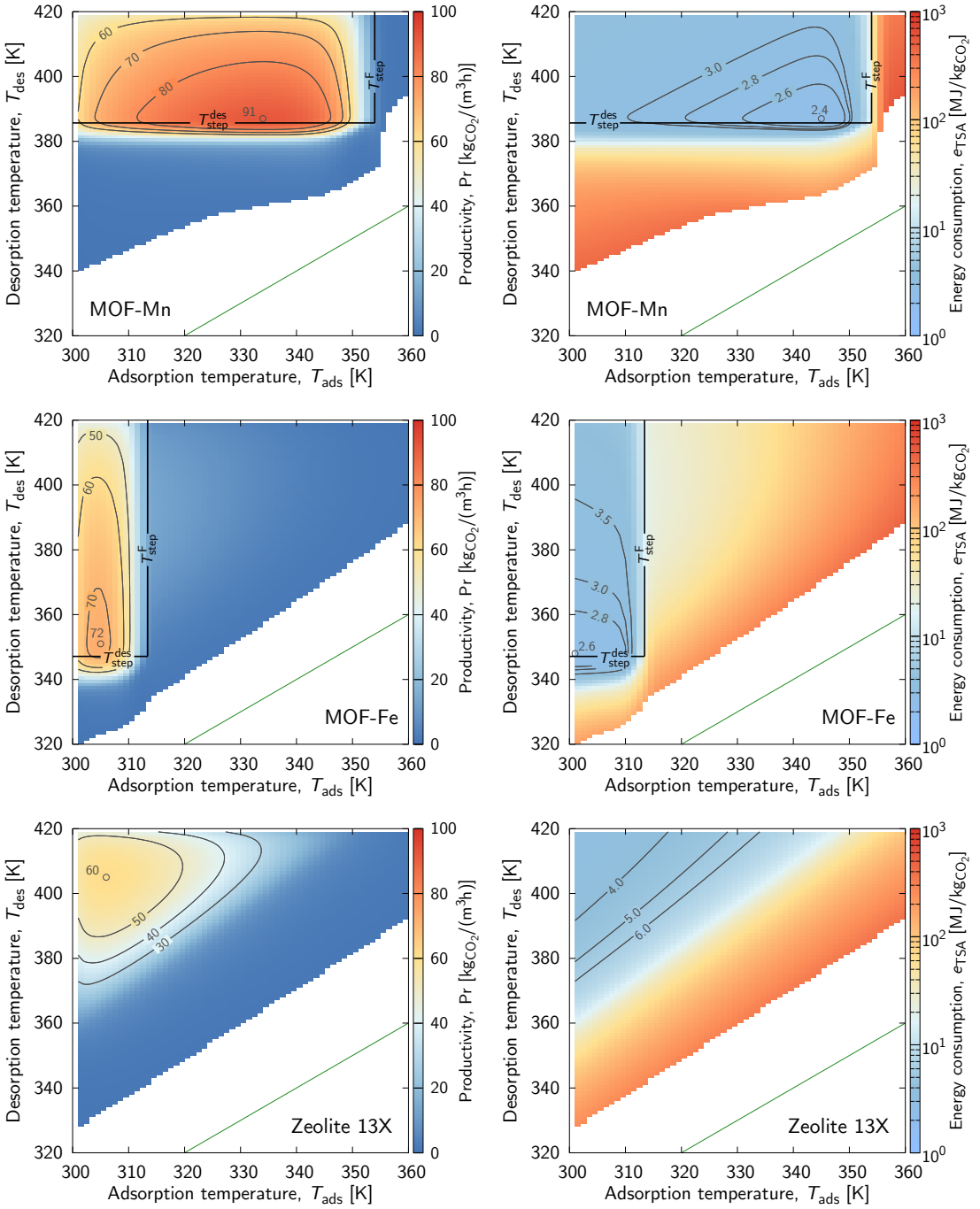

Figure 6.7. – Productivity and energy consumption contour maps for MOF-Mn, MOF-Fe and zeolite 13X. The diagonal, indicated by the green line, delimits the unfeasible region (below) from the feasible region. The gap between the diagonal and the colored region stems from numerical issues in the calculations; however the performance for those operating points is so poor (purity, recovery and productivity are very low and the energy consumption is very high) that these points are anyhow not of interest.

6.3.2.2 *Productivity and energy consumption*

The productivity and specific energy consumption contour maps are shown in Figure 6.7. High productivity is achieved for operating conditions presenting a large cyclic capacity and a short cycle time. As expected, for the MOF-M materials higher productivity is achieved in the same rectangular region as seen in Figure 6.6. The cycle time increases for increasing desorption temperature and decreasing adsorption temperature because of the reduced driving force for heat transfer during heating and cooling, respectively, hence leading to lower productivity. Even though their nominal cyclic capacity is almost identical, using MOF-Mn leads to a maximum productivity 20 % higher than that obtained with MOF-Fe. The reason is that, effectively, in case of MOF-Fe only part of the nominal capacity is exploited, because even at the lowest adsorption temperature of around 300 K the adsorbed phase concentration is still far from saturation (refer to the isobars of MOF-Fe in Figure 6.4), while in the case of MOF-Mn saturation conditions are effectively already reached at this temperature.

The lowest energy consumption values coincide also to a large extent with the region delimited by the solid lines in Figure 6.7. It is worth noting that the minimum energy consumption lies within the considered range of operating conditions for the MOF-M materials, as opposed to zeolite 13X, whose minimum energy consumption is achieved for adsorption/desorption temperatures beyond the range of investigated operating conditions, as discussed by Joss et al.[61] Similar values of the minimum specific energy consumption are achieved for both MOF-Mn and MOF-Fe. In fact, while MOF-Mn has a larger heat of adsorption, its effect on the energy consumption is compensated by a slightly lower temperature swing, and a slightly larger cyclic capacity (refer to Figure 6.5).

6.3.2.3 *Material screening*

The performance of the same TSA process operated with different materials can be compared in a fair way only after optimizing the process for each material. To this aim the detailed model is used.

Figure 6.8 (left) shows a comparison of the optimal achievable recovery and purity for the five MOF-M materials and for zeolite 13X.

The region corresponding to CCS specifications, i.e. recovery $\geq 90\,\%$ and purity $\geq 96\,\%$,[100] is highlighted in the upper right corner. A trade off between purity and recovery is visible. Moving from left to right along the Pareto set, the adsorption time increases and so does the purity because the adsorption column is used more completely. After the CO_2 front reaches the end of the column during the adsorption step, any further increase in the adsorption time results in a greater fraction of CO_2 lost in the waste product, hence in a drop in recovery. The purity approaches a limit, which is governed by the amount of CO_2 and the amount of nitrogen contained in the adsorption column at the end of the adsorption step.

The Pareto sets of MOF-Mg and MOF-Mn can be viewed as consisting of two sections, i.e. one where the recovery is high and the purity is low, and a second where the recovery is low and purity is at its upper limit; these are connected by a transition region. The sharp drop in the recovery is a consequence of a steep shock-like concentration profile that evolves during the adsorption step. On the contrary, the Pareto sets of MOF-Co, MOF-Zn and MOF-Fe exhibit a more rounded shape and an inflection point, which is a consequence of the disperse profile arising during the adsorption step (refer also to Figure 6.6). Note that MOF-Fe and MOF-Zn reach their highest purity at very low recovery only.

The only materials reaching CCS specifications are MOF-Mn and zeolite 13X. The poor performance of MOF-Co and MOF-Mg is expected: as seen in Figure 6.5, the temperature range of the step for these two adsorbents is not contained within the range of temperature delimited by T_{cool} and T_{heat}. As a consequence, the process is such that the CO_2 adsorption is always below the step (MOF-Co), or above the step (MOF-Mg), thus leading to only a partial exploitation of the nominal cyclic capacity. On the other hand, the temperature ranges of the step of MOF-Fe, MOF-Zn and MOF-Mn belong to the interval delimited by T_{cool} and T_{heat}, as seen in Figure 6.5. Still, poor performance is observed in Figure 6.6 (left) for MOF-Fe and MOF-Zn. The reason is that the temperature at which the adsorption occurs is too close to the step temperature, $T^{\text{F}}_{\text{step}}$, and already a temperature increase (due to adsorption) in excess of 15 K results in a drastic drop in the adsorbed phase concentration. Hence, the step is not used efficiently and only

a fraction of the nominal cyclic capacity is exploited (refer also to Figure 6.4). For MOF-Mn, the adsorption temperature is sufficiently distant from $T_{\text{step}}^{\text{F}}$ such that most of the nominal capacity is used, thus allowing for high purity at high recovery. It is worth noting, that this is true for the considered case study with heating and cooling temperatures of 420 K and 300 K, respectively. The choice of these temperature levels, however, is specific to the available heat sources and sinks, and a variation thereof will affect the achievable recovery and purity of the different materials, as discussed in section 6.4.2.

Figure 6.8 (right) shows the Pareto sets of the process performance in terms of energy consumption and productivity for the materials achieving CCS specifications, i.e. MOF-Mn and zeolite 13X. Note that the total energy consumption is considered, accounting for both the energy penalty of the TSA process and that of the drying unit. The Pareto sets were obtained by solving the optimization problem (6.17). Clearly, with MOF-Mn a higher productivity at lower energy consumption is achievable; indeed, the productivity is almost doubled while the energy consumption can be lowered by more than 20 % with respect to zeolite 13X.

6.4 DISCUSSION

In the previous section, the performance of five MOF-M materials was assessed for their use in a TSA process for post-combustion CO_2 capture operated with available heat sources and sinks at 420 K and 300 K for heating and cooling, respectively. In the following, the discussion is broadened by considering first the possibility of tuning the material sorption isotherms to identify an optimal adsorbent, and then by assessing the performance of the MOF-M adsorbents for a generic post-combustion scenario, where multiple temperature levels are available for heating and cooling.

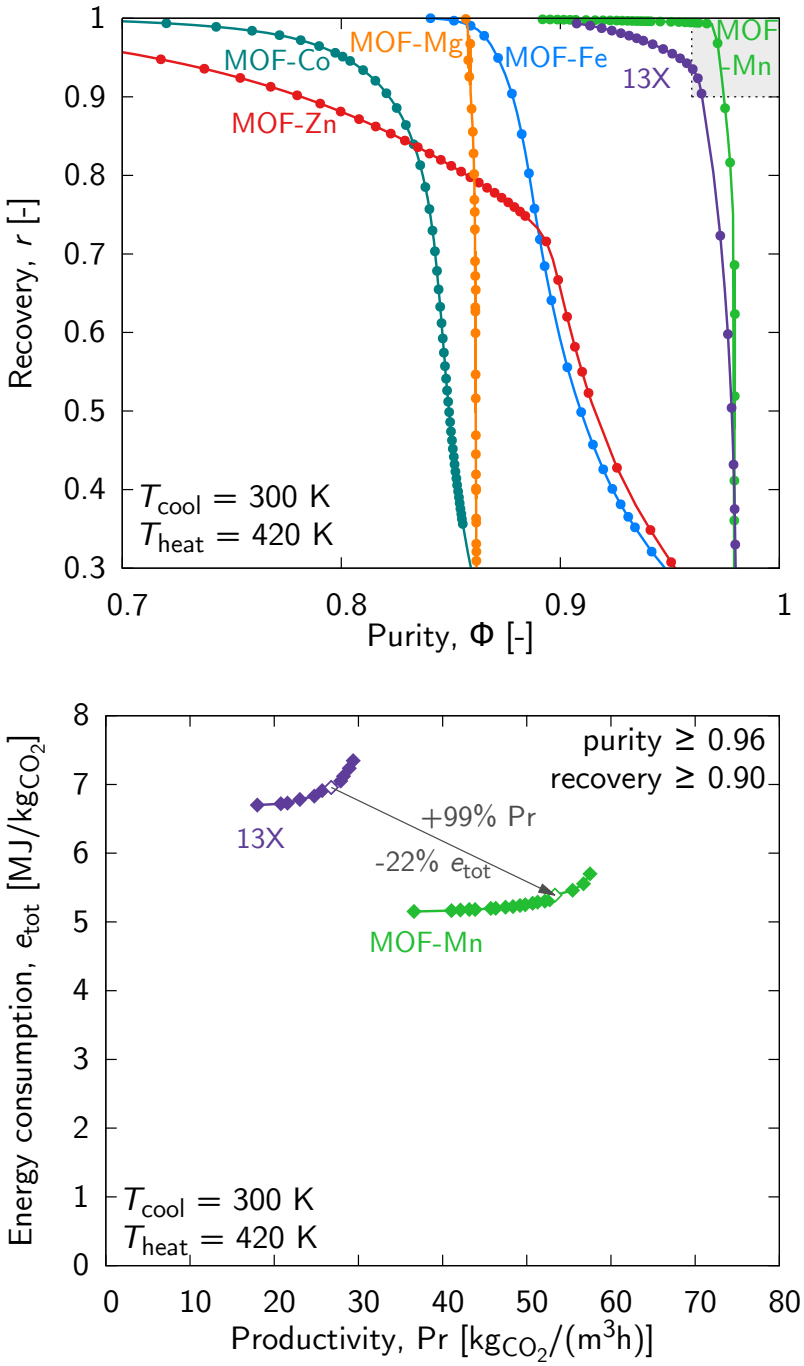

Figure 6.8. – Pareto frontiers of the best feasible separation specifications and performance for the five MOF-M materials and zeolite 13X predicted by the detailed model. Left: purity and recovery. Right: productivity and energy consumption for operating conditions achieving CO_2 purity ≥ 0.96 and CO_2 recovery ≥ 0.90.

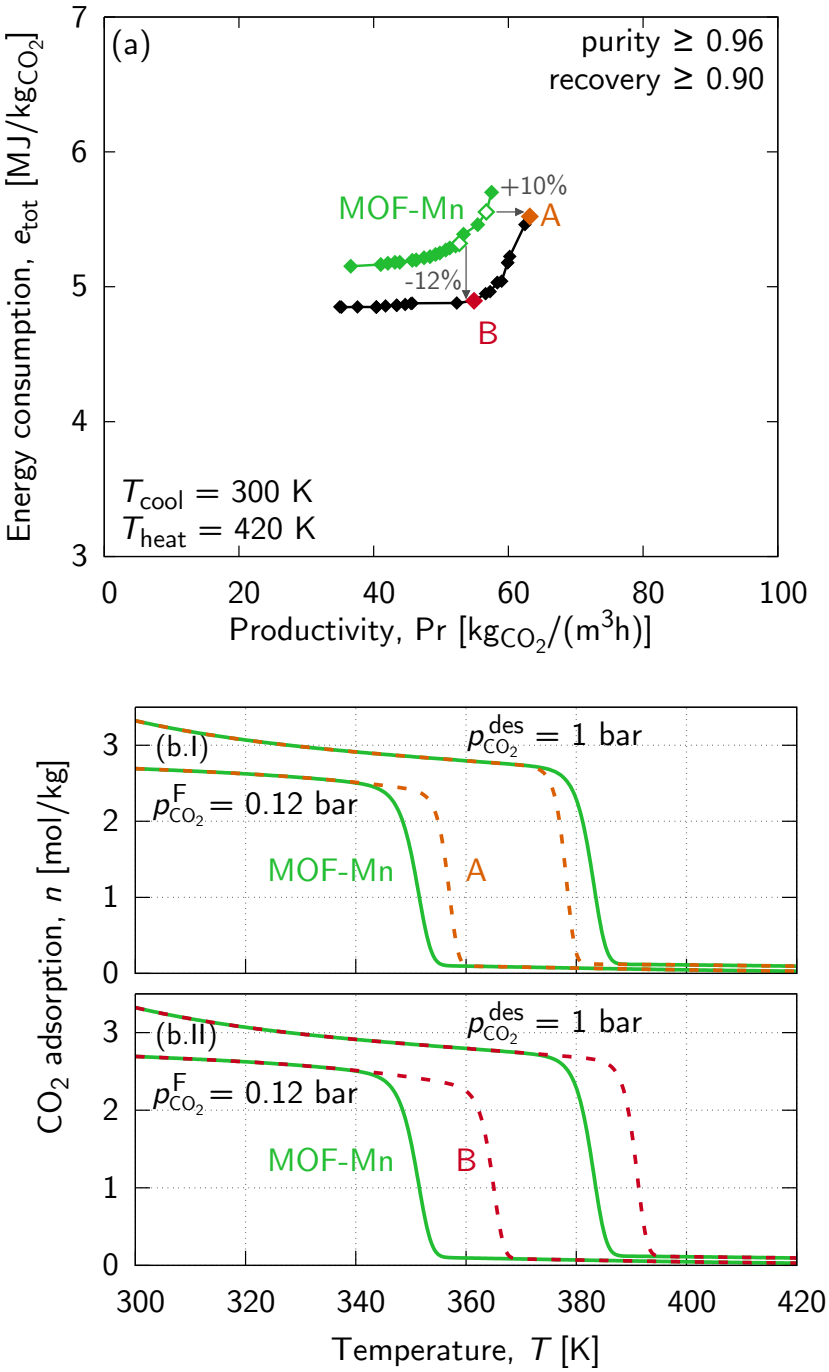

Figure 6.9. – (a): Pareto frontiers of MOF-Mn and the set of hypothetical optimized materials. (b): Isobars at adsorption and desorption pressure for MOF-Mn and two materials of particular interest.

6.4.1 Optimal MOF-M adsorbent

The position and temperature dependence of the step is mainly governed by the strength of the metal-diamine bond.[44] Therefore, it is thinkable to tune the step position by changing either the metal center or the diamine. Based on this remark, it is worth considering the following question. Can one design optimized materials "in silico" by solely changing the properties of the step? Specifically, we ask if there exist parameters that describe the step pressure p_{step}, i.e. $p_{\text{step},0}$ and H_{step} in equation (6.7), yielding an improved process performance as compared to MOF-Mn. To this end, we solve the optimization problem (6.17) and seek optimal values for $p_{\text{step},0}$, H_{step} and the duration of the steps of the TSA cycle, i.e. utilizing the decision variable vector $\boldsymbol{x} = \{t_{\text{ads}}, t_{\text{heat}}, t_{\text{cool}}, p_{\text{step},0}, H_{\text{step}}\}$; $p_{\text{step},0}$ is allowed to vary between the lowest and the highest observed for the five MOF-M materials, i.e. 0.5 mbar (MOF-Mg) and 450 mbar (MOF-Co), respectively. To explore materials with temperature intervals between T^{F}_{step} and $T^{\text{des}}_{\text{step}}$ narrower than those of MOF-M materials investigated so far, the limits imposed on H_{step} were -50 kJ/mol and -120 kJ/mol. All other isotherm parameters were held constant, so as the step pressure is shifted to lower or higher CO_2 partial pressures while retaining the same nominal cyclic capacity, Δn^{∞}.

The process performance at CCS specifications (recovery ≥ 0.90 and purity ≥ 0.96) for the *set* of optimal hypothetical materials is shown in Figure 6.9 (a) at a cooling temperature of 300 K in the form of a Pareto set. It is important to note that each point of the Pareto set in Figure 6.9 (a) corresponds to a unique (hypothetical) material with a different step pressure. Isobars for MOF-Mn as a reference along with those of hypothetical materials of particular interest as labeled in the Pareto set are shown in Figure 6.9 (b). The resulting parameters along with the averaged heat of adsorption for these materials are summarized in Table 6.5.

As shown in Figure 6.9 (a), the Pareto set of the set of hypothetical optimal materials is shifted to lower specific energy consumption (e_{tot}) and to higher productivity (Pr) as compared to MOF-Mn.

The highest productivity is reached for material A, and the isobars shown in Figure 6.9 (b.I) are closer to each other than the correspond-

Table 6.5. – Optimized materials parameters and averaged heat of adsorption.

optimized material	$p_{step,0}$ [mbar]	H_{step} [kJ/mol]	$\Delta\overline{H}_{ads}$ [kJ/mol]
A	0.5	-113.3	64.3
B	0.5	-97.9	62.4

ing ones of MOF-Mn, thus reducing the required temperature swing. This results in an increased driving force for both heating and cooling, which are then shorter and lead to higher productivity. A material with properties that lead to a lower energy consumption is material B, the isobars of which are shown in Figure 6.9 (b.II). They are shifted to the right relative to those of MOF-Mn because the adverse effect on the cyclic capacity due to the temperature increase during the adsorption step is minimized. Indeed, the adsorbed phase concentration averaged over the length of the column at the end of the adsorption step for material B is 2.19 mol/kg, while for MOF-Mn it is 1.90 mol/kg. The fact that more CO_2 is collected during the heating step in the case of material B leads to a lower value of the specific energy consumption e_{tot}.

Thus concluding, optimized materials yielding superior performance in CO_2 capture by TSA could be identified by solely tuning the step properties, and their characteristics rationalized based on the features described above.

6.4.2 Comparison to state-of-the-art processes

To put the performance of these novel materials for a CO_2 capture process by TSA into perspective, a comparison is made with the adsorbent that is hitherto used most frequently for adsorption based post-combustion capture, i.e. zeolite 13X, first, and then with amine-based absorption.

The performance of the TSA process is sensitive to the considered temperature levels for heating and cooling. To assess their performance in more general terms, the constraint on the temperature levels of the heat sources and sinks is relaxed. While in the previous

sections the heating and cooling temperatures were constrained to specific values, in the following they are optimized within the range between 293 K and 500 K together with the step durations, i.e., the decision variable vector used for the optimization problem (6.17) is: $\boldsymbol{x} = \{t_{\text{ads}}, t_{\text{heat}}, t_{\text{cool}}, T_{\text{cool}}, T_{\text{heat}}\}$. The difference in quality of the energy content made available or removed at different temperature levels is accounted for by optimizing the overall exergy, e_{x}, instead of the thermal energy consumption. The individual contributions of the TSA process, $e_{\text{x,TSA}}$, and of the drying step, $e_{\text{x,dry}}$, are estimated by multiplying the corresponding thermal energy consumption with the Carnot efficiency, which is calculated between the hot temperature level and ambient temperature (T_{amb} = 298 K). Hence, the exergy is defined as:

$$e_{\text{x}} = e_{\text{x,TSA}} + e_{\text{x,dry}} = e_{\text{TSA}} \left(1 - \frac{T_{\text{amb}}}{T_{\text{heat}}}\right) + e_{\text{dry}} \left(1 - \frac{T_{\text{amb}}}{T_{\text{dry}}}\right) \quad (6.19)$$

where T_{heat} is the hot temperature level for the TSA and T_{dry} is the regeneration temperature of the drying unit, taken as a constant value of 423 K.

Figure 6.10 shows the performance of the MOF-M materials in terms of exergy and productivity. The comparison to absorption processes is carried out based on the heat duty of the stripper. The exergy is calculated also in this case by accounting for the Carnot efficiency between the reboiler temperature and ambient temperature.

For the considered process parameters, MOF-Mn and MOF-Mg are the only MOF-Ms that reach the required specifications for the given TSA cycle. The lowest exergy using MOF-Mn is 20 % lower than for MOF-Mg. Indeed, at the minimal exergy the required heating and cooling temperatures are closer to each other for MOF-Mn (T_{cool} = 293 K, T_{heat} = 397 K) than for MOF-Mg (T_{cool} = 308 K, T_{heat} = 447 K). This reflects the position of the step: The step temperatures for adsorption and desorption conditions are at lower values and span a narrower range for MOF-Mn than for MOF-Mg (Figure 6.5). Moving along the Pareto sets towards higher productivity, the temperature difference between the heating and the cooling temperature increases; the highest productivity is achieved when the heating temperature is maximal (500 K) and the cooling temperature is minimal (293 K) for

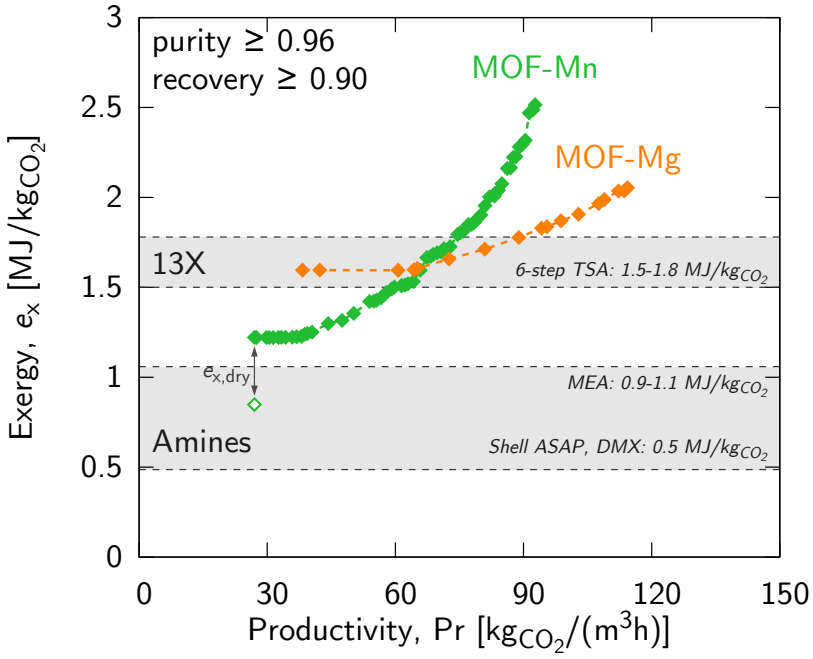

Figure 6.10. – Comparison of the process performance of MOF-Mn, MOF-Mg with state-of-the-art zeolite 13X using a 6-step TSA cycle from Joss et al.[151] and amine processes. For MOF-Mn an additional (empty) point is shown, which indicates the minimal exergy without considering the contribution of the drying step ($e_{x,dry}$). Finally, three variants of amine absorption processes are shown. The references are: MEA (Abu-Zahra et al.[152]), DMX (Raynal et al.[153], 154), Shell ASAP (Singh et al.[155]).

both materials. At productivity of 65 $kg_{CO_2}/(m3\,h)$ the Pareto sets of MOF-Mg and MOF-Mn intersect, and the use of MOF-Mg leads to an improved process performance; this is understandable because the cyclic capacity, which is higher for MOF-Mg than MOF-Mn, is used efficiently for heating temperatures higher than 450 K. To summarize, MOF-Mn is the preferred material when the temperature level of the heat source is below 450 K, while MOF-Mg is the better option if higher heating temperatures are available.

The designed and optimized TSA processes are compared to a state-of-the-art TSA process operated with a 6-step cycle and based on zeolite 13X.[151] In order to allow for a fair comparison, the exergy of the six step TSA process is calculated considering the overall thermal energy consumption excluding any heat integration. The minimal

exergy of MOF-Mn is significantly lower (almost 20 %) than that of the more complex 6-step TSA process reported in Joss et al.[151].

Finally, a comparison to three different absorption-based processes is made. The first of these amine based processes is one that uses the classical monoethanolamine (MEA) solvent, and it is based on the work by Abu-Zahra et al.[152]. The exergy of their process is between 0.9–1.0 MJ/kg_{CO_2}. The second variant is based on the results of industrial pilot tests of the DMX process. This process uses a special solvent that forms two immiscible phases for low and high CO_2 loading. Only the fraction of the solvent with high CO_2 loading is regenerated in the stripper, thus lowering the energy consumption of the regeneration.[153] The exergy is approximately 0.5 MJ/kg_{CO_2} using 105 °C as stripper temperature.[153] The third variant considered is by Singh et al.[155], using a mixture of two amines (AMP/HMDA) as solvent. Results obtained from the Shell Pilot Plant ASAP Unit suggested a similar value for the exergy as obtained for the DMX process.

Amine based processes still outperform the adsorption process based on the MOF materials considered in this work (Figure 6.10). Adsorption processes are, however, not as mature as absorption processes yet.

6.5 CONCLUSIONS

In this work, we investigated the potential of a novel class of adsorbent materials which was recently reported to exhibit step-shaped CO_2 adsorption isotherms with negligible hysteresis and change in volume. The presence of such a step is indeed interesting for CO_2 capture by TSA, since it allows to exploit the material's cyclic capacity upon a smaller temperature swing as compared to traditional materials with type I CO_2 adsorption isotherms. The presented comprehensive modeling study enabled to identify critical features of the operation of a four step TSA process with these materials, and to identify design criteria that result in an optimal and robust operation.

By optimizing the operating conditions of a TSA cycle, we show that for a feed representative of the flue gas of a coal fired power plant,

a two-fold productivity increase and a reduction in the specific energy consumption by more than 20 % can be expected when MOF-Mn is used instead of commercial zeolite 13X. The performance of the TSA process is sensitive to the temperature levels of the heat sources and sinks. Hence, it was assessed in more general terms by considering multiple temperature levels. The minimal exergy of MOF-Mn was shown to be almost 20 % lower than for zeolite 13X.

As such, this study represents the first quantitative assessment of the process performance that can be achieved with this novel class of materials in a TSA process for CO_2 capture. While detailed studies of the interaction of these materials with pure CO_2 and under equilibrium conditions are available in the literature, the equilibrium and dynamic multi-component adsorption behavior is not yet well characterized. In this work, we assumed negligible N_2 adsorption and accounted for a drying step upstream of the TSA that completely removes water vapor. Mass and heat transfer coefficients were assumed to be similar as those reported for fixed beds packed with zeolite particles. As a consequence, the accuracy of the obtained results is limited by the applied assumptions; a refinement thereof will require an extensive characterization of the multi-component adsorption equilibrium and of the mass and heat transfer coefficients. As a next step, alternative process solutions should be investigated to exploit the potential of these materials in a more complete manner. For example, more complex cycle configurations could lead to improvements in the process performance.

The results obtained in this work nevertheless indicate that TSA is a feasible option for post-combustion CO_2 capture. The near future will show if MOF-M materials could actually be used at pilot scale, i.e. if they can be produced in quantities at larger than lab-scale, if they can be pelletized and if they are sufficiently stable, i.e. from a mechanical and chemical point of view. Due to the complexity of the synthesis and its maturity, it is expected that the production of MOF-M would be more expensive than for zeolites. On the other hand, there is a chance that employing MOF-M materials makes a drying step redundant and the moist flue gas could be fed directly to the TSA process, potentially lowering capital and operational costs.

The energetic penalty of TSA processes is still larger as compared to amine-scrubbing processes, however, adsorption processes are not as mature. TSA processes offer heat integration opportunities both internally between heating and cooling steps as well as from low-grade heat sources, potentially lowering the energy penalty. By combining the lessons learned and the ability of material scientists to tailor the materials properties, more specifically the position of the step, these materials could be exploited for a variety of CO_2 separation tasks with varying CO_2 content in the feed.

7 CONCLUSIONS AND OUTLOOK

Temperature swing adsorption (TSA) is considered an interesting alternative to liquid based separation processes for CO_2 capture. In fact the use of solid sorbents avoids environmental issues due to solvent slip or possible degradation. Particularly, adsorbents that can be regenerated at moderate temperatures are attractive because the regeneration can be driven by thermal energy, which could be provided from waste heat or low grade heat sources.

Several features of TSA processes render their design complex: (i) they are non-steady state processes that involve non-linear dynamics; (ii) their operation is determined by many degrees of freedom, including the pressure levels, temperature levels, adsorbent material, column geometry and cycle configuration; (iii) multiple columns operating simultaneously are involved, which allows for interesting opportunities to integrate heat and mass flows between adsorption columns. The aim of this thesis was to develop, validate and apply several modeling-based methods to study TSA processes in a systematic way.

In this chapter, we first present a summary of the most relevant results achieved in this thesis. Next, three critical research challenges that have been identified are considered in more detail: a brief overview of their importance and of the state-of-the-art is given, and preliminary results are presented, were applicable. Finally, a reflection on the applicability and future implementation of TSA processes for the capture of CO_2 is made and conclusions are drawn.

7.1 SUMMARY

A crucial component of model-based process design consists in the calibration and validation of the mathematical model by comparison to experimental results. In chapter 3, a one-dimensional mathematical model previously applied to study PSA processes was calibrated for the sorbent-sorbate system 13X-CO_2/N_2 under conditions relevant to a TSA process. Single column dynamic experiments performed for a range of temperatures from 25 °C to 100 °C and for two superficial velocities were employed for the estimation of heat and mass transfer parameters. The calibrated model was then validated by comparison to cyclic TSA experiments. The good agreement between predicted and measured temperature-, composition- and flow rate profiles and between predicted and experimentally determined overall performance metrics (purity, recovery and productivity) indicate a successful calibration of the model.

Due to the low sensitivity of the breakthrough experiments to the mass transfer coefficients, and the empirical description of the heat transfer resistance, care should be taken when extrapolating the obtained set of transport parameters to significantly different conditions with respect to those considered in chapter 3. Otherwise, alternative experimental procedures should be considered in order to obtain a more accurate and first-principles based description. Nevertheless, the successful experimental validation of the mathematical model for the operation of a TSA cycle at cyclic steady state is a strong argument for using the model in parametric studies to investigate the effect of the many degrees of freedom involved in TSA processes, e.g. the cycle configuration and the step times.

In chapter 4, a shortcut model of a four step TSA cycle was devised. The method of characteristics was applied to obtain a semi-analytical solution of the cyclic steady state by assuming equilibrium between gas and solid phases, negligible pressure drop and an isothermal adsorption step. The developed shortcut model has been validated against detailed simulations. The main discrepancy stems from the description of the adsorption step; in fact, by neglecting heat and mass transfer resistances, the shortcut model overestimates the breakthrough time and does not account for the width of the composition

front. This leads to the overestimation of the achievable purity, recovery, productivity and to the underestimation of the required energy consumption.

Although the shortcut model is not appropriate to obtain quantitative accurate information about the process, it was proven very useful in gaining a thorough understanding of the specific TSA cycle for the recovery of the more retained component. The semi-analytical solution gave insight into the propagation of compositions fronts at cyclic steady state (CSS), which is a pre-requisite for the design of well-conditioned cycles. Moreover, the fast computation of the CSS, i.e., a reduction in computing time by a factor of about 600 as compared to the detailed model, was exploited to perform thorough parametric analysis. The evaluation of the effect of the heating temperature and of the heat transfer resistance demonstrated its utility for the interpretation of detailed simulations, and to obtain relative quantitative data. In fact, relative differences in the achieved productivity and energy consumption upon changes in operating conditions and in the used adsorbent material were shown to be comparable for both shortcut and detailed models.

In chapter 5, a methodology for the design of TSA processes for post-combustion CO_2 capture is presented. The insights gained in chapter 4 were applied to rationally design more elaborate TSA cycles with the aim of enhancing the achievable CO_2 purity and recovery, and of improving the process performance in terms of productivity and energy consumption. The detailed model validated in chapter 3 was used to quantitatively evaluate the performance of these cycles by performing extensive parametric analysis of the operating conditions. Thereby, two main results were achieved.

The effect of the cycle configuration and of the operating conditions, i.e., step types and times, on the key performance indicators was rationalized, and the effect of external components was assessed, e.g. the energy penalty associated to the flue gas drying, the possible heat recovery and the productivity decrease due to idle times. The numerous operating conditions investigated enabled a comprehensive analysis of these effects on the achievable overall process performance, and it was shown that the energy penalty of an additional drying unit should always be accounted for in the calculations of the specific

energy penalty, as it may change for varying operating conditions, and make up for a significant fraction of the overall energy requirement (up to 20%). The potential for heat integration was estimated by considering opportunities both within the cycle, i.e., by coupling two columns subject to a cooling and a heating step, as well as integration with an external heat stream, e.g. the hot flue gas itself.

A specific cycle was selected for a CO_2 capture and storage separation task, and its operating conditions were optimized such as to account for drying of the flue gas, heat integration and an appropriate cycle scheduling. The selected six step cycle shows exceptional performances. In fact, it allows to achieve stringent specifications given as 96% CO_2 purity and 90% CO_2 recovery with heating temperatures below 150 °C and a commercial 13X adsorbent material for the first time. Moreover, the maximum productivity and minimum overall thermal energy consumption of the TSA process considering a standard shell and tube geometry are comparable to commercial amine-based absorption processes. This result is very encouraging for TSA processes, as it is not a mature technology; there remains room for improvement, particularly in the use of columns with intensified heat transfer properties and in the use of materials whose affinity to CO_2 is not reduced in the presence of water.

Reversible step-shaped adsorption isotherms, as those observed for the adsorption of CO_2 onto a class of recently developed materials, is believed to be a novel paradigm in adsorption processes. The potential of these materials has been investigated for their use in a TSA process for post-combustion CO_2 capture in chapter 6 by assessing the performance of five materials exhibiting step-shaped adsorption isotherms with a four step TSA cycle. Optimization of the operating conditions indicate that these materials can be very promising as compared to commercial adsorbents, requiring up to 30% less energy and increasing the achievable productivity twofold. Extensive parametric analysis allowed to identify pivotal features of the step shaped isotherms and to identify design criteria that result in an optimal and robust operation. These features were subsequently confirmed by optimizing the isotherm parameters that govern the position of the step, such as to yield hypothetical materials that maximize productivity and minimize energy consumption. By combining the lessons learned from this

analysis, and the ability of material scientists to tailor the position of the step, these materials could be exploited for a variety of CO_2 separation tasks with varying CO_2 content in the feed.

In the present thesis, some relevant tools for the design and optimization of TSA processes aimed at capturing CO_2 from flue gases of industrial- and power-plants have been developed and applied by focusing on the design of sound and feasible cycle configurations, and on gaining a sound understanding of how different operating modes affect the performance. Ultimately, in order to design a groundbreaking and efficient process, one should consider all the available technology elements (materials, column design, cycle configuration, heat integration, etc.), select the optimal constellation by exploiting synergies, and optimize the operating conditions.

7.2 RESEARCH CHALLENGES

7.2.1 Rigorous optimization of temperature swing adsorption cycles[1]

In chapter 5, we showed that in order to make full use of the TSA advantages, there is the need to optimize the process systematically. While optimal conditions can be identified using extensive parametric analysis, as was performed in this thesis, a more sophisticated optimization algorithm could potentially save significant computational time.

There exist different approaches to tackle the optimization of cyclic adsorption processes. Convergence may be accelerated by using an equation-oriented approach, as proposed by Nilchan and Pantelides[156]. This approach relies on the full discretization of the model equations to obtain large optimization problems involving several tens of thousands equations typically solved with a standard nonlinear equation solver. This approach is efficient for simple models, however, the

1. The method presented in this section was devised in collaboration with Emanuele Martelli, Politecnico di Milano, and the results have been presented in Joss, L.; Capra, F.; Gazzani, M.; Mazzotti, M.; Martelli, E. MO-MCS: An Efficient Multi-objective Optimization Algorithm for the Optimization of Temperature/Pressure Swing Adsorption Cycles. *Comput. Aided Chem. Eng.* **2016**, *38*, 1467–1472.

solver may fail due to error accumulation induced by the complete discretization,[157] or because of steep fronts.[30] In order to avoid these issues, Jiang et al.[30] proposed a simultaneous tailored approach, that uses an *ad hoc* solver for the column model, but still achieves faster convergence by enforcing the CCS condition as a constraint on the optimization problem. This way, convergence to the optimum and to the CSS is achieved simultaneously, thereby reducing computational time. However, this implies that the initial conditions of the column are treated as decision variables, making the size of the optimization problem much larger (more than 300 decision variables for a binary separation and discretization in 50 grid points) and requiring gradient-based, hence local, optimization algorithms. Due to the nonlinear and non-convex nature of the objectives and constraints, there is the risk of not finding a feasible solution or of finding a local minimum. To avoid such risks, the less efficient, but more robust black-box approach integrated with a global optimization algorithm is often preferred.

Most of the studies adopting the black-box approach use multi-objective genetic algorithms[23,33] without considering potentially more efficient approaches, such as model-based derivative-free algorithms, which use a local model of the black-box function so as to save computationally expensive evaluations. Preliminary work carried out in collaboration with Emanuele Martelli, Politecnico di Milano, has focused on the use of an alternative multi-objective optimization method based on a revised version of the multi-level coordinate search (MCS) algorithm of Huyer and Neumaier[149] for the optimization of TSA cycles.

MO-MCS OPTIMIZATION ALGORITHM FOR TSA CYCLES The optimization problem of interest is defined as follows:

$$\begin{aligned} \underset{\boldsymbol{x}}{\text{minimize}} \quad & (e_{\text{th}}(\boldsymbol{x}), -\text{Pr}(\boldsymbol{x})) \\ \text{subject to} \quad & r(\boldsymbol{x}) \geq r_{\text{min}}, \\ & \Phi(\boldsymbol{x}) \geq \Phi_{\text{min}}, \\ & \boldsymbol{u} \leq \boldsymbol{x} \leq \boldsymbol{v}. \end{aligned} \tag{7.1}$$

Where e_{th} is the specific energy consumption of the process, Pr its productivity, r_{min} and Φ_{min} are the specifications on the recovery and

purity of the CO_2 product, respectively. The decision variables $\boldsymbol{x}$ are the cycle step times of a given cycle. The specific energy consumption, productivity, recovery and purity are determined by a simulator which solves the material and energy mass balances for each cycle step sequentially for as many cycles as is required to reach a cyclic steady state.

In a recent review by Rios and Sahinidis[158], the MCS algorithm was identified as one of the most promising non-commercial derivative-free algorithms for non-convex, bounded, and low-dimensional (less than 7 variables) problems. MCS proceeds by dividing the search space into boxes. Each box is assigned a level that is an increasing function of the number of times the box has been processed. At each iteration, MCS selects boxes with the lowest objective value for each level and marks them as candidates for splitting. A local search based on a quadratic model is performed on the boxes which have reached a maximum level of splitting. In this work we have extended MCS to specifically solve Problem 7.1 by making the following *ad hoc* modifications: (i) transformation of the multi-objective problem into a sequence of single-objective problems with the normalized normal constraint (NNC) method,[159] (ii) introduction of an adaptive penalty strategy to handle non-linear relaxable constraints, (iii) parallelization of the single objective optimization problems, (iv) use of a memory structure to save black-box function evaluations. Several methods to transform a multi-objective problem into a sequence of single objective problems exist. Normalized normal constraint is of particular interest, as it can handle non-convex Pareto frontiers and yield well-distributed points.[160] On the other hand, it requires a priori knowledge of the extreme points of the Pareto. Figure 7.1 shows the resulting block-flow scheme for the overall multiobjective multi-level coordinate search (MO-MCS) algorithm. First, two single objective optimizations with respect to energy consumption and productivity are carried out in parallel to identify the extreme points of the Pareto frontier (maximum productivity at $\boldsymbol{x}_1^*$ and minimum energy consumption at $\boldsymbol{x}_2^*$). Next, a user-specified number N_P of intermediate Pareto-optimal points

are determined by solving a set of N_P nonlinear constrained single-objective optimization problems:

$$
\begin{aligned}
&\underset{x}{\text{minimize}} && \bar{e}_{\text{th}}(\boldsymbol{x}) \\
&\text{subject to} && \\
&g_1(\boldsymbol{x}): && r_{\min} - r(\boldsymbol{x}) \leq 0, \\
&g_2(\boldsymbol{x}): && \Phi_{\min} - \Phi(\boldsymbol{x}) \leq 0, \\
&h(\boldsymbol{x}, \alpha_i): && \boldsymbol{U}\left(-\overline{\text{Pr}}(\boldsymbol{x}); \bar{e}_{\text{th}}(\boldsymbol{x})\right) - \alpha_i \left(-\overline{\text{Pr}}(\boldsymbol{x_1^*}); \bar{e}_{\text{th}}(\boldsymbol{x_1^*})\right) + \\
& && + (1-\alpha_i)\left(-\overline{\text{Pr}}(\boldsymbol{x_2^*}); \bar{e}_{\text{th}}(\boldsymbol{x_2^*})\right) \leq 0, \\
&\mathbf{u} \leq \boldsymbol{x} \leq \boldsymbol{v}. && \qquad i = 1, \ldots, N_P
\end{aligned}
\tag{7.2}
$$

where $\bar{e}_{\text{th}}$ and $\overline{\text{Pr}}$ are the objectives normalized with respect to the extreme points of the Pareto frontier, $\boldsymbol{U}$ is the utopia line vector connecting the single objective optima and $0 < \alpha_i < 1$ is a parameter which determines the position of the normal constraint in the objective space. The Pareto frontier is resolved by solving N_P problems with different values of α_i. In order to handle the nonlinear relaxable constraints of problems 7.2, a quadratic penalty approach has been adopted converting the constrained problem into a sequence of bound-constrained problems whose objective function is the sum of the specific energy consumption and a penalty parameter multiplied by the square of the constraint violation value. Then, for each value of α_i, a sequence of bound-constrained single-objective problems, corresponding to increasing values of the penalty parameter, is solved to optimality with the MCS algorithm. If the solution of a bound-constrained problem does not violate any constraints, it is a Pareto-optimal point of problem 7.2, otherwise the penalty parameter is increased (multiplied by 1.5) and a bound-constrained problem with higher penalty is optimized. This approach, typically adopted for gradient-based algorithms, may appear suboptimal when dealing with computationally expensive black-box functions as the MCS search algorithm is repeated several times. To this end, an efficient memory structure has been developed which allows a significant reduction of the number of black-box evaluations. The key observation which motivated the use of a memory structure is that increasing the penalty parameters of the bound-constrained single-objective problems does not considerably alter the shape of the objective function. Since MCS

is a deterministic algorithm, it is highly likely that for each bound-constrained problem generated by the adaptive penalty approach, the MCS algorithm samples the same points, especially in the global search iterations. Also at the level of the NNC approach there is a considerable overlap of MCS sampling points since the small increment of the parameter α_i necessary to discretize the Pareto frontier leads to small changes of the single-objective optimization problems 7.2. For these two reasons, memorizing all the sampled points leads to an effective reduction of number of black-box evaluations with an associated saving of computational time. The memory structure is also used to determine an advantageous initial state of the column for the cyclic simulations. In order to take advantage of multiple-core computers, single-objective optimization problems corresponding to different values of α_i can be solved in parallel, as indicated in Figure 7.1 for three cores. To avoid overwriting issues, each core has a dedicated memory partition but, to maximize the information exchange, the different cores read data from all the partitions.

CASE STUDY AND ASSESSMENT METRICS The well-studied five step cycle B presented in chapter 5 is considered for a CO_2 capture and utilization (CCU) application, i.e., the step times are optimized to maximize the productivity and minimize the energy consumption, subject to minimum separation specifications of 90% CO_2 purity and 30% CO_2 recovery. Note that for this case study, both drying and scheduling are not accounted for. This case study is used as benchmark to test the proposed algorithm: the results are compared to four different multi-objective optimization algorithms for which a Matlab implementation is available, i.e., direct multi-search (DMS), simulated annealing (SA), particle swarm (MOPSO) and the non-sorting genetic algorithm (NSGA). The comparison is assessed based on the obtained Pareto frontiers in terms of optimality, equidistribution and extent by using the indices suggested by Zitzler et al.[161]:

$$M_1 = \frac{1}{N_X} \sum_{\boldsymbol{a} \in X} \min\{\|\boldsymbol{a} - \boldsymbol{a}^*\|; \boldsymbol{a}^* \in X^*\} \tag{7.3}$$

$$M_2 = \frac{1}{N_X - 1} \sum_{\boldsymbol{a} \in X} |\{\boldsymbol{b} \in X; \|\boldsymbol{a} - \boldsymbol{b}\| > \sigma\}| \tag{7.4}$$

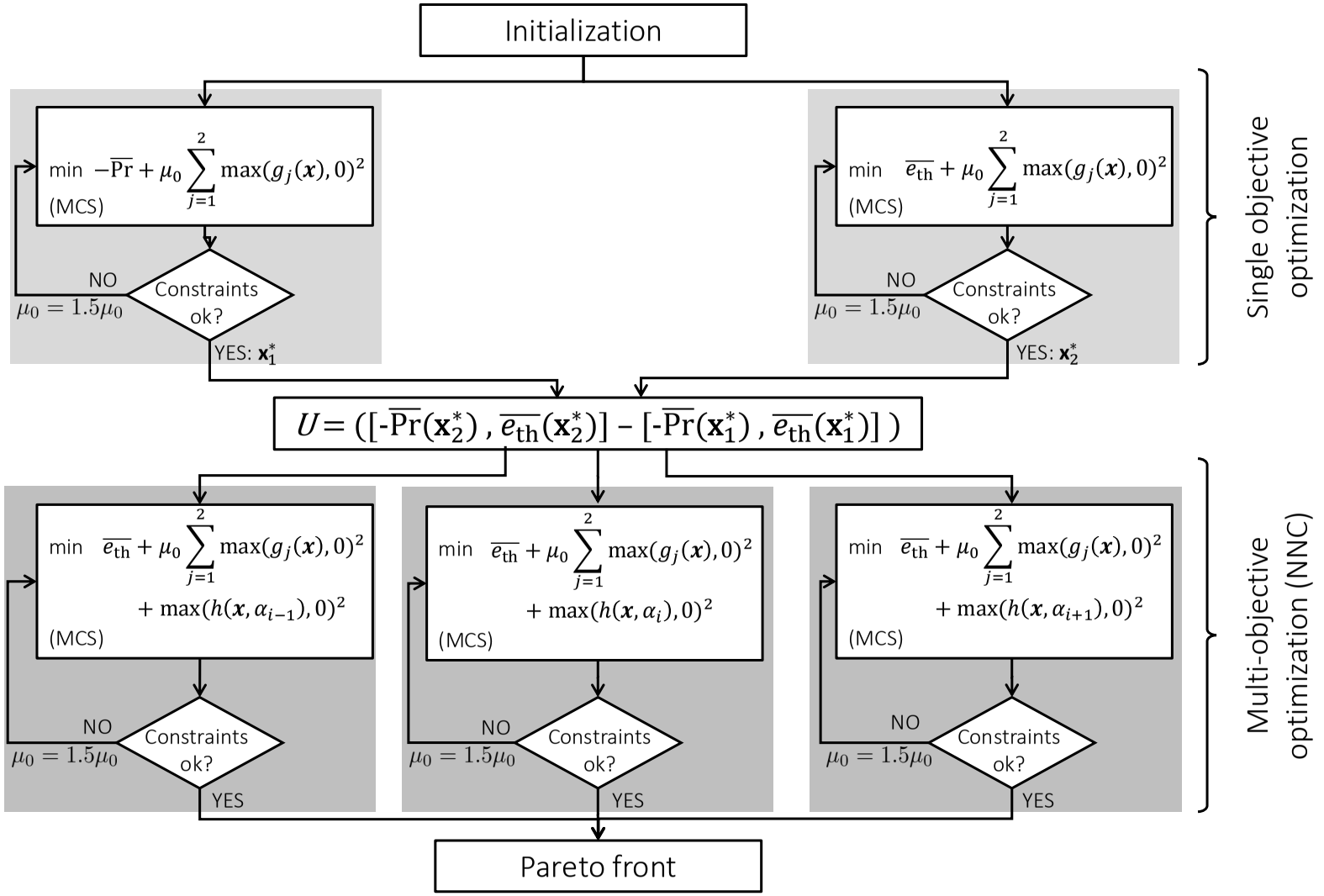

Figure 7.1. – Scheme of the MO-MCS algorithm. Exemplary parallelization with three cores, where α_{i-1}, α_i and α_{i+1} are distinct values between 0 and 1.

$$M_3 = \sqrt{\sum_{i=1}^{N_X} \max\{\|a_i - b_i\|; \boldsymbol{a}, \boldsymbol{b}, \in X\}} \tag{7.5}$$

where X is the Pareto vector obtained from an algorithm, N_X is the number of points of the Pareto set, X^* is the *best* Pareto estimated by combining all the known points from the different runs, $\sigma > 0$ is a neighborhood parameter and $\|\cdot\|$ is a distance metric, taken here as the phenotypic distance between two points, i.e., the sum of the absolute distance between two points in all dimensions. Note that these indices are calculated by considering the Pareto sets taken after a maximum of 3000 function calls in order to make a fair comparison.

RESULTS AND DISCUSSION Problem 7.1 was solved by the suggested MO-MCS algorithm for the application presented in section 7.2.1. The Pareto frontiers obtained are shown in Figure 7.2(a). The benefit of the memory structure is confirmed by its considerable use, i.e., the simulator was run for only 50–65% of the function calls. Moreover, the parallelization allows for a substantial decrease in computation time, to the point that on a 3.4 GHz computer 50 min were required to obtain the Pareto frontier of the five step cycle using three cores, as opposed to 120 min required in sequential computation. The results of the five step cycle are compared to four different multi-objective algorithms for which a Matlab implementation is available, i.e., direct multi search (DMS), simulated annealing (SA), particle swarm (MOPSO) and non-sorting genetic algorithm (NSGA).

It is clear from the obtained Pareto sets shown in Figure 7.2 and from the indices listed in Table 7.1 that MO-MCS yields the best Pareto in terms of optimality and extent. Although the Pareto points are well distributed, the equidistribution coefficient (M_2) is the lowest due to the limited number of Pareto points. The improvement in terms of CPU time is particularly striking as compared to the extensive parametric analysis carried out in chapter 5, with a reduction by more than a factor 20.

As compared to evolutionary multi-objective algorithms, the proposed MO-MCS algorithm determines a Pareto frontier with fewer points, but with a larger extent, more accurate solutions and considerably less computation time. These preliminary results suggest that

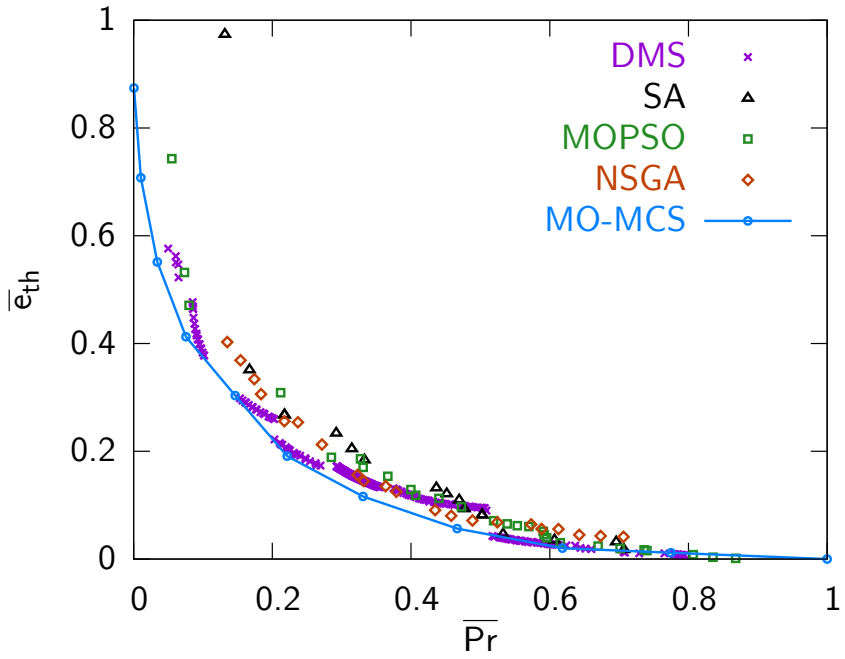

Figure 7.2. – Pareto frontiers in the normalized plane obtained from different algorithms for the five step cycle (cycle B) for the specifications given as 90% purity and 30% recovery.

MO-MCS might be an efficient tool for the optimization of operating conditions of TSA processes, however, the performance of this algorithm was observed to strongly depend on the chosen penalty factor for the non-linear constraints, and more extensive testing is required.

Table 7.1. – Comparison of the MO-MCS algorithm to different derivative-free multi-objective algorithms for the five step cycle, and to the results obtained from the parametric analysis performed in chapter 5. Indexes calculated as suggested by Zitzler et al.[161]

Algorithm	CPU time (min)	Optimality (M_1)	Equidistribution (M_2)	Extent (M_3)
MO-MCS	50	5.6×10^{-4}	11	1.4
DMS	130	1.3×10^{-2}	227	1.1
MOPSO	122	3.1×10^{-2}	25	1.2
SA	135	4.7×10^{-2}	13	1.2
NSGA	130	3.3×10^{-2}	19	1.0
parametric	1160	2.2×10^{-2}	31	1.3

7.2.2 Heat integration of temperature swing adsorption cycles

Indirectly heated temperature swing adsorption (TSA) processes involve multiple columns undergoing heating and cooling steps in a cyclic way, and appropriately shifted in time. Due to the rather long heating and cooling times, typical cycle schedules are such that several columns are being heated and cooled simultaneously, hence different temperature levels coexist. Such an operation could strongly benefit from a well-designed heat integration of the thermostatting fluid. In chapter 5, two strategies for heat recovery were identified, and preliminary calculations were performed:

- Internal heat recovery: Every column will cycle through a series of steps, which involve at least one heating step and one cooling step. Simultaneous start of a heating step and of a cooling step can be enforced in the cycle schedule, such that it is reasonable to recycle the heat from a hot column being cooled to a cold column being heated.
- Heat recovery from a low-grade heat stream: Whenever a continuous low-grade heat stream is present, heat could theoretically be efficiently recovered by contacting the hot stream with the warmest column first, then with the second warmest, and so on.

In the present thesis, the potential for both heat recovery strategies was determined in a rather simplistic way, i.e., internal heat recovery was estimated by accounting for the heat that could be exchanged between two columns until the column being cooled has a temperature in excess of 30 K as compared to the column being heated. The energy recovery from the hot flue gas was simply estimated by accounting for the heat it releases upon a decrease in temperature of 100 °C. While the applied estimates are rather simplistic, they suggest that heat integration could play a considerable role in reducing the energy penalty (about 12% reduction). A more accurate estimation of the true potential for heat recovery should, however, use a more sophisticated approach.

Although pinch analysis is most often applied to continuous processes, with suitable modifications it can also be applied to batch or cyclic processes such as TSA. Standard pinch analysis tools for batch

systems consist in the time average model, and the times slice model. In the former case, time constraints are neglected, and it is assumed that heat can be exchanged between all the streams; this model is used to estimate the maximum possible heat exchange. On the other hand, the time slice model accounts for the effect of time by splitting the process into time intervals. During each interval, every stream is assumed to have constant properties (temperature and heat flow), such that the standard techniques for continuous processes can be applied.

The heat integration possibilities could be estimated by extending the TSA model with a systematic pinch analysis applied to a certain cycle schedule. For each time slice, all the columns can be represented as virtual streams, either sources or sinks, existing in that specific time slice only and with a given heat load. Such an analysis should be able to quantify the reduction in energy penalty more accurately, and it should also reveal how to optimally couple the two strategies that have been identified, and how the extent of heat recovery depends on the chosen schedule and number of columns.

7.2.3 Measuring and describing mass transfer resistances in porous adsorbents

In chapter 3, lumped mass transfer coefficients were estimated from breakthrough experiments. Thereby several issues were encountered such that only an approximate mass transfer coefficient could be determined, which can hardly be extrapolated to different conditions. Nevertheless, mastering the art of measuring and describing mass transfer resistances in porous adsorbents accurately is a crucial element to obtain reliable predictive simulations. Being able to predict the overall mass transfer coefficient becomes especially important when considering multi-component mixtures, where the position and width of several fronts must be accurately controlled with respect to the position of adsorbent layers within a fixed bed in order to ensure the required process performance. However, a purely empirical description would require many experiments in order to obtain an accurate characterization valid over the relevant range of temperature, pressure, and composition. A more fundamental understanding of

the underlying mechanisms that control transport of multi-component mixtures in porous adsorbent beds could result in a first-principles predictive description.

The intrinsic adsorption rates are very fast, such that the overall uptake rate is usually controlled by diffusional resistances of the sorbate to the adsorption sites. The most important resistances that can be encountered are: (i) diffusion through the macropores of the formulated particles, (ii) diffusion through the intracrystalline micropores, (iii) surface barriers. While macropore diffusion is rather well understood,[76] micropore and surface resistances remain the topics of ongoing research. There exist several sophisticated microscopic tools to selectively study these phenomena at the single crystal or even subcrystal scale, such as pulsed-field gradient NMR, inference microscopy or quasi-elastic neutron scattering.[162] Although single crystal experiments are very valuable to obtain a truly fundamental understanding of the diffusive transport, a multitude of crystals are contained within each single adsorbent particle of a packed bed. Variation amongst crystals, e.g. in size, shape and surface defects, are such that single crystal measurements will most probably not reflect the macroscopic behavior, unless a significant number of experiments are considered.

It is therefore of merit to consider macroscopic experimental procedures that reduce heat effects and allow to identify both micropore and macropore resistances for bi-disperse particles. Zero length column (ZLC) experiments and frequency response experiments (FR) both constitute established experimental procedures that allow to determine the rate-limiting resistance and to estimate the corresponding transport diffusivity. Coupling of such experiments to a thermodynamically sound theoretical framework for the description of multi-component transport could ultimately allow identifing conditions for which a lumped mass transfer coefficient is sufficient for the description of a cyclic separation process, and obtain a relation between adsorbate/adsorbent properties and the mass transfer coefficient.

7.3 CONCLUSIONS AND OUTLOOK

In order to satisfy the 2 °C target,[3] the energy mix for power generation of the future will require a combination of the possible and available low-carbon energy supply technologies. Among these, CCS will most probably play an important role to enable a sustainable use of fossil fuels and to support the transition to renewable energy sources.[4,5] In my opinion, it is worthwhile to develop several solutions throughout the CCS value chain in order to make its implementation at the industrial scale a reality. This thesis has focused on the use of TSA processes for post-combustion capture of CO_2 from flue gases, and it has been shown that these processes can indeed be used to carry out the desired separation using state-of-the-art technology, i.e., a commercial zeolitic adsorbent material and columns of the shell and tube type.

The capture of CO_2 by adsorption is not yet a mature technology, and improvements with respect to the results obtained in this thesis could be achieved via the use of novel adsorbent materials, columns with intensified heat transport properties, and cycle configurations with an increased level of heat integration. Nonetheless, the obtained results give the basis for the design and implementation of a capture process based on solid materials that requires mostly thermal energy. In principle the next steps towards industrial implementation could now be undertaken: (i) the demonstration of the technology by scale-up to a pilot unit, including the validation the predictive capability of a one-dimensional model for scale-up; (ii) the quantification of the process costs, including both operational (OPEX) and capital (CAPEX) expenditures; and (iii) the assessment of the environmental sustainability of the process through a comprehensive life-cycle assessment of the direct emissions, the indirects emissions and the operational risks.

By undertaking these three activities to complement the work carried out in this thesis, it is expected that a more comprehensive evaluation of the potential of TSA processes as compared to other current and future technologies for the capture of CO_2 will be achieved.

BIBLIOGRAPHY

(1) Conference of the Parties (COP), U. Adoption of the Paris Agreement Proposal by the President., 2015 (cit. on p. 1).

(2) Tollefson, J.; Weiss, K. R. Nations approve historic global climate accord. *Nature* **2015**, *528*, 315–316 (cit. on p. 1).

(3) IPCC, *Climate Change 2014: Synthesis Report. Contribution of Working Groups I, II and III to the Fifth Assessment Report of the Intergovernmental Panel on Climate Change*; Pachauri, R. K., Meyers, L., Eds.; IPCC: 2014 (cit. on pp. 1, 175).

(4) Rogelj, J.; McCollum, D. L.; Reisinger, A.; Meinhausen, M.; Riahi, K. Probabilistic cost estimates for climate change mitigation. *Nature* **2013**, *493*, 79–83 (cit. on pp. 2, 175).

(5) Bruckner, T. Decarbonizing the Global Energy System: An Updated Summary of the IPCC Report on Mitigating Climate Change. *Energy Technol.* **2016**, *4*, 19–30 (cit. on pp. 2, 175).

(6) Wilcox, J.; Haghpanah, R.; Rupp, E. C.; He, J.; Lee, K. Advancing Adsorption and Membrane Separation Processes for the Gigaton Carbon Capture Challenge. *Annu. Rev. Chem. Biomol. Eng.* **2014**, *5*, 479–505 (cit. on pp. 2, 50).

(7) Reynolds, A. J.; Verheyen, T. V.; Adeloju, S. B.; Meuleman, E.; Feron, P. Towards commercial scale postcombustion capture of CO_2 with monoethanolamine solvent: Key considerations for solvent management and environmental impacts. *Environ. Sci. Technol.* **2012**, *46*, 3643–3654 (cit. on p. 2).

(8) Da Silva, E. F.; Booth, A. M. Emissions from postcombustion CO_2 capture plants. *Environ. Sci. Technol.* **2013**, *47*, 659–660 (cit. on p. 2).

(9) Figueroa, J.; Fout, T.; Plasynski, S.; Mcilvried, H.; Srivastava, R. Advances in CO_2 capture technology—The U.S. Department of Energy's Carbon Sequestration Program. *Int. J. Greenh. Gas Control* **2008**, *2*, 9–20 (cit. on p. 2).

(10) D'Alessandro, D. M.; Smit, B.; Long, J. R. Carbon dioxide capture: Prospects for new materials. *Angew. Chemie - Int. Ed.* **2010**, *49*, 6058–6082 (cit. on pp. 2, 84).

(11) Internation Energy Agency (IEA) *IEA Statistics: CO_2 Emissions From Fuel Combustion: Highlights*; tech. rep.; Paris, France: IEA, 2015 (cit. on p. 2).

(12) Filippi, E.; Zardi, F. Process for the preparation and recovery of carbon dioxide from waste gas or fumes produced by combustible oxidation. *U.S. Pat.* **2006**, 7,153,344 (cit. on pp. 3, 110).

(13) Thomas, J. M. The existence of endothermic adsorption. *J. Chem. Educ.* **1961**, *38*, 138–139 (cit. on p. 3).

(14) Skarstrom, C. W. Method and apparatus for fractionating gas mixtures by adsorption. *U.S. Pat.* **1960**, 2,944,627 (cit. on pp. 5, 84).

(15) Voss, C. Applications of Pressure Swing Adsorption Technology. *Adsorption* **2005**, *11*, 527–529 (cit. on pp. 5, 49).

(16) Ahn, H.; Lee, C.-H. Adsorption dynamics of water in layered bed for air-drying TSA process. *AIChE J.* **2003**, *49*, 1601–1609 (cit. on pp. 6, 49).

(17) Nastaj, J.; Ambrożek, B.; Ambrożek, B. Modeling of Drying of Gases Using Solid Desiccants. *Dry. Technol.* **2009**, *27*, 1344–1352 (cit. on pp. 6, 49).

(18) Bart, H.-J.; Gemmingen, U. In *Ullmann's Encycl. Ind. Chem.* VCH Publishers Inc.: 1988; Chapter Adsorption (cit. on p. 6).

(19) Diagne, D.; Goto, M. New PSA process with intermediate feed inlet position operated with dual refluxes: application to carbon dioxide removal and enrichment. *J. Chem. Eng. Japan* **1994**, *27*, 85–89 (cit. on p. 6).

(20) Diagne, D.; Goto, M.; Hirose, T. Parametric studies on CO_2 separation and recovery by a dual reflux PSA process consisting of both rectifying and stripping sections. *Ind. Eng. Chem. Res.* **1995**, *34*, 3083–3089 (cit. on p. 6).

(21) Ebner, A. D.; Ritter, J. A. Equilibrium theory analysis of rectifying PSA for heavy component production. *AIChE J.* **2002**, *48*, 1679–1691 (cit. on pp. 6, 10, 50).

(22) Reynolds, S. P.; Mehrotra, A.; Ebner, A. D.; Ritter, J. a. Heavy reflux PSA cycles for CO_2 recovery from flue gas: Part I. Performance evaluation. *Adsorption* **2008**, *14*, 399–413 (cit. on pp. 7, 8, 78, 84, 93).

(23) Haghpanah, R.; Nilam, R.; Rajendran, A.; Farooq, S.; Karimi, I. A. Cycle synthesis and optimization of a VSA process for post combustion CO_2 capture. *AIChE J.* **2013**, *59*, 4735–4748 (cit. on pp. 7, 84, 164).

(24) Casas, N.; Schell, J.; Joss, L.; Mazzotti, M. A parametric study of a PSA process for pre-combustion CO_2 capture. *Sep. Purif. Technol.* **2013**, *104*, 183–192 (cit. on pp. 7, 8, 25, 26, 52, 67, 75, 84, 86, 87, 129, 227–234, 251).

(25) Wang, L.; Liu, Z.; Li, P.; Yu, J.; Rodrigues, A. E. Experimental and modeling investigation on post-combustion carbon dioxide capture using zeolite 13X-APG by hybrid VTSA process. *Chem. Eng. J.* **2012**, *197*, 151–161 (cit. on pp. 7, 13, 88).

(26) Xiao, G.; Xiao, P.; Lee, S.; Webley, P. A. CO_2 capture at elevated temperatures by cyclic adsorption processes. *RSC Adv.* **2012**, *2*, 5291 (cit. on p. 7).

(27) Agarwal, A.; Biegler, T.; Zitney, S. A Superstructure-Based Optimal Synthesis of PSA Cycles for Post-Combustion CO_2 Capture. *AIChE J.* **2010**, *7*, 1813–1828 (cit. on pp. 7, 8).

(28) Dowling, A. W.; Sree, V. R. R.; Biegler, L. T. Large-Scale Optimization Strategies for Pressure Swing Adsorption Cycle Synthesis. *AIChE J.* **2012**, *58*, 3777–3791 (cit. on pp. 7, 84).

(29) Haghpanah, R. et al. Multiobjective Optimization of a Four-Step Adsorption Process for Postcombustion CO_2 Capture Via Finite Volume Simulation. *Ind. Eng. Chem. Res.* **2013**, *52*, 4249–4265 (cit. on pp. 8, 9, 23, 50, 84).

(30) Jiang, L.; Biegler, L. T.; Fox, V. G. Simulation and optimization of pressure-swing adsorption systems for air separation. *AIChE J.* **2003**, *49*, 1140–1157 (cit. on pp. 9, 164).

(31) Ko, D.; Moon, I. Multiobjective Optimization of Cyclic Adsorption Processes. *Ind. Eng. Chem. Res.* **2002**, *41*, 93–104 (cit. on pp. 9, 109).

(32) Hasan, F.; Baliban, R. C.; Elia, J. A.; Floudas, C. A. Modeling, Simulation, and Optimization of Postcombustion CO_2 Capture for Variable Feed Concentration and Flow Rate. 2. Pressure Swing Adsorption and Vacuum Swing Adsorption Processes. *Ind. Eng. Chem. Res.* **2012**, *51*, 15665–15682 (cit. on pp. 9, 84).

(33) Beck, J.; Friedrich, D.; Brandani, S.; Fraga, E. S. Multi-Objective Optimisation using Surrogate Models for the Design of VPSA Systems. *Comput. Chem. Eng.* **2015**, *82*, 318–329 (cit. on pp. 9, 164).

(34) Deb, K., *Multi-Objective Optimization using Evolutionary Algorithms*; John WIley & Sons, Inc.: New York, NY, 2001 (cit. on p. 9).

(35) Boukouvala, F.; Hasan, M. M. F.; Floudas, C. A. Global optimization of general constrained grey-box models: new method and its application to constrained PDEs for pressure swing adsorption. *J. Glob. Optim.* **2015**, DOI: 10.1007/s10898-015-0376-2 (cit. on p. 9).

(36) Nikolaidis, G. N.; Kikkinides, E. S.; Georgiadis, M. C. Model-Based Approach for the Evaluation of Materials and Processes for Post-Combustion Carbon Dioxide Capture from Flue Gas by PSA/VSA Processes. *Ind. Eng. Chem. Res.* **2016**, acs.iecr.5b02845 (cit. on p. 9).

(37) Riboldi, L.; Bolland, O. Evaluating Pressure Swing Adsorption as a CO_2 separation technique in coal-fired power plants. *Int. J. Greenh. Gas Control* **2015**, *39*, 1–16 (cit. on p. 10).

(38) Konduru, N.; Lindner, P.; Assaf-anid, N. N. M. Curbing the Greenhouse Effect by Carbon Dioxide Adsorption with Zeolite 13X. *AIChE J.* **2007**, *53*, 3137–3143 (cit. on pp. 10, 84).

(39) Tlili, N.; Grévillot, G.; Vallières, C. Carbon dioxide capture and recovery by means of TSA and/or VSA. *Int. J. Greenh. Gas Control* **2009**, *3*, 519–527 (cit. on p. 10).

(40) Wilmer, C. E.; Farha, O. K.; Bae, Y.-S.; Hupp, J. T.; Snurr, R. Q. Structure–property relationships of porous materials for carbon dioxide separation and capture. *Energy Environ. Sci.* **2012**, *5*, 9849 (cit. on p. 11).

(41) Li, Z.; Xiao, G.; Yang, Q.; Xiao, Y.; Zhong, C. Computational exploration of metal–organic frameworks for CO_2/CH_4 separation via temperature swing adsorption. *Chem. Eng. Sci.* **2014**, *120*, 59–66 (cit. on pp. 11, 79).

(42) Lin, L.-C. et al. In silico screening of carbon-capture materials. *Nat. Mater.* **2012**, *11*, 633–41 (cit. on pp. 11, 51, 79).

(43) Sjostrom, S.; Krutka, H. Evaluation of solid sorbents as a retrofit technology for CO_2 capture. *Fuel* **2010**, *89*, 1298–1306 (cit. on p. 11).

(44) McDonald, T. M. et al. Cooperative insertion of CO_2 in diamine-appended metal-organic frameworks. *Nature* **2015**, *519*, 303–308 (cit. on pp. 11, 83, 119, 122–126, 133, 135, 137, 152).

(45) Mason, J. A. et al. Application of a High-Throughput Analyzer in Evaluating Solid Adsorbents for Post-Combustion Carbon Capture via Multicomponent Adsorption of CO_2, N_2, and H_2O. *J. Am. Chem. Soc.* **2015**, 150406124538003 (cit. on pp. 11, 122, 132).

(46) Vlaisavljevich, B. et al. CO_2 induced phase transitions in diamine-appended metal organic frameworks. *Chem. Sci.* **2015**, DOI: 10.1039/C5SC01828E (cit. on p. 11).

(47) Mérel, J.; Clausse, M.; Meunier, F. Carbon dioxide capture by indirect thermal swing adsorption using 13X zeolite. *Environ. Prog.* **2006**, *25*, 327–333 (cit. on pp. 11, 49).

(48) Clausse, M.; Merel, J.; Meunier, F.; Mérel, J. Numerical parametric study on CO_2 capture by indirect thermal swing adsorption. *Int. J. Greenh. Gas Control* **2011**, *5*, 1206–1213 (cit. on pp. 11, 13, 19, 51, 62, 78, 84, 109).

(49) Rezaei, F. et al. Modeling of rapid temperature swing adsorption using hollow fiber sorbents. *Chem. Eng. Sci.* **2014**, *113*, 62–76 (cit. on pp. 11, 13, 84, 119).

(50) Ko, D.; Kim, M.; Moon, I.; Choi, D.-k. Novel Thermal Swing Adsorption Process with a Cooling Jacket for Benzene–Toluene–p-Xylene Purification. *Ind. Eng. Chem. Res.* **2001**, *40*, 4973–4982 (cit. on p. 12).

(51) Bonjour, J.; Chalfen, J.-B.; Meunier, F. Temperature Swing Adsorption Process with Indirect Cooling and Heating. *Ind. Eng. Chem. Res.* **2002**, *41*, 5802–5811 (cit. on pp. 12, 51).

(52) Walton, K. S.; LeVan, M. D. A Novel Adsorption Cycle for CO_2 Recovery: Experimental and Theoretical investigations of a Temperture Swing Compression Process. *Sep. Sci. Technol.* **2006**, *41*, 485–500 (cit. on pp. 12, 92).

(53) Grande, C. A.; Ribeiro, R.; Rodrigues, A. E. Challenges of electric swing adsorption for CO_2 capture. *ChemSusChem* **2010**, *3*, 892–8 (cit. on p. 12).

(54) Ntiamoah, A.; Ling, J.; Xiao, P.; Webley, P. A.; Zhai, Y. CO_2 Capture by Temperature Swing Adsorption: Use of hot CO_2-Rich Gas for Regeneration. *Ind. Eng. Chem. Res.* **2015**, acs.iecr.5b01384 (cit. on pp. 12, 13, 19, 84, 109).

(55) Mérel, J. et al. Experimental Investigation on CO_2 Post-Combustion Capture by Indirect Thermal Swing Adsorption Using 13X and 5A Zeolites. *Ind. Eng. Chem. Res.* **2008**, *47*, 209–215 (cit. on pp. 13, 121).

(56) Plaza, M. G.; García, S.; Rubiera, F.; Pis, J.; Pevida, C. Post-combustion CO_2 capture with a commercial activated carbon: Comparison of different regeneration strategies. *Chem. Eng. J.* **2010**, *163*, 41–47 (cit. on pp. 13, 109).

(57) Thiruvenkatachari, R.; Su, S.; Yu, X. X.; Bae, J.-S. Application of carbon fibre composites to CO_2 capture from flue gas. *Int. J. Greenh. Gas Control* **2013**, *13*, 191–200 (cit. on p. 13).

(58) Liu, Z. et al. Zeolite Apgiia for Adsorption Based Carbon Dioxide Capture. *Sep. Purif. Technol.* **2013**, *48*, 388–402 (cit. on pp. 13, 19, 51, 78, 84, 109).

(59) Rajagopalan, A. K.; Avila, A. M.; Rajendran, A. Do adsorbent screening metrics predict process performance? A process optimisation based study for post-combustion capture of CO_2. *Int. J. Greenh. Gas Control* **2016**, *46*, 76–85 (cit. on p. 12).

(60) Marx, D.; Joss, L.; Hefti, M.; Gazzani, M.; Mazzotti, M. CO_2 Capture from a Binary CO_2/N_2 and a Ternary $CO_2/N_2/H_2$ Mixture by PSA: Experiments and Predictions. *Ind. Eng. Chem. Res.* **2015**, *54*, 6035–6045 (cit. on pp. 15, 19, 86, 88, 250).

(61) Joss, L.; Gazzani, M.; Hefti, M.; Marx, D.; Mazzotti, M. Temperature Swing Adsorption for the Recovery of the Heavy Component: An Equilibrium-Based Shortcut Model. *Ind. Eng. Chem. Res.* **2015**, *54*, 3027–3038 (cit. on pp. 15, 49, 91, 123, 129, 144, 147, 250).

(62) Joss, L.; Gazzani, M.; Mazzotti, M. Rational Design of Temperature Swing Adsorption Cycles for Post-Combustion CO_2 Capture. *Chem. Eng. Sci.* **2016**, *under review* (cit. on pp. 15, 83, 250).

(63) Joss, L.; Hefti, M.; Bjelobrk, Z.; Mazzotti, M. Investigating the potential of phase-change materials for CO_2 capture. *Faraday Disc.* **2016**, DOI: 10.1039/C6FD00040A (cit. on pp. 15, 121, 136, 250).

(64) Joss, L.; Gazzani, M.; Zanco, S.; Mazzotti, M. A six step temperature swing adsorption process for for the recovery of CO_2 at high purity. *Patent filed May 25th* **2016** (cit. on pp. 15, 83, 251).

(65) Gazzani, M.; Joss, L.; Mazzotti, M. A five step temperature swing adsorption process for the recovery of CO_2 at high purity. *Patent filed March 8th* **2016** (cit. on pp. 15, 83, 251).

(66) Shafeeyan, M. S.; Wan Daud, W. M. A.; Shamiri, A. A review of mathematical modeling of fixed-bed columns for carbon dioxide adsorption. *Chem. Eng. Res. Des.* **2014**, *92*, 961–988 (cit. on p. 17).

(67) Farooq, S.; Ruthven, D. M. Heat Effects in Adsorption COlumn Dynamics. 1. Comparison of One- and Two-Dimensional Models. *Ind. Eng. Chem. Res* **1990**, *29*, 1076–1084 (cit. on pp. 18, 33).

(68) Kim, M.-B.; Moon, J.-H.; Lee, C.-H.; Hyungwoong, A.; Wonihl, C. Effect of Heat Transfer on the Transient Dynamics of Temperature Swing Adsorption Process. *Korean J. Chem. Eng.* **2004**, *321*, 703–711 (cit. on pp. 18, 33).

(69) Grande, C. A.; Rodrigues, A. E. Electric Swing Adsorption for CO_2 removal from flue gases. *Int. J. Greenh. Gas Control* **2007**, *2*, 194–202 (cit. on p. 18).

(70) Shen, C.; Grande, C. A.; Li, P.; Yu, J.; Rodrigues, A. E. Adsorption equilibria and kinetics of CO_2 and N_2 on activated carbon beads. *Chem. Eng. J.* **2010**, *160*, 398–407 (cit. on p. 18).

(71) Mulgundmath, V. P.; Jones, R.; Tezel, F. H.; Thibault, J. Fixed bed adsorption for the removal of carbon dioxide from nitrogen: Breakthrough behaviour and modelling for heat and mass transfer. *Sep. Purif. Technol.* **2012**, *85*, 17–27 (cit. on p. 18).

(72) Farooq, S.; Ruthven, D. M. A comparison of linear driving force and pore diffusion models for a pressure swing adsorption bulk separation process. *Chem. Eng. Sci.* **1990**, *45*, 107–115 (cit. on p. 18).

(73) Sircar, S.; Hufton, J. R. Intraparticle Adsorbate Concentration Profile for Linear Driving Force Model. *AIChE J.* **2000**, *46*, 659–660 (cit. on p. 18).

(74) Sircar, S.; Hufton, J. R. Why Does the Linear Driving Force Model for Adsorption Kinetics Work ? *Comp. Gen. Pharmacol.* **2000**, 137–147 (cit. on p. 18).

(75) Nastaj, J.; Ambrożek, B. Analysis of gas dehydration in TSA system with multi-layered bed of solid adsorbents. *Chem. Eng. Process. Process Intensif.* **2015**, *96*, 44–53 (cit. on p. 19).

(76) Ruthven, D. M., *Principles of Adsorption and Adsorption Processes*; Wiley, John & Sons: New York, 1984 (cit. on pp. 19, 126, 174).

(77) Casas, N.; Schell, J.; Pini, R.; Mazzotti, M. Fixed bed adsorption of CO_2/H_2 mixtures on activated carbon: experiments and modeling. *Adsorption* **2012**, *18*, 143–161 (cit. on pp. 19, 86, 135).

(78) Webley, P. A. Fast solution-adaptive finite volume method for PSA/VSA cycle simulation; 1 single step simulation. *Comput. Chem. Eng.* **2000**, *23*, 1701–1712 (cit. on p. 22).

(79) Javeed, S.; Qamar, S.; Seidel-Morgenstern, A.; Warnecke, G. Efficient and accurate numerical simulation of nonlinear chromatographic processes. *Comput. Chem. Eng.* **2011**, *35*, 2294–2305 (cit. on pp. 22, 23).

(80) LeVeque, R. J., *Finite Volume*; Cambridge University Press: Cambridge, 2002 (cit. on pp. 22, 23).

(81) Minceva, M.; Pais, L. S.; Rodrigues, A. E. Cyclic steady state of simulated moving bed processes for enantiomers separation. *Chem. Eng. Process.* **2003**, *42*, 93–104 (cit. on pp. 26, 87).

(82) Marx, D.; Joss, L.; Hefti, M.; Mazzotti, M. Temperature Swing Adsorption for post-combustion CO_2 capture: Single- and multicolumn experiments and simulations. *Ind. Eng. Chem. Res.* **2016**, *54*, 1401–1412 (cit. on pp. 27, 86, 121, 129, 134, 135, 250).

(83) Hefti, M.; Marx, D.; Joss, L.; Mazzotti, M. Adsorption equilibrium of binary mixtures of carbon dioxide and nitrogen on zeolites ZSM-5 and 13X. *Microporous Mesoporous Mater.* **2015**, *215*, 215–228 (cit. on pp. 28, 33, 63, 85, 88, 130, 133, 205, 226, 250).

(84) Schell, J.; Casas, N.; Marx, D.; Mazzotti, M. Precombustion CO_2 Capture by Pressure Swing Adsorption (PSA): Comparison of Laboratory PSA Experiments and Simulations. *Ind. Eng. Chem. Res.* **2013**, *52*, 8311–8322 (cit. on pp. 29, 86).

(85) Marx, D.; Joss, L.; Casas, N.; Schell, J.; Mazzotti, M. Prediction of non-isothermal ternary gas-phase breakthrough experiments based on binary data. *Adsorption* **2014**, *20*, 493–510 (cit. on pp. 31, 35, 251).

(86) Mohamadinejad, H.; Knox, J. C.; E., S. J. Experimental and Numerical Investigation of Two-Dimensional CO_2 Adsorption/Desorption in Packed Sorption Beds Under Non-ideal Flows. *Sep. Sci. Technol.* **2003**, *38*, 3875–3904 (cit. on p. 33).

(87) Dixon, A. G. Fixed Bed Catalytic Reactor Modelling – the Radial Heat Transfer Problem. *Can. J. Chem. Eng.* **2012**, *90*, 507–527 (cit. on pp. 35, 195, 206).

(88) De Wasch, A.; Froment, G. F. Heat transfer in packed beds. *Chem. Eng. Sci.* **1972**, *27*, 567–576 (cit. on pp. 35, 46, 206, 210).

(89) Froment, G. F.; Bischoff, K. B., *Chemical Reactor Analysis and Design*, 2nd; Wiley: New York, NY, 1990 (cit. on pp. 35, 206, 209, 210).

(90) Specchia, V.; Baldi, G.; Sicardi, S. Heat Transfer in Packed Bed Reactors With One Phase Flow. *Chem. Eng. Commun.* **1980**, *4*, 361–380 (cit. on pp. 35, 46, 201, 206, 210, 211).

(91) Gnielinski, V.; Ducts, P. P.; Wagner, W., *VDI Heat Atlas*; Springer Berlin Heidelberg: Berlin, Heidelberg, 2010; Vol. 2010, p 1608 (cit. on pp. 35, 211).

(92) Giesy, T. J.; Wang, Y.; LeVan, M. D. Measurement of Mass Transfer Rates in Adsorbents: New Combined-Technique Frequency Response Apparatus and Application to CO_2 in 13X Zeolite. *Ind. Eng. Chem. Res.* **2012**, *51*, 11509–11517 (cit. on p. 39).

(93) Hu, X.; Mangano, E.; Friedrich, D.; Ahn, H.; Brandani, S. Diffusion mechanism of CO_2 in 13X zeolite beads. *Adsorption* **2014**, *20*, 121–135 (cit. on p. 39).

(94) Dixon, A. G. An improved equation for the overall heat transfer coefficient in packed beds. *Chem. Eng. Process.* **1996**, *35*, 323–331 (cit. on pp. 46, 200, 210).

(95) Mason, J. A.; Sumida, K.; Herm, Z. R.; Krishna, R.; Long, J. R. Evaluating metal–organic frameworks for post-combustion carbon dioxide capture via temperature swing adsorption. *Energy Environ. Sci.* **2011**, *4*, 3030 (cit. on pp. 49, 79, 84, 122).

(96) Su, F.; Lu, C. CO_2 capture from gas stream by zeolite 13X using a dual-column temperature/vacuum swing adsorption. *Energy Environ. Sci.* **2012**, *5*, 9021 (cit. on p. 49).

(97) Sculley, J. P.; Verdegaal, W. M.; Lu, W.; Wriedt, M.; Zhou, H.-C. High-throughput analytical model to evaluate materials for temperature swing adsorption processes. *Adv. Mater.* **2013**, *25*, 3957–61 (cit. on p. 49).

(98) Pirngruber, G. D.; Guillou, F.; Gomez, A.; Clausse, M. A theoretical analysis of the energy consumption of post-combustion CO_2 capture processes by temperature swing adsorption using solid sorbents. *Int. J. Greenh. Gas Control* **2013**, *14*, 74–83 (cit. on pp. 49, 51, 62).

(99) Sumida, K. et al. Carbon dioxide capture in metal-organic frameworks. *Chem. Rev.* **2012**, *112*, 724–81 (cit. on pp. 49, 84, 122).

(100) Anantharaman, R. et al. *European best practice guidelines for assessment of CO_2 capture technologies*; tech. rep.; Politecnico di Milano and Alstom UK, 2011 (cit. on pp. 50, 110, 148).

(101) IEAGHG Incorporating Future Technological Imrovements in Existing CO_2 Post Combustion Capture Plants: Technical Review. *2013/TR5 May* **2013** (cit. on pp. 50, 117, 118).

(102) Chue, K. T.; Kim, J.-N.; Yoo, Y. J.; Cho, S.-H.; Yang, R. T. Comparison of Activated Carbon and Zeolite 13X for CO_2 Recovery from Flue Gas by Pressure Swing Adsorption. *Ind. Eng. Chem. Res.* **1995**, *34*, 591–598 (cit. on p. 50).

(103) Yoshida, M.; Ritter, J. A.; Kodama, A.; Goto, M.; Hirose, T. Enriching Reflux and Parallel Equalization PSA Process for Concentrating Trace Components in Air. *Ind. Eng. Chem. Res.* **2003**, *42*, 1795–1803 (cit. on p. 50).

(104) Xiao, P. et al. Capture of CO_2 from flue gas streams with zeolite 13X by vacuum-pressure swing adsorption. *Adsorption* **2008**, *14*, 575–582 (cit. on p. 50).

(105) Casas, N.; Schell, J.; Blom, R.; Mazzotti, M. MOF and UiO-67/MCM-41 adsorbents for pre-combustion CO_2 capture by PSA: Breakthrough experiments and process design. *Sep. Purif. Technol.* **2013**, *112*, 34–48 (cit. on p. 50).

(106) Rajendran, A.; Paredes, G.; Mazzotti, M. Simulated moving bed chromatography for the separation of enantiomers. *J. Chromatogr. A* **2009**, *1216*, 709–38 (cit. on p. 50).

(107) Chan, Y. Y. N. I.; Hill, F. F. B.; Wong, Y. W. Y. Equilibrium theory of a pressure swing adsorption process. *Chem. Eng. Sci.* **1981**, *36*, 243–251 (cit. on p. 51).

(108) Kayser, J. C.; Knaebel, K. S. Pressure swing adsorption: Development of an equilibrium theory for binary gas mixtures with nonlinear isotherms. *Chem. Eng. Sci.* **1989**, *44*, 1–8 (cit. on p. 51).

(109) Maring, B. J.; Webley, P. A. A new simplified pressure/vacuum swing adsorption model for rapid adsorbent screening for CO_2 capture applications. *Int. J. Greenh. Gas Control* **2013**, *15*, 16–31 (cit. on p. 51).

(110) Pan, C.-Y.; Basmadjian, D. An analysis of adiabatic sorption of single solutes in fixed beds: pure thermal wave formation and its practical implications. *Chem. Eng. Sci.* **1970**, *25*, 1653–1664 (cit. on p. 51).

(111) Pan, C. C.-Y.; Basmadjian, D. An analysis of adiabatic sorption of single solutes in fixed beds: equilibrium theory. *Chem. Eng. Sci.* **1971**, *26*, 45–57 (cit. on p. 51).

(112) Ruthven, D. M.; Farooq, S.; Knaebel, K. S., *Pressure Swing Adsorption*; VCH Publishers Inc.: New York, 1994 (cit. on pp. 57, 68, 220).

(113) Rhee, H.-K.; Aris, R.; Amundson, N. R., *First-Order Partial Differential Equations. I Theory and Application of Single Equations*; Dover Publication, Inc.: Mineola, NY, 1986 (cit. on p. 58).

(114) Ortner, F.; Joss, L.; Mazzotti, M. Equilibrium theory analysis of liquid chromatography with non-constant velocity. *J. Chromatogr. A* **2014**, *1373*, 131–140 (cit. on pp. 58, 251).

(115) Buonomenna, M.; Yave, W.; Golemme, G. Some approaches for high performance polymer based membranes for gas separation: block copolymers, carbon molecular sieves and mixed matrix membranes. *RSC Adv.* **2012**, *2*, 10745 (cit. on p. 83).

(116) Nugent, P. et al. Porous materials with optimal adsorption thermodynamics and kinetics for CO_2 separation. *Nature* **2013**, *495*, 80–4 (cit. on p. 83).

(117) Drage, T. C. et al. Materials challenges for the development of solid sorbents for post-combustion carbon capture. *J. Mater. Chem.* **2012**, *22*, 2815 (cit. on p. 83).

(118) Harlick, P. J.; Handan Tezel, F. An experimental adsorbent screening study for CO_2 removal from N_2. *Microporous Mesoporous Mater.* **2004**, *76*, 71–79 (cit. on p. 83).

(119) Samanta, A.; Zhao, A.; Shimizu, G. K. H.; Sarkar, P.; Gupta, R. Post-combustion CO_2 capture using solid sorbents: A review. *Ind. Eng. Chem. Res.* **2012**, *51*, 1438–1463 (cit. on p. 83).

(120) Lively, R. P.; Chance, R. R.; Koros, W. J. Enabling Low-Cost CO_2 Capture via Heat Integration. *Ind. Eng. Chem. Res.* **2010**, *49*, 7550–7562 (cit. on p. 83).

(121) García, S.; Gil, M.; Pis, J.; Rubiera, F.; Pevida, C. Cyclic operation of a fixed-bed pressure and temperature swing process for CO_2 capture: Experimental and statistical analysis. *Int. J. Greenh. Gas Control* **2013**, *12*, 35–43 (cit. on p. 84).

(122) Nikolic, D.; Kikkinides, E. S.; Georgiadis, M. C. Optimization of Multibed Pressure Swing Adsorption Processes. *Ind. Eng. Chem. Res.* **2009**, *48*, 5388–5398 (cit. on p. 84).

(123) Joos, L.; Swisher, J. a.; Smit, B. Molecular simulation study of the competitive adsorption of H_2O and CO_2 in zeolite 13X. *Langmuir* **2013**, *29*, 15936–42 (cit. on p. 86).

(124) Dantas, T. L. P. et al. Modeling the Fixed-bed Adsorption of Carbon Dioxide and a Carbon Dioxide-Nitrogen Mixture on Zeolite 13X. *Brazilian J. Chem. Eng.* **2011**, *28*, 533 –544 (cit. on pp. 88, 135).

(125) Mersmann, A. In *Ullmann's Encycl. Ind. Chem.* Gerharz, W., Ed., 5th; Wiley-VCH Verlag GmbH.: Weinheim, 2005; Chapter Adsorption (cit. on pp. 89, 128).

(126) Grande, C. A.; Lopes, F. V. S.; Ribeiro, A. M.; Loureiro, J. M.; Rodrigues, A. E. Adsorption of Off-Gases from Steam Methane Reforming (H_2, CO_2 , CH_4, CO and N_2) on Activated Carbon. *Sep. Sci. Technol.* **2008**, *43*, 1338–1364 (cit. on p. 93).

(127) Mehrotra, A.; Ebner, A. D.; Ritter, J. A. Arithmetic approach for complex PSA cycle scheduling. *Adsorption* **2010**, *16*, 113–126 (cit. on p. 93).

(128) Ramezan, M.; Skone, T. J.; Nsakala, y. N.; Lilijedahl, G. *Carbon Dioxide Capture from Existing Coal-Fired Power Plants*; tech. rep. December 2006; 2007 (cit. on pp. 117, 118).

(129) Just, P. E. Shell Cansolv - Advancing CCS Deployment Worldwide., 2013 (cit. on pp. 117, 118).

(130) Couturier, G. SaskPower Boundary Dam Carbon Capture Demonstration Project., 2014 (cit. on pp. 117, 118).

(131) Richardson, J.; Remue, D; Hung, J.-K Properties of ceramic foam catalyst supports: mass and heat transfer. *Appl. Catal. A Gen.* **2003**, *250*, 319–329 (cit. on p. 119).

(132) Rochelle, G. T. Amine scrubbing for CO_2 capture. *Science* **2009**, *325*, 1652–1654 (cit. on p. 121).

(133) Scholes, C. A.; Smith, K. H.; Kentish, S. E.; Stevens, G. W. CO_2 capture from pre-combustion processes – Strategies for membrane gas separation. *Int. J. Greenh. Gas Control* **2010**, *4*, 739–755 (cit. on p. 121).

(134) Habib, M. A. et al. Carbon capture by physical adsorption : Materials , experimental investigations and numerical modeling and simulations – A review. *Appl. Energy* **2016**, *161*, 225–255 (cit. on pp. 121, 122).

(135) Veltman, K.; Singh, B.; Hertwich, E. G. Human and environmental impact assessment of postcombustion CO_2 capture focusing on emissions from amine-based scrubbing solvents to air. *Environ. Sci. Technol.* **2010**, *44*, 1496–1502 (cit. on p. 121).

(136) Schell, J. et al. MCM-41, MOF and UiO-67/MCM-41 adsorbents for pre-combustion CO_2 capture by PSA: adsorption equilibria. *Adsorption* **2012**, *18*, 213–227 (cit. on p. 121).

(137) Xiang, S. et al. Microporous metal-organic framework with potential for carbon dioxide capture at ambient conditions. *Nat. Commun.* **2012**, *3*, 954 (cit. on p. 122).

(138) Caskey, S. R.; Wong-Foy, A. G.; Matzger, A. J. Dramatic tuning of carbon dioxide uptake via metal substitution in a coordination polymer with cylindrical pores. *J. Am. Chem. Soc.* **2008**, *130*, 10870–10871 (cit. on p. 122).

(139) Chowdhury, P.; Mekala, S.; Dreisbach, F.; Gumma, S. Adsorption of CO, CO_2 and CH_4 on Cu-BTC and MIL-101 metal organic frameworks: Effect of open metal sites and adsorbate polarity. *Microporous Mesoporous Mater.* **2012**, *152*, 246–252 (cit. on p. 122).

(140) Xiang, S. et al. A 3D canted antiferromagnetic porous metal-organic framework with anatase topology through assembly of an analogue of polyoxometalate. *J. Am. Chem. Soc.* **2005**, *127*, 16352–3 (cit. on p. 122).

(141) Boutin, A.; Neimark, A. V.; Fuchs, A. H.; Pierre, U. V. The Behavior of Flexible MIL-53 (Al) upon CH_4 and CO_2 Adsorption. *J. Phys. Chem. C* **2010**, *114*, 22237–22244 (cit. on p. 122).

(142) Alhamami, M.; Doan, H.; Cheng, C.-H. A Review on Breathing Behaviors of Metal-Organic-Frameworks (MOFs) for Gas Adsorption. *Materials (Basel).* **2014**, *7*, 3198–3250 (cit. on p. 122).

(143) Wu, D. et al. Thermodynamic complexity of carbon capture in alkylamine-functionalized metal–organic frameworks. *J. Mater. Chem. A* **2015**, *3*, 4248–4254 (cit. on p. 125).

(144) Remy, T.; Baron, G. V.; Denayer, J. F. M. Modeling the Effect of Structural Changes during Dynamic Separation Processes on MOFs. *Langmuir* **2011**, DOI: 10.1021/la203374a (cit. on p. 125).

(145) Smith, R. C., *Uncertainty Quantification: Theory, Implementation, and Applications*; SIAM: 2014 (cit. on p. 127).

(146) Zhang, W.; Shan, Y.; Seidel-Morgenstern, A. Breakthrough curves and elution profiles of single solutes in case of adsorption isotherms with two inflection points. *J. Chromatogr. A* **2006**, *1107*, 216–225 (cit. on p. 130).

(147) Ribeiro, A. M.; Grande, C. A.; Lopes, F. V. S.; Loureiro, J. M.; Rodrigues, A. E. Four Beds Pressure Swing Adsorption for Hydrogen Purification : Case of Humid Feed and Activated Carbon Beds. *AIChE J.* **2009**, *55*, 2292–2302 (cit. on p. 132).

(148) Pini, R. Interpretation of net and excess adsorption isotherms in microporous adsorbents. *Microporous Mesoporous Mater.* **2014**, *187*, 40–52 (cit. on p. 133).

(149) Huyer, W.; Neumaier, A. Global Optimization by Multilevel Coordinate Search. *J. Glob. Optim.* **1999**, *14*, 331–355 (cit. on pp. 136, 164).

(150) McDonald, T. M. et al. Capture of carbon dioxide from air and flue gas in the alkylamine-appended metal-organic framework mmen-Mg2(dobpdc). *J. Am. Chem. Soc.* **2012**, *134*, 7056–65 (cit. on p. 137).

(151) Joss, L.; Capra, F.; Gazzani, M.; Mazzotti, M.; Martelli, E. MO-MCS: An Efficient Multi-objective Optimization Algorithm for the Optimization of Temperature/Pressure Swing Adsorption Cycles. *Comput. Aided Chem. Eng.* **2016**, *38*, 1467–1472 (cit. on pp. 155, 156, 163, 250).

(152) Abu-Zahra, M. R. M.; Schneiders, L. H. J.; Niederer, J. P. M.; Feron, P. H. M.; Versteeg, G. F. CO_2 capture from power plants. Part I. A parametric study of the technical performance based on monoethanolamine. *Int. J. Greenh. Gas Control* **2007**, *1*, 37–46 (cit. on pp. 155, 156).

(153) Raynal, L. et al. The DMX^{TM} process: An original solution for lowering the cost of post-combustion carbon capture. *Energy Procedia* **2011**, *4*, 779–786 (cit. on pp. 155, 156).

(154) Raynal, L.; La Marca, C.; Mertens, J.; Normand, L.; Broutin, P. Demonstration of the DMX process description of the Octavius SP3 project., 2013 (cit. on p. 155).

(155) Singh, P.; Van Swaaij, W. P. M.; Brilman, D. W. F. Energy efficient solvents for CO_2 absorption from flue gas: Vapor liquid equilibrium and pilot plant study. *Energy Procedia* **2013**, *37*, 2021–2046 (cit. on pp. 155, 156).

(156) Nilchan, S; Pantelides, C. C. On the Optimisation of Periodic Adsorption Processes. *Adsorpt. J. Int. Adsorpt. Soc.* **1998**, *147*, 113–147 (cit. on p. 163).

(157) Ko, D.; Siriwardane, R.; Biegler, L. T. Optimization of a Pressure-Swing Adsorption Process Using Zeolite 13X for CO_2 Sequestration. *Ind. Eng. Chem. Res.* **2003**, *42*, 339–348 (cit. on p. 164).

(158) Rios, L. M.; Sahinidis, N. V. Derivative-free optimization: a review of algorithms and comparison of software implementations. *J. Glob. Optim.* **2013**, *56*, 1247–1293 (cit. on p. 165).

(159) Messac, A.; Ismail-Yahaya, A.; Mattson, C. A. The normalized normal constraint method for generating the Pareto frontier. *Struct. Multidiscip. Optim.* **2003**, *25*, 86–98 (cit. on p. 165).

(160) Marler, R.; Arora, J. Survey of multi-objective optimization methods for engineering. *Struct. Multidiscip. Optim.* **2004**, *26*, 369–395 (cit. on p. 165).

(161) Zitzler, E; L., K. D.; Thiele Comparison of multiobjective evolutionary algorithms: empirical results. *Evol. Comput.* **2000**, *8*, 173–195 (cit. on pp. 167, 171).

(162) Brandani, S. et al., *Adsoption and diffusion*; Karge, H. G., Weitkamp, J., Eds.; Springer: Berlin Heidelberg, 1998, p 359 (cit. on p. 174).

(163) Dixon, A. G.; Cresswell, D. L. Theoretical Prediction of Effective Heat Transfer Parameters in Packed Beds. *AIChE J.* **1979**, *25*, 663–676 (cit. on p. 206).

(164) Kunii, D.; Smith, J. M. Heat Transfer Characteristics of Porous Rocks. *AIChE J.* **1960**, *6*, 71–78 (cit. on p. 210).

(165) Hefti, M.; Joss, L.; Marx, D.; Mazzotti, M. An experimental and modeling study of the adsorption equilibrium and dynamics of water vapor on activated carbon. *Ind. Eng. Chem. Res.* **2015**, *54*, 12165–12176 (cit. on p. 250).

(166) Ortner, F.; Jermann, S.; Joss, L.; Mazzotti, M. Equilibrium Theory Analysis of a Binary Chromatographic System Subject to a Mixed Generalized Bi-Langmuir Isotherm. *Ind. Eng. Chem. Res.* **2015**, *54*, 11420–11437 (cit. on p. 250).

(167) Hefti, M.; Marx, D.; Joss, L.; Mazzotti, M. Model-based process design of adsorption processes for CO_2 capture in the presence of moisture. *Energy Procedia* **2014**, *63*, 2152–2159 (cit. on p. 251).

(168) Marx, D.; Joss, L.; Hefti, M.; Pini, R.; Mazzotti, M. The Role of Water in Adsorption-based CO_2 Capture Systems. *Energy Procedia* **2013**, *37*, 107–114 (cit. on p. 251).

(169) Joss, L.; Mazzotti, M. Modeling the extra-column volume in a small column setup for bulk gas adsorption. *Adsorption* **2012**, *18*, 381–393 (cit. on p. 251).

(170) Kluge, J.; Joss, L.; Viereck, S.; Mazzotti, M. Emulsion crystallization of phenanthrene by supercritical fluid extraction of emulsions. *Chem. Eng. Sci.* **2012**, *77*, 249–258 (cit. on p. 251).

(171) Kapałka, A.; Joss, L.; Anglada, Á.; Comninellis, C.; Udert, K. M. Direct and mediated electrochemical oxidation of ammonia on boron-doped diamond electrode. *Electrochem. commun.* **2010**, *12*, 1714–1717 (cit. on p. 251).

A HEAT TRANSFER CHARACTERIZATION

An attempt to characterize the radial effective conductivity of the bed was undertook by carrying out steady state experiments, for which the column jacket was kept at a high temperature of 100 °C, while cold argon gas (25 °C) was fed to the column at two different flow rates (43 L_N/min and 60 L_N/min). Thereby, the 2-dimensional temperature profile was recorded by radially moving the thermocouples.

A.1 MATHEMATICAL MODEL

An accurate description of heat transfer within the packed bed is crucial for a correct description of temperature swing adsorption processes. Despite the long history in research on heat transfer, there is no truly well established consensus to how the heat transfer in packed beds must be described.[87] When considering a pseudo-homogeneous model, i.e., under the assumption of thermal equilibrium between fluid and solid phases, one of the main issues is tied to the so-called wall effects. This refers to the increased porosity and the different nature in contact points (particle-wall, fluid-wall) which are present in the vicinity of the wall. This, together with a velocity profile which generally also varies more strongly at the wall, makes it impossible to describe the radial temperature profile of the bed with a constant effective thermal conductivity of the bed.

Generally, one of the two following approaches is followed. (1) The radial heat transfer is characterized by an effective thermal conductivity $K_r(r)$, which will depend on the radius. (2) A more classical and simple approach consists in considering a constant effective thermal conductivity K_r within the bed; all the wall effects are accounted for

by a resistance at the wall, which is characterized by a lumped wall heat transfer coefficient h_w.

The latter approach will be used to model the heat transfer within the packed bed. In order to do so, the parameters h_w and K_r will be determined by fitting steady state experiments to the corresponding 2D model:

$$\rho c_p v \frac{\partial T}{\partial z} = K_r \left(\frac{\partial^2 T}{\partial r^2} + \frac{1}{r} \frac{\partial T}{\partial r} \right) + K_a \frac{\partial^2 T}{\partial z^2} \tag{A.1}$$

$$-k_r \frac{\partial T}{\partial r} = h_w (T - T_w) \qquad \text{at } r = R \tag{A.2}$$

With boundary conditions:

$$\left. \frac{\partial T}{\partial z} \right|_{z=L} = 0 \quad ; \qquad T|_{z=0} = f(r) \quad ; \qquad \left. \frac{\partial T}{\partial r} \right|_{r=0} = 0 \tag{A.3}$$

An analytical expression for the temperature $T(r, z)$ can be obtained by making the following change of variables:

$$\theta = T - T_w \tag{A.4}$$

$$x = r \sqrt{\frac{K_a}{K_r}} \quad ; \qquad x_R = R \sqrt{\frac{K_a}{K_r}} \tag{A.5}$$

$$\tag{A.6}$$

Equations A.1,A.2 and A.3 can be rewritten:

$$0 = \frac{\partial^2 \theta}{\partial x^2} + \frac{1}{x} \frac{\partial \theta}{\partial x} + \frac{\partial^2 \theta}{\partial z^2} - 2k \frac{\partial \theta}{\partial z} \tag{A.7}$$

$$0 = \frac{\partial \theta}{\partial x} + H\theta \qquad \text{at } x = x_R \tag{A.8}$$

$$\left. \frac{\partial \theta}{\partial z} \right|_{z=L} = 0 \quad ; \qquad \theta|_{z=0} = F(x) \quad ; \qquad \left. \frac{\partial \theta}{\partial x} \right|_{x=0} = 0 \tag{A.9}$$

Equation A.7 can be solved by separation of variables. For the corresponding boundary conditions (equations A.8 and A.9) the solution is given by:

$$\theta(x,z) = \frac{2}{x_R}\sum_{s=1}^{\infty}\left[\exp\left\{z\left(k-\sqrt{k^2+\alpha_s^2}\right)\right\}\times \frac{\alpha_s^2 J_0(\alpha_s x)}{(H^2+\alpha_s^2)J_0^2(\alpha_s x_R)}\int_0^{x_R} x J_0(\alpha_s x)F(x)\,\mathrm{d}x\right] \tag{A.10}$$

where $J_n(x)$ is the Bessel function of order n and α_s are the roots of:

$$\alpha_s J_1(\alpha_s x_R) - H J_0(\alpha_s x_R) = 0. \tag{A.11}$$

HOMOGENEOUS INITIAL PROFILE $f(x) = \theta_0$. The integral of equation A.10 can be solved, and the final expression for the reduced temperature θ is:

$$\theta(x,z) = \frac{2\,\theta_0\,H}{x_R}\sum_{s=1}^{\infty}\exp\left\{z\left(k-\sqrt{k^2+\alpha_s^2}\right)\right\}\frac{J_0(\alpha_s x)}{(H^2+\alpha_s^2)J_0(\alpha_s x_R)} \tag{A.12}$$

PARABOLIC INITIAL PROFILE $f(x) = ax^2 + b$. In this case the integral of equation A.10 can be solved by parts, and the final expression for the reduced temperature θ is:

$$\theta(x,z) = \frac{2\,f(x_R)}{x_R}\sum_{s=1}^{\infty}\left[\exp\left\{z\left(k-\sqrt{k^2+\alpha_s^2}\right)\right\}\times \frac{J_0(\alpha_s x)}{(H^2+\alpha_s^2)J_0(\alpha_s x_R)}\left(H-\frac{2Ax_R}{f(x_R)}\frac{J_2(\alpha_s x_R)}{J_0(\alpha_s x_R)}\right)\right] \tag{A.13}$$

A.2 EXPERIMENTAL PROCEDURE

A simplified scheme of the PTSA setup including the relevant parts for the performed experiments is shown in Figure A.1. The experiments were conducted by maintaining the wall of the packed bed at 100 °C by flowing the thermo-fluid through the double jacket, and

flowing argon at atmospheric temperature through the packed bed at a given flow rate. Once at steady state, temperatures at different radial and axial positions were recorded. The thermocouples are located at fixed axial positions, but the radial position can be manually set by using custom built metal spacers. The temperature was measured at eight or nine different radial positions, all located in the column half furthest from the entrance of the thermocouple. This choice was deliberately made in order to minimize the effect of thermal conductivity through the thermocouple.

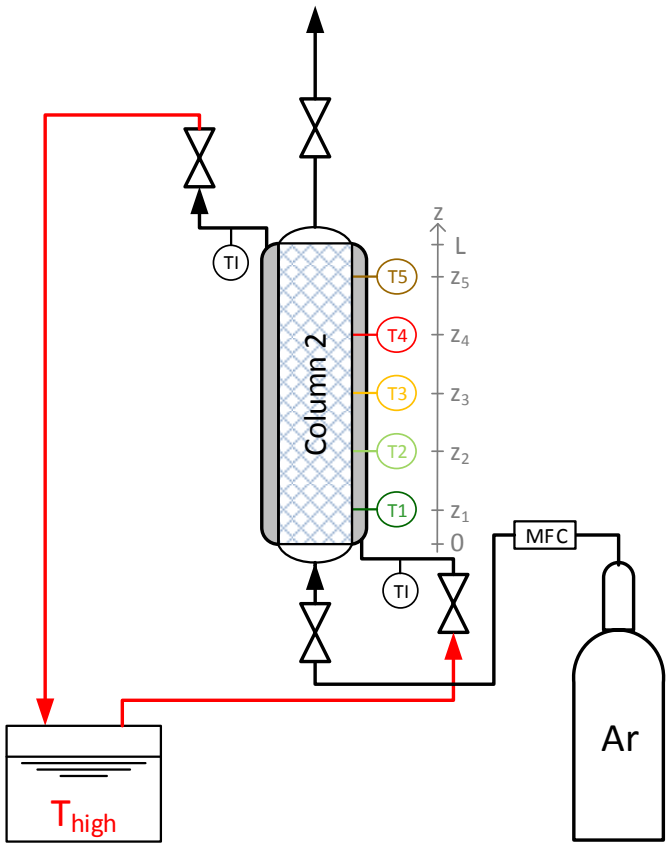

Figure A.1. – Scheme of the parts of the setup which are relevant for the conductivity experiments.

High flow rates ($\geq$ 40 Nl/min) are necessary in order to observe reasonable temperature gradients, because of the low heat capacity of the gas phase as compared to the adsorbent bed, and the relatively large distance between the thermocouples. The setup was not designed for these large flowrates, and a large pressure drop is observed

downstream of the column. This implies that experiments cannot be performed at pressures lower than ca. 4 bar to 5 bar. Nevertheless, the pressure drop across the packed bed is relatively low ($\leq$ 0.3 bar)

The evaluation of these experiments by comparing to a mathematical model requires the knowledge of the inlet temperature $F(r) = T_0$. However, the gas is heated as it passes through the flange, and therefore the real inlet temperature probable is higher than ambient temperature. Two different approaches have been assessed in order to solve this issue:

1. to fit a parabolic function $F(r)$ onto the first measured radial profile (at $z = z_1$) and then fit the remaining parameters onto the other radial profiles thereby considering a column with a shorter effective length ($L^* = L - z_1$);
2. to fit a constant initial temperature profile in $z = 0$ and the remaining model parameters simultaneously.

In both cases, the axial thermal conductivity parameter was fixed to $K_a = 20\,\mathrm{W/(m\,K)}$ because the model has a very low sensitivity to this parameter. The fitting was done by finding the maximum likelihood estimate (MLE) of each of the fitted parameters. For all parameters estimations, a global optimization was carried out by running local optimizations with an interior-point algorithm from several trial points. This was performed with the *GlobalSearch* routine provided in the optimization toolbox of Matlab together with the *fmincon* routine.

A.3 RESULTS

The experimental temperature profiles together with the profiles fitted according to the two investigated methods are shown in Figures A.2 and A.3 for two experiments performed under the conditions listed in Table A.1, respectively.

For both experiments, a more accurate description (lower value of the objective function) is obtained by fitting a constant initial temperature together with the effective thermal conductivity and the wall heat transfer coefficient. In fact, the thermocouples at the axial positions

Table A.1. – Experimental conditions. The presented experiments were performed under the same experimental conditions, with the exception of different flow rates.

parameter	value
Wall temperature	100 °C
Gas	Argon
Inlet temperature	ca. 25 °C
Flow rate	{43; 60} Nl/min
Pressure	{4.7; 7.0} bar

z_3–z_5 exhibit practically no gradient, and therefore carry a very low information level for the parameter fitting. When assigning an initial temperature profile at $z = z_1$, the first – and most pronounced – profile is not considered as an independent observation anymore.

The greater reliability of the fits performed considering all measurements and a constant initial temperature profile is confirmed by the values of the fitted parameters, which are listed in Table A.2. In fact, this approach yields reasonable parameters, which are in line with correlations. The parameters K_r and h_w can be combined into an overall heat transfer coefficient h_{bed}, which should be considered in the case of a 1D model, as suggested by Dixon[94]:

$$\frac{1}{h_{\text{bed}}} = \frac{1}{h_w} + \frac{R}{3K_r}\frac{\text{Bi}+3}{\text{Bi}+4} \qquad \text{with Bi} = \frac{h_w}{RK_r} \tag{A.14}$$

From these results, it can be concluded that the adopted methodology for determining the heat transport properties would in principle work, however the current setup is not adapted to carry out steady-state experiments at low Reynolds numbers. A setup with larger tubing, and a shorter bed with thermocouples positioned every couple of centimeters in the axial direction would be more appropriate.

Table A.2. – Experimental conditions. The presented experiments were performed under the same experimental conditions, with the exception of different flow rates.

Flow	Re [-]	h_w [W/(m^2 K)]	K_r [W/(m K)]	T_0 [K]	h_{bed} [W/(m^2 K)]
$\boldsymbol{f(r) = T_0}$					
43 Nl/min	91	59	0.67	306	46
60 Nl/min	125	48	0.43	306	35
$\boldsymbol{f(r) = ar^2 + b}$					
43 Nl/min	90	32	2.8	–	31
60 Nl/min	125	23	1.5	–	22
Specchia correlation[90]					
43 Nl/min	90	156	0.32	–	55
60 Nl/min	125	188	0.39	–	67

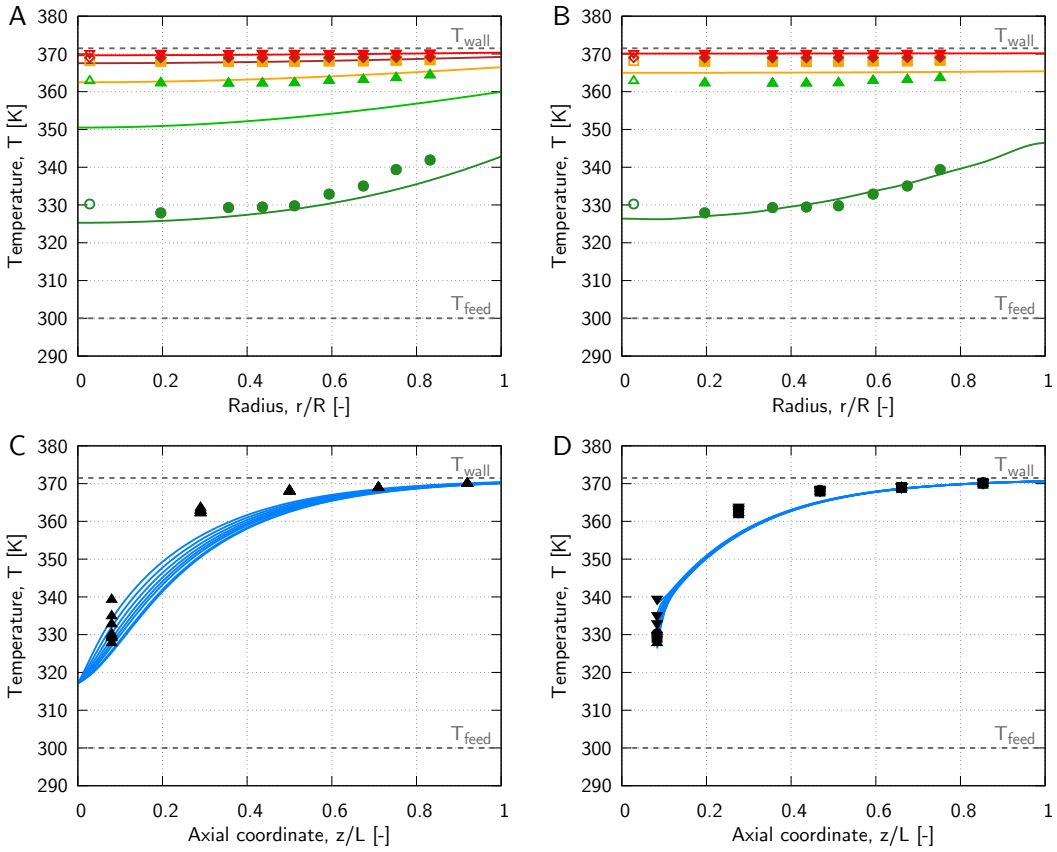

Figure A.2. – Experimental and fitted temperature profiles for a flow rate of 43 Nl/min. (A) and (C) Measured temperature profiles compared to fitting carried out with a constant initial temperature $f(r) = \theta_0$. (B) and (D) Measured temperature profiles compared to fitting carried out with a constant initial temperature $f(r) = ar^2 + b$

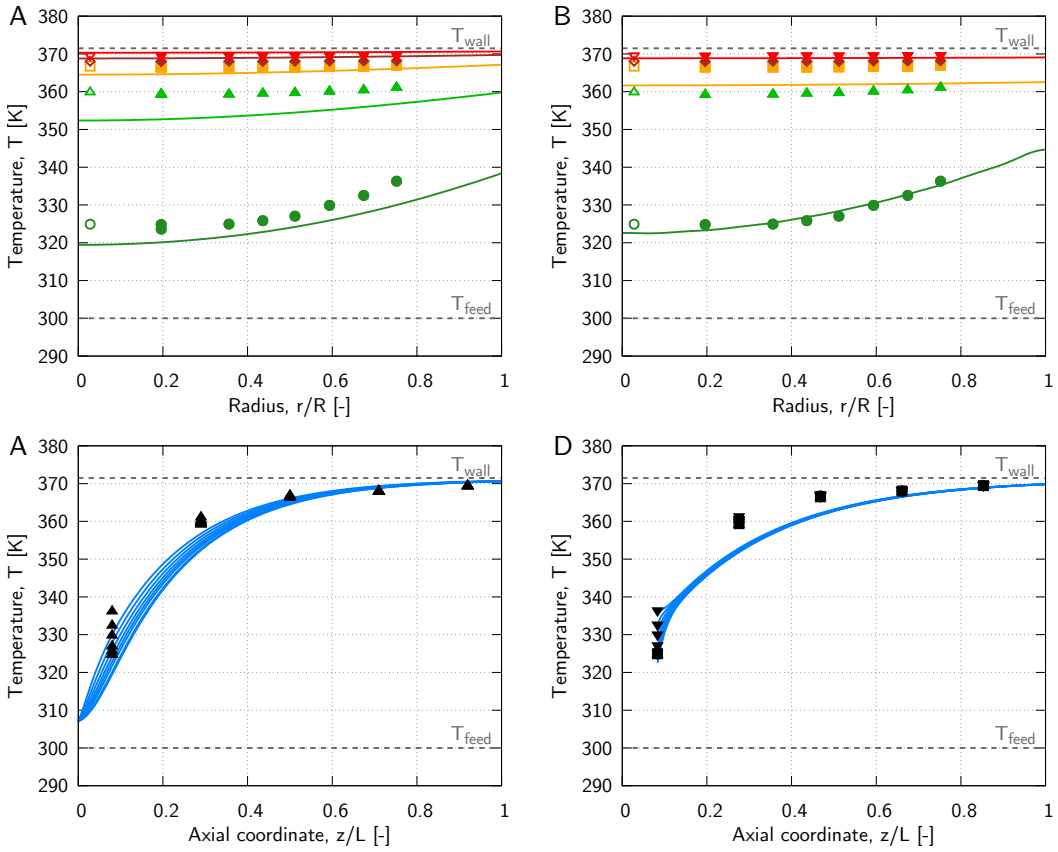

Figure A.3. – Experimental and fitted temperature profiles for a flow rate of 60 Nl/min. (A) and (C) Measured temperature profiles compared to fitting carried out with a constant initial temperature $f(r) = \theta_0$. (B) and (D) Measured temperature profiles compared to fitting carried out with a constant initial temperature $f(r) = ar^2 + b$

B SUPPLEMENTARY MATERIAL FOR CHAPTER 3

B.1 ISOTHERM PARAMETERS

The pure component adsorption isotherm of CO_2 and of N_2 on zeolite 13X were measured by Hefti et al.[83] and described with the Sips isotherm:

$$n_i^{\infty}(T) = n_{\mathrm{ref},i}^{\infty} \exp\left(\chi_i \left(\frac{T}{T_{\mathrm{ref}}} - 1\right)\right) \tag{B.1}$$

$$b_i(T) = b_{0,i} \exp\left(\frac{Q_{\mathrm{b},i}}{RT}\right) \tag{B.2}$$

$$c_i(T) = c_{\mathrm{ref},i} + \alpha_i \left(\frac{T}{T_{\mathrm{ref}}} - 1\right) \tag{B.3}$$

Table B.1. – Pure component adsorption isotherms for CO_2 and N_2 on 13X, as determined by Hefti et al.[83] The uncertainty is given in parentheses with respect to the last significant digit.

		CO_2	N_2
$n_{\mathrm{ref}}^{\infty}$	[mol/kg]	7.268(1)	4.051(2)
χ_i	[–]	−0.6168(3)	0
$b_{0,i}$	[bar^{-1}]	$1.129(1) \times 10^{-4}$	$5.8470(7) \times 10^{-5}$
$Q_{\mathrm{b},i}$	[kJ/mol]	28.389(2)	18.4740(3)
$c_{\mathrm{ref},i}$	[–]	0.424 56(8)	0.986 24(5)
α	[–]	0.723 78(7)	0

B.2 BREAKTHROUGH EXPERIMENTS ON 13X

Figures B.1 and B.2 shows the full set of results of the breakthrough experiments with the 12:88 CO_2:N_2 mixture on 13X together with the simulations obtained by fitting the heat transfer coefficient between the bed and the column wall, h_b.

B.3 HEATING AND COOLING EXPERIMENTS FOR TSA

Figure B.3 shows the results of the heating/cooling experiments with He along with the simulations obtained by fitting the heat transfer coefficient between the column wall and the heat exchange fluid, $h_{w,L}$.

B.4 HEAT TRANSFER IN THE PACKED BED

Correlations for the heat transfer in packed beds under flow conditions characterized by low Reynolds numbers are mainly found for pseudo-homogeneous models, i.e., where the solid and fluid phase temperatures are assumed to be in equilibrium, and either for one dimensional models[88,89] or for two dimensional models.[87,90] In the former case, a single parameter is necessary to describe the heat transfer resistance, whereas is in the latter case, two parameters are typically used: the effective thermal conductivity of the bed, and the heat transfer resistance at the column wall. Dixon and Cresswell[163] proposed an approach in order to combine the effective thermal conductivity (K_R) and the heat transfer resistance at the wall (α_w) into a single heat transfer resistance:

$$\frac{1}{h_L} = \frac{1}{\alpha_w} + \frac{r_i}{3K_R}\frac{\mathrm{Bi}+3}{\mathrm{Bi}+4} \tag{B.4}$$

where the Biot number is $\mathrm{Bi} = \alpha_w r_i / K_R$.

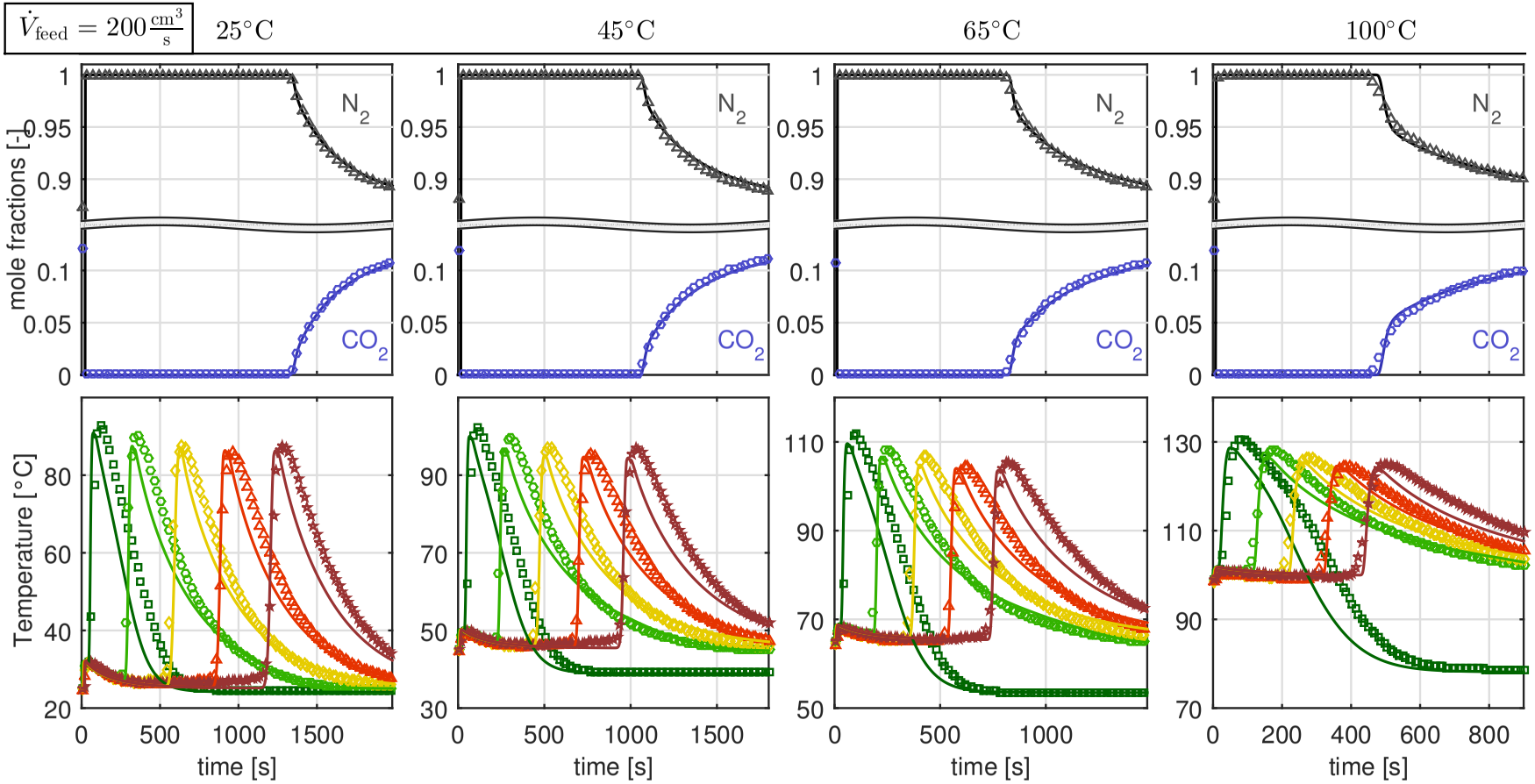

Figure B.1. – Concentration and temperature profiles for breakthrough experiments performed with a feed flow rate of 200 cm^3/s. Experimental data (*symbols*) are shown together with the simulations (*lines*) carried out with the heat transfer coefficient fitted to that experiment.

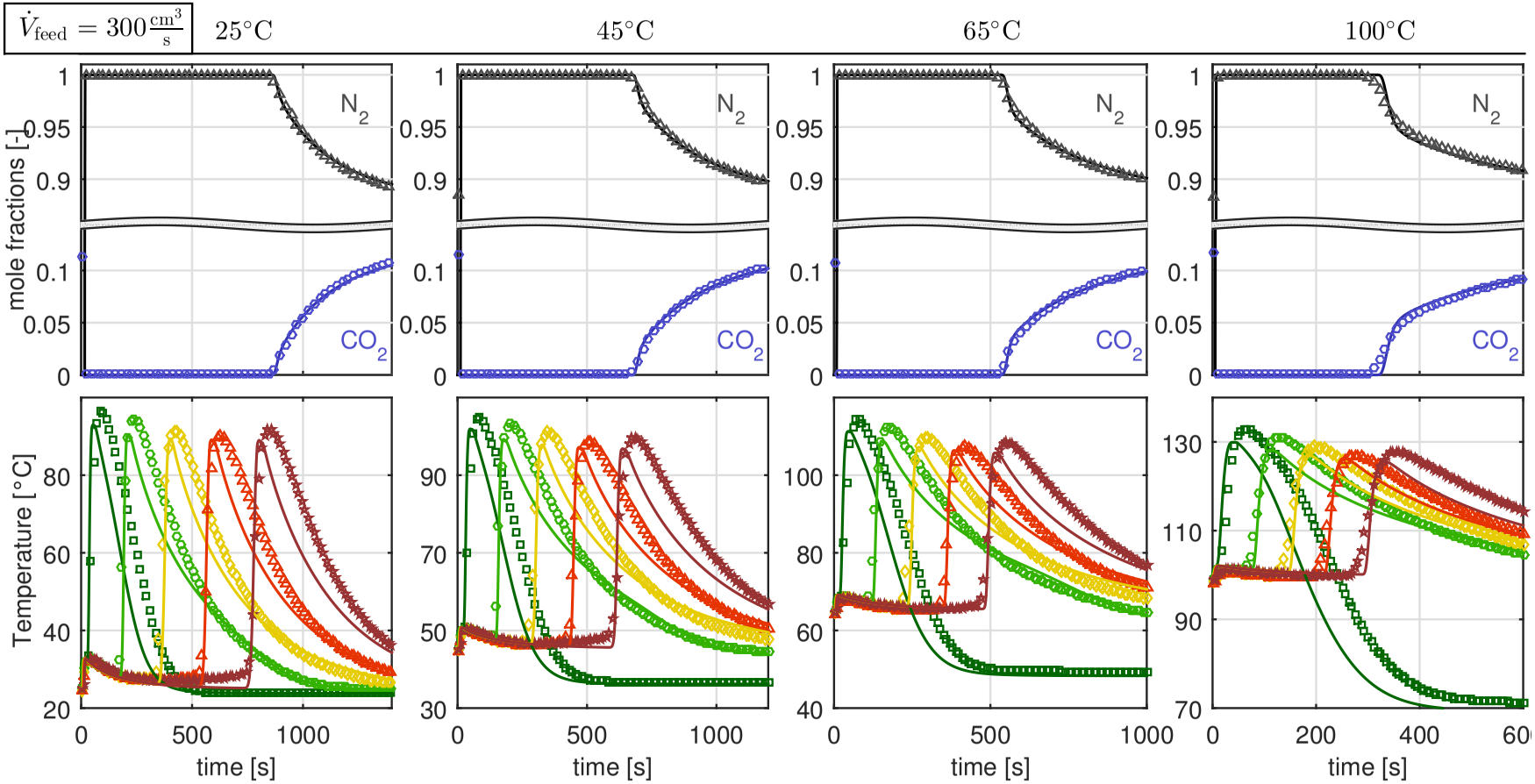

Figure B.2. – Concentration and temperature profiles for breakthrough experiments performed with a feed flow rate of 300 cm^3/s. Experimental data (*symbols*) are shown together with the simulations (*lines*) carried out with the heat transfer coefficient fitted to that experiment.

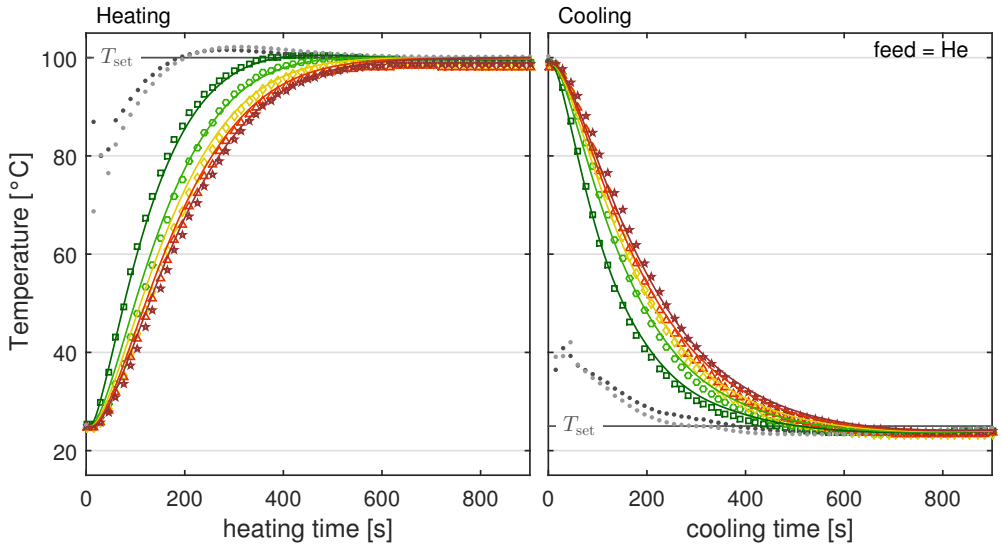

Figure B.3. – Temperature profiles inside the column during the heating and cooling experiment using the helium feed. Symbols are measurements at the five positions. The dots are the measured thermofluid temperature at the jacket inlet and outlet. Lines represent simulations. The arrows indicate the axial profile that developed within the column.

B.4.1 According to DeWasch and Froment

DeWasch and Froment found a linear relationship between the Nusselt and Reynolds numbers that is repeated here:[89]

$$\mathrm{Nu} = \mathrm{Nu}^0 + 0.033\mathrm{PrRe} \tag{B.5}$$

with the dimensionless numbers being

$$\mathrm{Nu} = \frac{h_b d_p}{\lambda_g} \qquad \mathrm{Nu}^0 = \frac{h_b^0 d_p}{\lambda_g} \qquad \mathrm{Pr} = \frac{\rho \nu C_p}{\lambda_g} \qquad \mathrm{Re} = \frac{v d_p}{\nu}$$

where h_b^0 is the static heat transfer coefficient in the bed. In an earlier work Froment had established this to be related to the static contribution of the effective thermal conductivity of the bed, λ_e^0, through the following equation:

$$h_b^0 = 2.583 \frac{\lambda_e^0}{d_t^{4/3}} \tag{B.6}$$

where d_t is the tube diameter. To find λ_e^0, an approach was followed that is reported by Froment and Bischoff and is based on the work of Froment and Bischoff[89] and Kunii and Smith[164]

$$\frac{\lambda_e^0}{\lambda_g} = \varepsilon \left(1 + \beta \frac{d_p \alpha_{rv}}{\lambda_g}\right) + \frac{\beta\,(1-\varepsilon)}{\frac{1}{\frac{1}{\phi} + \frac{\alpha_{rs} d_p}{\lambda_g}} + \frac{2}{3}\frac{\lambda_g}{\lambda_s}} \tag{B.7}$$

under the assumption that the radiative heat exchange is negligible (i.e., $\alpha_{rv} = 0, \alpha_{rs} = 0$) at these relatively low temperatures and that $\beta = 1$.

B.4.2 According to Specchia

Specchia et al. also determined the heat transfer through the bed and at the wall separately, considering for each a static component and a convective contribution.[90] The equations they used are summarized in Table B.2.

Note that the equation used to obtain the static contribution of the effective thermal conductivity of the bed, λ_e^0, is a simplified version of the one used by De Wasch and Froment[88]. The values obtained for α_w and K_R are then combined into the overall heat transfer coefficient according to the approach suggested by Dixon[94]

$$\frac{1}{h_L} = \frac{1}{\alpha_w} + \frac{R_i}{3K_R}\frac{\mathrm{Bi}+3}{\mathrm{Bi}+4} \tag{B.8}$$

where $\mathrm{Bi} = \frac{\alpha_w R_i}{K_R}$.

B.5 HEAT TRANSFER IN THE COLUMN JACKET

B.5.1 Estimating the heat transfer coefficient based on fluid properties

The VDI Heat Atlas (Part G2) provides expressions that describe the heat transfer for annular tubes, as is the case here, under laminar

Table B.2. – Equations used by Specchia et al. to determine heat transfer through the bed and at the wall.[90]

effective radial thermal conductivity

$$
\begin{aligned}
K_R &= \lambda_e^0 + k_{Rg} \\
\lambda_e^0 &= \lambda_g \left(\varepsilon_b + \frac{\beta(1-\varepsilon_b)}{\phi + \frac{\lambda_g}{\lambda_s}\gamma} \right) \\
&\quad \gamma = \tfrac{2}{3}, \qquad \beta = 1, \qquad \phi = 0.220\varepsilon_b^2 \\
k_{Rg} &= \frac{\mathrm{Re}\rho_g \nu C_p}{\mathrm{Pe}_H} \\
\mathrm{Pe}_H &= 8.65 \left(1 + 19.4 \frac{d_p}{2R_i} \right)
\end{aligned}
$$

wall heat transfer coefficient

$$
\begin{aligned}
\mathrm{Nu}_w &= \frac{\alpha_w d_p}{\lambda_g} = \mathrm{Nu}_w^0 + \mathrm{Nu}_w^c \\
\mathrm{Nu}_w^0 &= 2\varepsilon_b + \frac{1-\varepsilon_b}{\frac{\lambda_g}{\lambda_s}\gamma_w + \phi_w} \\
&\quad \gamma_w = \tfrac{1}{3}, \qquad \phi_w = 0.00240 \left(\frac{2R_i}{d_p} \right)^{1.58} \\
\mathrm{Nu}_w^c &= 0.0835\mathrm{Re}^{0.91}
\end{aligned}
$$

and turbulent flow condition, as well as for the transition region between the two regimes.[91] These expressions estimate the heat transfer coefficient based on the geometry (jacket length, diameter) and the physical properties of the fluid. The manufacturer of the thermofluid used (Therminol 62, Fragol GmbH, Germany) provides physical property data over a range of temperature, shown in Figure B.4. These properties can be approximated by the following equations:

$$
\begin{aligned}
\text{density :} \qquad & \rho(T) = \rho_0 + m_\rho T \\
\text{heat capacity :} \qquad & C_p(T) = C_{p,0} + m_{C_p} T \\
\text{thermal conductivity :} \qquad & \lambda(T) = \lambda_0 + m_\lambda T \\
\text{kinematic viscosity :} \qquad & \nu(T) = \nu_0 \exp\left(\frac{K_\nu}{T - T_0} \right)
\end{aligned}
$$

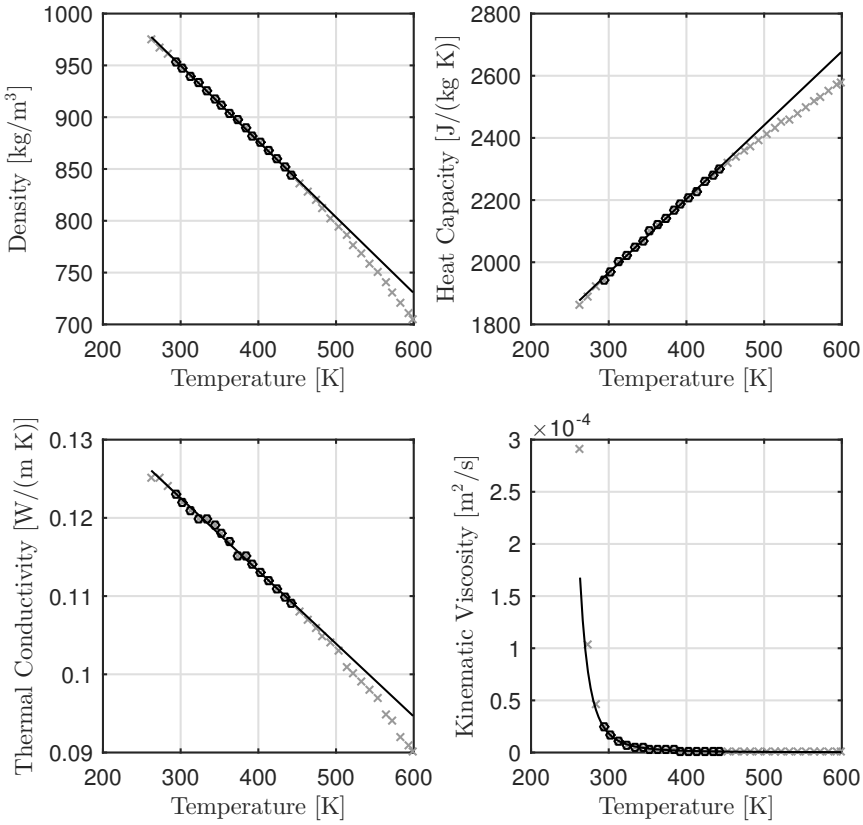

Figure B.4. – Physical properties of the thermofluid used in this work to control the column temperature. Symbols represent the data provided by the manufacturer, where the circles are the data points used to regress parameters for the models shown here as lines.

where the necessary parameters were fitted to the available data within the temperature range that is of interest in this work. The results can be seen in Figure B.4 together with the data. Based on these physical properties and the dimensions of the jacket, the relevant dimensionless numbers can be found:

$$\mathrm{Nu} = \frac{d_h h_w}{\lambda} \qquad \mathrm{Re} = \frac{d_h v}{\nu} \qquad \mathrm{Pr} = \frac{\rho \nu C_p}{\lambda} \qquad d_h = 2\left(r_w - r_o\right)$$

where r_w and r_o are the radii of the outside and inside wall of the jacket, respectively. For the Nusselt number the VDI Heat Atlas provides the following expressions, depending on the flow regime:

Laminar:

$$\begin{aligned}
\mathrm{Nu}_{\mathrm{lam}} &= \left(\mathrm{Nu}_1^3 + \mathrm{Nu}_2^3\right)^{\frac{1}{3}} \\
\mathrm{Nu}_1 &= 3.66 + 1.2a^{-0.8} \\
\mathrm{Nu}_2 &= 1.615\left(1 + 0.14a^{-0.5}\right)\left(\mathrm{RePr}d_h/L\right)^{\frac{1}{3}}
\end{aligned}$$

Turbulent:

$$\begin{aligned}
\mathrm{Nu}_{\mathrm{turb}} &= \frac{\xi/8\mathrm{RePr}}{k_1 + 12.7\sqrt{\xi/8}\left(\mathrm{Pr}^{2/3} - 1\right)} f_g \\
f_g &= \left(1 + \left(d_h/L\right)^{2/3}\right) 0.75a^{-0.17} \\
k_1 &= 1.07 + \frac{900}{\mathrm{Re}} + \frac{0.63}{1 + 10\mathrm{Pr}} \\
\xi &= \left(1.8\log_{10}\left(\mathrm{Re}^*\right) - 1.5\right)^{-2} \\
\mathrm{Re}^* &= \mathrm{Re}\frac{\left(1 + a^2\right)\ln\left(a\right) + \left(1 - a^2\right)}{\left(1 - a^2\right)\ln\left(a\right)}
\end{aligned}$$

For the transition region (Re between 2300 and 10000), the Nusselt number is estimated with a linear function between its value at Re = 2300 and at Re = 10 000, i.e.:

$$\begin{aligned}
\gamma &= \frac{\mathrm{Re} - 2300}{10^4 - 2300} \\
\mathrm{Nu} &= \mathrm{Nu}_{\mathrm{lam},2300}\left(1 - \gamma\right) + \mathrm{Nu}_{\mathrm{turb},10^4}\gamma
\end{aligned}$$

From the data provided by the manufacturer of the thermofluid and of the thermostat (Huber Kältemaschinenbau GmbH, Germany), the value of h_w can be estimated. However, the flow rate of the fluid depends on the characteristics of the pump used in the thermostat, the thermofluid used, and the resistance of the piping. For a range of flow rates, the estimated Nusselt number therefore varies; its calculated value for a range of flow rates is shown in Figure B.5. From the illustration it can be seen that the value of h_w for most conditions should be on the order of 200 W/(m^2 K). For a better description of the experiments, the heat transfer coefficient should be fitted to the experiment.

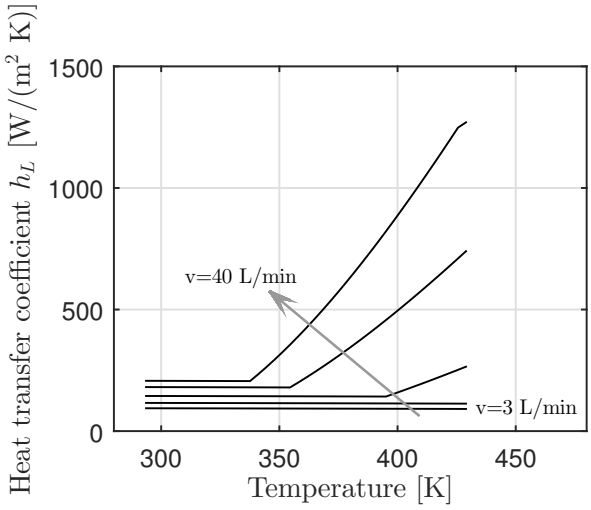

Figure B.5. – Heat transfer coefficient h_w calculated according to the VDI Heat Atlas for flow rates ranging from 3 L/min to 40 L/min.

B.5.2 Entrance effects in the heating jacket

For the region of the annular tube that exhibits hydrodynamically and thermally developing laminar flow, the VDI Heat Atlas provides another approximation:

$$\begin{aligned}
\mathrm{Nu}(x) &= \left(\mathrm{Nu}_1^3 + \mathrm{Nu}_2^3(x) + \mathrm{Nu}_3^3(x)\right)^{\frac{1}{3}} \\
\mathrm{Nu}_1 &= 3.66 + 1.2a^{-0.8} \\
\mathrm{Nu}_2(x) &= 1.615\left(1 + 0.14a^{-0.5}\right)\left(\mathrm{RePr}d_h/x\right)^{\frac{1}{3}} \\
\mathrm{Nu}_3(x) &= \left(\frac{2}{1+22\mathrm{Pr}}\right)^{1/6}\left(\mathrm{RePr}d_h/x\right)^{0.5}
\end{aligned}$$

It is clear from these equation that the entrance effects diminish with distance from the entrance, and for large ratios of L/d_h, Nu is very close to $\mathrm{Nu}_{\mathrm{lam}}$ seen above, as $\mathrm{Nu}_3(x)$ gets small. While the value of $\mathrm{Nu}_{\mathrm{lam}}$ depends on temperature and flow rate, the relationship $\mathrm{Nu}(x)/\mathrm{Nu}_{\mathrm{lam}}$ looks very similar under the whole range of conditions found in this work. This is illustrated in Figure B.7.

As discussed in the main manuscript, the aim of this analysis was to see if accounting for the entrance effect could yield a significantly

better description of the heat transfer in the column jacket. To test this, the column was viewed in a simplified manner, lumping heat capacities and heat transfer coefficients to arrive at the following equation:

$$(\rho C_p)_{\text{eff}} \frac{\mathrm{d}T_{\text{bed}}}{\mathrm{d}t} = U a_w (T_f - T_{\text{bed}})$$

Figure B.6 shows the development of the time derivatives of the temperature within the column as measured by the five thermocouples during the heating and cooling experiment using the helium feed. After an initial lag, the time derivative of the temperature shows a linear relationship with the temperature gradient to the thermofluid temperature. The data with $10\,\text{K} < |\nabla T| < 50\,\text{K}$ was then used to regress the quantity $(U a_w)((\rho C_p)_{\text{eff}})$ at each thermocouple position. The resulting slopes are illustrated in Figure B.7. The trend exhibited by this data along the length of the column is similar to that found for the estimates of the Nusselt number, shown in Figure B.7 on the right, albeit somewhat dampened by the effect of the heat transfer within the bed. It is therefore reasonable to consider entrance effects when simulating the heating and cooling experiments as well as the corresponding steps of the TSA experiments. This was done in the following manner: The heat transfer coefficient $h_w(x)$ at any position along the column was calculated as

$$h_w(x) = h_{w,L} \frac{\text{Nu}(x)}{\text{Nu}(L)} \tag{B.9}$$

where $\text{Nu}(x)/\text{Nu}(L)$ was calculated for conditions representative of the conditions present throughout a TSA cycle. The value of $h_{w,L}$, the heat transfer coefficient at the end of the column, was fitted to the heating and cooling experiments, along with the heat transfer coefficient within the bed, h_L, under the condition of (almost) no flow.

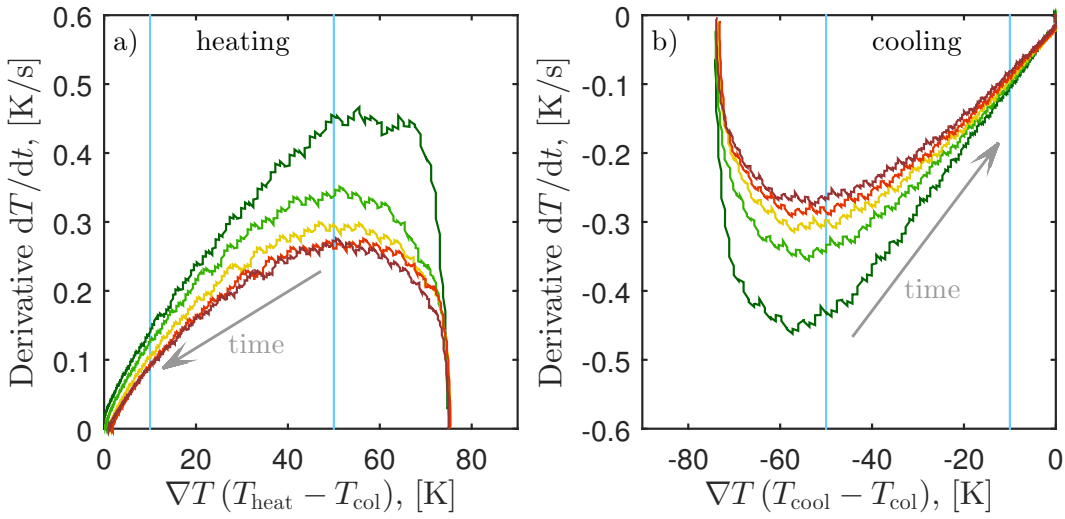

Figure B.6. – Time derivatives of the temperatures measured at each thermocouple throughout the heating (a) and cooling (b) experiment using helium as a feed. The thermocouples are colored according to their position. The light blue lines indicate the range of data used for the regression.

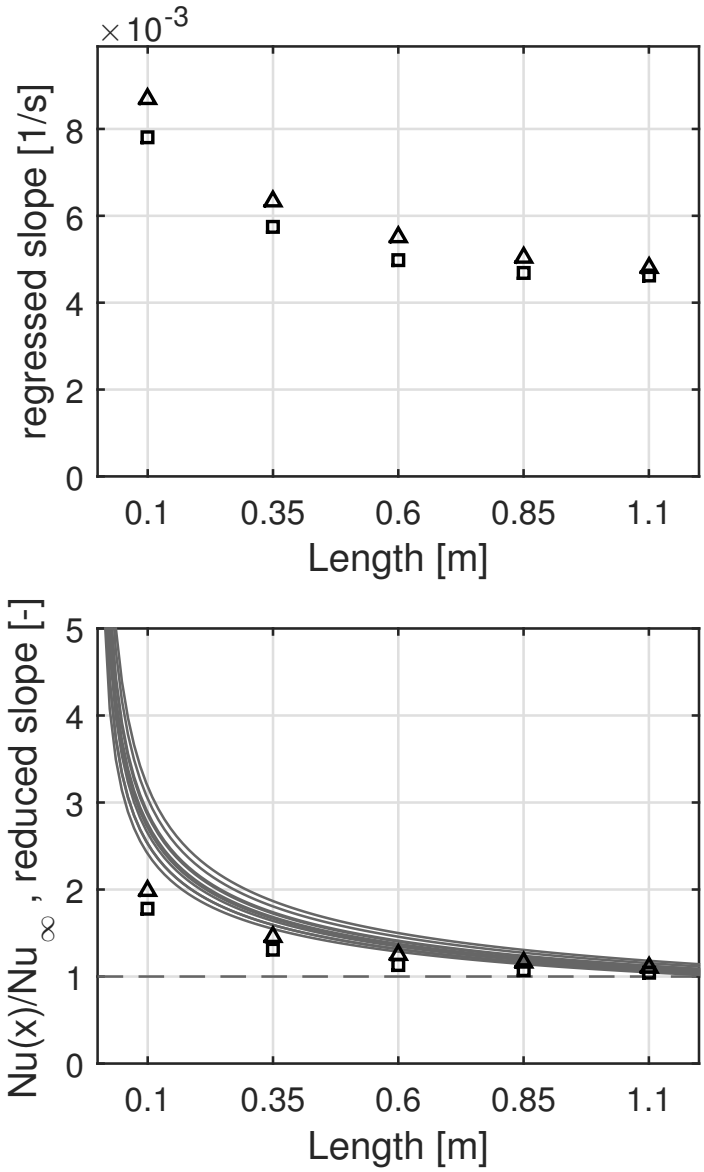

Figure B.7. – *Top:* Regressed estimates for $Ua_w/(\rho C_p)_{\text{eff}}$ along the column for the heating (□) and cooling (△) experiment. *Bottom:* Entry-region effects on the Nusselt number relative to its value at infinite length for temperatures ranging from 25 °C to 150 °C and flow rates from 0.2 kg/s to 0.6 kg/s (lines). Symbols show the apparent overall heat transfer coefficient at the position of each of the thermocouples during the heating (□) and the cooling (△) experiment with helium, relative to the lowest value fitted.

C SUPPLEMENTARY MATERIAL FOR CHAPTER 4

C.1 DETAILS ON THE MATHEMATICAL MODEL

C.1.1 Uniform composition within the heating step

At non-isothermal conditions and under the assumption of negligible pressure drop, the governing Eqs. (4.2) and (4.2) can be rewritten as:

$$\left(1+\omega_{y,1}\right)\frac{\partial y/T}{\partial t}+\left(\frac{-y}{T}+\omega_{T,1}\right)\frac{\mathrm{d}T}{\mathrm{d}t}+v\frac{\partial y}{\partial z}+y\frac{\partial v}{\partial z}=0 \tag{C.1}$$

$$\left(\omega_{y,1}+\omega_{y,2}\right)\frac{\partial y/T}{\partial t}+\left(\frac{-y}{T}+\omega_{T,1}\right)\frac{\mathrm{d}T}{\mathrm{d}t}+\frac{\partial v}{\partial z}=0 \tag{C.2}$$

with:

$$\omega_{y,i}(y,T)=\frac{RT}{p}\frac{\rho_b}{\epsilon}\frac{\partial n_i}{\partial y} \tag{C.3}$$

$$\omega_{T,i}(y,T)=\frac{RT}{p}\frac{\rho_b}{\epsilon}\frac{\partial n_i}{\partial T} \tag{C.4}$$

These two equations can be combined by eliminating $\frac{\partial v}{\partial z}$, yielding a PDE with the molar fraction as dependent variable:

$$-\frac{(1-y)\omega_{T,1}-y\omega_{T,2}}{1+(1-y)\omega_{y,1}-y\omega_{y,2}}\frac{\mathrm{d}T}{\mathrm{d}t}=\frac{\partial y}{\partial t}+\frac{v}{1+(1-y)\omega_{y,1}-y\omega_{y,2}}\frac{\partial y}{\partial z} \tag{C.5}$$

According to the method of characteristics, the composition, temperature, position and time along a characteristic are related according to the following equations:

$$\frac{\mathrm{d}z}{\mathrm{d}t}=\frac{v}{1+(1-y)\omega_{y,1}-y\omega_{y,2}} \tag{C.6}$$

$$\frac{\mathrm{d}y}{\mathrm{d}T} = -\frac{(1-y)\omega_{T,1} - y\omega_{T,2}}{1 + (1-y)\omega_{y,1} - y\omega_{y,2}} \tag{C.7}$$

Since equation C.7 does not depend explicitly on the position, it indicates that for an initially uniform composition in the column, there will be no transition in composition developing upon an increase in temperature. This is an analogous case to a blowdown step from an initially uniform composition profile.[112]

C.1.2 Pressurization step

For the investigated cases, i.e., an initial composition where the more adsorbed component is present at a larger molar fraction but a lower partial pressure as compared to the feed conditions, a sharp composition front will evolve within the bed. The solution of the internal profile at the end of this step can be determined by numerical simulations. Nonetheless, an estimate of the solution is provided by considering the extreme cases illustrated in Figure C.1, namely the formation of a pure wave-shock, and the case of perfect mixing.

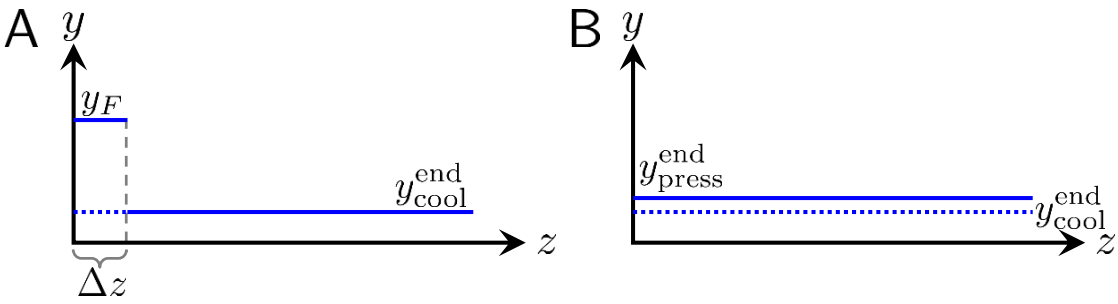

Figure C.1. – Schematic illustration of the considered extreme cases for the description of the composition profile at the end of the pressurization step. (A) a pure shock-wave forms, and a portion of length Δz of the bed is at equilibrium with the feed composition. (B) the composition profile is flat.

The maximum extent to which the front can penetrate the column can be easily calculated by considering the formation of a pure shock-wave, i.e, by considering that the CO_2 fed adsorbs instantaneously. This corresponds to a shock of composition y_F traveling through the column until enough material has been fed to pressurize the column.

The material balances relate the total amount fed N_{press} to the position of the front Δz:

$$N_{\text{press}} = A\Delta z \rho_b \sum_{i=1}^{2} n_i(y_F, P_H, T_L) + A(L-\Delta z)\rho_b \sum_{i=1}^{2} n_i(y_{\text{cool}}^{\text{end}}, P_H, T_L) + AL\left(\frac{\epsilon}{RT}(P_{\text{high}} - P_{\text{low}}) - \rho_b \sum_{i=1}^{2} n_{i,\text{end}}^{\text{cool}}\right) \tag{C.8}$$

$$y_F N_{\text{press}} = A\Delta z \frac{\epsilon}{RT}(y_F P_H - y_{\text{cool}}^{\text{end}} P_L) + A\Delta z \rho_b \left[n_1(y_F, P_H, T_L) - n_{1,\text{end}}^{\text{cool}}\right] \tag{C.9}$$

The distance traveled by the shock is determined by eliminating N_{press} from Equations C.8 and C.9 and solving for $\Delta z/L$

The other extreme case which can be considered, is if the composition profile remains completely homogeneous. At constant temperature, and for a given initial state ($P_L, y_{\text{cool}}^{\text{end}}$) and end pressure ($P_H$), the composition at the end of the pressurization can be determined with a mass balance, which yields an implicit equation in $y_{\text{press}}^{\text{end}}$:

$$\frac{\rho_b}{\epsilon} RT\left((1-y_F)(n_{1,\text{press}}^{\text{end}} - n_{1,\text{cool}}^{\text{end}}) - y_F(n_{2,\text{press}}^{\text{end}} - n_{2,\text{cool}}^{\text{end}})\right) + (y_{\text{press}}^{\text{end}} P_{\text{high}} - y_{\text{cool}}^{\text{end}} P_{\text{low}}) - y_F(P_H - P_L) = 0 \tag{C.10}$$

The assumption of a uniform composition at the end of the pressurization is reasonable provided that the amount fed of the more retained component is small as compared to the amount contained within the column. This can be verified by evaluating the relative difference in molar fraction at the end of the pressurization step to the molar fraction which would be present if pure light component was used to pressurize the column:

$$\epsilon_{\text{hom}} = \frac{y_{\text{press}}^{\text{end}} - y_{\text{cool}}^{\text{end}} P_L / P_H}{y_{\text{cool}}^{\text{end}}} \tag{C.11}$$

A further measure of the validity of this assumption is provided by the dimensionless maximal penetration depth of the shock-wave $\Delta z/L$, which should be small.

Figure C.2 shows the dimensionless maximal penetration depth of the CO_2 ($\Delta z/L$) and the relative deviation between the composition as determined from Eq. (C.10) for varying compositions at the end of the adsorption step and low pressure levels (P_L). Since the values of both indicators are small, the flat composition profile at the end of the pressurization step is considered to be a fair assumption.

C.2 RELATIVE CONTRIBUTION OF THE INDIVIDUAL STEP TIMES

The contribution of each step to the total cycle time is visible in Figure C.3, where the duration of each step divided by the total cycle time is shown in a stack graph in the plane T_L, T_H.

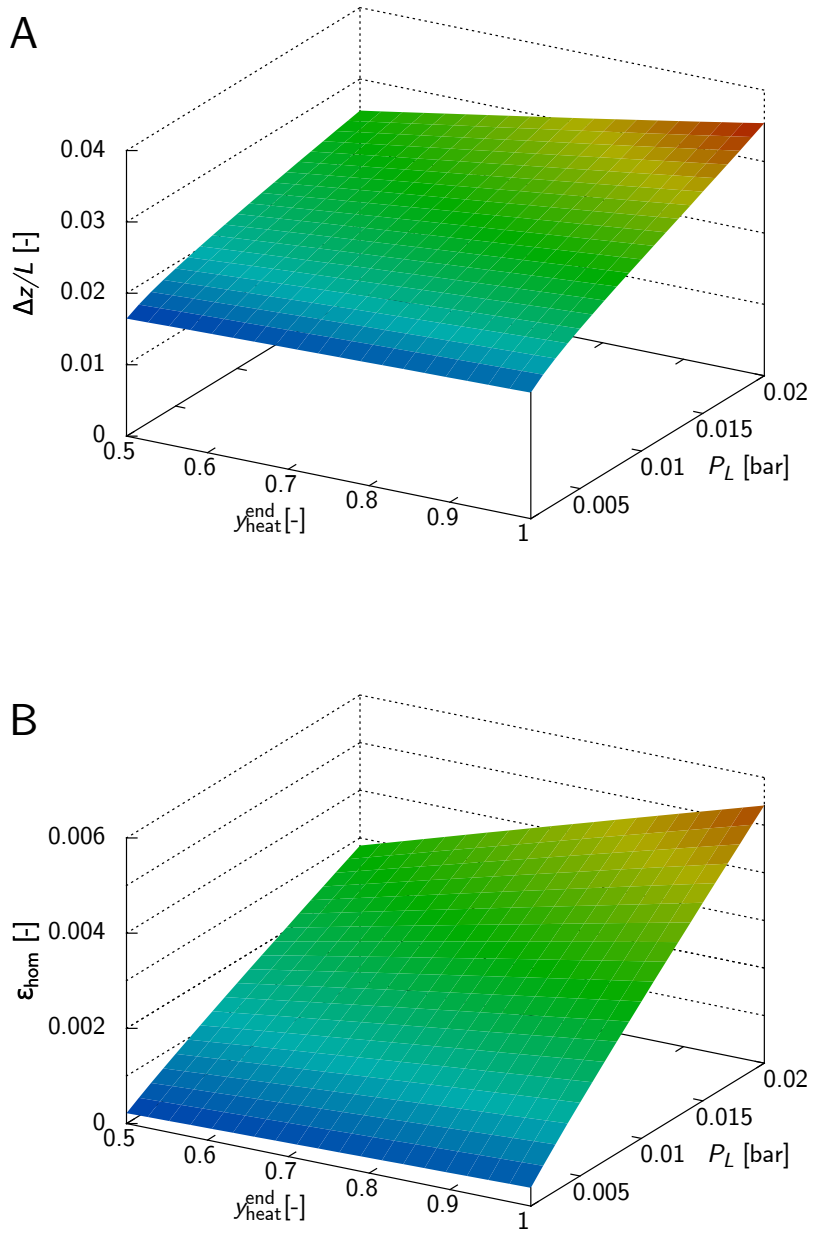

Figure C.2. – Maximal deviations of the extreme approaches in describing the pressurization step: (A) penetration depth of the front when considering that a single shock transition travels through the column; (B) deviation between the final CO_2 composition determined by considering a final homogeneous profile and the composition corresponding to the initial partial pressure.

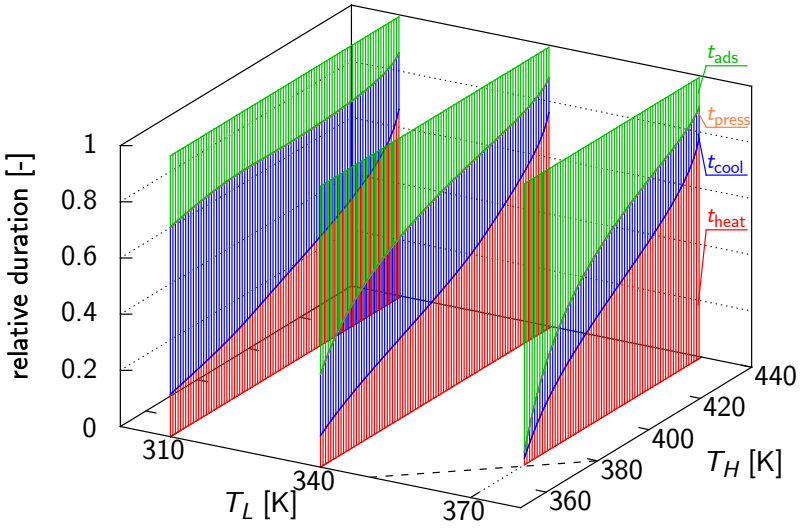

Figure C.3. – Relative contribution of the single steps to the total cycle duration as a function of the high and low temperatures levels. Simulations have been carried out with $T_{\text{cool}} = 300\,\text{K}$, $T_{\text{heat}} = 440\,\text{K}$, $P_H = 1\,\text{bar}$ and $y_F = 0.12$

C.3 COMPARISON TO THE DETAILED MODEL

The T-, P- and y-profiles calculated using the shortcut model are compared to those calculated with the detailed model at the CSS, for the operating conditions shown in Figure C.4.

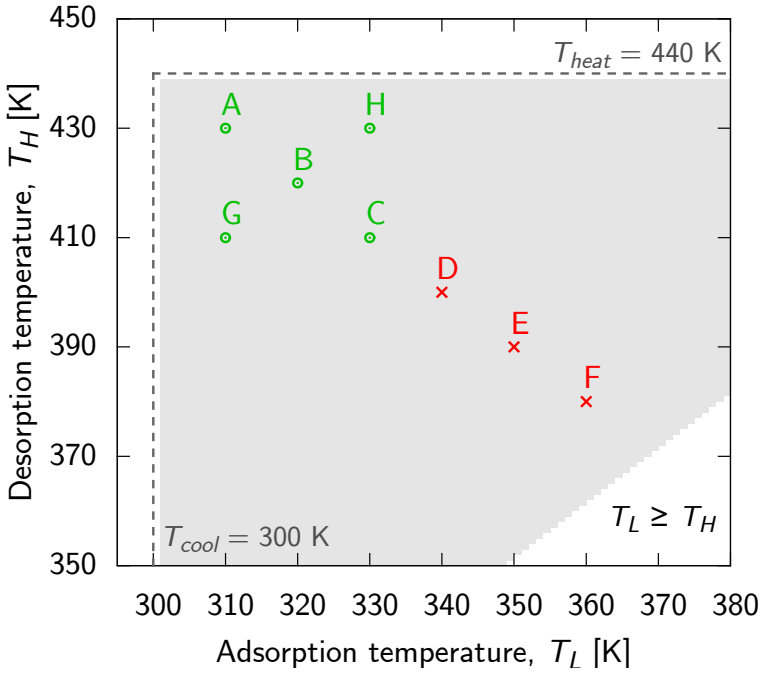

Figure C.4. – Summary of the operating conditions of Figures C.5 to C.12 in the (T_L, T_H) plane. The color scheme refers to the degree of agreement between the shortcut and detailed model predictions of the T-, P- and y-profiles: decent agreement (green circles) and poor agreement (red crosses).

The color of the points refers to the qualitative degree of agreement between the shortcut and detailed models. As seen in Figures C.5 to C.12, the points represented in green correspond to a decent agreement, in red to a poor agreement, and at conditions corresponding to point C the agreement is intermediate. Generally a sufficient agreement is observed for the conditions, which yield pure CO_2 at the end of the heating step, and high and low temperature levels of the bed (T_H and T_L) that are similar to the heating and cooling temperatures T_{cool} and T_{cool}, respectively. In fact, as the difference increases, the temperature of the wall in the detailed model will affect the dynamics of the heating

and cooling steps to a greater extent. It is however important to note that the conditions where the agreement is poor yield low CO_2 purity and recovery, which do not reach the target.

The detailed model equations are those presented in chapter 2 and the corresponding parameters are listed in Table C.1.

Table C.1. – Parameters for the adsorption column model

Parameter		Value	
Column length	L	1.2	m
Column inner diameter	d_i	0.030	m
Column outer diameter	d_o	0.032	m
Bulk density of the packing	ρ_b	708	kg/m^3
Particle density	ρ_p	1085	kg/m^3
Solid density	ρ_s	2360	kg/m^3
Particle size	d_p	2×10^{-3}	m
Solid heat capacity	C_s	920	J/K kg
Heat capacity of the wall	$C_{p,w}$	4×10^6	$J/K\,m^3$
Fluid viscosity	μ	1.9×10^{-5}	Pa s
Isotherm parameters	from Hefti et al.[83]		
Heat transfer coefficient	$h_{\text{wall-bed}}$	20	$W/m^2\,K$
Heat transfer coefficient	$h_{\text{HX-wall}}$	100	$W/m^2\,K$
Mass transfer coefficient	k_{CO_2}	0.15	s^{-1}
Mass transfer coefficient	k_{N_2}	0.50	s^{-1}

C.4 EFFECT OF THE WALL TEMPERATURE

In this work the temperature of the wall is assumed to be equal to that of the bed, resulting in an estimation of the minimum heat duty of the TSA cycle according to Eq. 4.21. However, in a real system the wall will take temperatures between that of the bed and that of the heat exchange fluid, and its value will depend on the relative magnitude of the convective heat transfer coefficients fluid/wall vs. wall/sorbent as illustrated in Figure C.13.

In order to assess the impact of this assumption on the predicted process performance, the other extreme case was considered, i.e., that

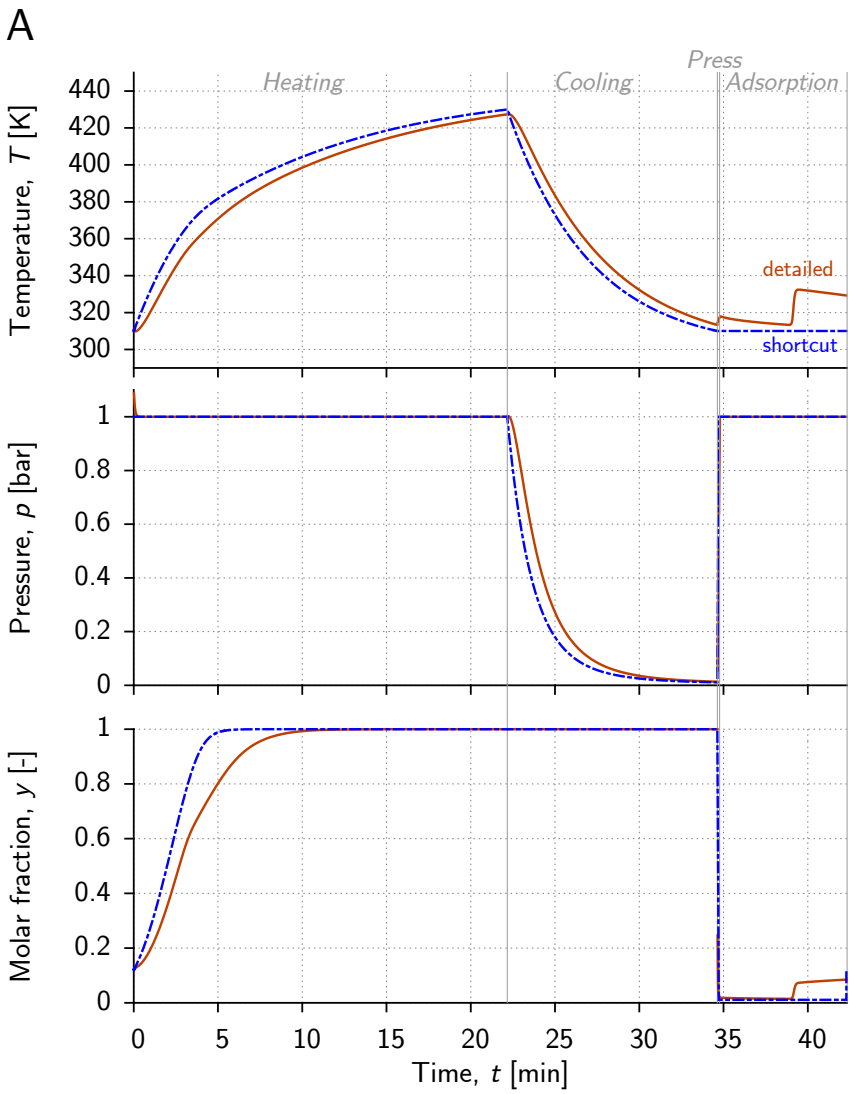

Figure C.5. – Temperature, pressure and composition profiles as predicted by the shortcut model (dashed lines) and by the detailed model [24] (solid lines) for the operating conditions defined by point A in Figure C.4. The profiles are those located according to the flow direction at $z = 0$ for the heating and cooling steps, and at $z = L$ for the pressurization and adsorption steps.

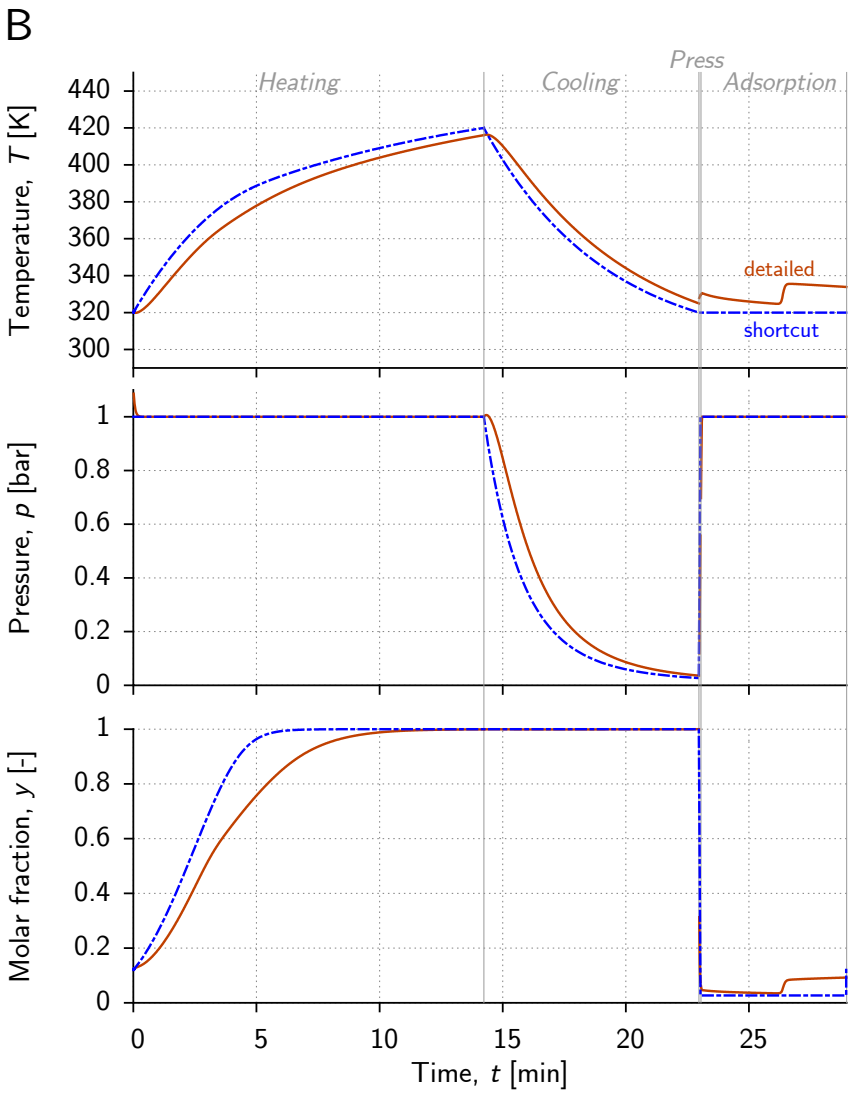

Figure C.6. – Temperature, pressure and composition profiles as predicted by the shortcut model (dashed lines) and by the detailed model [24] (solid lines) for the operating conditions defined by point B in Figure C.4. The profiles are those located according to the flow direction at $z = 0$ for the heating and cooling steps, and at $z = L$ for the pressurization and adsorption steps.

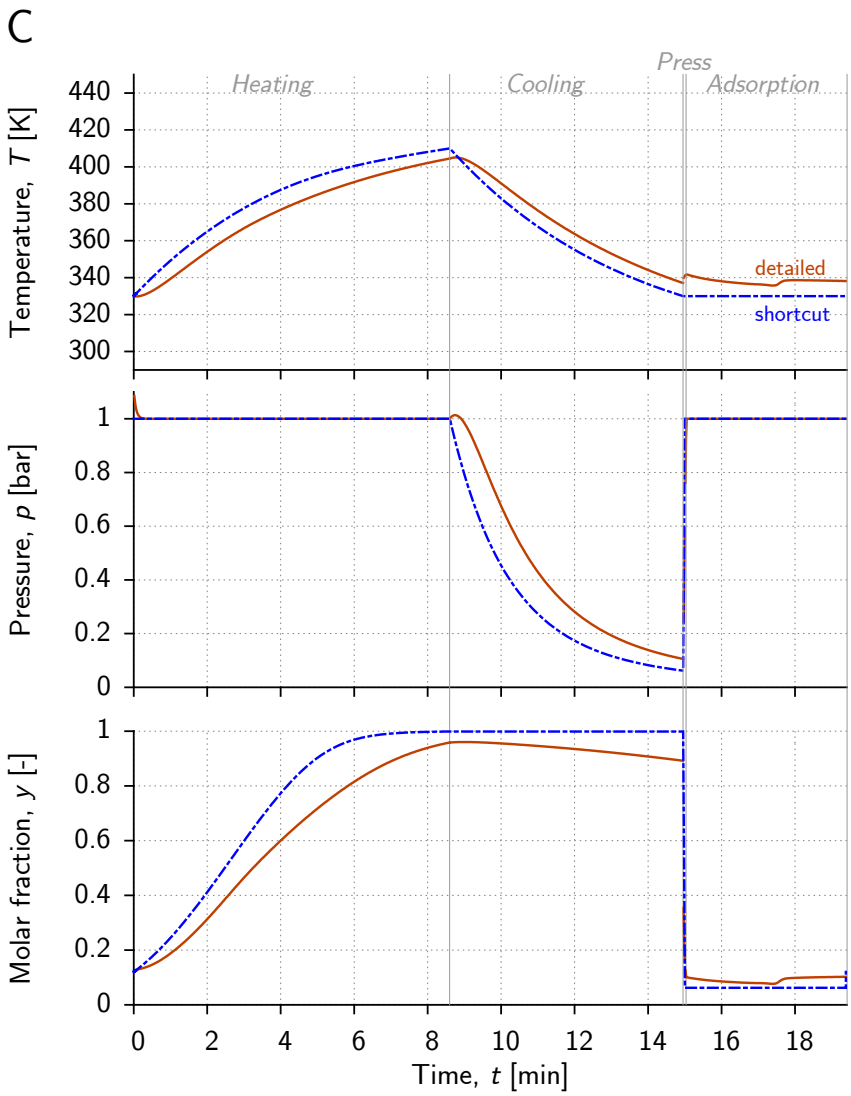

Figure C.7. – Temperature, pressure and composition profiles as predicted by the shortcut model (dashed lines) and by the detailed model [24] (solid lines) for the operating conditions defined by point C in Figure C.4. The profiles are those located according to the flow direction at $z = 0$ for the heating and cooling steps, and at $z = L$ for the pressurization and adsorption steps.

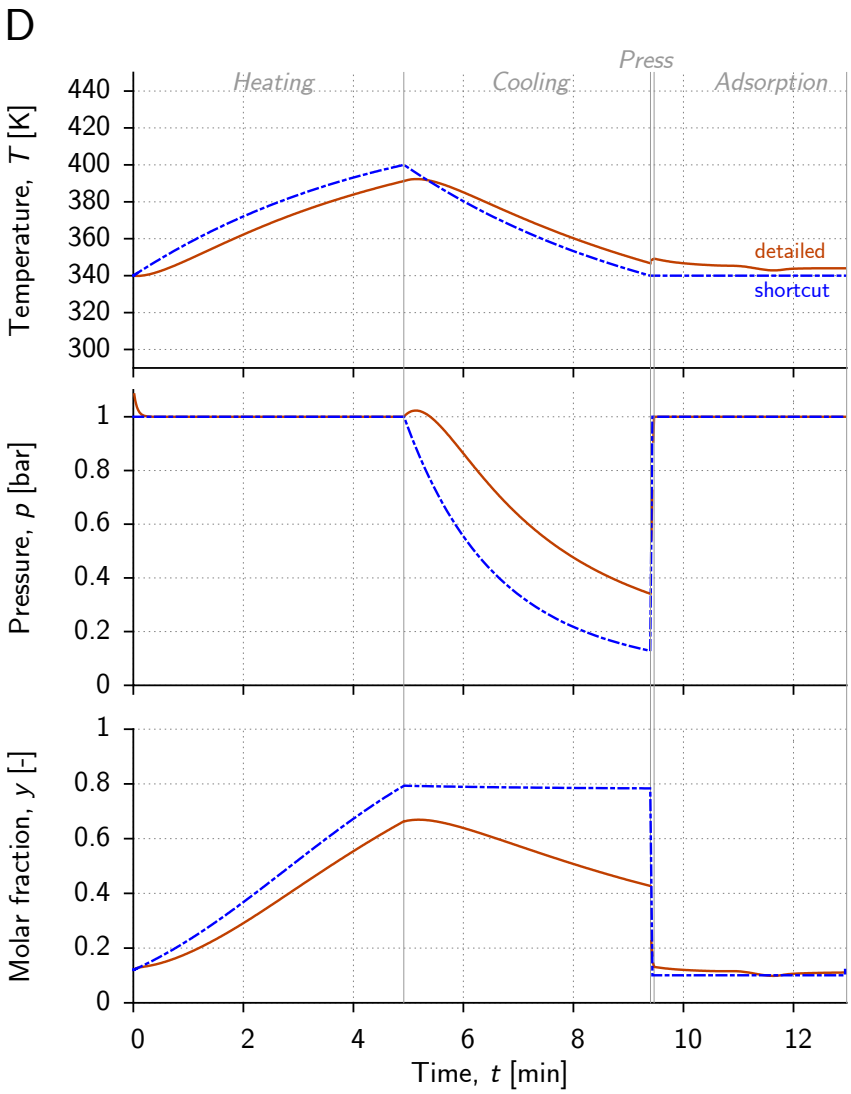

Figure C.8. – Temperature, pressure and composition profiles as predicted by the shortcut model (dashed lines) and by the detailed model [24] (solid lines) for the operating conditions defined by point D in Figure C.4. The profiles are those located according to the flow direction at $z = 0$ for the heating and cooling steps, and at $z = L$ for the pressurization and adsorption steps.

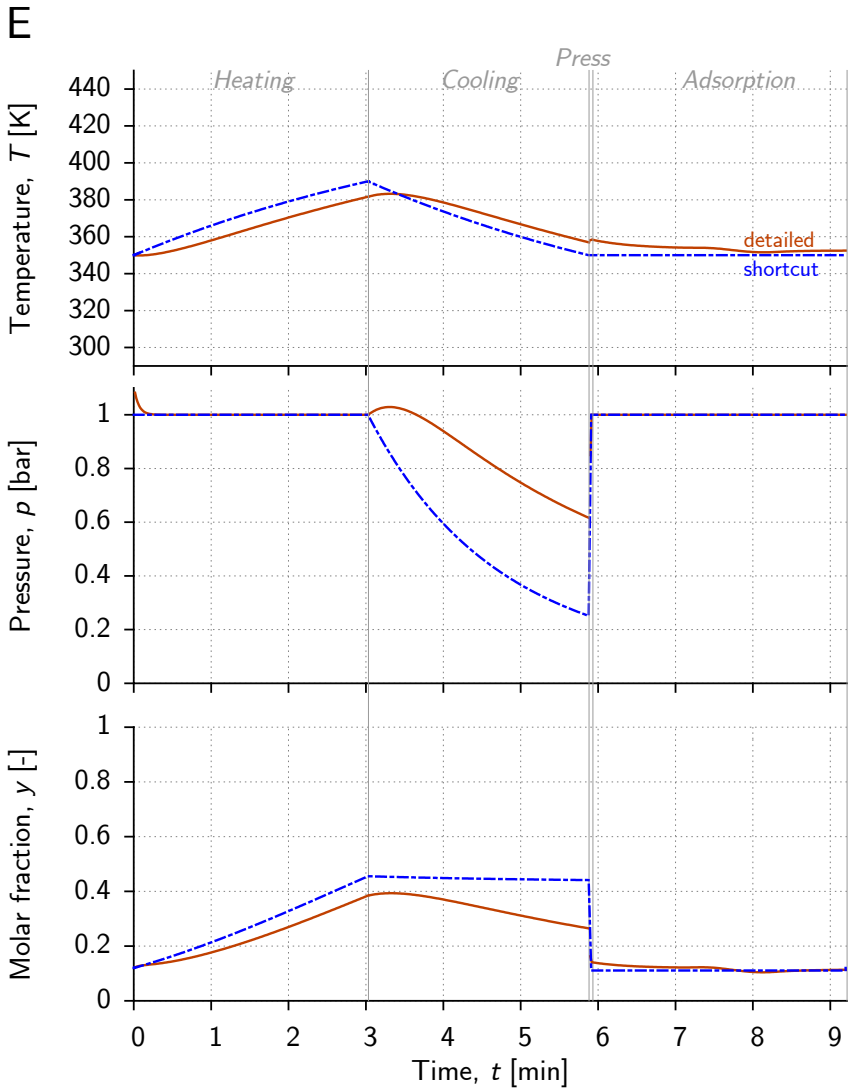

Figure C.9. – Temperature, pressure and composition profiles as predicted by the shortcut model (dashed lines) and by the detailed model [24] (solid lines) for the operating conditions defined by point E in Figure C.4. The profiles are those located according to the flow direction at $z = 0$ for the heating and cooling steps, and at $z = L$ for the pressurization and adsorption steps.

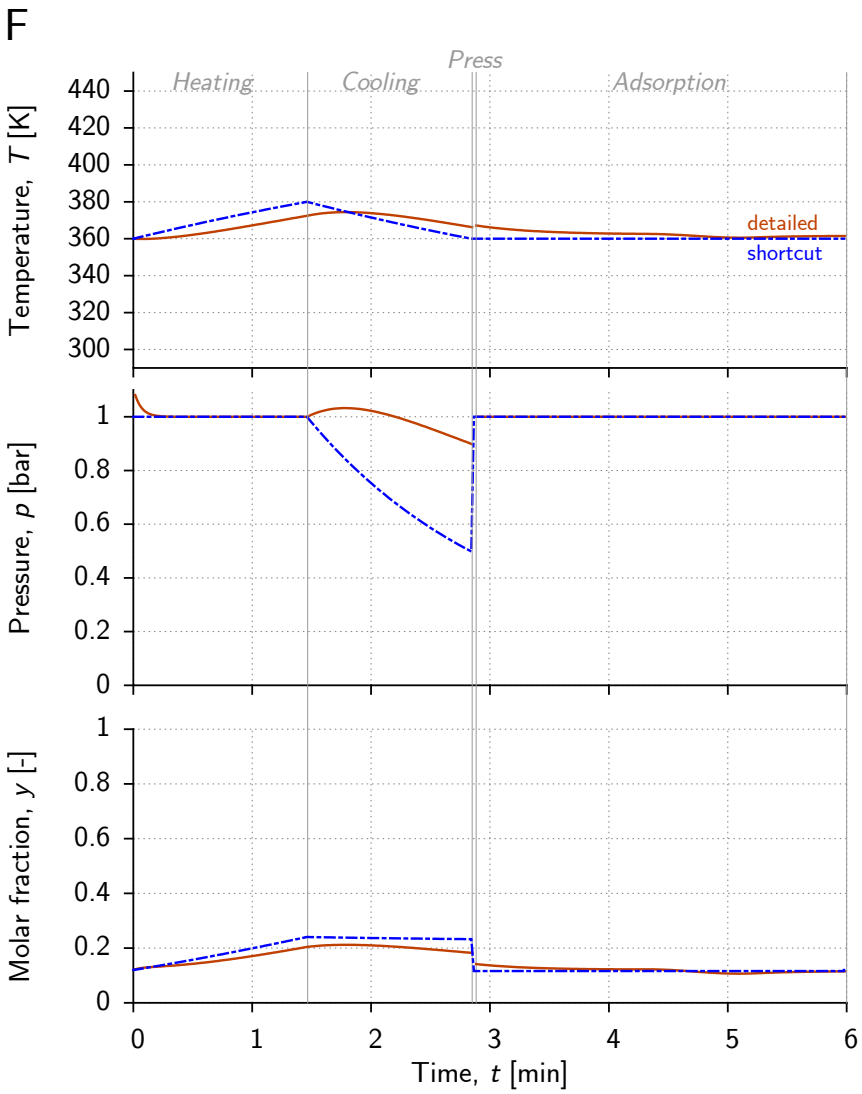

Figure C.10. – Temperature, pressure and composition profiles as predicted by the shortcut model (dashed lines) and by the detailed model [24] (solid lines) for the operating conditions defined by point F in Figure C.4. The profiles are those located according to the flow direction at $z = 0$ for the heating and cooling steps, and at $z = L$ for the pressurization and adsorption steps.

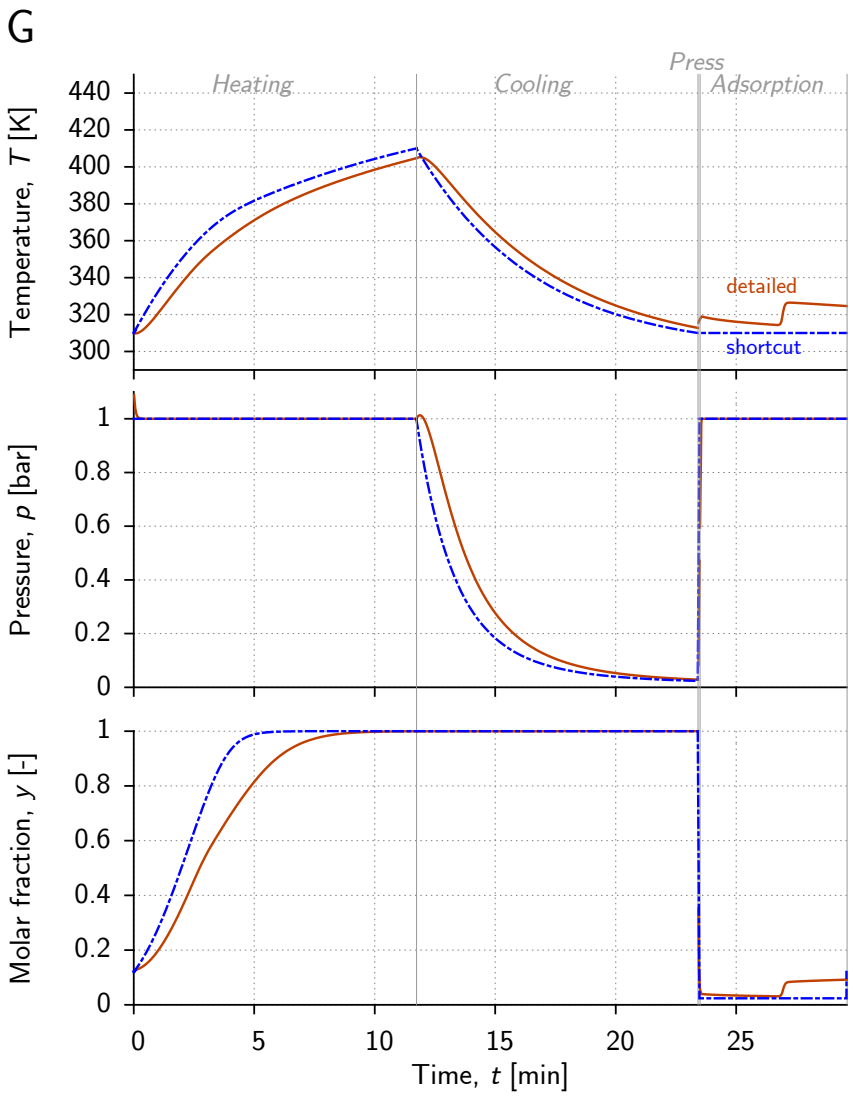

Figure C.11. – Temperature, pressure and composition profiles as predicted by the shortcut model (dashed lines) and by the detailed model [24] (solid lines) for the operating conditions defined by point G in Figure C.4. The profiles are those located according to the flow direction at $z = 0$ for the heating and cooling steps, and at $z = L$ for the pressurization and adsorption steps.

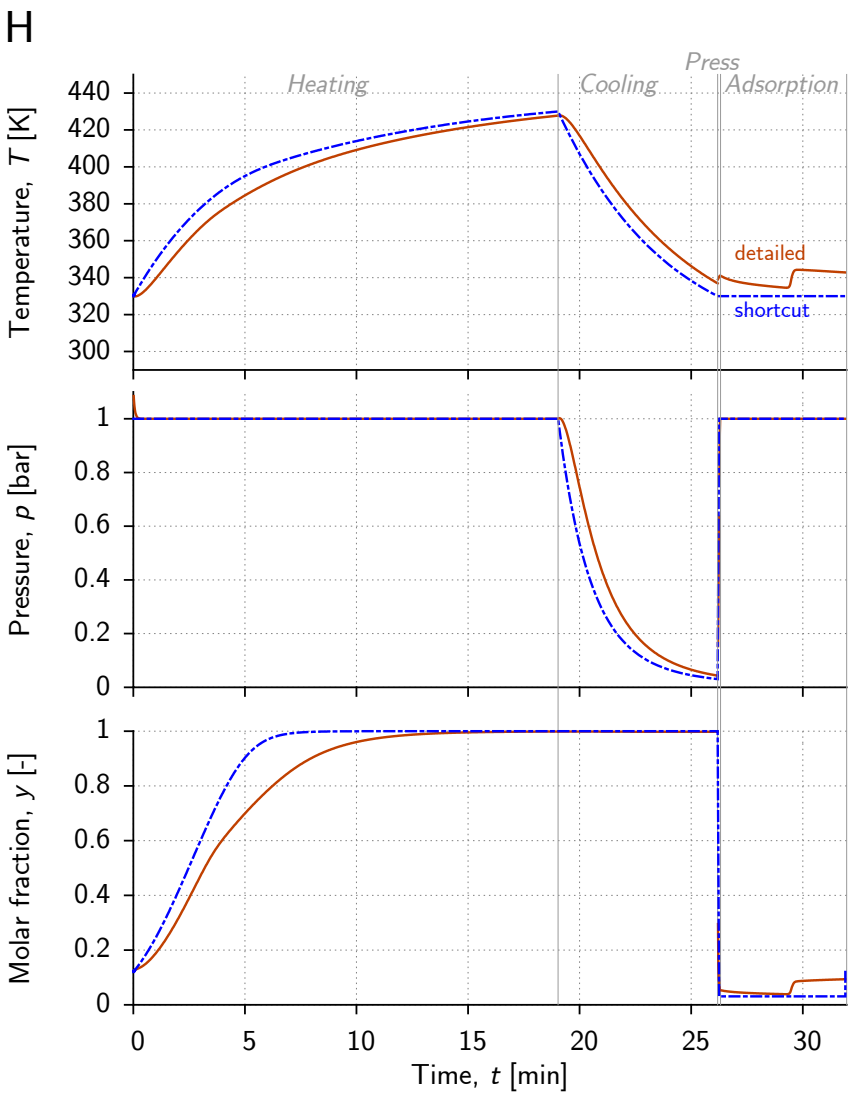

Figure C.12. – Temperature, pressure and composition profiles as predicted by the shortcut model (dashed lines) and by the detailed model [24] (solid lines) for the operating conditions defined by point H in Figure C.4. The profiles are those located according to the flow direction at $z = 0$ for the heating and cooling steps, and at $z = L$ for the pressurization and adsorption steps.

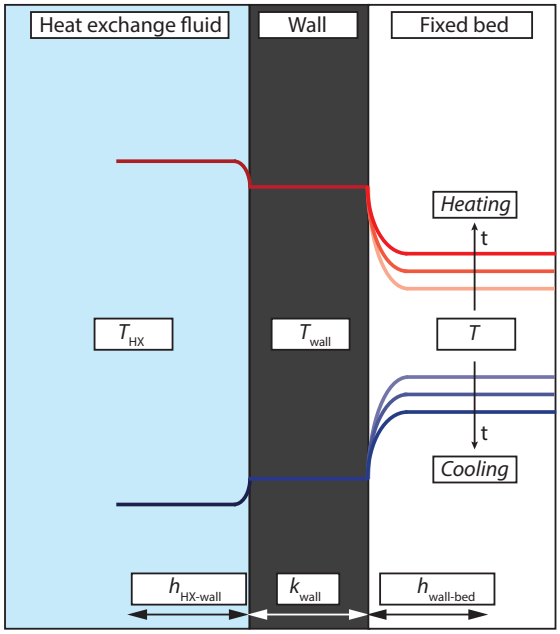

Figure C.13. – Schematic illustration of the temperatures of the heat transfer fluid, column wall and bed.

the temperature of the wall is equal to that of the heat exchange fluid. This results in the following expression for the heating duty Q^*_{TSA}:

$$Q^*_{\mathrm{TSA}} = V_{\mathrm{col}} \left(C_{p,b}(T_H - T_L) - \rho_b \sum_{i=1}^{2} \Delta n_i (-\Delta H_i) \right) + V_{\mathrm{wall}}\, C_{p,w}(T_{\mathrm{heat}} - T_{\mathrm{cool}}) \tag{C.12}$$

The pareto front for a heating temperature of $T_{\mathrm{heat}} = 440\,\mathrm{K}$ as predicted considering both cases $T_{\mathrm{wall}} = T_{\mathrm{bed}}$ (Q_{TSA}) and $T_{\mathrm{wall}} = T_{\mathrm{HX}}$ (Q^*_{TSA}) is shown in Figure C.14.

The difference becomes very small for the operating conditions which yield the smallest specific energy requirement. In fact, these operating conditions correspond to high and low temperature values of the bed which approach the heating and cooling temperatures. It is important to recall that for a real system the wall temperature cycles between values which are intermediate to these two extreme cases. This effect explains the deviation between the detailed and shortcut models only partly; the greater difference is due to heat and mass transfer effects during the adsorption step.

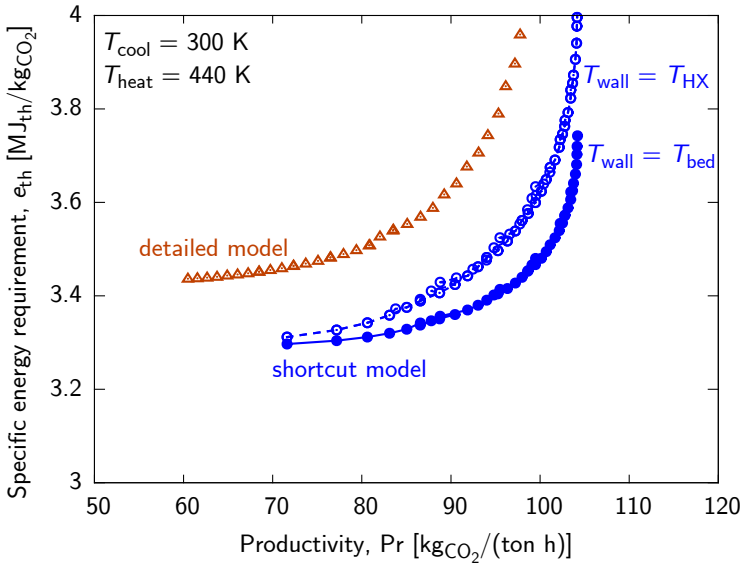

Figure C.14. – Comparison of the pareto predicted by the shortcut model when assuming a wall temperature equal to that of the heat transfer fluid or to that of the bed.

C.5 MINIMUM ENERGY REQUIREMENT

The thermal energy requirement is primarily governed by the ratio:

$$-\frac{\Delta n}{\Delta T} = \frac{n_{1,\text{ads}}^{\text{end}}(T_L) - n_{1,\text{heat}}^{\text{end}}(T_H)}{T_H - T_L} \tag{C.13}$$

The conditions at the end of the adsorption step are known, as well as those at the end of the heating step, with the exception of the composition. In a first approximation, this composition can be assumed to be pure CO_2 (y = 1). Hence equation C.13 can be evaluated for different pairs (T_L, T_H) provided the temperature dependent equilibrium relation and the feed composition are known.

This ratio is shown as a contour plot in the T_L, T_H plane for the CO_2/N_2 system on 13X and a feed composition of $y = 0.12$ in Figure C.15. Positive values of Δn (indicated with colors) require a minimum $\Delta T \approx 40\,K$, because $n_{1,\text{heat}}^{\text{end}}$ is evaluated at a larger partial pressure than $n_{1,\text{ads}}^{\text{end}}$. A maximum is observed at $T_L = 257, T_H = 456$, and the arrows emanating from this point indicate three directions

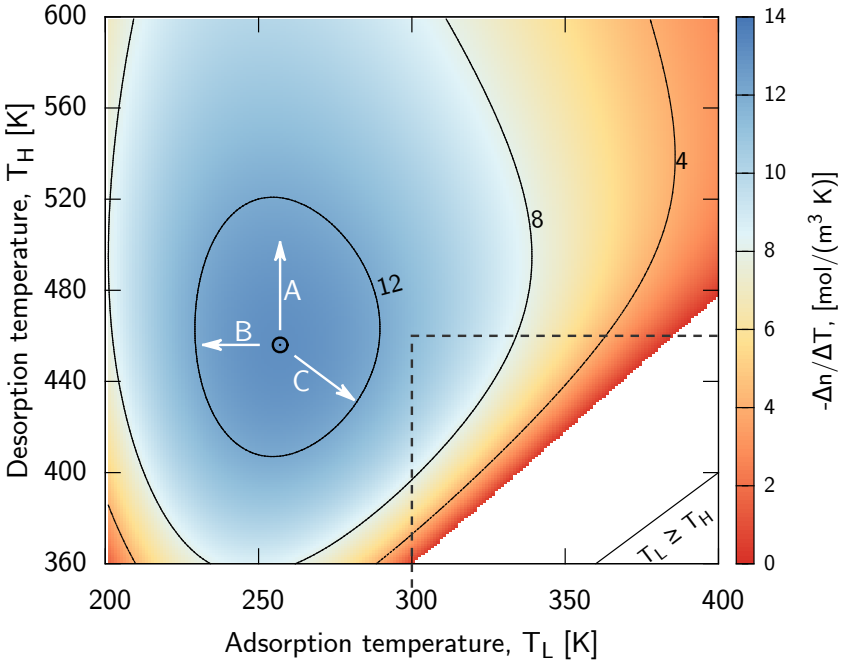

Figure C.15. – Map of the $\Delta n/\Delta T$ ratio in the T_L, T_H plane. The white arrows labeled with A, B and C represent directions along which different phenomena predominate the evolution of the surface. The dashed line indicates the typical temperature range for TSA applications.

along which a different phenomena predominates the decrease in $\Delta n/\Delta T$:

Paths A and B. The adsorbed amount in equilibrium with very large temperatures will tend to zero such that:

$$\lim_{T_H \gg} \left(-\frac{\Delta n}{\Delta T} \right) = \frac{n_{1,\text{ads}}^{\text{end}}(T_L)}{T_H - T_L} \tag{C.14}$$

The adsorbed amount in equilibrium with very small temperatures will tend to a constant value n_1^{∞}:

$$\lim_{T_H \gg} \left(-\frac{\Delta n}{\Delta T} \right) = \frac{n_1^{\infty} - n_{1,\text{heat}}^{\text{end}}(T_H)}{T_H - T_L} \tag{C.15}$$

Therefore the value of the ratio will decrease along directions A and B along which the numerator of Equations C.14 and C.15 stays constant and the denominator increases.

Path C. Along this direction the temperature difference decreases, and smaller ΔT values result in a smaller cyclic capacity. The provided heat is used less efficiently, and a smaller fraction is consumed for the actual desorption of CO_2 resulting in a larger share of "parasitic energy", or a less efficient desorption.

Reasonable temperature ranges for TSA applications will typically be such as to not enclose the global maximum of $\Delta n / \Delta T$ as shown by the dashed lines in Figure C.15. In fact, CO_2 saturation on commercial physisorbents is usually at much lower temperatures than ambient, and it is sensible to increase the regeneration temperature only if this causes a larger cyclic capacity, since higher desorption temperatures imply a higher cycle duration and higher energy requirement. Therefore, within typical temperature ranges for TSA applications, the specific energy requirement will monotonically decrease with increasing decrease with increasing ΔT.

C.6 SEMI-QUANTITATIVE PREDICTION OF THE PRODUCTIVITY

The shortcut model provides semi-quantitative prediction of trends, as shown in Figs. 6(A) and 8(A) for the shortcut model and detailed model, respectively. At constant specific energy consumption, the productivity increases by 25% to 30% upon an increase in heating temperature of 20 K; and decreased by 30% to 35% upon a decrease in heating temperature by 20 K. This exercise can be performed for the entire range of specific energy consumption values, which are common to two pareto fronts. Figure C.16 shows the the number distribution of the absolute change in productivity associated a decrease or an increase in heating temperature by 20 K from $T_{\text{heat}} = 440\,\text{K}$. Generally a good agreement is observed in the range of change in productivity predicted by both models.

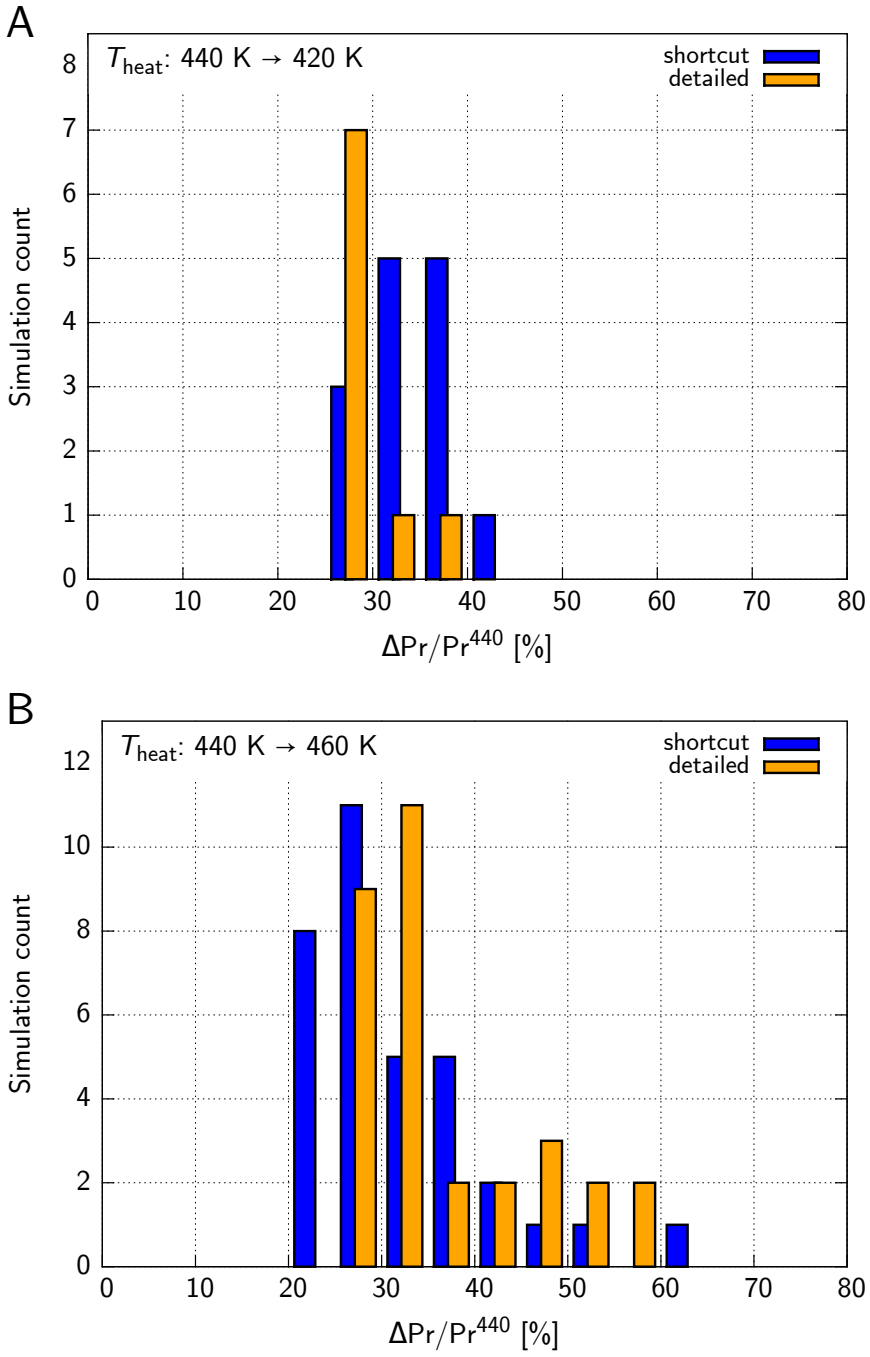

Figure C.16. – Distribution of the absolute change in productivity at constant specific energy consumption. (A) Upon a decrease in heating temperature from 440 K to 420 K. (B) Upon an increase in heating temperature from 440 K to 460 K. Bin width: 5%

D SUPPLEMENTARY MATERIAL FOR CHAPTER 6

D.1 MODEL COMPARISON

Temperature and composition profiles for exemplary operating conditions resulting in an adsorption temperature of 305 K and in a desorption temperature of 410 K are shown in Figure D.1. Let us start this analysis at the end of the adsorption step, i.e., with the column saturated with the feed mixture at 305 K. As it is heated, CO_2 desorbs until it completely step the nitrogen contained in the gas phase (see Figure D.1). A plateau in the temperature profile is observed at about 380 K and 340 K for MOF-Mn and MOF-Fe, respectively. In fact, due to the presence of a step in the isotherm, most of the CO_2 is desorbed within a narrow temperature range in the vicinity of the step temperature at 1 bar ($T_{\text{step}}^{\text{des}}$). While the heating, cooling and pressurization steps are qualitatively similar for both materials, the exit composition profile of the adsorption step is noticeably different. In the case of MOF-Mn, a shock transition separates the initial state from the feed state, while in the case of MOF-Fe, a shock-wave-shock transition is observed (note that the wave is fairly flat). The corresponding performances are reported in Table D.1. Since the bed density, the specific heat and the cyclic capacity for the chosen operating conditions are similar for both materials, the resulting purity, productivity and energy consumption are also similar. A striking difference is observed in the achieved recovery: while MOF-Mn recovers over 98%, MOF-Fe achieves only a recovery of 56% due to the disperse composition front that evolves during the adsorption step.

The shortcut model profiles are compared to those predicted by the detailed model for the same operating conditions. A good agreement between the two models is observed during the heating, cooling and pressurization steps for both MOF-Mn and MOF-Fe. There are,

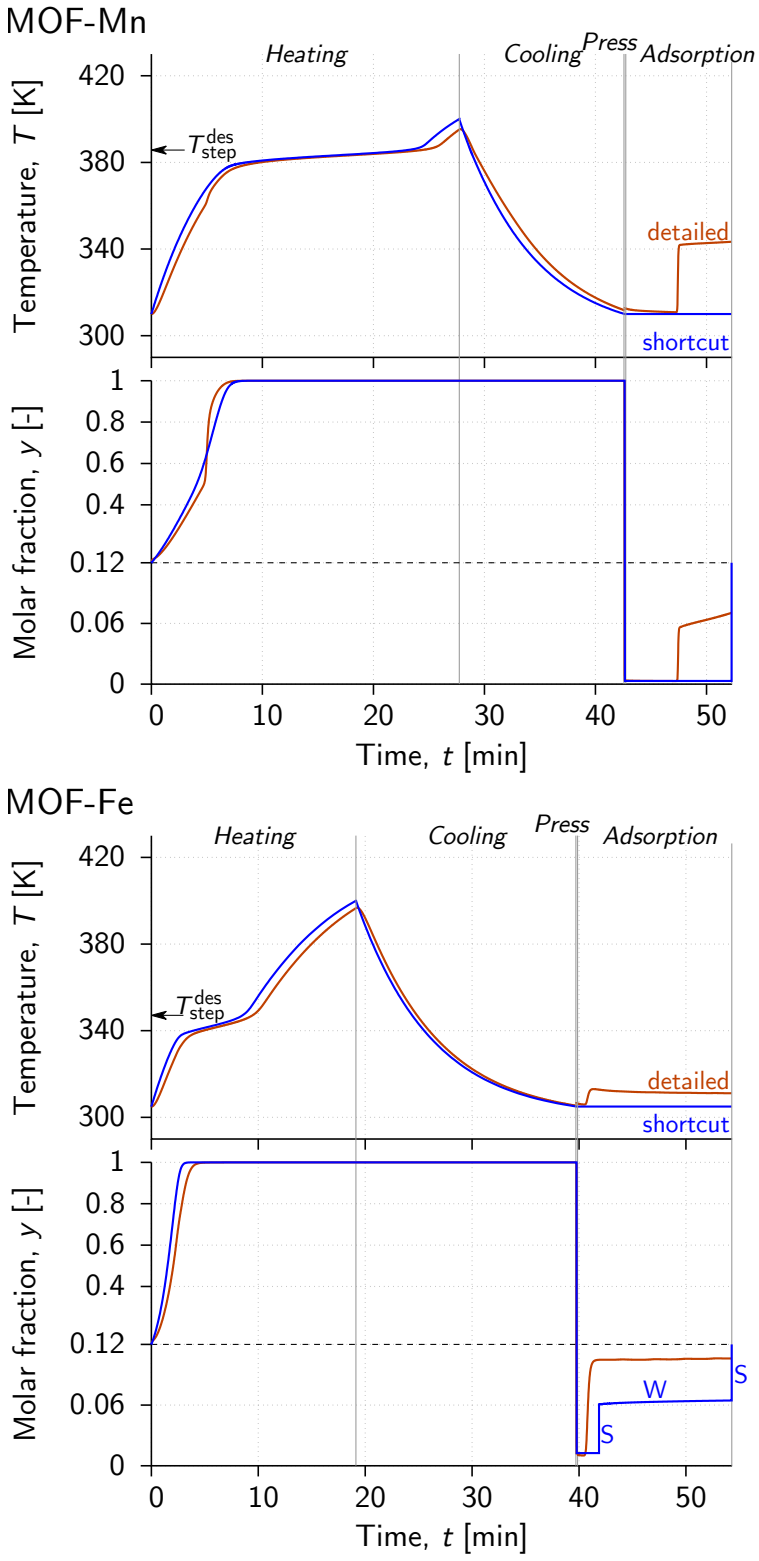

Figure D.1. – Temperature and composition profiles at cyclic steady state predicted by the shortcut and detailed model for MOF-Fe. The operating conditions are such that an adsorption temperature of $T_{ads} = 305\,K$ and a desorption temperature of $T_{ads} = 410\,K$ are achieved with the shortcut model.

Table D.1. – Performance indicators of the cycles shown in Figure D.1 predicted by the shortcut model.

		MOF-Mn	MOF-Fe
CO_2 purity, Φ	$[-]$	0.981	0.978
CO_2 recovery, r_{TSA}	$[-]$	0.986	0.56
Productivity, Pr	$[kg_{CO_2}/(m^3h)]$	67.3	61.1
Energy cons. e_{TSA}	$[MJ/kg_{CO_2}]$	3.34	3.68

however, significant differences during the adsorption step, where the breakthrough of CO_2 occurs earlier according to the detailed model due to the dispersed front predicted by it because of the finite heat and mass transfer rates. Nevertheless, the rather good agreement supports the use of the shortcut model as a tool to perform a preliminary screening of the materials.

While the temperature and composition profiles provide useful insight into the operation of the TSA process, it is worthwhile to perform a parametric analysis of the process performance in order to obtain a comparative performance assessment, and to appreciate the importance of the step-shape of the isotherm on the TSA process.

D.2 PERFORMANCE OF AN OPTIMAL MATERIAL

The Pareto fronts in the space of the separation specifications are shown in Figure D.2 for the optimal materials presented in section 6.4.1.

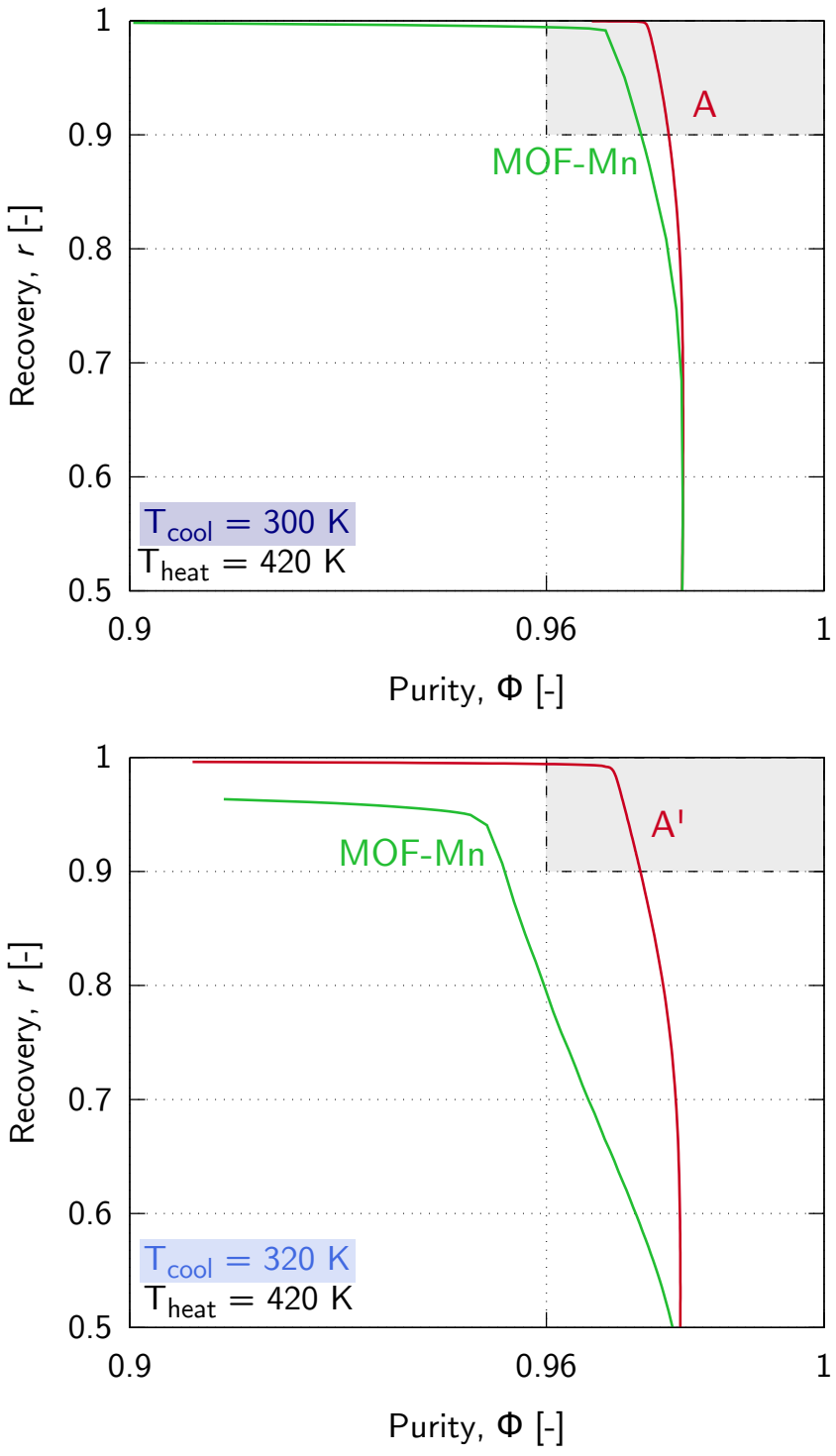

Figure D.2. – Reachable specifications for MOF-Mn and material A at cooling temperature 300 K (top) and for MOF-Mn and material A′ at cooling temperature 320 K (bottom).

D.3 MINIMUM ENERGY CONSUMPTION

Under the assumption of negligible heat capacity of the sorbate (gas and adsorbed phases), and of negligible N_2 adsorption, the specific energy consumption is given by:

$$e_{\mathrm{TSA}} \approx V_{\mathrm{col}} \overline{C}_{p,col} \frac{\Delta T}{\Delta n} + (-\Delta H) \tag{D.1}$$

where $\Delta T = T_{\mathrm{des}} - T_{\mathrm{ads}}$ and $\Delta n = n(p_{\mathrm{ads}}, T_{\mathrm{ads}}) - n(p_{\mathrm{des}}, T_{\mathrm{des}})$. The analysis of the function $f(T_{\mathrm{ads}}, T_{\mathrm{des}}) = \Delta T / \Delta n$, reveals that a minimum exists for the pairs of adsorption and desorption temperatures that satisfy the following conditions:

$$\left.\frac{\partial n}{\partial T}\right|_{p_{\mathrm{ads}}, T_{\mathrm{ads}}} = \left.\frac{\partial n}{\partial T}\right|_{p_{\mathrm{des}}, T_{\mathrm{des}}} = -\frac{\Delta n}{\Delta T} \tag{D.2}$$

$$\left.\frac{\partial^2 n}{\partial T^2}\right|_{p_{\mathrm{ads}}, T_{\mathrm{ads}}} < 0 \tag{D.3}$$

$$\left.\frac{\partial^2 n}{\partial T^2}\right|_{p_{\mathrm{des}}, T_{\mathrm{des}}} > 0 \tag{D.4}$$

These conditions can be easily represented graphically with adsorption isobars at the adsorption and desorption partial pressures. The state of the column representing the optimal adsorption and desorption conditions (T_{ads}, $n(p_{\mathrm{ads}})$, T_{ads} and T_{des}, $n(p_{\mathrm{des}}, T_{\mathrm{des}})$, respectively should be such that the derivative of both isobars is the same and equal to the slope of the chord connecting the two states states. Figure D.3 illustrates this condition for MOF-Mn and for zeolite 13X; the steeper chord of the MOF-Mn material as compared to zeolite 13X is representative of a smaller value $\Delta T / \Delta n$, more particularly, there is a factor two difference between MOF-Mn and 13X. Although the specific heat capacity and the isosteric heat of adsorption of the investigated MOFs are rather large, the specific energy consumption of a TSA process might still be lower than for commercial materials, due to the large cyclic capacity upon a small temperature difference.

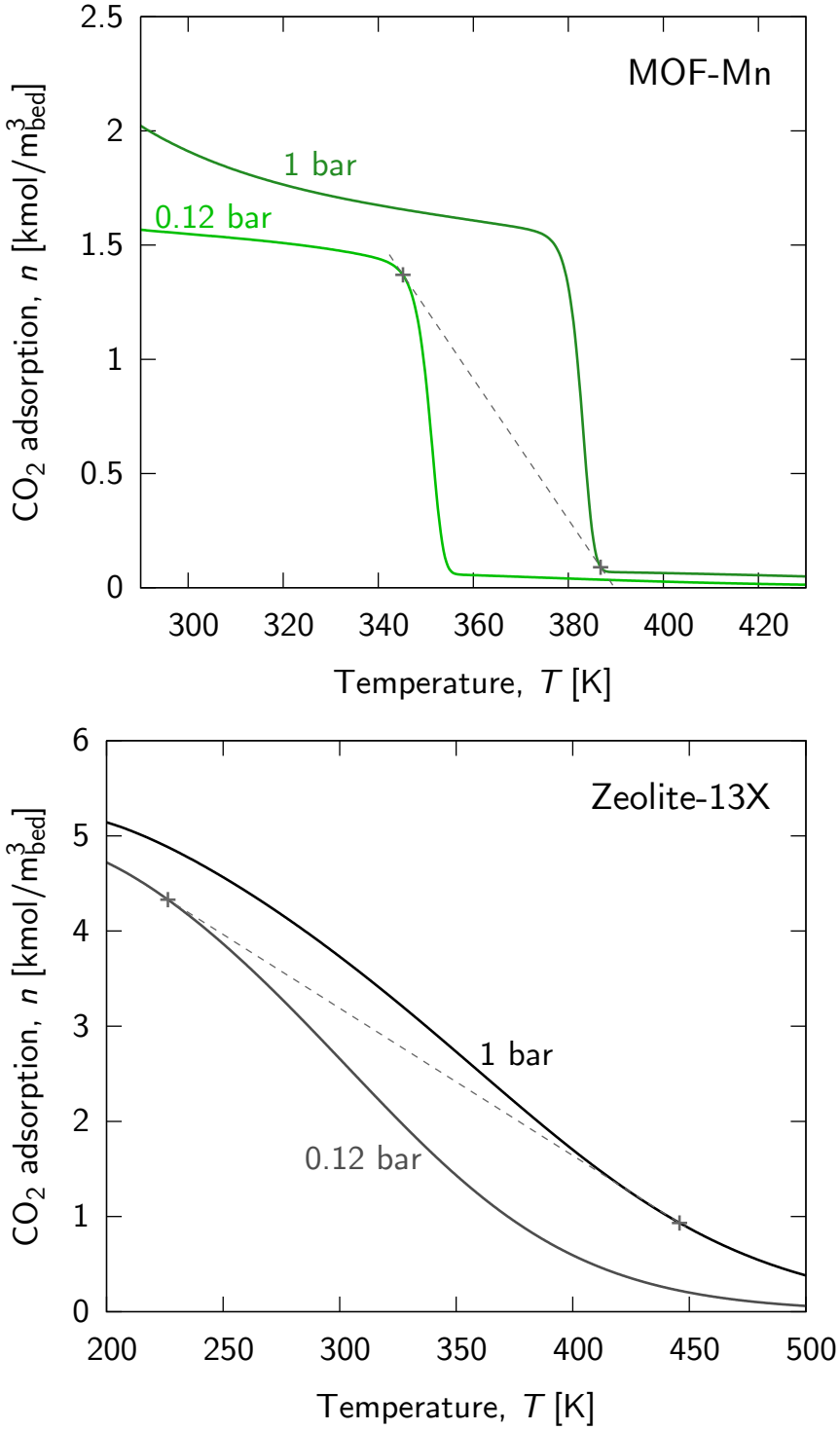

Figure D.3. – Graphical interpretation of the minimum energy constraint for MOF-Mn and zeolite 13X. The dashed line connects the adsorption and desorption conditions that satisfy equations D.2 to D.4 and result in a minimal specific energy consumption.

ACRONYMS

BPR	back pressure regulator
CAPEX	capital expenditures
CCS	CO_2 capture and storage
CCU	CO_2 capture and utilization
COP	conference of the parties
CSS	cyclic steady state
DACCS	direct air carbon capture and storage
IAST	ideal adsorbed solution theory
KPI	key performance indicator
LDF	linear driving force
MCS	multi-level coordinate search
MO-MCS	multiobjective multi-level coordinate search
MEA	monoethylamine
MFC	mass flow controller
MOF	metal organic framework
MS	mass spectrometer
NNC	normalized normal constraint
ODE	ordinary differential equation
OPEX	operational expenditures
PDAE	partial differential algebraic equation
PDE	partial differential equation
PSA	pressure swing adsorption
TSA	temperature swing adsorption
UNFCCC	united nations convention on climate change
USC	ultra super critical
VSA	vacuum swing adsorption
w-DSL	weighted dual site Langmuir